The Development of an In Vitro Model of Spinal Cord Injury Using Microfabrication

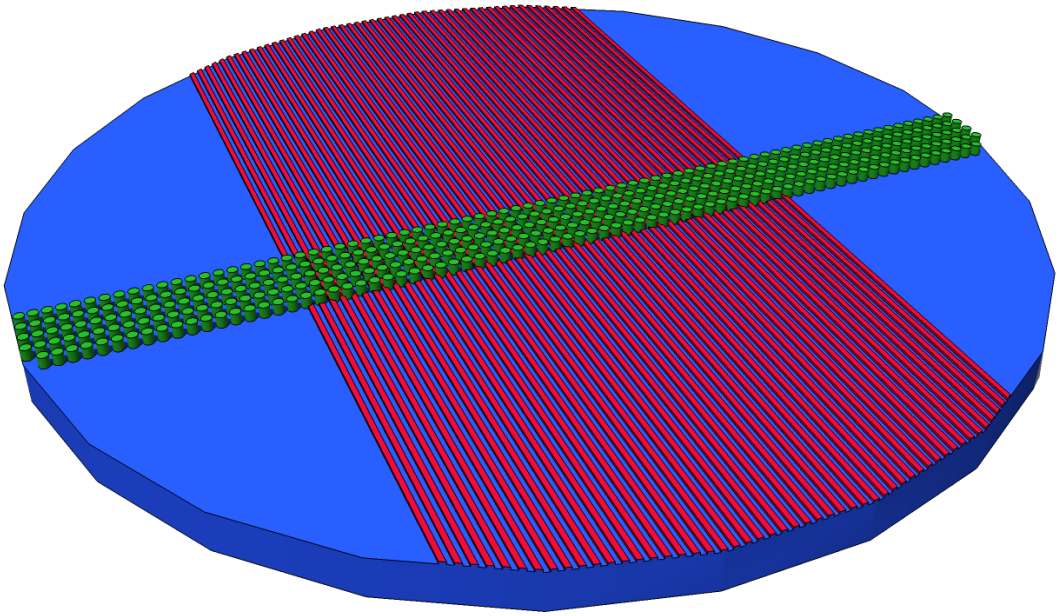

Lewis Ross BEng, MRes

Submitted in fulfilment of the requirements for the Degree of PhD

Centre for Cell Engineering
Institute of Molecular, Cell and Systems Biology
College of Medical Veterinary & Life Sciences
University of Glasgow

September 2012

Abstract

This project aimed to develop an *in vitro* model of spinal cord injury. A device was developed that could, in conjunction with an existing myelinating culture system, aligned axons into parallel rows and contain the soma to a predefined area; thus creating a structure similar to the spinal cord. It was intended for the device to be simple to produce and use, provide easy accesses to the axons for wounding and allow simple measurement of axonal regrowth. An additional aim of the project was to develop a method of cell wounding that was reproducible, precise and allowed observation of the wounding process.

A series of ridges were created on PDMS devices, which were used to align the axons. These ridges were 5 µm deep and 12.5, 25 or 50 µm wide. The 12.5 µm ridges aligned an average of 54% of the axons within 10° of the axis parallel to the ridges. The 25 and 50 µm only managed to align 37% and 28% in this direction. Flat control devices aligned 16% of the axons in an equivalent direction, which corresponded to a random alignment. From this it was concluded that 12.5 µm ridges should be used to align the axons.

Rows of 25 µm high, 20 µm diameter pillars were placed across the devices in an attempt to contain cells to one side of the device. The pillars had gaps between them of 6, 8 or 10 µm. MG63 cells were used to test the pillars' containment ability. It was found that the cells could climb over the pillars and so multiple rows of pillars where created to attempt to trap the cells. The multiple rows did not full contain the cells but it was found that 5 rows with gaps sizes of 6 µm could slow the cells migration across the devices.

It was found that the pillar rows were not necessary to contain the neuronal soma, as they would not migrate far from their initial seeding area. However, the pillars had an effect on the axons' alignment. One, three and five rows of pillars reduced the alignment to 40%, 24% and 28% respectively. It was hypothesised that the axons were using the pillars as a "turning post".

An automated method of wounding the cells was developed using a microscope and micromanipulator. This method was trialled on layers of astrocytes and MG63s grown on flat and grooved PDMS. Cutting astrocytes perpendicular to the grooves resulted in wounds with an area five times larger than those caused by cutting parallel to the grooves. Perpendicular wounds were also twice the area of those on flat PDMS. Similar effects were seen on MG63s. It was hypothesised that the difference in wounds sizes was due to the ridges causing the cells to make stronger mechanical connections longitudinally with the grooves.

Acknowledgements

Firstly I'd like to thanks my supervisors, Mathis, Sue & Nikolaj for provide guidance and motivation; and the occasional prod to get things rolling.

A very special thanks goes to Dr. Stephanie Boomkamp whom I worked alongside during this project and who provide the images of the myelinating cultures present within this thesis.

My family, Veronica, Irvine & Finn provided me with many kinds words of encouragement and chocolate when required. A special mention goes to mum for consistently trying to understand what I was doing.

Thanks to everyone in the Centre for Cell Engineering for showing an engineer how to do biology and for putting up with my rants about fonts.

Thanks also go to all of the technicians and users of the James Watt Nanofabrication Centre for providing fabrications assistance and tips. A special thanks to Dr. Corrie Farmer who was having similar AZ problems, and provided much great advice on working with it.

Thanks are also due to all my friends who have kept me sane during my lab work and write up. There are too many of you to mention by name but I owe you all a pint.

Finally I'd like to dedicate this thesis to Alfred Firth and Dorothy Wylie who both passed away during my PhD work.

Table of Contents

List of Tables

List of Figures

Chapter 1:

List of Accompanying Materials

Listed in alphabetical order:

Video 1: Astrocyte Flat

Video 2: Astrocyte Parallel

Video 3: Astrocyte Perpendicular

Video 4: C2C12 1-6

Video 5: C2C12 1-8

Video 6: C2C12 1-10

Video 7: C2C12 3-10

Video 8: C2C12 5-8

Video 9: C2C12 5-10

Video 10: C2C12 Pillar Squeezing

Video 11: MG63 Flat Pullback

Video 12: MG63 Parallel Pullback

Video 13: MG63 Perpendicular Pullback

Chapter 1

Introduction

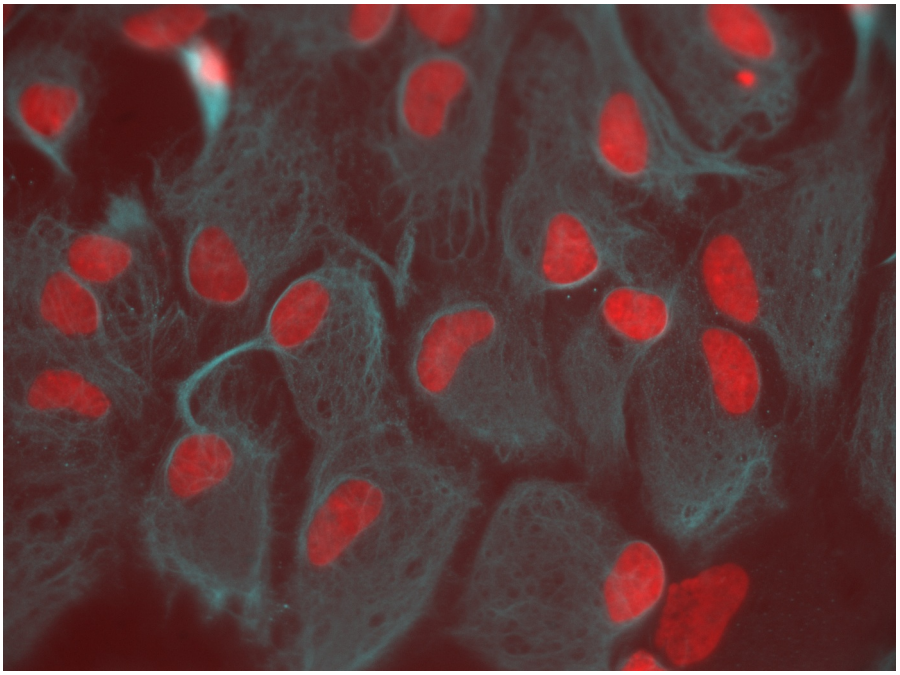

1.1 Project Overview

Damage to the central nervous system causes highly debilitative injuries to victims due to the loss of motor control and sensory data from, potentially, large areas of the body. The lack of growth factors and the formation of a scar consisting of densely packed glial cells prevents severed spinal axons, whose cell bodies survive, from re-growing past the site of injury, which can result in permanent damage to the spinal cord. According to The National Spinal Cord Injury Statistics Centre, there are approximately 270,000 people living with spinal cord injury (SCI) in the USA today, with roughly 12,000 new injuries occurring each year (NSCISC, 2012).

Currently the most widely used method to SCI is to directly wound animals; this is both time consuming and expensive. Large numbers of animals are also required to give statistical significance to the data. Development of an *in vitro* model for SCI will, firstly, reduce the number of animals required for studies as they will only be needed for the harvesting of neuronal cells. Secondly, the animals used will not be exposed to the long-term suffering caused by *in vivo* experiments of the kind needed. Finally, the complexity of the experimental procedure will be reduced, as experiments will not be conducted on whole organisms.

This project aims to development microfabricated device that will form part of an *in vitro* model of SCI and a method of inflicting reproducible wounds on cultures grown on the device. The device will have to fulfil three roles: providing an environment conducive to the growth of neurons, provide guidance cues to the axons so that they can be patterned out on the device and, finally, contain the neurons' soma to an area to prevent them migrating around the device.

1.2 Neuronal Cells

Neurons consist of three main parts: the soma, dendrites and the axon. The soma is the cell body, which contains the nucleus and governs the majority of protein synthesis within the neuron. The dendrites form a net of fibres that extend from the soma and receive connections from other neurons and thus aiding in inter-cellular communication. The axon is a long, thin fibre that extends from the soma, in humans these tend to be ~1 µm thick and can be over a meter in length. The axon is used to form connections with cells that are situated a long distance away from the soma, this is done through a form of electrical signalling know as the action potential (Moore and Cole, 1960). Within most invertebrates and some non-invertebrates an insulating layer known as myelin wraps the axons. The myelin prevents signal leakage during the conduction of the action potential and thus helps to speed the movement of the action potential down the axon. Myelin is not produced by the neuron itself; one of two forms of glial cell synthesise the myelin and ensheath the mature axon in it. The Schwann cells in the peripheral nervous system (PNS) and the oligodendrocytes in the central nervous system (CNS) play this role. A diagram of a human neuron is shown in Figure 1.

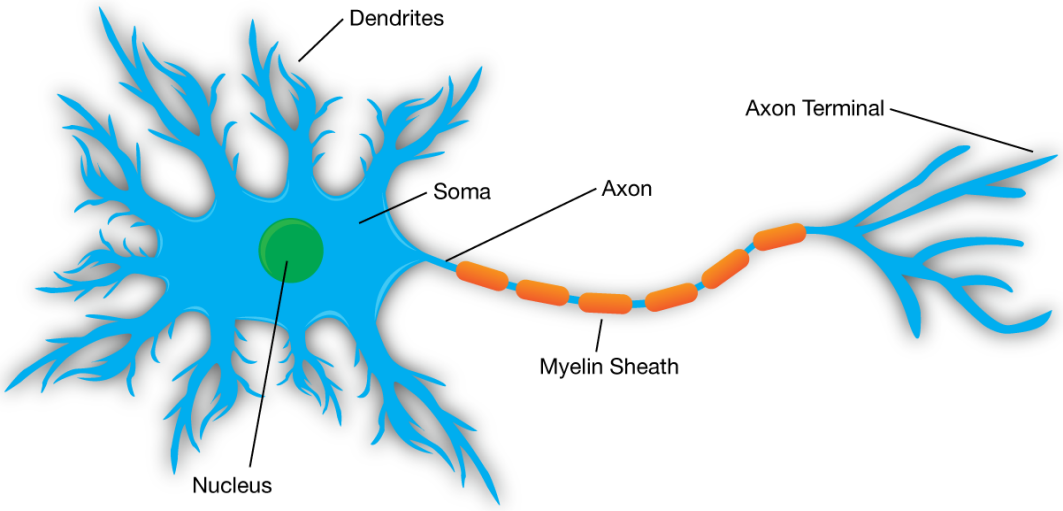

Figure 1: A typical human neuron, the axon would be ensheathed by Schwann cells in the PNS or oligodendrocytes in the CNS. At the dendrite and soma, information is passed to the neuron. The axon can then transmit any resultant signals to other cells via its terminal end. The connection between the neuron and other cells are known as synapse.

1.2.1 Axonal growth

During development neurons connect with distant neurons by the pathfinding of the growth cone. The growth cone is a structure at the leading end of the axons that seeks out guidance cues and directs the growth of the axon. It consists of two distinct types of structure, the lamellipodia and the filopodia (Gordon-Weeks, 2008). These structures are shown in Figure 2.

The filopodia are small, cylindrical projections from the leading edges of the growth cone. Their main role is to seek out guidance cues and form bonds with the substrate, know as focal adhesions, if a positive cue is found. They will usually retract if a negative cue is found. Guidance cues can be either chemical or topographical in nature. Filopodia are constantly extended and retracted from the lamellipodia and appear to be created by rearrangement of the cells actin filaments.

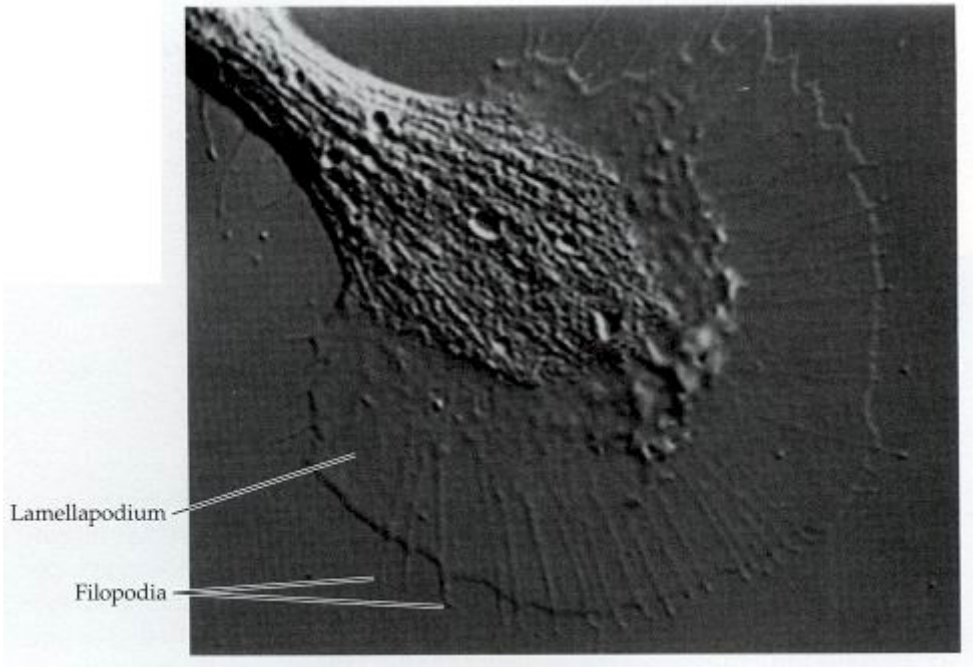

Figure 2: The growth cone of a neuron. The lamellipodium contains a mesh like area of actin filaments. Filopodia project out from the lamellipodium as small finger-like structures. They seek out guidance cues and form focal adhesions if a positive cue is found or will retract back into the lamellipodium if a negative cue is found. There is an almost constant retrograde flow of actin within the growth cone, which serve to drive the cone forward and assemble the axon behind it. Diagram from (Purves, 2008).

The lamellipodia is a large, flat structure that mainly consists of actin filaments. Whereas the actin filaments with the filopodia are in an ordered, tubular structure, those within the lamellipodia are arranged in a mesh like structure.

During extension of the growth cone there will be a retrograde flow of actin filaments that is promoted by positive attractant cues. Microtubules will also be moved towards the positive cue and assembled to form the cytoskeleton of the axons. These forward movements of actin filaments and microtubules are the process by which the growth cone moves.

1.2.2 Other cell types within the CNS

Neurons are not the only cell type present within the CNS, roughly half the brain is made up of glial cells (Azevedo et al., 2009). Neuroglia cells were first described by Virchow in 1846 (Virchow, 1846), their names translates as "neuron glue" as it was originally thought their role was to maintain the structure of the brain and spinal cord. There are five main types of neuroglia: astrocytes, oligodendrocytes, microglia, ependymal cells and radial glia (Purves, 2008).

Oligodendrocytes are the myelin producing cell within the CNS. Unlike Schwann cells in the PNS, oligodendrocytes can ensheath multiple axons at the same time.

Microglia are a type of macrophage that are tasked with providing immune defence within the brain and spinal cord. Due to the blood-brain barrier, the CNS is separated from the rest of the body's immune system and so the microglia are the CNS' main defence against infection and general degeneration of neuronal and glial cells.

Ependymal cells form an epithelial membrane lining the CNS. These cells produce cerebrospinal fluid (CSF) and help to circulate it throughout the CNS. Two of the CSF's roles are to provide mechanical protection to the brain and spinal cords against small

jolts and impacts. It also helps to remove waste products from cells and flush it through the blood-brain barrier.

Radial glia's main role is in the development of the CNS. They are progenitor cells for neurons and also provide immature neurons with guidance cues. In the mature brain these cells aid in communication between neurons.

Astrocytes are a versatile, star shaped cells that play a wide variety of roles within the CNS. They provide support to neurons by expressing factors such as glial cell derived neurotrophic factor (GDNF) and basic fibroblast growth factor (BFGF). They also transport glucose from the vascular system to neurons that are not directly in contact. Astrocytes play a key role in injury response within the CNS, this is discussed in the section below. In conjunction with oligodendrocytes, astrocytes form a functional syncytium that allows calcium signals to be passed over a wide area (Nagy and Rash, 2003, Newman, 2001). The syncytium also allows provides a means of clearing excess potassium from around neurons, allowing them to operate correctly. Astrocytes will uptake potassium and pass it through gap junctions to other astrocytes, which are in an area with a lesser potassium concentration, to be released (Walz, 2000).

The syncytium is created by the astocytes forming gap junctions with each other and the oligodendrocytes, these junctions allow the passing of ions and metabolites from cell to cell. The main components of the gap junctions in astrocytes are the connexin proteins, Cx26, Cx30, Cx43 (Nagy et al., 2004, Olk et al., 2009). The connexins are not the only proteins that govern cell-cell interaction and attachment within astrocytes. Neural cadherin (Tomaselli et al., 1988), also know as CDH2, along with α- & β-catenin (Nelson, 2008) form the cadherin adhesion complex which regulates astrocyte cell-cell adhesion. CDH2 in astrocytes is also know to play an important role in the outgrowth of processes from neurons (Tomaselli et al., 1988). Astrocyte adhesion to the extracellular matrix and migration are governed by the integrins αvβ5 and αvβ5 respectively (Milner et al., 1999). Integrins, specifically the β1 subunit, are also known to be integral to astrocytes' reponce to wounding (Peng et al., 2008).

1.3 Neuronal Injury and Regeneration

The nervous system within the human body can be slit into two distinct regions, the central nervous system (CNS) and the peripheral nervous system (PNS). The CNS consists of the brain and spinal cord while the PNS incorporates the outlying neurons, which allow the transfer of sensory and motor data to and from the CNS. There are two categories of injury, primary and secondary. Primary injury is damage that is a direct result of the wound inflicted, such as the death of severed axons. Secondary injury covers all degenerative process that follow on from primary damage, such as the retraction of healthy axons away from the wound site. As injury to the brain is an extremely complex issue and beyond the scope of this project, we will just concern ourselves with the injury and repair of the PNS and spinal cord. As response to injury varies across species (Kaslin et al., 2008, Tsonis, 2000), all following uses of PNS and CNS refer to those of mammals in general or of humans in particular.

1.3.1 Basic injury response and regeneration in the PNS

One factor that sets the PNS apart from the CNS is its response to injury and its ability to regenerate severed axons. After an injury is inflicted on the PNS the following reactions will occur (Levison, 2008, Reid and Roberts, 2005). Shortly after injury the distal end of a severed axon will die and begin to degenerate. Macrophages will then infiltrate the wound site and, with the aid of Schwann cells (Stoll et al., 1989), start to remove the myelin debris from the distal stump. During this process the outer layer of the nerve fibres, know as the neurolemma, is left intact. After the debris has been removed the Schwann cells begin to line the interior of the neurolemma and secrete growth factors. Some axonal sprouts from the proximal end of the injury, which are attracted by the growth factors, will eventually link up with the neurolemma and use it as an additional guidance cue. Finally the Schwann cells re-myelinate the axons. A diagram of this process is shown in Figure 3.

The process of axon degeneration and myelin clearance is know as Wallerian degeneration, named after Augustus Volney Waller who first observed the process in

1850. In the PNS Wallerian degeneration takes around one to two weeks. Re-growth of the axon can be at speeds of up to 1 mm per day. However, it can take years for full sensation and motor control to be restored to affected areas because of the distances involved and the fact that not all re-growing axons will be able to link up with an intact neurolemma. In addition, some neurons will not innervate their original target, this leads to an increased recovery time as the brain must adapted to this 'rewiring'.

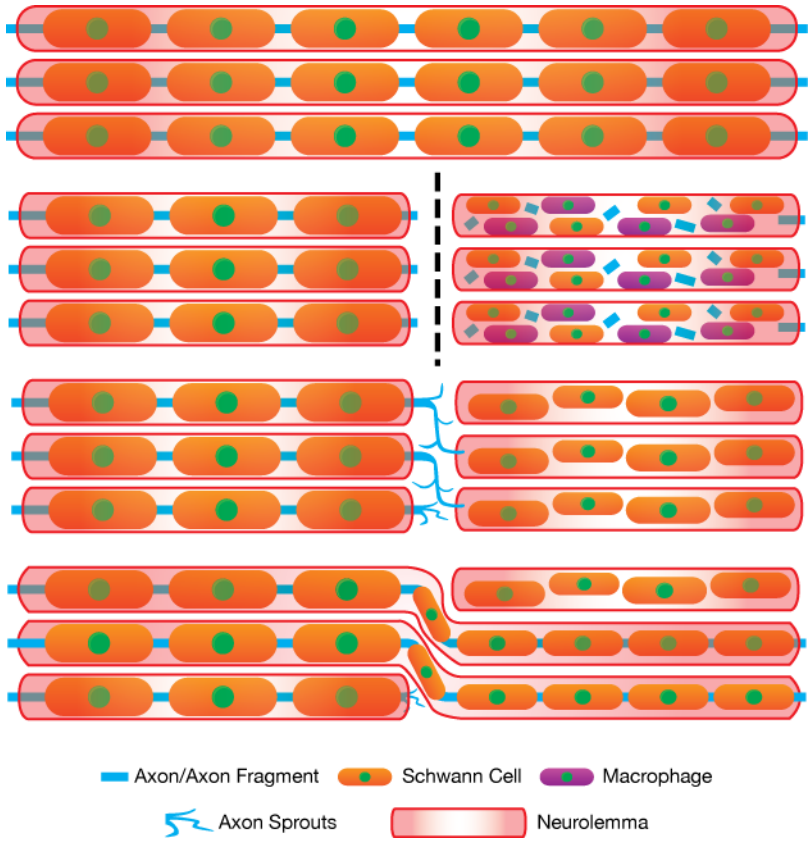

Figure 3: Stages of regeneration in the PNS. During the first stage of recovery macrophages and Schwann cells will clear away the axonal and myelin debris left after the injury. After debris clearance, the neurolemma will be left intact and Schwann cells will begin to line it and secrete growth factors. The re-growing axons will link up with the neurolemma and use it for further guidance. Finally the axons will be remylinated.

1.3.2 Basic injury response in the CNS

Due to the difference in the types of cells found within the CNS and their extracellular environment, the response to injury is quite different from the PNS. The following will occur after damage occurs to the spinal cord (Norenberg et al., 2004).

The initial response is similar to that of the PNS, firstly the distal end of the severed axon will die off and some macrophages will move in to begin clearing debris. However, the entry of additional macrophages to the wound area is somewhat slower than in the PNS, the reasons for this are discussed in the section below. Astrocytes will also begin to gather around the wound site and start synthesising intermediate filaments such as glial fibrillary acidic protein (GFAP). The wound site eventually becomes swamped by large amounts of astrocytes which have swollen in size, know as hypertrophy, and attached to each other with tight junctions; this dense mass is known as the glial scar (Silver and Miller, 2004). A fluid filled cyst, know as a syrinx, can also form at the site of injury, which creates a further physical barrier. Regenerating axons are unable to penetrate the glial scar or syrinx and so there is a permanent loss of motor control and sensory data from all areas distal of the scar. A diagram of this process is shown in Figure 4**.** Within the CNS, the time scale of the equivalent of Wallerian degeneration can be measured in months or years, if it occurs at all.

1.3.3 Reasons for the CNS's inability to regenerate

In their review paper Vargas and Barres (Vargas and Barres, 2007) discuss the reasons for the differences between the PNS' and CNS' responses to injury. Some of the causes of these differences are summarised below.

There are several myelin-associated inhibitors of axonal regeneration (He and Koprivica, 2004). These include MAG, OMgp, Nogo-A and Sema 4D. MAG, OMgp and Nogo-A are know to act through the NgR receptor on the neuron's growth cone. Sema 4D is thought to act through the growth cone receptor protein Plexin B1. It is clear that the

clearance of myelin, and hence the removal of these inhibitors, is an important factor in axonal regeneration.

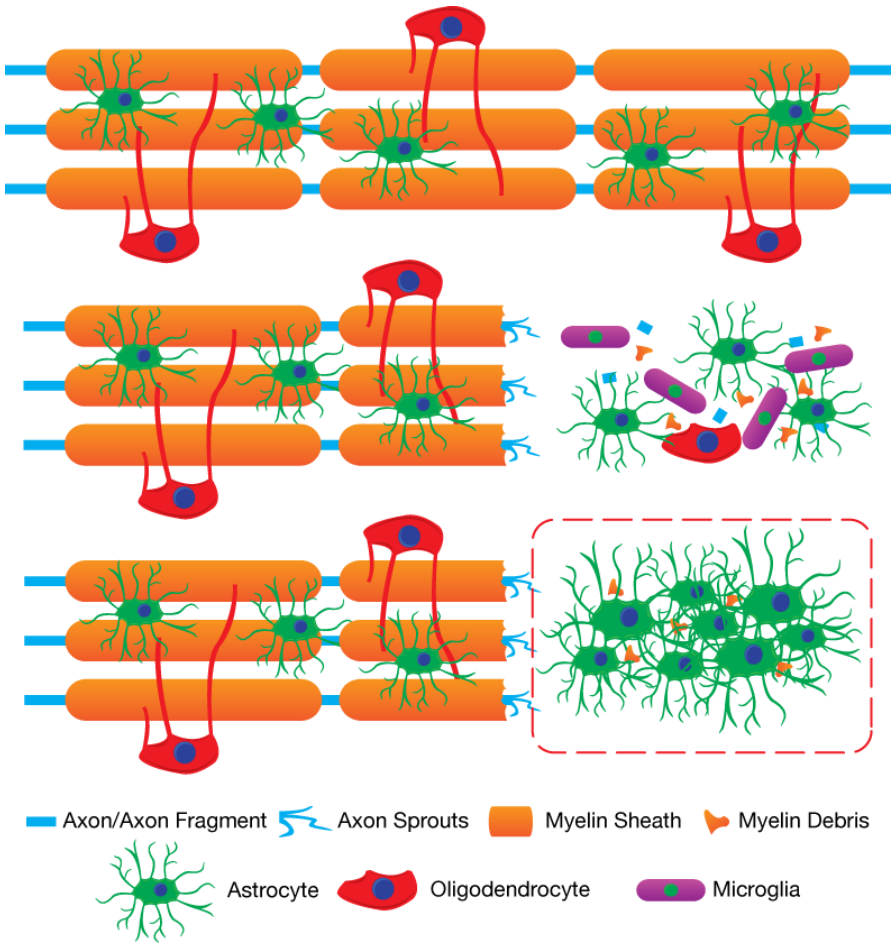

Figure 4: Response to injury in the CNS. After injury to the CNS there is a small influx of macrophages to the wound site, which will begin to clear the myelin debris. Astrocytes will also enter the area and begin to synthesise GFAP. A large mass of hypertrophic astrocytes and polymerised GFAP will clog the wound site and form what is know as the glial scar, outlined here by the red dashed box. Regenerating axons are unable to penetrate this scar and so damage to the CNS will be permanent.

One of the key differences between the PNS and the CNS is the presence of Schwann cells within the PNS, which respond to axonal injury in several ways: Within 48 hours of injury the Schwann cells in contact with an injured axon will cease production of myelin and begin to separate its myelin sheath from the axon. The cell will then begin to degrade its own myelin and phagocytose extra-cellular myelin debris.

The Schwann cells do not act alone in the clearance of myelin debris. After an injury is inflicted upon the PNS, Schwann cells will begin to produce a variety of factors, such as leukemia inhibitor factor (LIF) and macrophage chemoattractant protein-1 (MCP-1), to attract macrophages to the site of injury. Once macrophages arrive at the wound site, the Schwann cells will move myelin debris into the extra-cellular space so that it can undergo phagocytosis by the macrophages.

It is also of note that Schwann cells will begin to proliferate after an injury occurs thus providing further help in myelin clearance and creating a sufficient supply of cells for remyelination to occur. However, it is only cells that are in contact with a damaged axon that will enter the cell cycle (Murinson et al., 2005). The exact signals required to trigger proliferation are still unknown.

Through these three methods (clearance, macrophage recruitment and proliferation) the Schwann cells play a crucial role in making conditions after an injury favourable for axonal regeneration. In comparison to the Schwann cells active roles after injury, the oligodendrocytes within the CNS are comparatively passive. The majority of oligodendrocytes in contact with injured axons will enter a dormant resting state, or will apoptose, this is thought to be because they require regular signals from healthy neurons to survive and become active. Some oligodendrocytes will phagocytose myelin debris but these are a very small number when compared to the amount of cells that become inactive (Vaughn and Pease, 1970).

Another important difference between the CNS and the PNS is the presence of the microglia as the main macrophage. As the CNS is separated from the rest of the body's immune system by the blood brain barrier, it must rely upon the microglia as its first response to injury or infection. However, the microglia phagocytose myelin debris at a far slower rate than other macrophages. Debris clearance is also slowed by the limited amount of additional macrophages that manage to enter the wound site. This is partly due to a lack of active recruitment of macrophages, as opposed to the situation in the injured PNS, and partly because non-CNS based macrophages can only move directly into the CNS at a site where the blood brain barrier has been compromised.

The presence of astrocytes within the wound site also limits the spinal cords ability to heal. After injury astrocytes will swamp the wound site and enter a "reactive" state (Eng and

Ghirnikar, 1994). In this state the cells begin to synthesise large amounts of GFAP, swell up and become hypertrophic in a process know as astrogliosis. This results in a layer of cells that form a glial scar. This glial scar tissue is so dense that other cells cannot penetrate, thus physically stopping axons from re-growing, or other cells types from entering e.g. to break down the scar tissue. This type of injury response is unique to the CNS and there is no equivalent process within the PNS. It has been proposed (Faulkner et al., 2004) that the astrogliosis developed as a means to re-establish the blood-brain barrier as quickly as possible after injury and thus prevent further damage occurring around the site of the injury.

The relative inactivity of the oligodendrocytes combined with the microglias' limited phagocytosis abilities and the restricted influx of macrophages result in very slow clearance of myelin debris which in turn results in inhibited axon regeneration. This also gives ample time for the glial scar to form and further block any axonal regeneration.

Possible evolutionary reasons for the CNS's inability to repair damage are presented in a paper by Weil et al (Weil et al., 2008). They hypothesize that the highest risk of CNS infection is in the post-reproductive age therefore selection would not occur in this case and that, before the advent of modern medical technology, most CNS injuries would be fatal. Alternatively, they propose that the injury response is a side effect of the processes that evolved in the healthy spinal cord system.

1.4 A brief history of contact guidance via topography

As contact guidance plays an important part in both the development and regeneration of neurons, it is pertinent to review the literature concerning this subject. The term, contact guidance, was first coined by Weiss in 1945 (Weiss, 1945). In this work he identified that neurite outgrowths from chick embryo spinal ganglia would follow scratches made on a mica surface. He also showed that rat nerve explants would align to glass wool fibres with a thickness of 8 or 26 μm. The alignment was shown to occur both in liquid and clotted culture media. This was significant as previous experiments (Harrison, 1914) had shown cells could follow fibres in liquid culture but had not provided alternative means of cell migration i.e. Weiss' rat nerve explants could freely extend out into the plasma clot but preferentially followed the fibres, while they could not extend into the liquid media. He also found that cells from the rat nerve explants would extend out a longer distance on the glass fibres when compared to plasma only cell extensions. Weiss attributed the alignment of cells to changing stress on the exudate laid down by the cells. He thought that the fibres would apply stress to the exudate and force it to align to the fibres, the cells would then conform to this alignment.

Several years later Curtis and Verde (Curtis and Varde, 1964) performed experiments to see whether arrays of micro-scale ridges could effect cell behaviour. These experiments were conducted with chick-heart fibroblasts. They compared silica fibres, ranging from 8 to 40 μm in diameter, to ridges of 12.5 and 25 μm diameter. They found that the cells would follow the ridges in a similar manner to the fibres and that this threw into question Weiss' hypothesis on the cause of contact guidance. They concluded that "it is thus surprising that the microexudate could orient cell movement similarly on both ridges and grooves where surface-tension effects controlling the microexudate would be contrary". They also suggested that contact guidance was due to direct contact between the cell and the surface, and not due to the exudate; and that tension within the cell layer was one of the factors that drove the cells' outgrowth along the ridges.

During the late 1980s Adam Curtis formed a partnership with the engineer Chris Wilkinson to harness the microfabrication techniques, developed by the electronics industry, and gain further insight into contact guidance. This partnership would produce several seminal papers on the subject (Clark et al., 1987, Clark et al., 1990, Curtis and Wilkinson, 1997, Curtis and

Wilkinson, 1998). One paper of particular interest is Clark's 1990 paper (Clark et al., 1990) regarding the reaction of various cell types to grooved substrates. They grew baby hamster kidney (BHK), Madin Darby canine kidney (MDCK) and chick embryo cerebral neurons on Perspex, which had grooves etched into the surface. The grooves had pitches ranging from 4 to 24 μm and depths ranging from 0.2 to 1.9 μm. They found that both the pitch and the depth of the grooves had a significant effect on the alignment of cells to the ridges. Alignment appeared to be inversely proportional to pitch and proportional to depth; with depth having a more dramatic effect than pitch. Also of note was that the MDCK cells showed poor alignment when part of a colony but aligned well when they were isolated. Although they could not establish a solid mechanism for contact guidance from their data, Clark et al suggested that minimising cytoskeletal distortion was a factor in the cells alignment to the grooves. This was backed up by observations that cells that had less organised cytoskeletons were less likely to align to topographies. They also hypothesised that lamellipodia that extended near a ridge edge had less chance of finding good purchase and so it was more likely that extensions parallel to the ridges would form adhesions and guide the cell. In addition they noted that tension within the cell layer appeared supersede contact guidance, as was seen in the colonies of MDCK cells.

As was evident in the case of the MDCK cells, it was possible for other forces to overcome contact guidance, however it was not know if other guidance cues could also override topography. To study this, Britland et al. (Britland et al., 1996) fabricated grooved substrates with a depths ranging from 0.1 to 6 μm and widths of 5 to 100 μm. Adhesive and non-adhesive tracks, of identical width to the ridges, were then patterned so that they ran either parallel or perpendicular to the ridges. Controls with only ridges or only chemical patterning were also created. BKH cells were then cultured on the surfaces and their alignment to the ridges was quantified. They found that the combined parallel adhesive tracks and ridges aligned a far greater number of cells than the devices that had only chemical patterning or topography. However, the results of more interest were obtained on the device that aligned the adhesive tracks perpendicular to the ridges. The cells preferentially aligned to the adhesive tracks on all width and height combinations. Although an increasing number of cells aligned to the ridges as their height increased. They observed that within a single cell f-actin filaments would align to both competing guidance cues and so concluded that cells were capable of responding to multiple cues at the same time but prioritised one cue over others. Their data also threw into question the hypothesis that cells followed the ridges due to an inability to

form adhesions close to a ridge edge as they observed cells attaching to the top of ridges, the bottom of the troughs and the sidewalls at the same time while following the adhesive tracks.

To try and understand the mechanism behind contact guidance within the neuronal growth cone, Rajnicek et al. conducted experiments with two types of neuron on ridged topographies (Rajnicek et al., 1997). Quartz devices were fabricated with ridges of 1, 2 and 4 μm width; and depths ranging from 14 nm to 1.1 μm. Rat hippocampal and xenopus spinal neurons were then grown on the substrates and their alignment was quantified. The majority of the xenopus neurons aligned parallel to the grooves regardless of dimensions. Rat hippocampal neurons aligned parallel to deep, wide grooves, however, as the groove width and depth decreased they aligned perpendicular to the grooves. The growth cones were even capable of making 90° turns to align to the grooves if they approached from a non-grooved area. They also observed that the age of the cells could effect their alignment; E16 rat hippocampal neurons would align perpendicular to the 2 μm ridges while E19 neurons would align parallel to them. This data showed that even within the same cell type, species and age could have a profound effect on a cell's alignment. Rajnicek and McCaig also published a companion paper that investigated the cytoskeleton elements and signalling pathways involved in contact guidance of the growth cone (Rajnicek and McCaig, 1997). They used various drugs to inhibit the cytoskeleton and found that neither filopodia nor microtubules within the growth cone were crucial for contact guidance. However, they believed that actin played a role in alignment parallel to the grooves. They also found that protein kinase C, which is involved in the regulation of actin expression, was required for perpendicular alignment. They concluded that different mechanisms were used to align the cell perpendicular to the ridges than those used to align the cells parallel. This, once again, highlighted the cells' ability to sense multiple guidance cues and respond to them in a hierarchical manner.

Another potential factor in contact guidance was investigated by Walboomers et al; the effect of substrate material on alignment (Walboomers et al., 1999). They fabricated microgrooves of various widths on surfaces made of polystyrene (PS), poly-l-lactane acid (PLL), silicone (SIL) and titanium (Ti). Rat fibroblasts were cultured on the surfaces; and the wettability, elastic modulus and cell alignment of each surface were measured. They found that cells on the PS substrate aligned to the grooves and had flattened morphologies. Cells on the Ti and SIL surfaces were similar to those on PS, however the Ti surface had slightly less cell alignment. Cells on the PLL surfaces appear slightly rounded and did not align well to the grooves. They concluded that substrate material was an important factor in the cells response

to the topographies and that it was likely that surface stiffness and wettability played roles in contact guidance.

From this brief look at the literature on contact guidance, it becomes clear that the cues involved are manifold and the processes behind them are complex. Some of the factors involved are: groove depth and width; cell type and species; cell age; surface chemistry and surface stiffness. Cells are capable of sensing all of these factors and reacting to them in a hierarchical manner. The use of these factors to align and pattered axons is discussed further in Section 1.9.

1.5 Current Trends in SCI Treatment

It is clear that if we wish to overcome the permanent damage caused by SCI that medical intervention is required. Some of the possible methods for aiding regeneration are transplanting myelinating glia from other areas in the body, blocking of myelin-associated inhibitors, use of neurotrophic factors and various neuronal guidance techniques. We will briefly look at the first three techniques here while neuronal guidance techniques are discussed in more detail later in this chapter.

1.5.1 Neural cell transplants

As has been previously described, the oligodendrocytes close to a site of injury do not aid in the regeneration of injured axons. It has been hypothesised that the transplant of myelinating glial cells from other parts of the body may create an environment that can encourage axon re-growth. Several candidates have been proposed for this role; namely the oligodendrocyte precursor cells, Schwann cells and olfactory ensheathing cells (OEC).

In one of their review papers Barnett and Riddell (Barnett and Riddell, 2004) describe the selection criteria for one of these candidates: "it should be feasible to obtain the relevant tissue from the patient in order to enable autologous transplants to be performed (to avoid graft rejection) and it must be possible to generate the appropriate cells in culture in sufficient numbers". The criteria dismiss oligodendrocyte precursor cells, as it has not been possible to maintain cultures of these human cells. In comparison, Schwann cells seem like an ideal candidate; they fulfil both criteria and, as has been previously discussed, provide a great deal of aid during regeneration in the PNS. However, Schwann cells will not cohabit with astrocytes (Lakatos et al., 2000), which eliminates them as a candidate.

OECs inhabit the olfactory system, which has two interesting abilities. Firstly, it is unique in allowing neurogenisis to occur throughout an animal's life and, secondly, it is one of the few areas in which axons can cross over from the PNS into the adult CNS and synapse with other neurons (Farbman, 1990). It appears that these properties may be due to the influence of

OECs (Doucette, 1990). OECs also fulfil the criteria set out by Barnett and Riddell as they can be extracted from biopsies of the olfactory mucosa and cultured in sufficient quantities.

Several studies have been conducted to assess the effectiveness of OEC transplants; a wide variety of results have been reported, from substantial recovery (Ramon-Cueto et al., 2000) to no discernable effects (Steward et al., 2006). Within some experiments conducted on mice, partial functionality has been restored to limbs affected by induced SCI. Three possible mechanisms by which the OECs aid in repair have been suggested (Barnett and Riddell, 2007): these are 1) they actively encourage axonal regeneration and remyelinate axons once they have regenerated; 2) they secret factors which induce increased plasticity in surviving neurons and thus encourage axonal sprouting and increase synapse efficacy; 3) they release neurotrophic factors which reduce secondary damage such as the death of neurons around the wound site and surviving neurons withdrawing their axons from the area.

It is clear that more research will have to be conducted before a more complete understanding of OECs can be assembled. It is also likely that transplantation alone will not provide a cure to SCI and that a combination of strategies will have to be employed.

1.5.2 Neurotrophic factors

Neurotrophic factors are a group of proteins that aid in neuronal growth, guidance and survival, such as neurotrophins that have been extensively studied. Five proteins in this family are known to relate to SCI and regeneration (Schmidt and Leach, 2003): nerve growth factor (NGF), neurotrophin-3 (NT-3), ciliary neurotrophic factor (CNTF) and the fibroblast growth factors (aFGF and bFGF). An additional protein, glial cell line-derived growth factor (GDNF), is involved in crossing over of nerves from the PNS to the CNS.

Delivery of NGF to the site of injury in mice spinal cords has been shown to encourage neuronal regeneration (Oudega and Hagg, 1996, Nakahara et al., 1995). It also encourages sensory neurons from the PNS to regenerate and cross over into the CNS. However treatment with NGF can also lead to sprouting of uninjured axons, which can result in hyperalgesia and chronic pain (Romero et al., 2001).

NT-3 plays a similar role to NGF in encouraging regeneration within the spinal cord and across the PNS-CNS division (Nakahara et al., 1995). It also aids in axonal path finding (Tobias et al., 2003).

CNTF is known to promote motor neuron survival and growth. Also, increased levels of CNTF are found close to wounds in the spinal cord (Oyesiku et al., 1997). However, it does not appear to have any beneficial effect on regeneration (Kelleher et al., 2006).

FGFs have similar properties to NGF and NT-3 (Nakahara et al., 1995, Romero et al., 2001). They are also involved in angiogenesis (Friesel and Maciag, 1995) and so could help to reduce further secondary damage to the CNS.

The molecular mechanisms by which all of the neurotrophins work and their exact effects on regenerating neurons are not yet fully understood. Methods of delivering them only to the exact area of injury must be developed to avoid side effects such as the chronic pain that can occur from NGF's interaction with healthy axons. Delivery methods must also provide a steady supply of neurotrophins to avoid variations in responses (Schmidt and Leach, 2003). It is likely that the delivery of neurotophins will have to be use in combination with some form of axonal guidance technique to encourage regenerating axons to link up with appropriate targets.

1.5.3 Suppressing growth inhibitors

As previously mentioned there are several myelin-associated inhibitors of axonal growth. Clearance of myelin within the CNS is a very slow process and so inhibitors have a large presence around the wound site. It is thought that the blocking of these inhibitors could allow axons to regenerate and thus facilitate wound recovery.

Known inhibitors are: Nogo-A, myelin-associated glycoprotein (MAG), oligodendrocyte myelin glycoprotein (OMgp), transmembrane semaphorin 4D (Sema4D) and ephrin B3. Other non-myelin-associated inhibitors of note are the chondroitin sulphate proteoglycans (CSPGs) that are associated with astrocytes. A diagram showing the inhibitors and their receptors is shown in Figure 5. As can be see, the signal pathways associated with the

inhibitors are not yet fully understood. This can make blocking inhibitors problematic as blocking one segment of a pathway could lead to unwanted downstream effects.

A large number of experiments with various targets and blocking methods have been conducted; reviewed in (He and Koprivica, 2004, Yiu and He, 2006, Yang and Schnaar, 2008). Of particular note the review by Yiu and He (Yiu and He, 2006) which lists the target, intervention method, injury model and results of a large number of in vivo studies. The outcomes of these experiments have either shown no apparent regeneration or short-range regeneration. This shows that the targeting of certain identified pathways could aid the regenerating axons. However, inhibitor blocking seems not to encourage the long-range and long-lasting growth that would be required after SCI. Once again, this evidence supports the view that a combination of strategies will be required to restore functionality to the injured spinal cord.

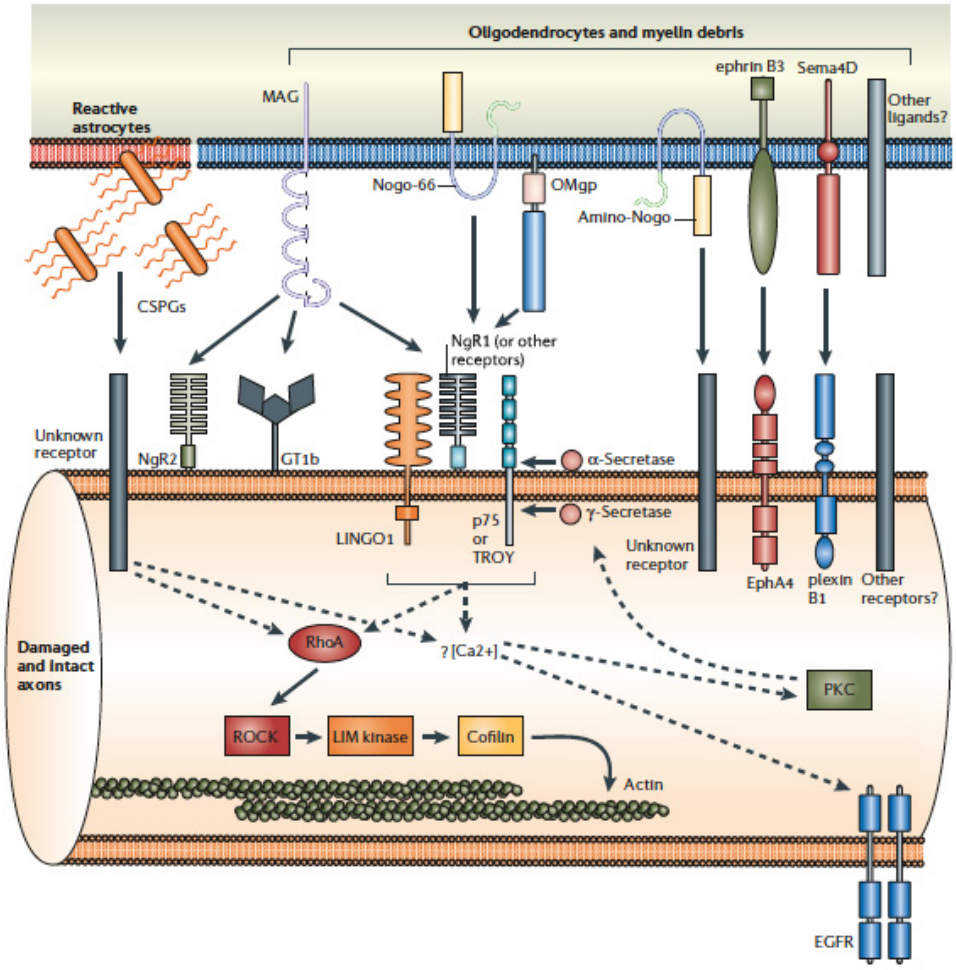

Figure 5: Glial secreted inhibitors of axonal regeneration, their receptors and downstream pathways. From left to right these are: ephrin B3, MAG (myelin-associated glycoprotein), Nogo-66, OMgp (oligodendrocyte myelin glycoprotein), Amino-Nogo, ephrin B3, Sema4D (transmembrane semaphorin 4D), and CSPG's (chondroitin sulphate proteoglycans). These interact with the following receptors on the axon: NgR2 (a Nogo-66 receptor homolog), GT1B (a ganglioside), LINGO1, NgR1 (Nogo-66 Receptor 1), p75 or TROY (member of the tumour necrosis factor receptor family), EphA4 (Ephrin receptor A4), and Plexin B1. What is not known is how differential receptor occupancy by these ligands lead to axonal and neuronal degeneration and death. It is thought that several of the receptors act upon the RhoA (Ras homolog gene family, member A) signalling pathway, or indirectly through PKC (protein kinase C). It is also possible that downstream inhibition of EGFR (epidermal growth factor receptor) may occur. Known interactions are shown with solid arrows while possible interactions are shown with dashed arrows. Reproduced from (Yiu and He, 2006).

1.6 Models of SCI

1.6.1 *In vivo* models

As has already been discussed, the effects of SCI are complex and involve several cells types and diverse intercellular communications that are not yet fully understood. The current solution to this problem is to conduct *in vivo* experiments, where the full compliment of neuronal and glial cells are present. There are multiple well-established *in vivo* models of SCI (Robins and Fehlings, 2008, LaPlaca et al., 2007, Onifer et al., 2007), most of which fall into three main injury categories: contusion, laceration and chemical. As there are a very large number of *in vivo* model, the general characteristics and advantages of each type will be reviewed, whilst presenting three examples of each type.

Contusion or crush injury models use blunt trauma to wound the spinal cord. This category can be further divided into models that use sudden impact, and those that apply the force over a longer period of time. An example of impact models is the one used by Scheff et al. (2003), while an example of the later type is Dolan and Tators (1979) compression model. The injury device used by Scheff et al. consisted of a stainless-steel impactor mounted on a stepper motor, which allowed precise control of the force applied. The method developed by Dolan and Tator used a modified aneurysm clip that could be attached to a section of exposed spinal cord and apply a constant compressive force. The force applied to the spinal cord was dependant on the type of spring used in the clip. When compared to other *in vivo* models, contusion models have the advantage of simplicity, as they can be as straightforward as dropping a weight on the exposed spinal cord. These models are also highly reproducible as the force and position of the impact or load can be easily controlled. Contusion injuries are the most common type of SCI in human, and so these types of model have the most clinical relevance.

The second model are those that fully, or partially sever the spinal cord using e.g. a sharp edge such as a scalpel. An example of a full transection model is that used by Lu et al. (Lu et al., 2012), where the spinal cord was cut with iridectomy scissors. A partial transection method

was used by Toft et al. (2007). They inserted a wire knife (Albert, 1969) into the spinal cord and raised it through the dorsal column to perform a partial transection. While this type of injury model has less clinical relevance, they allow easier identification of regenerating axons within the wound area when compared to contusion models, as a large cell free area is created at the wound site.

The final types of models are those that use chemically induced injuries. One example of this type is Hughes et al.'s (2003) model, which induced focal lesions by application of endothelin-1, a protein that regulates blood pressure by constricting blood vessels, leading to local occlusion, and stroke like effects. Chemical injuries are primarily used to model secondary damage to the spinal cord but lack clinical relevance for primary damage.

In *in vivo* models, the exact area of the spinal cord that is injured depends upon the type of injury being studied, e.g. in studies of dysreflexia injuries are inflicted above the T6 level (Rabchevsky, 2006). The outcome measure to be used can also govern the type of injury inflicted, for example, if food retrieval was used as an outcome then the motor neurons governing the forepaws would be wounded (Schrimsher and Reier, 1993).

1.6.2 *In Vitro* Models of SCI

As shown in the previous section, there are many *in vivo* models of SCI that allow the modelling of almost any type of injury. However, *in vivo* experimentation has several disadvantages; it subjects animals to long-term suffering; requires skilled, licensed technicians to rear the animals; large numbers of animals are required to give the data statistical significance; assay times are long as batches of animals must first be reared; rearing large batches of animals is costly; experiments are complex as the entire body of the animal is involved; and, finally, all aspects of the procedures used have to be specifically licensed in the UK by the Home Office – or equivalent elsewhere; all procedures have to be carried out by a named, and specifically trained, as well as Home Office licensed researcher.

In vitro models of SCI have several advantages over *in vivo* study. Fewer animals are required, as they are only used for harvesting primary cell cultures or small organ slices. Additionally, animal suffering is eliminated as cells are extracted after the animal is killed. Experimental

complexity is also reduced, as animals are not directly used for experimentation. Finally, costs are reduced, as large numbers of mature animals are not required.

There are currently several *in vitro* models under development or in use (Abu-Rub et al., 2010, Robins and Fehlings, 2008, LaPlaca et al., 2007). These can be broadly split into organotypic slices; culture models; and those using a device to alter cell growth.

Organotypic models use a section of spinal cord that has been removed from an animal and left intact. The tissue slices, typically a few hundred micrometers thick, are then cultured and treated as required. One example of this type of model is the one developed by Krassioukov et al. (2002). In this model ~ 8x 400 μm thick slices were cut from the thoracic region of six week old mice, kept in culture and used for experiments. These types of model benefit from leaving the structure of the spinal cord section being left intact and so closely mimic the *in vivo* environment. However, they require a highly skilled technician to perform the dissection. They are also structurally more complex than a standard culture model, which can make analysis more difficult.

Cell culture-based models use CNS cells that have been dissociated from the brain or spinal, which are then cultured to form layers that are simpler to interpret than a tissue slice. Some example of this type of model are the myelinating cultures developed in the lab of Prof. Sue Barnett's group (Sorensen et al., 2008) and the culture system used by Mukhin et al. (1997). The Barnett model seeds disassociated rat spinal cord cultures on top of a 10-day old layer of cultured astrocytes derived from neurospheres. This model contains all of the cell types present within the spinal cord and has been shown to be capable of myelination and remain viable for greater than 28 days. In Mukhin et al.'s system they disassociated glial cultures from the cortices of 1-3 day old rats. These glial cultures were grown for 10 days before mixed neuron and glial cultures were seeded on top of them. This resulted in an even distribution of neurons throughout the cultures, which could remain in culture for 3-4 weeks. Both of these cultures will not form some of the structures found within the spinal cord, such as parallel-aligned axons, which limits their clinical relevance.

The final type of model uses a device to alter cell growth and is always used in conjunction with a culture model. These models tend to either attempt to mimic the structures of the spinal cord or further isolate cells to make experimentation easier. These models come in a wide variety of forms; a few examples are presented here. East el al. (2010) mixed astrocytes

and neurons into 3D collagen gels, which were then stretched. The stretching caused the astrocytes to align parallel to the applied force. This allowed them to study the effect of astrocyte alignment on neurite outgrowth and alignment in a 3D space. Taylor et al. (Taylor et al.) designed a microfluidic device, shown in Figure 6, that consisted of two chambers linked by microfluidic channels. Neurons were seeded in one chamber and extended axons through the channels to the other chamber. Hydrostatic pressure isolated the two chambers chemically and thus allowed drugs to be tested on the chamber containing only axons without affecting the soma. Delivopoulos et al. (2009) developed a method for patterning neuronal cultures into parallel lines by using alternating adhesive and non-adhesive strips. Silicon oxide or parylene-c strips were fabricated on the device's surface, which was then immersed in horse serum. The serum bonded to the parylene-c strips, making them adhesive to cells, while the silicon oxide strips remained non-adhesive. This particular method is discussed in more detail in the axon guidance techniques section.

Individual devices within this final group allow easy access to the cells; or can be rapidly and easily produced; or are easy to use; or allow the observation of the wounding process. A device that could combine all of these qualities would provide a valuable addition to the models available. This project aimed to achieve this through the use of microfabrication techniques.

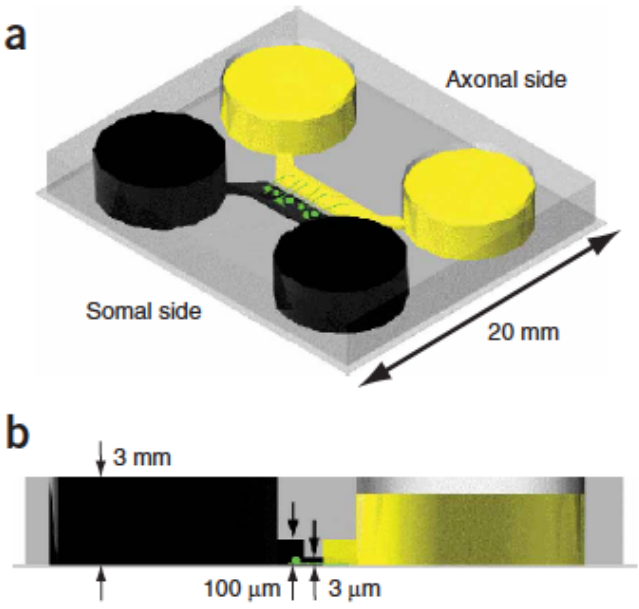

Figure 6: Taylor et al.'s PDMS microfluidic device for drug testing on isolated axons. A) Neurons, shown in green, were seeded into the chamber on the black side of the device via the large wells. Axons then extended through the small channel to the chamber on the yellow side of the device. The yellow chamber was chemically isolated by hydrostatic pressure. B) Side view of the device showing the difference in liquid levels that cause the pressure differential. Reproduced from (Taylor et al., 2005).

1.6.3 *In vitro* wounding methods

All of the *in vitro* model described above simulate the spinal cord but most also require an external method of inflicting injury so that regeneration can be studied. There are numerous methods to induce SCI *in vitro* (LaPlaca et al., 2007, Abu-Rub et al., 2010, Robins and Fehlings, 2008), for the purpose of this introduction we will examine five different methods that use blunt trauma, stretch injury, axotomy by blade, laser dissection and micro-scale injury.

Fayaz and Tator (2000) created a device to inflict blunt trauma that used a rubber impactor mounted on a motor driven shaft. The tip of the impactor was 500 μm wide and 6.25 mm long, which allowed them to injury every culture lane in their devices if required. This injury method has the advantage of being both easy to use and relevant to the most common clinical injuries.

Magou et al. (2011) developed a high throughput method for injuring cells by stretching the substrate they were grown on. This was achieved by increasing the air pressure on one side of a silicone membrane so that it was pushed outward and thus stretched the cells that were grown on it. This allowed entire 24 well plates fitted with the membranes to be injured at the same time. Multiple plates could also be injured in quick sucession. However, this method does not allow precise injury as the entire culture will be affected by the stretching, and as the extent, and direction of stretch varies across the culture dish, e.g. with little to none at the edge.

Que et al. (2011) used a simple approach to create an incision model of SCI. They grew cultures in standard culture dishes, printed a 4 x 4 mm grid onto pieces of cardboard with the same radius as the dishes and then affixed the cardboard grids to the backs of the dishes. A sterile razor blade was then used to cut cultures following the lines. This method allows wounds of any size to be created, unlike the methods above that have inherent wound sizes. However, reproducibility as with the model established by the Barnett group will be dependant on the consistency of the person doing the cutting.

Hellman et al. (2010) used a pulsed laser to sever axons. The 532 nm laser was pulsed in the picoseconds range to deliver 400 or 800 nJ of energy and was focused through an inverted microscope. This allowed them to sever individual axons and observe the instantaneous effects

of the ablation via the microscope. However, this type of ablation injury is unlikely to be encountered in a clinical setting and the method is relatively expensive compared to the others described here.

Finally, Stretavan et al. (2005) used microfabrication techniques to create silicon nitride blades that were 5 – 200 μm long with a cutting edge radius of curvature of only 20 nm. The blades were suspended in small frames, ~ 1 mm^2, to allow handling by micromanipulators. The small size of the blades allowed individual axons to be cut even in cultures with multiple neurites present. However, the manufacture of these blades is not a simple task and their size means they would not be suitable for creating larger injuries.

All of these methods offer various advantages and disadvantages; and no one can be classed as superiour to the others. The wounding method chosen by a researcher will largely depend on the exact type of injury being studied, the data acquisition method and resources available.

1.7 Microfabrication

Micofabrication (Madou, 2002) provides a series of methods for creating micro scale structures upon a substrate; these structures can then be used to alter the way cells proliferate and migrate(Curtis and Wilkinson, 1997), and thus can be used to provide guidance for axons. Most of these techniques were developed for use in the field of electronic engineering and so focus on the fabrication of ever smaller features on semiconductor substrates. In its simplest form, microfabrication consists of layering a thin film of material on top of a substrate such as silicon and then selectively removing parts of the film to expose the substrate, this is known as patterning. Further processing of the exposed areas of the substrate can then be performed, such as removing material with an acid etch or depositing metal onto the surface. If the thin film is then not required it can be removed with a process called stripping.

Some of the most common substrate materials are silicon (Si), gallium arsenide (GaAs) and quartz. These substrates come in the form of a wafer, which is a circular piece of material that is polished on one side. Traditionally wafers diameters are measured in inches, with wafer sizes increasing by increments of one inch. However, wafer thickness tends to be measured in micrometers. Wafer dimensions vary from 1 to 12 inches diameter and thicknesses of 25 to 1000 μm.

Most coating and patterning techniques make use of photo active thin film materials know as photoresists. These are classed as either positive, where exposed material becomes vulnerable to a developer, or as negative, where exposure results in resistance to the developer. Most resists are either exposed with a UV light source, the process is then known as photolithography; or a beam of electrons, where the process is know as electron beam (e-beam) lithography. Both of the exposure methods have various merits and flaws but it is simplest to summarise them as follows; e-beam offers high resolution and very small feature sizes but is slow and expensive; photolithography is fast and relatively cheap but cannot attain the resolution and feature sizes of e-beam.

Patterning of features upon the substrate can be achieved in several ways. E-beam uses a raster scanning method where the beam is selectively turned on and off during the scan thus

patterning the resist. Some less common forms of photolith, such as laser patterning, also use raster scanning. However, the most prevalent photolithography technique uses a photomask, also know as a mask plate, to pattern the resist. The mask is a piece of glass with one side coated in metal, which has been removed in selected areas to create the desired pattern. The mask is positioned between the UV source and the wafer during exposure. The photons can only pass through the metal free areas of the mask and so selective exposure of the resist is achieved.

Mask plates are designed with computer aided design (CAD) software and are usually patterned using raster scanning techniques. These masks use an opaque chromium coating and, if damaged, can be expensive to replace. To reduce potential costs, copies of the masks can be made on ferric oxide coated plates using optical techniques, such as photolithography. The ferric copies also have the advantage of being semi-transparent to the eye, aiding in alignment during multi-layer fabrication, while still remaining opaque to UV light.

Additional fabrication steps can be performed after lithography if required. One of the most common is etching of the wafer. There are two forms of etching, wet and dry. In wet etching the wafer is immersed in a liquid that attacks the silicon surface and removes material at a known rate. This process tends to produce isotropic etching. Dry etching uses plasma to remove silicon from the exposed areas. Dry etching is generally anisotropic and allows more control over the etching process, i.e process temperature and gas flow rates, when compared to wet etching. However, it is a more time consuming and expensive process.

Once the desired features have been obtained on the wafer, a process know as soft lithography can be used to make multiple, inexpensive polymer copies of the structures. This process is carried out by pouring an uncured polymer onto the silicon wafer, know as the master; the polymer is then cured and peeled from the master, which will result in an inverse copy of the structures on the master. Surface modification(Ni et al., 2009) of the polymer, such as increasing hydrophilicity or pacification, can then be performed if required. An example process flow using some of the techniques discussed above is shown in Figure 7.

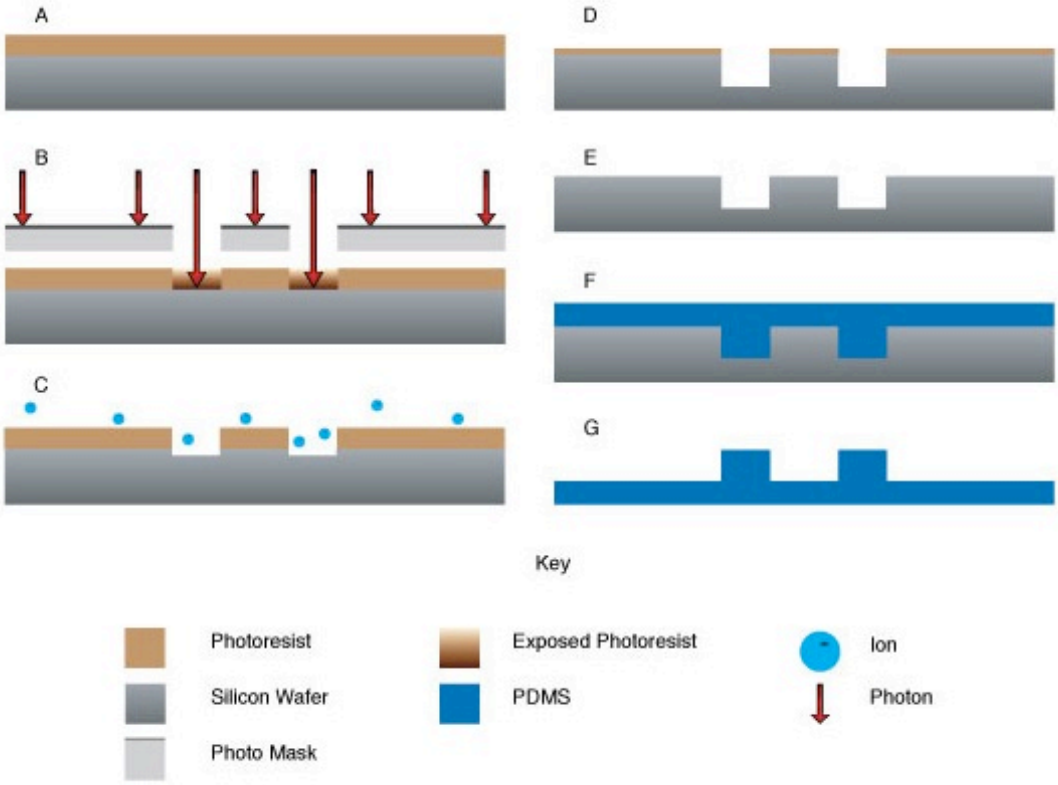

Figure 7: A & B, Fabrication processes for photolithography; C,D & E, reactive ion etching (RIE), a form of dry etching; and F & G soft lithography. A) A photoresist is spin coated onto a silicon wafer. This is then soft baked to remove solvent from the photoresist. B) A photo mask is aligned between the wafer and a UV source. Areas of the photo mask that are clear of metal coating will allow the photons to pass through and expose the resist below. In the case of the negative resist shown here, this will cause the polymer to break down and be removed by the developer. C) During RIE, parts of the silicon wafer not protected by the photoresist are exposed to plasma. The plasma removes silicon from the wafer by a combination of chemical reactions and sputtering. D) Because the ions are only chemically reactive with silicon, a deeper etch will be made into the silicon than the photo resist. E) After etching, the left over photo resist can be stripped from the wafer. F) Soft lithography is performed by pouring an un-crosslinked polymer, in this case polydimethylsiloxane (PDMS), on top of the wafer. G) After curing, the polymer can be peeled from the wafer. This will create structures that are the inverse of those on the wafer.

1.8 Axon Guidance Techniques

As discussed in the section on *in vitro* models above, patterning out axons so that they resemble the structure of the spinal cord allows the collection of more biologically relevant data. Several methods have been developed to allow the guidance of axons. Some of the main techniques are topographical guidance, surface patterning, optical guidance and electric fields.

The use of substrate topography to control cell behaviour is a relatively young yet well-established field (Curtis and Wilkinson, 1997). The use of various ridges and troughs is a widely used technique and has been used to both contain neuronal soma and guide axons. As we have already seen, work by Rajnicek et al (Rajnicek et al., 1997) established that the groove width and depth affected axonal alignment and that different cell types would react differently to the grooves. They used quartz substrates with grooves etched into them, grooves varied between 1 and 4 μm in width and between 14 to 1100 nm in depth. Rat hippocampal neurons aligned perpendicular to shallow, thin grooves but preferred to align parallel to deep, wide grooves. In contrast, Xenopus spinal cord neurons preferred to align parallel to grooves of any size.

Research has also been conducted on the effect different ridge shapes have on axonal guidance. Lee et al. (Lee et al., 2007) used patterns of either straight, dashed or zig-zagging fibronectin coated ridges etched into silicon dioxide upon a quartz substrate. They found that mouse N2a neuroblastoma cells had better adhesion, alignment and longer neurites on the zig-zag pattern. However, they did not vary the channel depths or widths.

Uni-directional guidance has been achieved by Hallstrom et al (Hallstrom et al., 2009). Gold nanowires were grown on gallium phosphide substrates and then coated with laminin to encourage neuronal growth. The wires were arranged into echelon formations, these echelons then formed channels 'pointing' up or down the device. Superior cervical ganglions from wild type mice and from green fluorescent protein (GFP) expressing transgenic mice were seeded on opposite sides of the device. The axons would only grow in the direction 'pointed' to by the echelons of nanowires i.e. axons from the right would grown to the left only in channels were the echelons pointed left. This is shown in Figure 8. There is great potential for using

this nanowire guidance technique for sorting growing neurons and avoiding clogging of guidance channels with multiple regenerating axons from multiple directions.

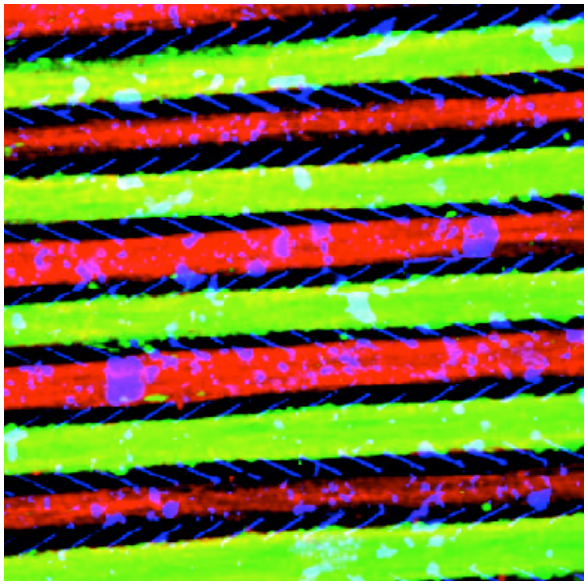

Figure 8: Axons guidance with the aid of nanowire echelons. The blue echelons are the arrays of nanowires while the red and green areas are the axons. Each echelon is ~ 10µm long. The red axons are wild type and seeded to the left of the device, the green axons are GFP expressing and seeded to the right. Reproduced from (Hallstrom et al., 2009).

All of the experiments using topographical guidance cues described so far have only been conducted with neurons. As has been previously discussed, the glial cells play key roles in neurogenesis and axonal regeneration, and so the affect of topography on mixed cell cultures must be investigated. Sorensen et al. used myelinating neuronal cultures that contained the full complement of cells from the spinal cord (Sorensen et al., 2007). There experiments used polycaprolactone (PCL) devices with grooves embossed into them. The grooves were 5 µm deep and had a range of widths; namely 5, 12.5, 25, 50 and 100 µm. Two different sets of devices were used with one set only coated with polylysine (PLL) while the other set had a monolayer of astrocytes seeded onto them. Mixed spinal cord cultures from embryonic rats were then plated onto the devices and neurite growth was monitored over three weeks. Neurite density on the PLL coated devices was found to be significantly less than that on the astrocyte coated devices. Neuron survival on the PLL coated devices was poor beyond one week while there was a steady increase in density on the astrocyte monolayers. It was found that groove width between 12.5 to 25 µm provided the greatest degree of neurite alignment on both PLL coated devices and the astrocyte monolayers.

Guidance of neurons can also be achieved by patterning substrate surfaces with various materials or proteins. Hydrophilic and hydrophobic areas can be created and thus cells can be contained to certain regions of a device. There are three commonly used techniques for surface patterning, they are selective molecular assembly patterning (SMAP) (Michel et al., 2002), molecular assembly patterning by lift-off (MAPL) (Feller et al., 2008) and microcontact printing (MCP) (Wilbur et al., 1994). MCP has already been used to provide neuronal guidance in short-term cell culture (Offenhausser et al., 2007). A paper by Lussi et al. (Lussi et al., 2006) compares the viability of patterning techniques over time. SMAP, MAPL and MCP were used to pattern poly L-lysine-g-poly(ethyleneglycol) (PLL-g-PEG) onto substrates appropriate for the techniques. They used GFP labeled 3T3 fibroblast for their experiments and measured the cells containment to the patterned areas over thirteen days. There was degradation in all of the patterns over time with almost total outgrowth from the SMAP patterning. The stability of the MAPL proved quite variable, while MCP patterned areas gave the greatest degree of containment with only slight outgrowth from the patterns after fourteen days. To test whether the loss of containment was due to the cells or the serum containing culture medium the experiment were repeated. However, this time instead of adding the cells on day one the patterned areas were exposed to only the cell culture medium. Cells were then added after 1, 5, 8 or 13 days. Similar results to the previous experiments, where cells were present throughout, were observed. Thus it is likely that the cell culture medium was affecting the adhesion between the various substrates and the PLL-g-PEG. Further study will be required to discover the long-term viability of these patterning techniques. It should also be note that the effect of MCP, SMAP and MAPL on mixed cell cultures is yet to be investigated.

A simple technique for integrating surface patterning into normal microfabrication has recently been introduced. In a method similar to SMAP, Delivopoulos et al (Delivopoulos et al., 2009) used silicon wafers with a 200 nm layer of SiO_2 grown on them as substrates. These were then coated with a 100 - 120 nm layer of Parylene-C, which was etched to create patterns of stripes with various widths from 20 to 100 μm. These devices were then submerged in horse serum so that proteins from the serum would absorb onto the Parylene patterns and provide a hospitable environment for cell adhesion and growth. Neurons and glial cells from mouse hippocampi were cultured on the devices for seven days. They found that the Parylene stripes provided a high degree of alignment for both neurons and glial cells;

and that alignment was independent of the stripe width. These results are highly encouraging as they show that mixed cell cultured can be patterned in a relatively simple fashion.

Another new method of axonal guidance that is of note is optical guidance through the use of lasers (Carnegie et al., 2008). In this method a laser spot is shone on the leading edge of the growth cone, when the spot is then slowly moved the growth cone will follow it. With this method average growth rates of up to 111 μm/h can be achieved and growth cones can turn through angles of ~20° to follow the spot. However, only ~20% of cells will follow the laser dot and guidance can only be sustained for 20 – 30 minutes. The exact mechanism through which optical guidance works has not yet been established but it has been hypothesized that it may be because of optical torque (Parkin et al., 2007) acting on the cells filopodia.

There is also another technique that is reputed to provide axonal guidance. Several claims have been made that electrical fields can encourage and guide axonal growth. The importance of electrical fields in biology is reviewed in a paper by McCaig et al (McCaig et al., 2005) that covers several of the guidance experiments in a positive fashion and suggests that neurites are attracted to cathodes. However, another recent paper by Robinson and Comrie (Robinson and Cormie, 2008) review several *in vitro* neuronal guidance experiments and find that there is no conclusive basis for electrical field guidance of mammalian neurons within the literature. The experiments that showed enhanced growth of neurons were all conducted on Xenopus laevis, an amphibian, while all of the experiments on mammalian neurons either showed no enhanced growth or asymmetrical growth due to inhibition either at the cathode or anode. The results also seemed to be highly dependant on cell type, substrate used, the strength of the electrical field, the method used to apply the field and the batch of serum used for culturing. It seems that more rigorous experimentation will be required to settle this debate.

1.9 Project Goals

Finally, to review the project goals; this project had two main goals, with three sub-goals:

1) The development of a microfabricated device for modelling SCI *in vitro*.

I) Create an environment conducive to neuronal gorwth that will allow the cultures to grow for 28 days.

II) Provide guidance to the axons so they pattern out into parallel lines, a structure similar to that of the spinal cord.

III) Contain the soma to a defined area of the device so that they do not move around the device and interfere with wounding, recovery or observation.

2) The development of a reproducible method of wounding that will allow in-depth observation of the wounding process.

Chapter 2

Engineering

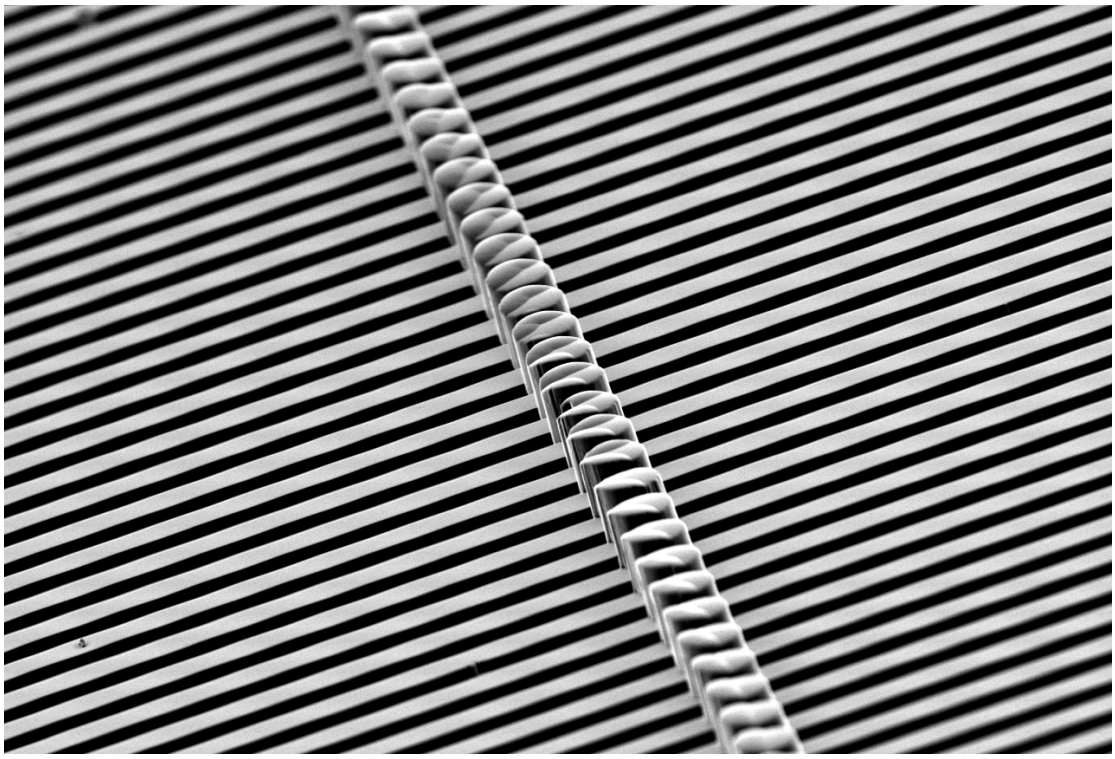

2.1 Introduction

2.1.1 Design Considerations

The devices had to perform three duties: provide an environment upon which the neuronal and glial cells could grow; contain the neuronal soma so that they did not migrate around the device and interfere with wounding and measurements of axonal healing; and pattern out the axons so that they were easily accessible for wounding and examination.

As researchers who are unlikely to have any engineering training will eventually use the devices, care was taken throughout the project to try and use the simplest methods for device modification and handling from the soft lithography step onwards.

Axonal guidance via the use of ridge or grooved structures is a well-studied phenomenon (Sorensen et al., 2007, Rajnicek et al., 1997, Lee et al., 2007, Recknor et al., 2004, Stepien et al., 1999). Sorensen et al (Sorensen et al., 2007) used this technique to achieve guidance of myelinating spinal cord cultures. However, this work used a different material, polycaprolactone (PCL), than the one chosen for this project. So re-characterisation of the structures was required. In addition, to reduce the variety of devices required, only the 12.5, 25 and 50 μm wide and 5 μm high devices were used. These dimensions were chosen as they had shown the greatest degree of alignment.

In 2001 Zeck and Fromherz developed an elegant solution for single soma containment (Zeck and Fromherz, 2001). They generated a small corral of pillars and placed the soma of a snail neuron in the middle. The spaces between the pillars were small enough so that the soma could not squeeze through, and high enough that the cells would not climb over them either, however, the axons could still fit through the gaps between the pillars. A modified version of this was developed where, instead of a single soma, large groups of cells where prevented from migrating to certain areas of the device by rows of pillars.

The 3000 series SU-8 photoresist (del Campo and Greiner, 2007) was chosen for initial use in this project. SU-8 is a negative tone photoresist that allows high aspect ratio designs (Choi et al., 2003) that still have vertical sidewalls(Lee et al., 1995). A single layer can be between 4 and 120 μm thick and multiple layers can be used to create thicker or more complex devices (Alvaro et al., 2006). The 3000 series of SU-8 has been designed to have increased adhesive properties, which aids in multilayer fabrication. SU-8 is biocompatible and, in addition, there are chemically modified versions of SU-8 that can be easily covalently modified (Tao et al., 2008).

For reactive ion etching (RIE) etch masks the S1800 and AZ4500 series positive resists were selected. The S1800 series is a commonly used family of resists that provide very good adhesion and allows layers of up to 4 μm to be spun when using the S1828 variant. AZ4500 series allow layers up to 9 μm thick to be created in a single spin. This series of resists have a lower concentration of photoactive compound when compared to other resists. This ensures correct exposure throughout thick layers.

The polymer chosen for soft lithography was polydimethylsiloxane (PDMS) (Hillborg and Gedde, 1999). PDMS allows rapid and easy production of devices and is relatively cheap compared to other biocompatible polymers. PDMS is transparent and so allows many optical techniques that are problematic with opaque polymers, such as PCL. However, untreated PDMS is hydrophobic and thus cells will not readily attach to it in large numbers. Exposing the polymer to a plasma will change its surface chemistry and renders it hydrophilic, however, the surface can recover its original hydrophobicity (Fritz and Owen, 1995). Kim et al (Kim et al., 2004) plasma treated samples of PDMS so that they had a surface contact angle of less than 10° and then kept them in various storage medias. Untreated control samples had contact angles of 110 - 120°. They found that if stored in air or phosphate buffered saline (PBS) the PDMS will recover to 90 - 100° in ~ 1 week. However, storage in water reduces the recover to 50° in a week and 60° after 45 days. Recovery in culture media was not studied and so to further guarantee long term cell adhesion modification of the surface(Zhou et al., 2010, Zhou et al., 2012) is prudent. Details of the surface modifications are shown in Chapter 3.

2.1.2 Device Design

The alignment devices were designed to have ridges with 12.5, 25 or 50 μm width and a height of 5 μm. The ridges were spaced to have an equal pitch to their width. The devices needed to fit into the wells of a 24-well plate and so were designed to be cut into 13 mm diameter disks. The disks were initially 2 mm thick but this was later reduced to 0.5 mm to improve their optical properties for fluorescence microscopy. The ridges covered ~ 50% of the device, this allowed flat areas above and below the ridges which formed a built-in control. Numbers were placed above the ridges to indicate the ridge width.

The first generation of containment devices used the same 13 mm disk format but omitted any ridges. In the centre of each device were two rows of pillars and two solid walls that formed a rectangular containment area. The pillars had a diameter of 15 μm and gaps between them of 2, 4, 6, 8 or 10 μm. The walls were 40 μm wide and were scaled to created contained areas of 1, 3, 5, 7 or 9 mm^2.

All masks for the devices were designed so that they had the same general layout and had alignment marks in the same places. This allowed them to be combined to make multilayer devices using any combination of designs.

2.2 Materials & Methods

2.2.1 Wafer Cleaning

Masters for all the devices were fabricated on 100 mm Si wafers. The wafers were washed in acetone, methanol and isopropanol with sonication for 5 minutes each. The wafer was then dried with nitrogen gas. A dehydration bake was then performed at 180 °C for 10 min.

2.2.2 SU-8 Photolithography

SU-8 3005 was spin coated to form layers 5 or 10 μm thick, while 3050 was used for layer of 50 or 100 μm. The wafer was then soft-baked on a hotplate at 95 °C. The photoresist was given at least 15 mins to cool before being exposed on a Suss MicroTec MA6 mask aligner that had an energy output of 7.1 mW/s; soft contact mode was used. A post-exposure bake (PEB) was then performed on a hotplate for 1 min at 65 °C and 4 mins at 95 °C. The unexposed SU-8 was developed off using EC solvent. The surface was then rinsed with IPA and RO water. The suppliers recommended spin speeds, soft baking times and exposure energies are shown in Table 1.

SU-8 Type	Layer Thickness (μm)	Spin Speed (RPM)	Soft Back (min)	Exposure Energy (mW/cm^2)
3005	5	3000	10	150 – 200
	10	1000	15	150 - 200
3050	50	3000	20 – 30	200 – 250
	100	1000	30 - 40	200 - 275

Table 1: Recommended spin speeds, bake times and exposure energies for SU-8 3005 & 3050.

2.2.3 AZ4562 Etch Masks

Wafers were spin coated with primer and then allowed a 2 min relaxation delay. A 6 um layer of AZ4562 was then spun onto the wafer at 3000 rpm. Excess solvent in the resist could form bubbles in the layer during soft baking and so a 10 min delay was allowed before baking so the solvent could evaporate. The wafer was then baked at 50 °C for 5 mins and then 100 °C for 10 mins on a vacuum hotplate.

As the presence of water is required inside the resist for the photoreaction to occur during exposure (MicroChemicals, 2010), a 60 min delay in a 50% humidity room was allowed for rehydration. Exposure was performed on the MA6 mask aligner with hard contact mode to obtain the greatest resolution. Nitrogen gas is produced during the exposure and so a 20 min relaxation delay was performed to allow the gas to defuse out of the resist. Exposed resist was developed using AZ400K developer in a 1:4 concentration in DI water. The wafer was then rinsed for 5 min in DI water and dried with nitrogen. Any remaining resist residue was then removed with oxygen plasma by ashing the sample for 2 min at 100 W in a GaLa PlasmaPrep5 barrel asher.

2.2.4 S1828 Etch Masks

Wafers were spin coated with primer and then allowed a 2 min relaxation delay. A 2.8 um layer of S1828 was then spun onto the wafer at 3000 rpm. The resist was then soft baked for 3 mins at 120 °C. Exposure was 5 secs under a 7.1 mW/cm^2 UV source using hard contact mode. Development was performed for ~ 5 mins using Microposit Concentrate diluted at a 1:1 ratio in DI water. The wafer was then washed in DI water and dried.

2.2.5 Dry Etching

Etching was performed using a Surface Technology Systems Inductively Coupled Plasma (ICP) tool. This tool uses the Bosch process to perform deep reactive-ion etching (DRIE). The settings used were: coil power 600 w; platen power 10 W; chamber pressure 10 mTorr; C_4F_8 flow 50 sccm; SF_6 40 sccm. An etch time of 27 mins was used to create 30 µm pits. 5 mins of etching was used to create 5 µm ridges.

2.2.6 Wafer Silanisation

Silanisation of the master was performed to reduce adhesion between the wafer's surface and the polymer during soft lithography. To coat the wafer, it was placed in a lidded Petri dish with a drop of (tridecafluoro-1,1,2,2-tetrahydrooctyl) trichlorosilane (ABCR GmbH & Co). The Petri dish was then placed onto a hotplate heated to 150 °C and left for ~ 15 mins. This caused the silane to turn into a vapour and settle unto the master, forming a thin coating.

2.2.7 PDMS Casting

The master was placed into a moulding jig, which consisted of a bottom, securing plate; a flanged plate to secure the master to the bottom plate and set the height of the chamber; and a Perspex top plate with two inlet/outlet holes.

The PDMS (Dow Corning, Sylgard 184) was mixed with ten parts base to every one part curing agent and then placed in an vacuum chamber to remove any air bubbles. The PDMS mixture was then injected into the mould, which was then left to cure at 80° for 2 hours. After curing, the sheet of PDMS was cut from the mould and the individual devices were cut out with a cork borer to form 13 mm diameter disks.

2.2.8 Epoxy Mould

A PDMS copy of the silicon master was cast using a base to curing agent ratio of 10:1. Epoxy resin (Loctite, Double Bubble) was then mixed and spread across the inside of a large Petri dish lid. The PDMS sheet was then embossed into the epoxy resin. This was achieved by placing the PDMS sheet face down onto the epoxy layer and then placing a large flat weight on top of the PDMS sheet. The epoxy was left for 10 mins at room temperature to set before the weight was removed and the PDMS peeled from the epoxy. PDMS copies of the epoxy mould where then cast.

2.2.9 Metrology

Devices were imaged inside a Hitachi S3000 scanning electron microscope (SEM). For PDMS devices a beam voltage of 5 kV was used, while silicon was imaged with a 15 kV beam. The devices were typically viewed from 0° and 90° for measurements and 30° for illustrative images. All non-conductive samples were coated with a 18 nm layer of gold-palladium to allow viewing.

All images created by the S3000 had attached information such as beam voltage and a scale bar. The images were imported into ImageJ and the scale bars were used to set an internal scale. Feature sizes were then measured using this scale. The average over 5 measurements was used for each dimension.

As the masks plates would not fit inside the SEM and they were too valuable to cleave, they were measured with the aid of an optical microscope using the same technique as described above. Scale bars were obtained for these images with the aid of a graticule. This method was also used for other valuable samples and those that could not easily be cleaved.

2.3 Results and Discussion

2.3.1 Alignment Device Fabrication

Problems were encountered when working with SU-8 for the first time. When using SU-8 3005, the recommended spinning protocol was to dispense 1 ml of resist per inch of wafer diameter in a small puddle in the centre of the wafer. When this protocol was used a small area of increased height could be seen where the resist puddle was before spinning. To avoid this, a layer of resist was spread across the entire surface of the wafer. If an insufficient amount of resist was used, dewetting of the surface occurred and small pores could be observed opening in the resist layer. It was found that ~2 ml of resist per inch of wafer provides a sufficient amount to coat the wafer and prevented dewetting. Normal spin speeds and bake times were then be used.

Additional problems were encountered during exposure of the resist layer, as SU-8 is a very viscous and sticky photoresist. When the mask plate was brought into contact with the wafer, the mask and wafer became stuck together. This resulted in lengthy cleaning processes for the mask that did not always remove all debris. The first solution to this problem was to use proximity exposure mode on the mask aligner. This mode left a gap between the mask and the wafer and thus prevented sticking. However, as there was an air gap present, poorer resolution was achieved when compared to contact mode. A second solution was then employed where a longer soft bake and extended cooling time were used. The extended soft bake allows more solvent to evaporate from the resist layer, reducing the amount of dissolved resist present. A longer cooling time ensured there was no liquid resist on the surface of the resist layer. Soft contact mode was then used on the mask aligner. This mode brings the mask and wafer into contact only using pressure as apposed to the vacuum that is used in hard contact mode. This mode was chosen to reduce the chance of SU-8 debris being transferred to the mask.

An exposure dose test was performed to establish the optimal exposure time for the 5 μm high ridges. The results of this test are shown in Figure 9. Good adhesion was obtained with all exposures and there was a swelling of the feature dimensions as the exposure increased. A comparison of the resultant feature sizes is shown in Table 2. An exposure of 10s was chosen as this resulted in features comparable in size to the features on the ferric mask.

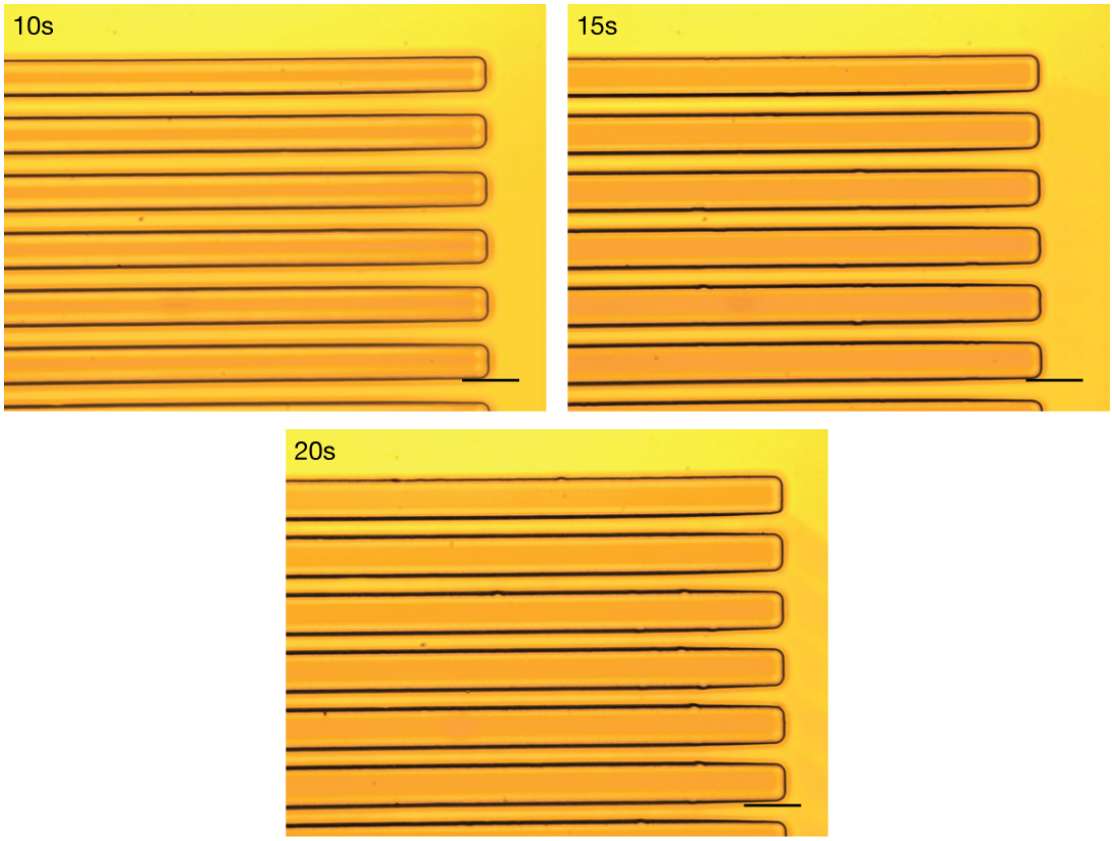

Figure 9: Exposure dose test of SU-8 ridges on silicon. The ridges were designed to be12.5 µm wide and 5 µm high. The resist was exposed under a 7.1 mW/cm² UV source. Exposure times are shown in the top right of each image. Swelling of the ridges occurred as exposure increased. Good adhesion was obtained with all doses. Small defects were seen on some of the ridges, these were caused by dirt on the mask plate. Scale bars are 25 µm.

	Ferric	10 s	15 s	20 s
Line Width	14.2 +/- 0.4	14.0 +/- 0.2	15.0 +/- 0.2	15.8 +/- 0.2
Space Width	10.4 +/- 0.5	11.2 +/- 0.4	10.4 +/- 0.3	9.5 +/- 0.2

Table 2: Line and space width resulting from increasing exposure dose of a 5 µm layer of SU-8 3005. The resist was exposed under a 7.1 mW/cm² UV source. The dimensions of the ferric mask plate are shown for comparison. All measurements are shown in µm.

2.3.2 Containment Device Fabrication

The first generation of containment devices consisted of a rectangular area surrounded by a rows of pillars on two sides, and two walls on the other two sides. The pillars were 15 µm in diameter, the walls were 100 µm wide, the pillar and wall height was 100 µm, the contained areas were either 1, 3, 5, 7 or 9 mm^2 and the gaps between the pillars were 2, 4, 6, 8 or 10 µm. A sketch of the design can be seen in Figure 10.

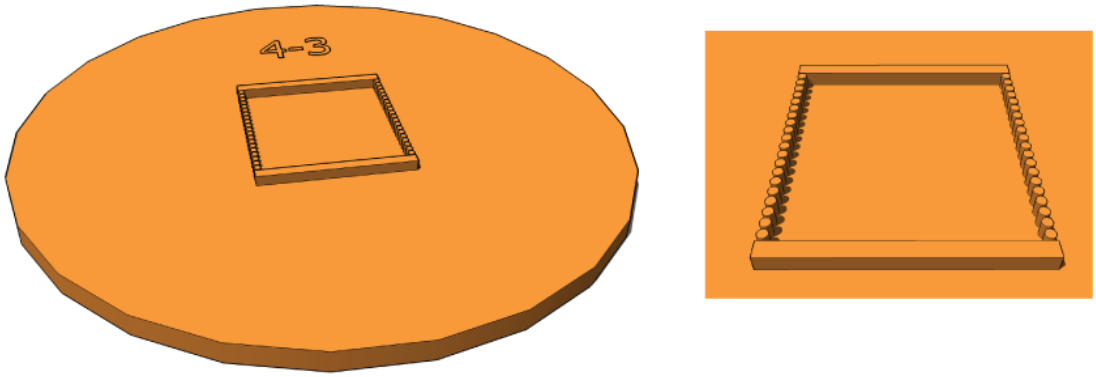

Figure 10: Sketch of the first generation of containment devices. The contained area consisted of two walls and two rows of pillars. Dimensions of the devices are described above. The "4-3" showed that the gaps between the pillars were 4 µm and the contained area was 3 mm^2. Note that the sketch is not to scale.

Initial fabrication of the master was not wholly successful. Large cracks formed around the corners of the walls and around the pits, shown in Figure 11. This was likely due to the large surface area of SU-8 being exposed. This can cause tensions to build up in the layer during post exposure baking, which is then released in the form of cracking when the layer cools or during development.

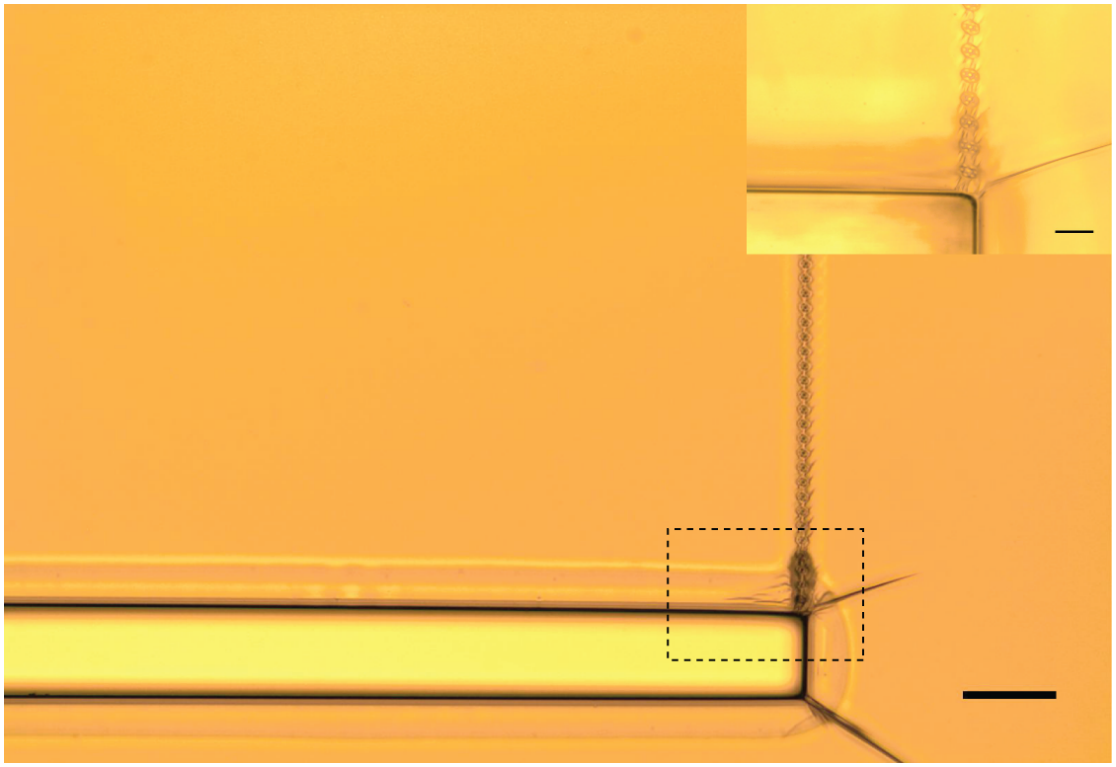

Figure 11: Cracks formed in a 100 µm layer SU-8 3050 due to the large area exposed. The pits also failed to form correctly and appeared slightly skewed and linked by cracks. The highlighted area is shown at higher magnification in the top right. Scale bars are 100 µm in the main image and 25 µm in the insert.

However, the master could be used to cast PDMS to investigate the use of the design for biology. It was found that there were several practical problems associated with the first containment design. Firstly, manually manoeuvring a pipette tip into the containment area was tricky and error prone. Secondly, a microscope was needed to easily see the smaller areas. Finally, the seeding was a slow process, requiring ~ 1 - 2 hours for 25 devices. Due to these problems the devices were redesigned.

2.3.3 Containment Device Mk.2

The second generation of containment devices had several modifications. A single line of pillars was placed across the device to screen off half of the surface. The pillars diameter was increased to 30 µm to make fabrication easier; gap dimensions remained the same. A large number that was visible to the eye was placed inside the containment area; this indicated the gap size and also aided in the positioning of the pipette tip to the correct area.

The containment area was increased to 23.04 mm^2, compared to a maximum of 9 mm^2 in the previous devices; this was done to prevent the "wash out" problem encountered during cell seeding. The larger area also made accurate pipette placement less critical and in turn removed the need for a microscope.

Gap sizes were kept to 2, 4, 6, 8 and 10 µm. The lack of a variable containment area reduced the device variants to 5, down from 25. This both increased device yield during fabrication and simplified experiments. A sketch of a 8 µm gap device is shown in Figure 12.

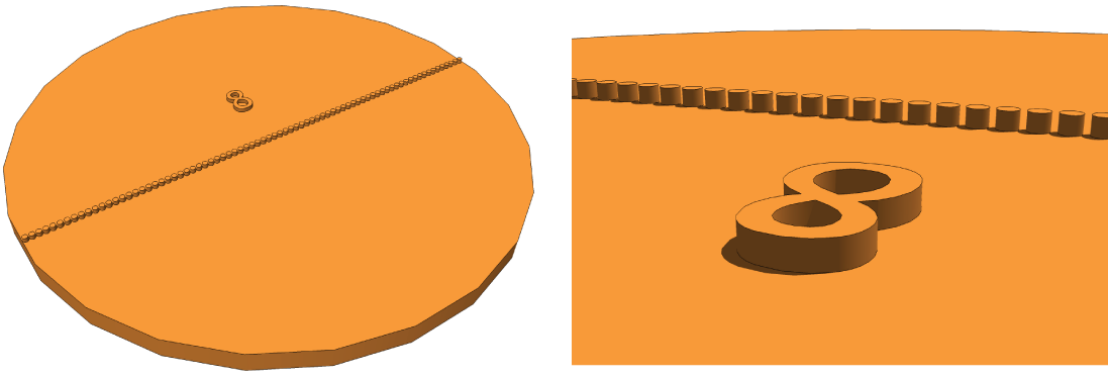

Figure 12: Sketch of the Mk.2 containment device. The pillar placement was changed to contain a region of the device instead of forming a walled rectangle. The pillar diameter was also increased from 15 to 30 µm. The number indicated the gap size. Note that the sketch is not to scale.

However, fabrication of the devices proved problematic. Attempts were made to create a negative master where pits were formed in a layer of SU-8, which then produced pillars when cast in PDMS. A range of exposure doses where used to find the optimal fabrication parameters. Similarly to the Mk.1 devices, during the development step cracks formed in the resist and the bottoms of the pits failed to develop out correctly, which resulted in debris remaining in the structures. This caused the PDMS pillars to be malformed. Micrographs of the master are shown in Figure 13 and SEM images of the PDMS devices cast from the master are shown in figure 12.

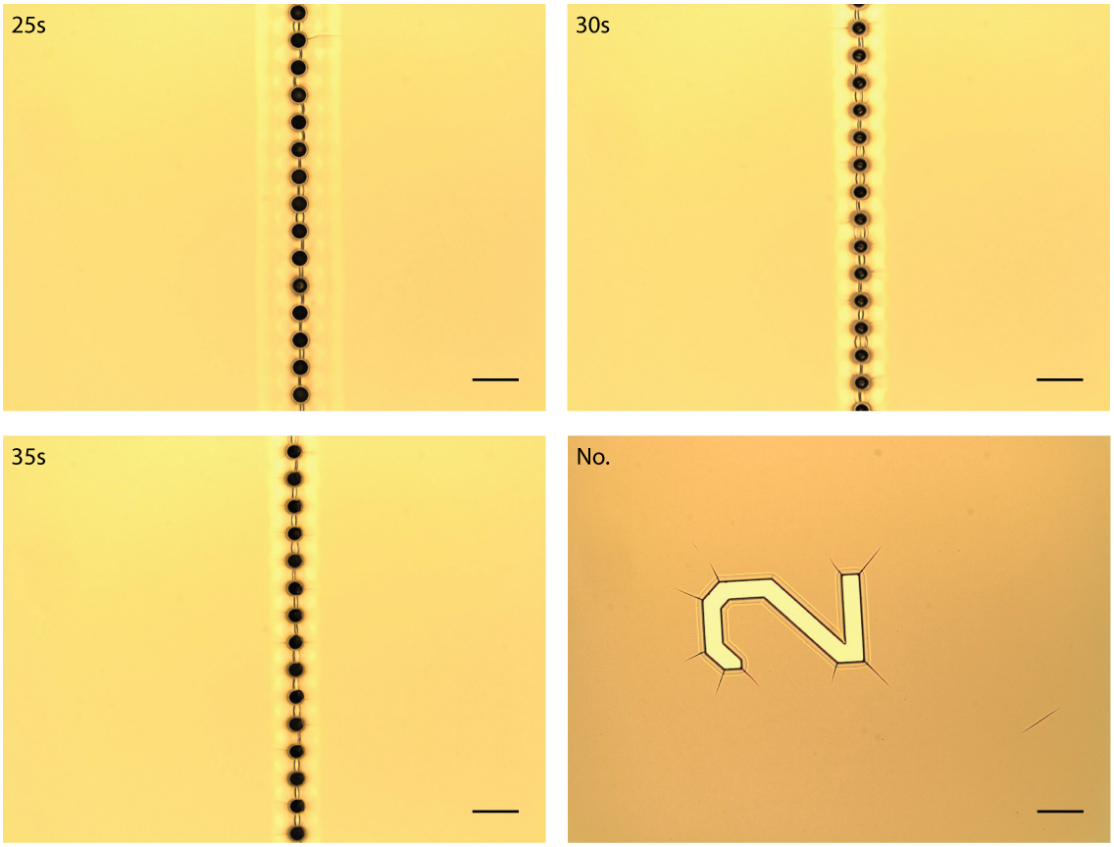

Figure 13: 50 µm thick layer of SU-8 3050 on a silicon wafer. The resist was exposed under a 7.1 mW/cm^2 UV source. Exposure times are shown on each image. The number indicator, labelled "No.", was exposed for 25s. The wafer was immersed in developer for 1 hour with mild agitation. The pits were designed to have 30 µm diameter and gaps of 10 µm. Scale bars are 50 µm. Large cracks can be seen emanating from the gap indicator number. Cracks can also been seen between the pits. Debris is also evident at the bottom of the pits.

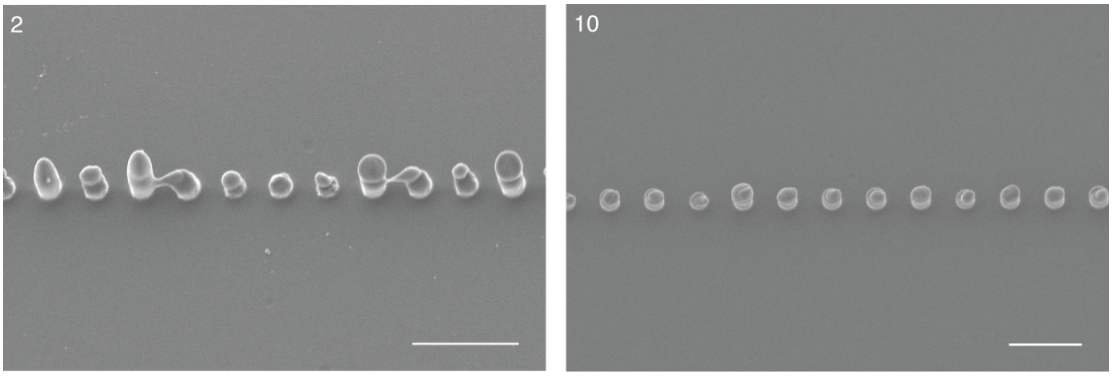

Figure 12: SEM micrographs of a PDMS device cast from the master shown in figure 11. It was cast from an area that had a 25 s exposure. The device was coated with an 18 nm layer of gold-palladium to allow imaging. The pillars were designed to be 50 µm high, have 30 µm diameter and gaps of 2 µm between each pillar. Scale bars are 50 µm. The cracks and debris that was present on the master caused considerable distortion to manifest in the PDMS pillars. The linking of pillars is due to the cracks and the debris at the bottoms of the pits caused their squat form. The larger gaps size is due to a lower than optimal exposure dose on the master.

A longer development time was trialled as a means of removing the photoresist that was left at the bottom of the pits after the 1 hour development. A wafer was immersed in EC solvent overnight but this resulted in large numbers of cracks forming across the photoresist surface and some debris was still present at the bottom of the pits, as shown in figure 13.

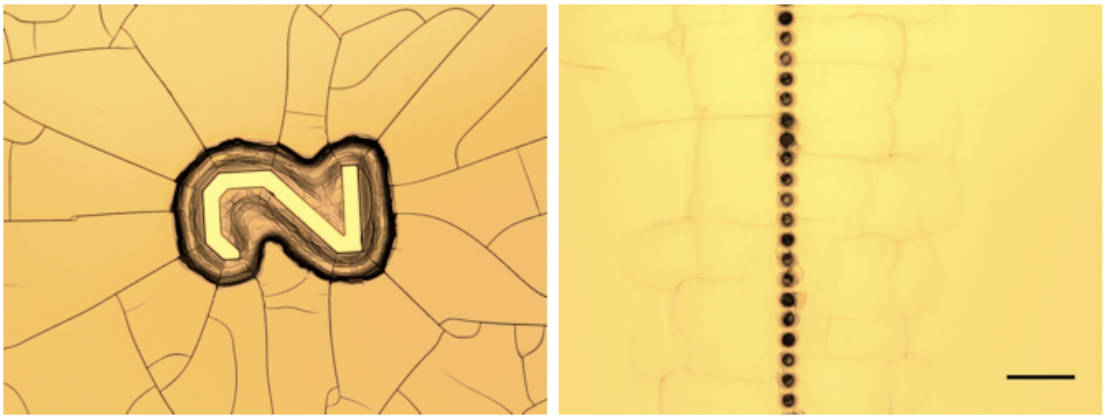

Figure 13: SU-8 master created in the same manner as the one shown in figure 11. The wafer was left overnight in developer. Both images are from the 2 µm gap area. The area shown on the left had an exposure dose of 25 s while the area on the right was exposed for 35 s. Cracks covered the entire surface of the photoresist. Around the areas with features, even greater amounts of cracks could be seen and the features had become distorted. As can be seen in the right image, debris still remained at the bottom of some of the pits.

There were two possible solutions to this problem. One was to use dry etching to create the pits directly in the silicon. This method would only require a thin etch mask made out of photoresist thus eliminating the problem of trying to develop to the bottom of the 50 µm layer. Another solution was to create a positive master, cast a PDMS sheet from the SU-8/silicon master and then use the PDMS as a master itself. The PDMS would require chemical modification of its surface, such as fluorination, to prevent further PDMS from bonding to it.

The second solution was trialled first as it was the simplest to carry out and did not require a new protocol. The exposure dose test for the SU-8 pillars is shown in Figure 14.

Extremely low exposure doses were required to prevent occlusion, this resulted in poor adhesion between the pillars and substrate. A possible solution to this was to reduce the pillar

height and thus the dose required for good adhesion. However this could result in poor containment of the cells.

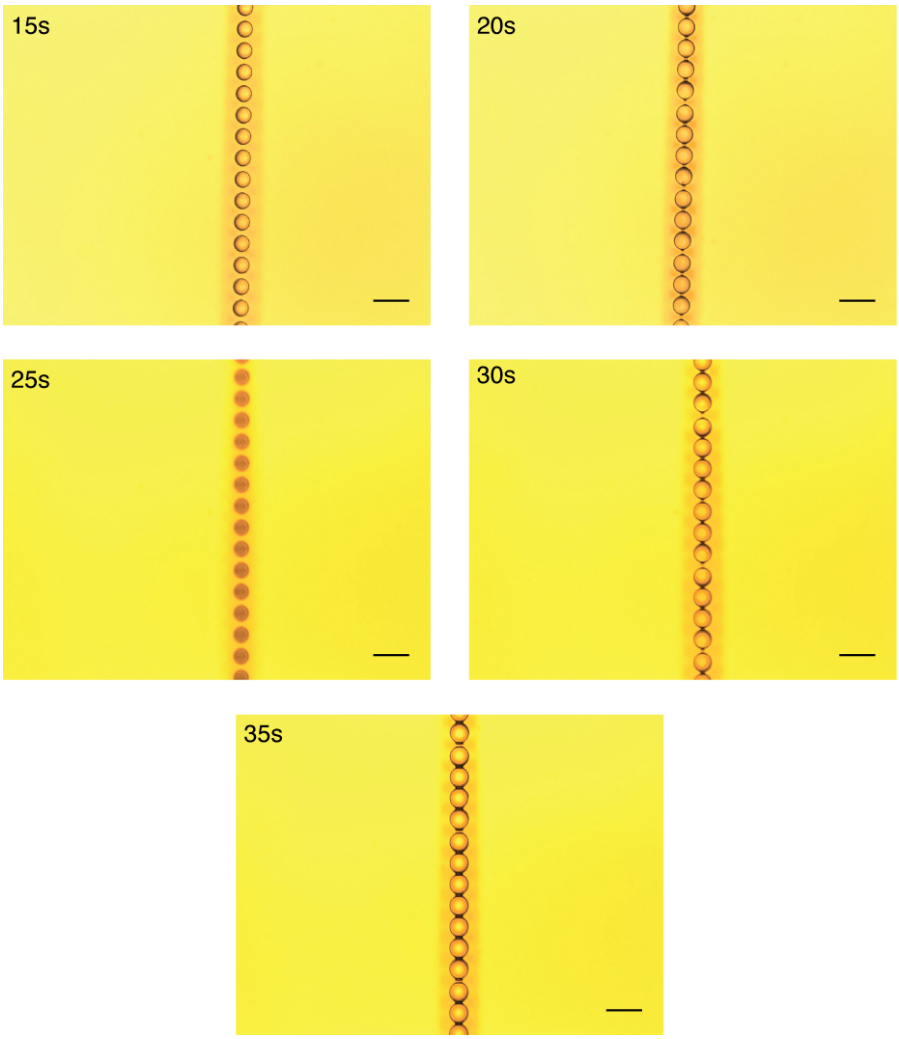

Figure 14: Exposure dose test of SU-8 pillars on a silicon wafer. The resist was exposed under a 7.1 mW/cm^2 UV source; the exposure time is indicated on each image. The pillars were 50 µm high and were designed to be 20 µm in diameter with 10 µm gaps between each pillar. Scale bars are 50 µm. A dose of 35 s results in almost complete occlusion of the gaps. Similar effects can be observed as low as a 20 s exposure. Doses of 15 and 20 s caused poor adhesion between the pillars and the substrate. As a result, large amounts of pillars detached from the surface during the washing and drying phase of development.

2.3.4 Containment Device Etching

As it was apparent that accurately fabricating the pillars in SU-8 was not possible, dry etching was used as an alternative fabrication technique. To do this, an etch mask was created in AZ4562 photoresist. Deep reactive-ion etching (DRIE), a specialised version of RIE intended for very deep structures, was the used to create the pits. The first DRIE run performed is shown in Figure 15.

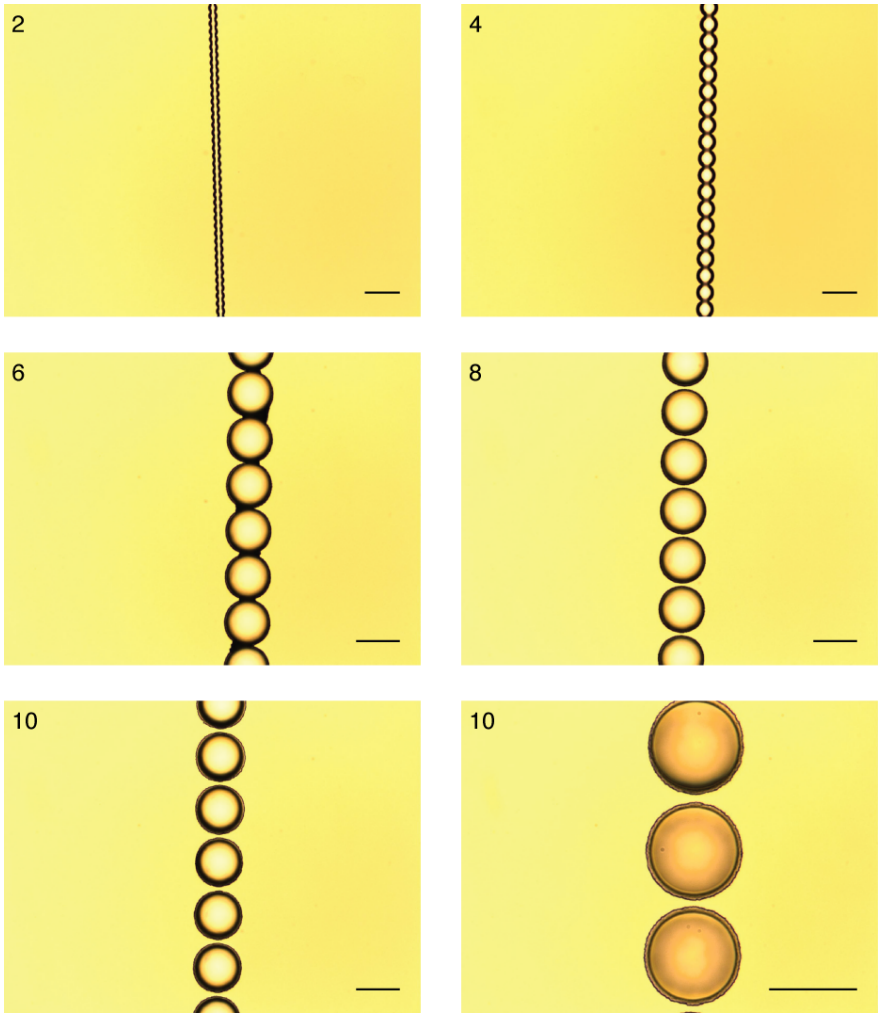

Figure 15: DRIE performed on a silicon wafer. A 6 µm AZ4562 etch mask was used and the wafer was etched at a rate of 1.08 µm/min for 27 mins. The pits were designed to be 20 µm in diameter and ~30 µm deep. The designed gap widths between the pits are shown in the top left corner of each image. The top left image has a 100 µm scale bar, the top right is 50 µm, all other images have a 25 µm scale bar. The 2, 4 & 6 pits had several defects, which resulted in partial or complete linking of the pits. The 8 & 10 pits had clear gaps between them with only minor defects in some areas. As can be seen in the lower right image, the sidewalls at the opening of the pits showed some roughness.

The resulting structures provided two usable variations of gap distance. However, as the size of the pits had been somewhat distorted during processing, measurement would have to be performed to find their exact dimensions. To this end, PDMS devices were cast from the silicon master and were examined under an SEM. The height and width of the pillars was measured at ~25 µm. Due to swelling of the pillars' dimensions, the 10 gaps had shrunk to 4.5 µm and the 8 gaps were 3 µm. The SEM micrographs are shown in Figure 16.

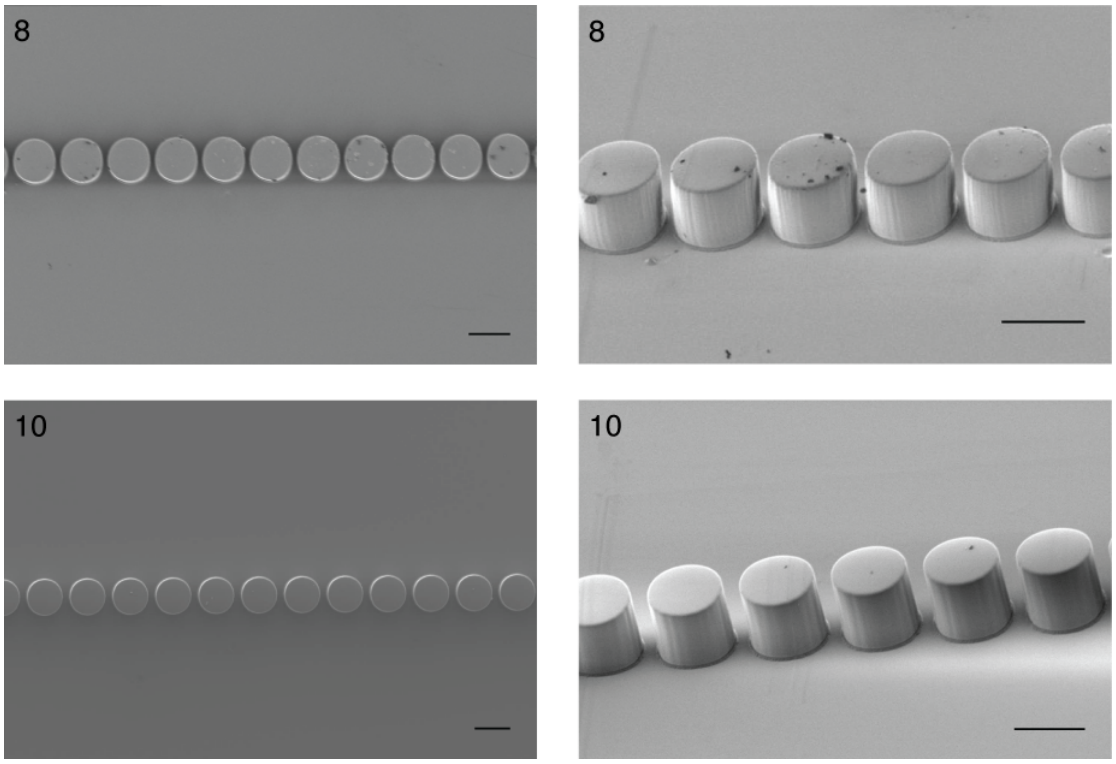

Figure 16: SEM micrographs of PDMS pillars cast from the masters shown in Figure 15. The number on each images indicated the designed gap size between the pillars. Scale bars are 25 µm. The pillars changed slightly from their designed height of 30 µm and 30 µm diameter to a measured height and diameter of 25 µm. The 8 gaps have shrunk to 3 µm and the 10 gaps have become 4.5 µm. The sidewalls of the pillars appear to be smooth despite the slight roughness that appeared on the master. Some small pieces of debris can be seen on the 8 gap images. These are most likely to be particles of carbon paste that is used to secure the sample to the SEM stage.

Despite the alterations in dimensions, the 8 and 10 devices could be used for some initial cell containment experiments, which are described later in chapter 3. While these experiments were ongoing, attempts were made to refine the fabrication of the smaller gap sizes. AZ4562 is a relatively tricky photoresist to work with, as it requires multiple relaxation and rehydration steps during processing. Timing the processing accurately is crucial to obtaining smooth

structures. After practice more accurate etch masks could be produced and thus improve the structures created during etching. The improved results are shown in Figure 17.

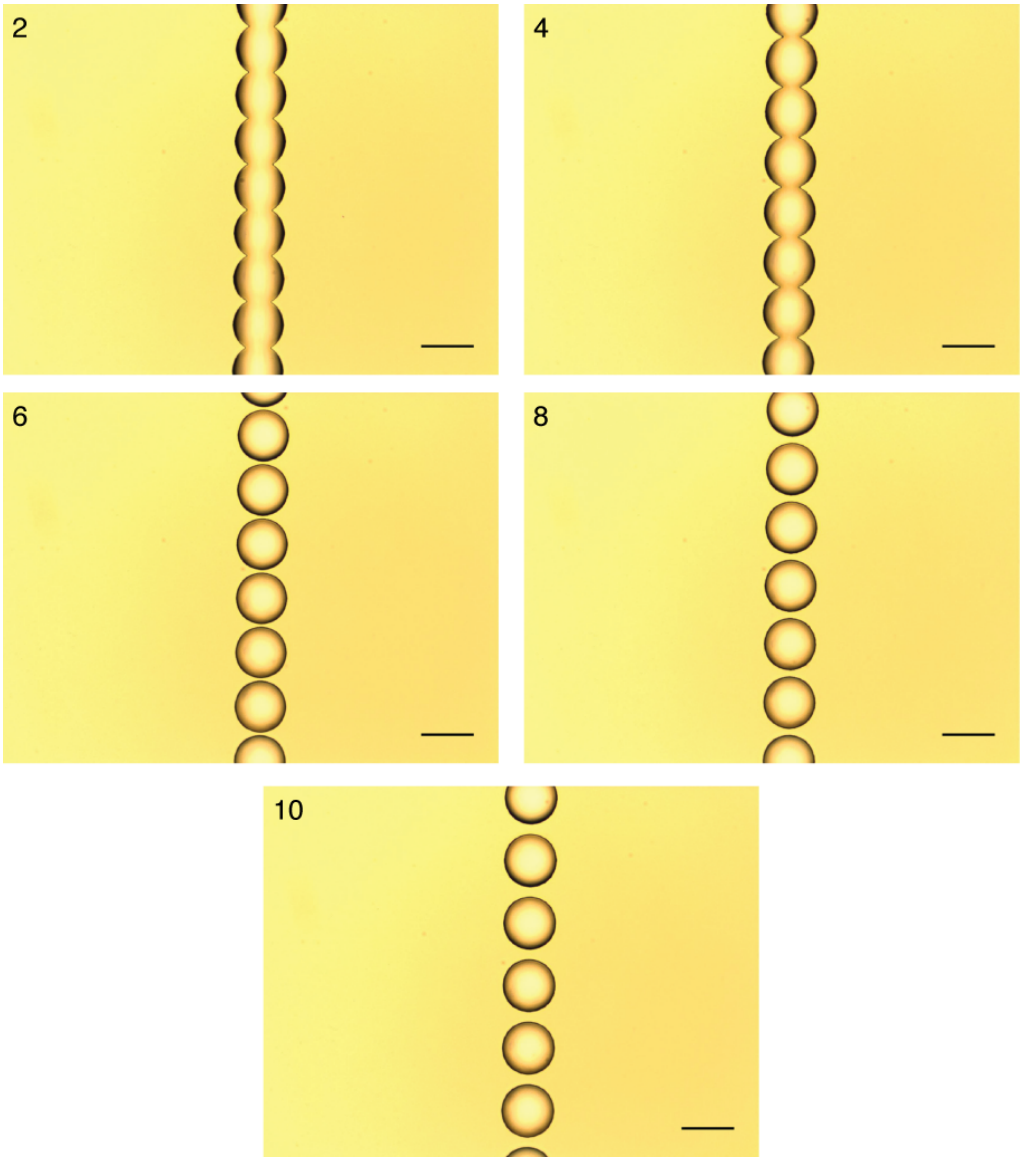

Figure 17: DRIE performed on a silicon wafer with improved etch mask fabrication. A 6 µm AZ4562 etch mask was used and the wafer was etched at a rate of 1.08 µm/min for 27 mins. The pits were designed to be 20 µm in diameter and ~30 µm deep. The designed gaps between the pits are shown in the top left corner of each image. Scale bars are 25 µm. The improvements in etch mask fabrication resulted in far clearer etching when compared with those in Figure 15. The 2 & 4 pits have still linked together, however the 6, 8 & 10 all have clear gaps between them and are free of defects.

Attempts were then made to integrate the containment devices with the previously fabricated alignment devices. One possible method was to create SU-8 ridges on top of etched pits. This method would require a new photo mask to be fabricated, which is an expensive and time-consuming process. A cheaper but more time consuming method of combining the structures

was to perform two dry etch runs, one to create the ridges and another to create the pits. This method also had the advantage that if a problem occurred during photolithography, the AZ4562 layer could be stripped from the wafer and the processing could be repeated. This is not possible when working with SU-8.

When the first etch mask for the ridges was fabricated using AZ4562, poor adhesion between the resist and the wafer was obtained. The exposure dose for these structures had to be adjusted to obtain good lithography. Micrographs of the structures obtained after two different doses are shown in Figure 18. The results of the combined ridge and pit etches are show in Figure 19, SEM images of PDMS devices cast from those structures are shown in Figure 20.

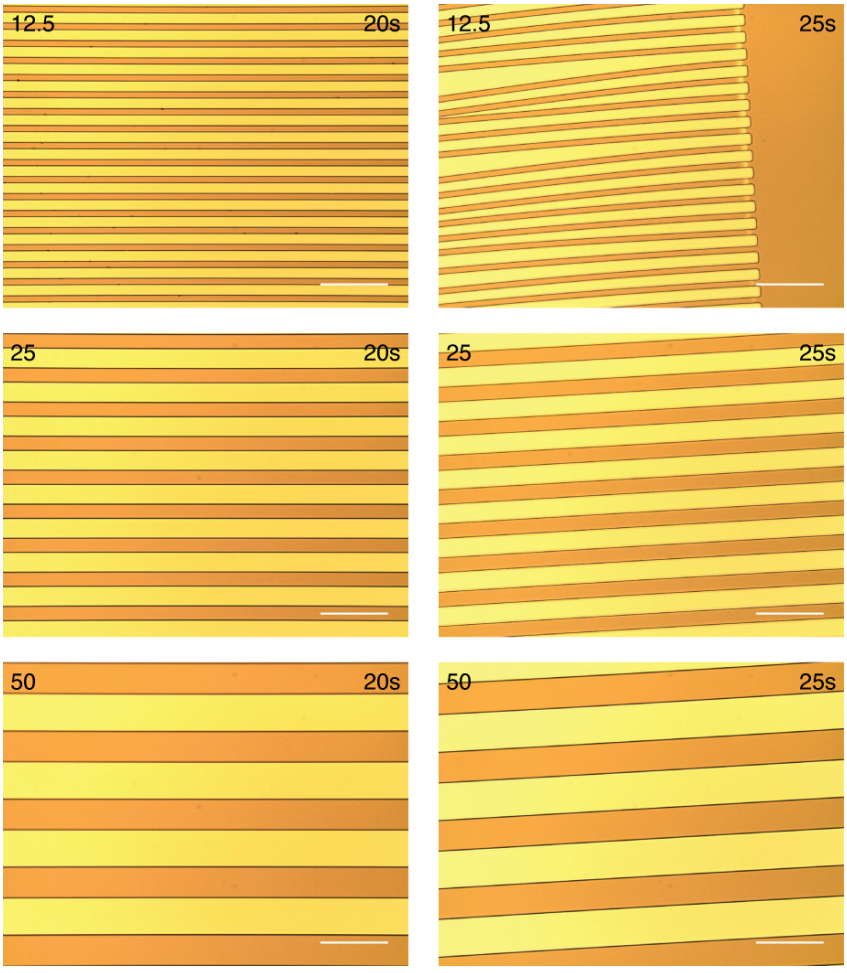

Figure 18: Does test for ridge layer AZ4562 etch mask on a silicon substrate. The number in the top left of each image indicates the width of the ridges in µm. The top right is the exposure time. The resist was exposed under a 7.1 mW/cm² UV source. Scale bars are 100 µm. On the 25 s devices, thinning of the structures and, in the case of the 12.5 µm, poor adhesion was observed. These are signs of an over exposed negative resist. The 20 s exposure resulted in good adhesion and so was used for all future AZ4562 ridges.

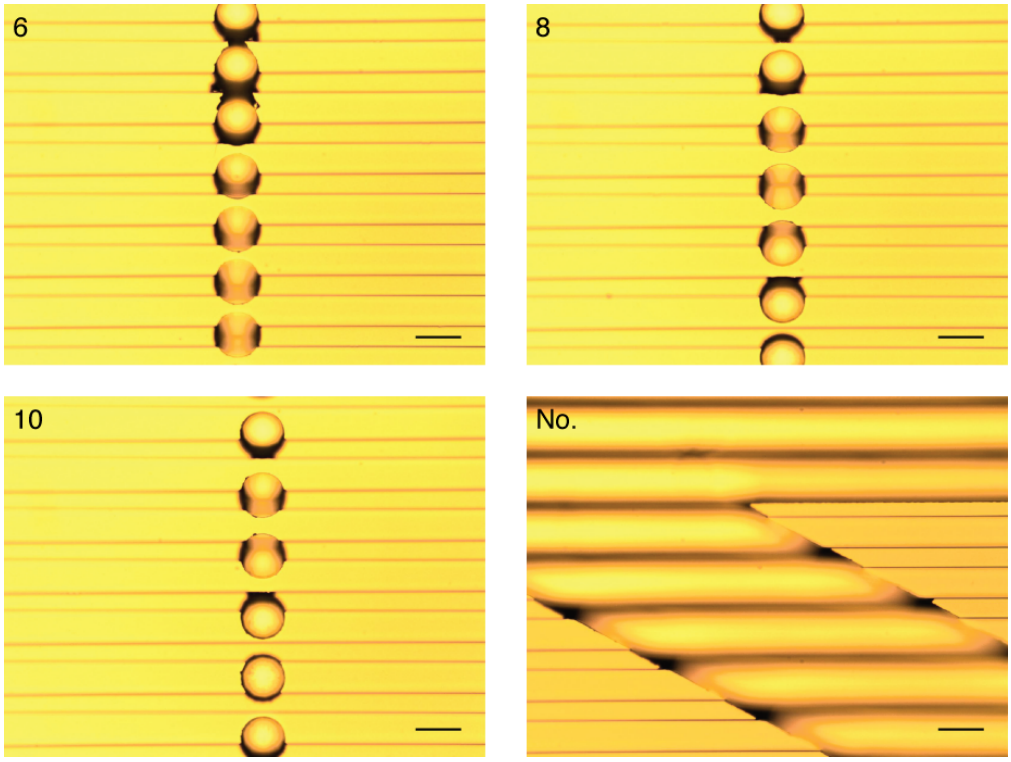

Figure 19: Micrographs of combined ridge and pit etches. A 6 µm AZ4562 etch mask was used for both etches. The number in the top left of the image shows the designed gap distance between the pits. "No." shows the area that contains the numerical gap indicator on one of the devices. The ridges are 12.5 µm in diameter and were etched to a depth of 5 µm. The pits are 30 µm in diameter and ~30 µm deep. The 2 & 4 gap devices' pits became linked (not shown). Several defects were present in the 6 gap devices. The 8 & 10 device showed only minor defects and some roughness around the pit edges. The slight roughness was more readily apparent on the edges of the numerical indicators.

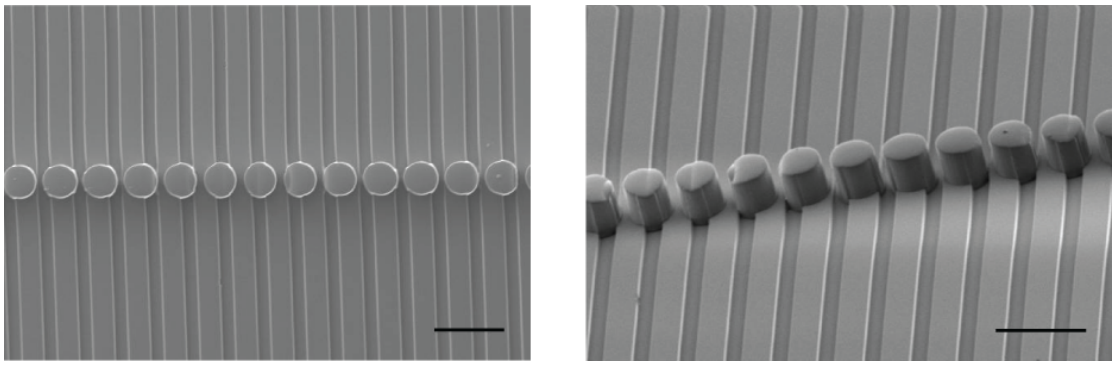

Figure 20: SEM images of PDMS devices cast from the master shown in Figure 19. The ridges are 12.5 µm wide, the pillars are ~25 µm in diameter and height. Gaps between the pillars ere design to be 10 µm. Scale bars are 50 µm. The pillars and ridges had flat, smooth sidewalls. Some defects in the pillars were observed. These were cause by the method of etching the pillars through pre-existing ridges on the substrate. In these images it appears that the ridges are slightly distorted; this is actually an artefact caused by problems with the stigmator on the SEM.

Despite the minor defects in the pillars, the PDMS devices were usable. The only method to entirely eliminate the defects was to create a new mask that had gaps in the ridges for the pits. However, this would have eliminated the option to move the pillar row to different positions on the ridges. As it had also become apparent that fabrication of gap sizes below 6 μm would not be possible, new masks were quickly redesigned to only contain 6, 8 and 10 μm gaps. This helped to greatly increase the amount of usable devices that could be created during one PDMS casting.

In case pillar height played a crucial role in preventing cells from escaping containment, attempts were made at deeper etches. A 7 μm thick AZ4562 etch mask was used and the surface was etched for an hour. This resulted in some areas of the etch mask being totally removed so that some unwanted areas of the surface were etched. Large amounts of defects were present across the entire wafer; these are shown in Figure 21. The defects were most likely caused by too thin an etch mask. However, a colleague attempted a 1 hour etch with a 10 μm AZ4562 mask and found similar results to those discussed here. Furthermore, another colleague found that cells were capable of climbing onto 80 μm high structures. Therefore the idea of higher pillars was dropped.

A method of printing BSA on top of the pillars, discussed in chapter 3, was developed to attempt to prevent crossover. It became clear that this method was not working and so other solutions were considered. Evidence (Miyoshi et al., 2010) showed that multiple, interlaced grooves could cause cells to change the direction of movement and screen them from areas of a device. Multiple rows of pillars would form a similar topography and so efforts were made to create a new master with 1, 3 or 5 rows of pillars. A new photomask was not required for this as multiple exposures could be made with the single row mask to create the extra rows.

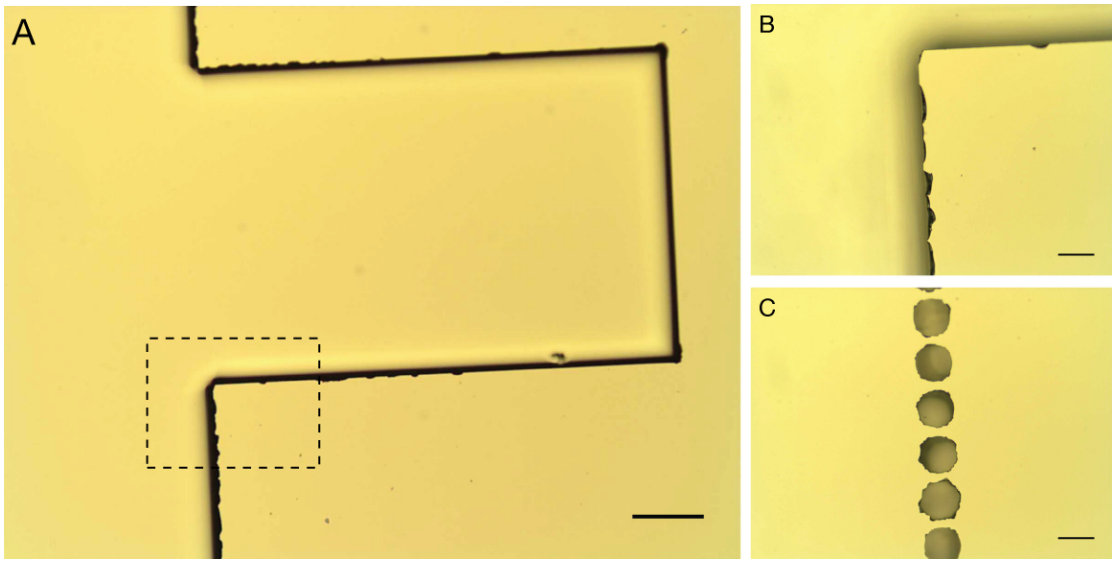

Figure 21: A ~60 µm deep etch performed on silicon with a 7 µm AZ4562 etch mask. In some areas of the wafer, the etch mask had been entirely etched away and unwanted areas of the surface were exposed. A) A low magnificent image of the area around one of the cross-shaped alignment marks. Rough edges were noticeable even at this magnification. B) A higher magnification of the hashed area shown in A. Large areas of sidewall roughness were cause by the long etch time. C) All of the 10 gap pits showed defects around their openings. Scale bars: A) 100 µm, B) & C) 25 µm.

However problems were encountered when trying to fabricate the master. During development of the ridges it was found that the AZ4562 resist would develop at different rates across the wafer. This was despite using the same protocol that had been successful in fabricating the ridge and pillar master shown in Figure 19. The differential development is shown in Figure 22.

Differential baking of the resist by the hotplate may have caused these problems. The top part of the wafer had been at a lower temperature than the bottom; this probably caused solvent to still be present in the top portion of the resist. The solvent interferes with the exposure process and so during development the top and middle portions of the resist could not develop correctly. The solution to this problem was to use a vacuum hotplate that gave more even heating across the wafer. However, this did not solve the adhesion problem.

Repeated attempts were made to obtain good adhesion between the resist and the wafer. Firstly, lower exposure times were trialled. After this proved ineffective, it was speculated that the primer might require baking to activate it. To eliminate this possibility, the use of the primer was varied to see if it was the cause of the problem. The results of these trials are shown in Figure 23.

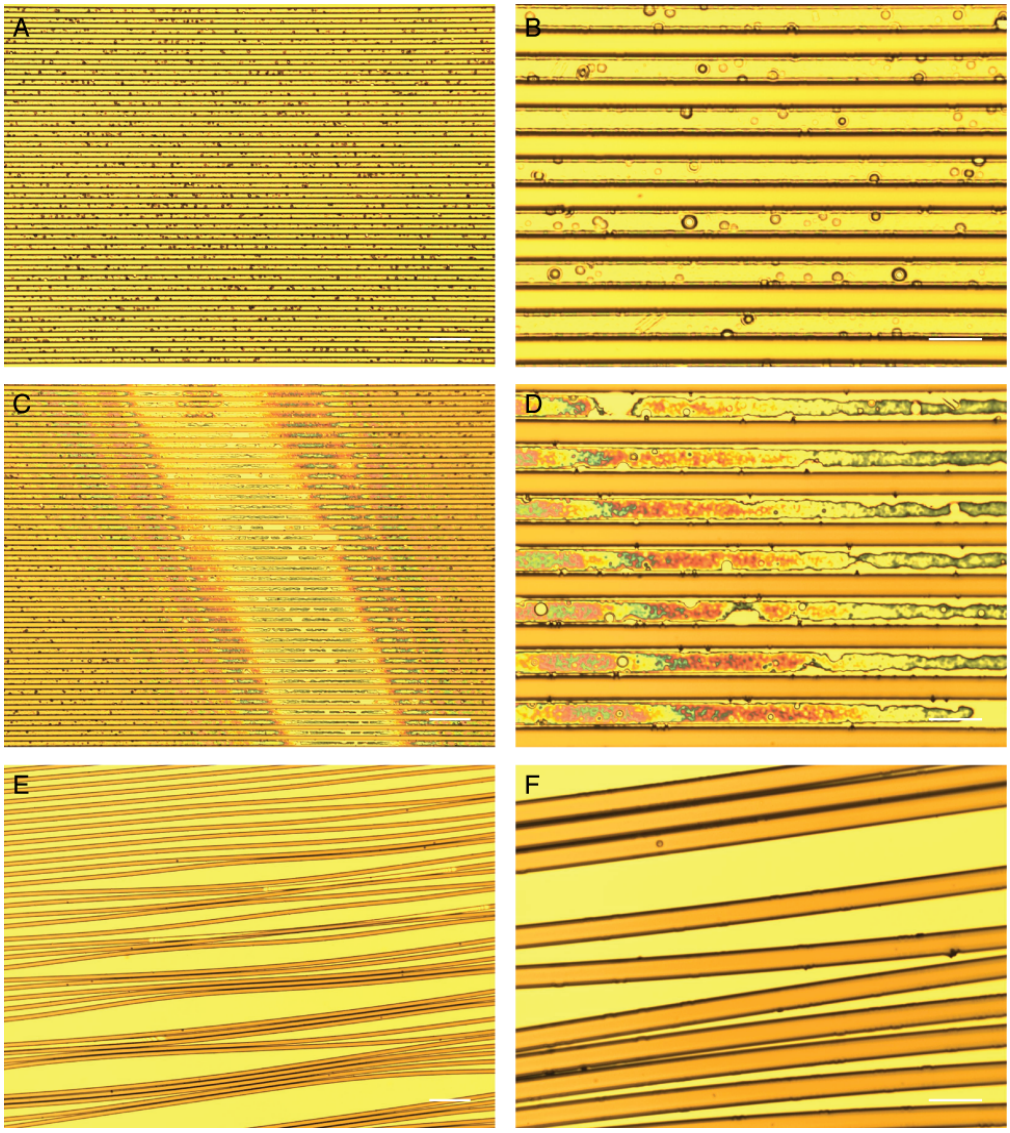

Figure 22: Non-uniform development of AZ4562 ridges on a silicon wafer. The resist was exposed for 20s under a 7.1 mW/cm^2 UV source. It was then developed for 3 min in AZ 400K developer. All pictures show 12.5 µm wide ridges. A & B were from the top of the wafer, C & D from the middle and E & F from the bottom. Incomplete development can be seen in A & B. Partial development has occurred in C & D. Complete development has occurred in E &F but poor adhesion has been obtained.

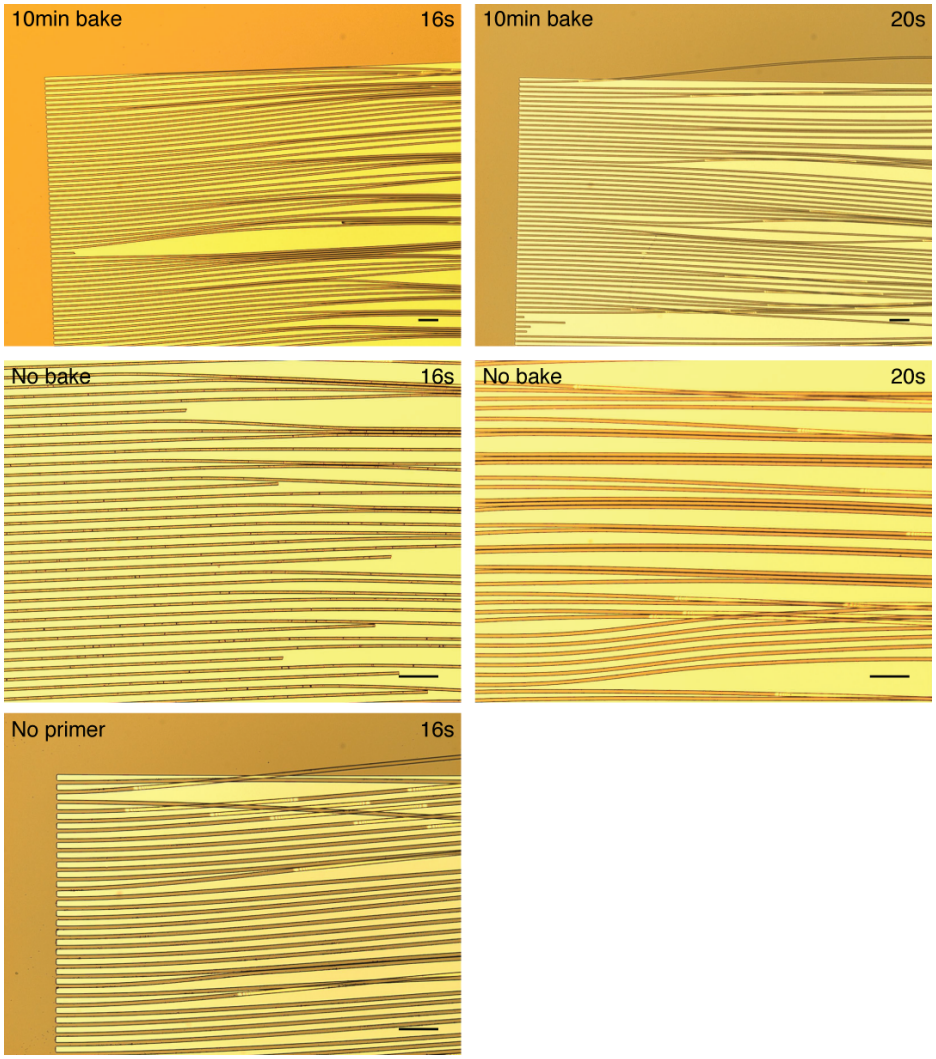

Figure 23: AZ4562 ridges on silicon wafers with no primer, unbaked primer or primer baked for 10 mins. The resist was exposed for the times indicated under a 7.1 mW/cm^2 UV source. The wafers were either coated with a primer prior to resist coated or left uncoated. In addition, the primer was either baked at 120 °C for 10 mins or not baked. The ridges were 12.5 µm wide and 6 µm high. Scale bars are 100 µm. Poor adhesion was obtained on all wafers.

All the methods trialled resulted in the same poor adhesion. As there was no readily apparent solution to the adhesion problem, a work around solution was developed. The ridges did not require a long etch time and so another type of resist could be used for that stage of the fabrication. S1828 gives a layer 2.8 µm thick which was sufficient for the 5 µm etch required for the ridges. The lower aspect ratio structures created by the S1828 provide better adhesion than the AZ4562 structures. In addition, S1828 had a far simpler protocol than the AZ4562, which sped up the fabrication process.

2.3.5 Multi-pillar Devices

The S1828 protocol allowed the first trial of the fabrication of a multi-pillar device. As the mask only had a single row of pits the following method had to be used to create the multiple rows. The first pit row was aligned and exposed; the mask was then realigned and moved in the x plane by 20 µm; a second exposure was then performed; further realignments and exposure were then performed as required. The developed resist layer created using this process is shown in Figure 24.

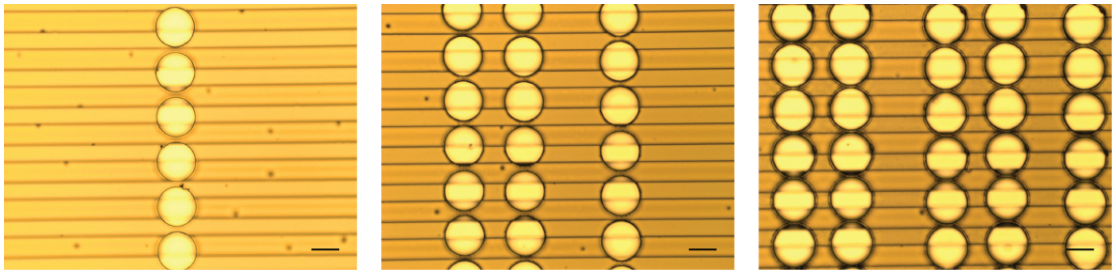

Figure 24: AZ4562 etch mask created for the multi-pillar devices. Resist thickness was 6 µm and exposure was performed for 25 s using a 7.1 mW/cm^2 UV source. Scale bars are 25 µm. All pictures show 10 gap devices. Alignment of the pit rows was performed as described above. Pits were intended to be spaced by 20 µm in the x plane. The gaps between the pits have occluded slightly. The alignment was imperfect, which caused the non-uniform spacing of the rows.

Accurately aligning the rows proved difficult; this was due to three main issues. Firstly, after each exposure the wafer carrier had to be slid out and then back into the mask aligner so that another cycle of alignment and exposure could be performed. During this movement the wafer was not held in place by a vacuum and so it could shift around on the carrier, which meant a full alignment had to be performed before each exposure. Secondly, the design of the alignment marks had been intended for quick alignments were a few microns inaccuracy would not matter. This made precise alignment challenging and created inaccuracies in the placement of the row pillars relative to each other. Finally, a difference between unexposed and exposed resist could not be seen through the mask plate while performing alignment. This made it impossible to check the alignment of the mask relative to the last exposure.

In addition to the uneven spacing of the pit rows, the gaps between the pits had narrowed somewhat. This could have been due to insufficient rehydration or the resist nearing its expiry date.

Despite the fabrication defects, an etch was performed in an attempt to obtain some usable devices. Micrographs of the etched wafer are shown in Figure 25.

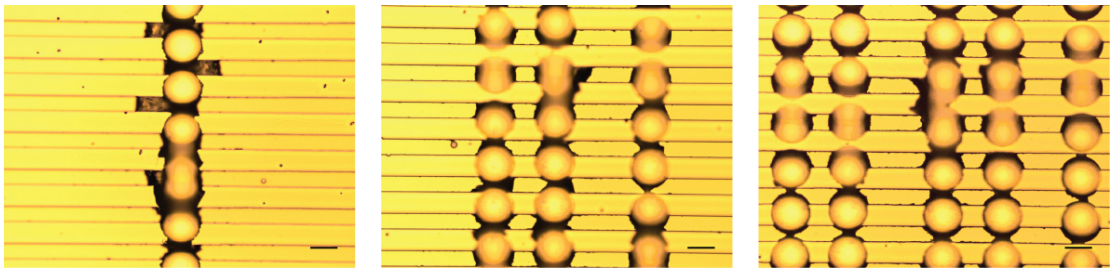

Figure 25: DRIE performed using the etch mask shown in Figure 24. All pictures show 10 gap devices. Scale bars are 25 µm. Major defects could be observed around the etched areas. A larger amount of the pits had fused and in some areas the spaces between rows had been etched away.

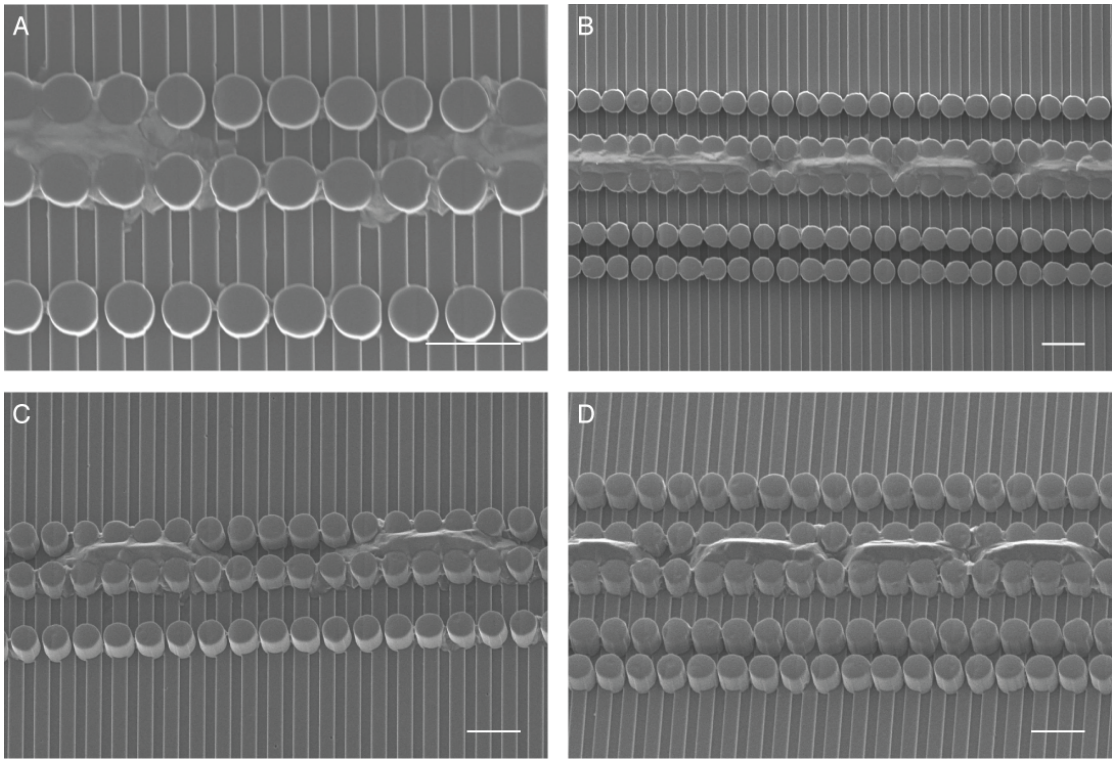

Figure 26: SEM images of PDMS devices cast from the multi-pillar master discussed above. All images show 10 gap devices. Scale bars are 50 µm. A) & B) show the devices from a 0° angle. C) & D) where taken at 30°. A large number of the pillars had fused together. Some of the areas between rows had been etched, this resulted in large mounds linking the two rows and obstructing the gaps.

The defects observed around the pits were caused by poor adhesion between the resist and the wafer. This allowed the etchant gas to infiltrate under the resist layer and etch unwanted areas. It was unclear how deep the defects where and so SEM images were taken of PDMS replicas cast from the wafer. These are shown in Figure 26.

The defects penetrated deep into the silicon and, when cast in PDMS, resulted in large mounds that were higher than the pillars. These devices were unusable for experiments with neurons; however, they were used to begin experiments on the effect of multiple barriers on cell migration.

2.3.6 Multi-pillar Mk.2

It was decided that creating multiple pillars via manual alignment was not a viable option as the exact spacing of the rows would not be reproducible. This necessitated the design of a new mask, which allowed a couple of minor problems with the design of the old mask to be corrected. The new design had gaps of 6, 8 or 10 µm and 1, 3 or 5 rows of pillars. The ridge layer was altered slightly by opening "pit windows" to reduce the distortion created by etching through the ridges. A sketch of the devices is shown in Figure 27. The chrome and ferric mask plates for the new design can be seen in Figure 28 and Figure 29. Dimensions of the masks and the intended dimensions are show in Table 3.

Creation of the multi-pillar silicon master was relatively straight forward as most fabrication problems had been eliminated at this point. Etching of the ridge layer resulted in clean lines with only very minor defects around the pit windows. These can be seen in Figure 30.

An AZ4562 etch mask was created for the pit layer. Alignment of this layer with the ridge layer was quite tricky as the 20 µm diameter pits needed to be placed on top of the pit windows. This was largely successful and only small amounts of overlap can be seen in Figure 31.

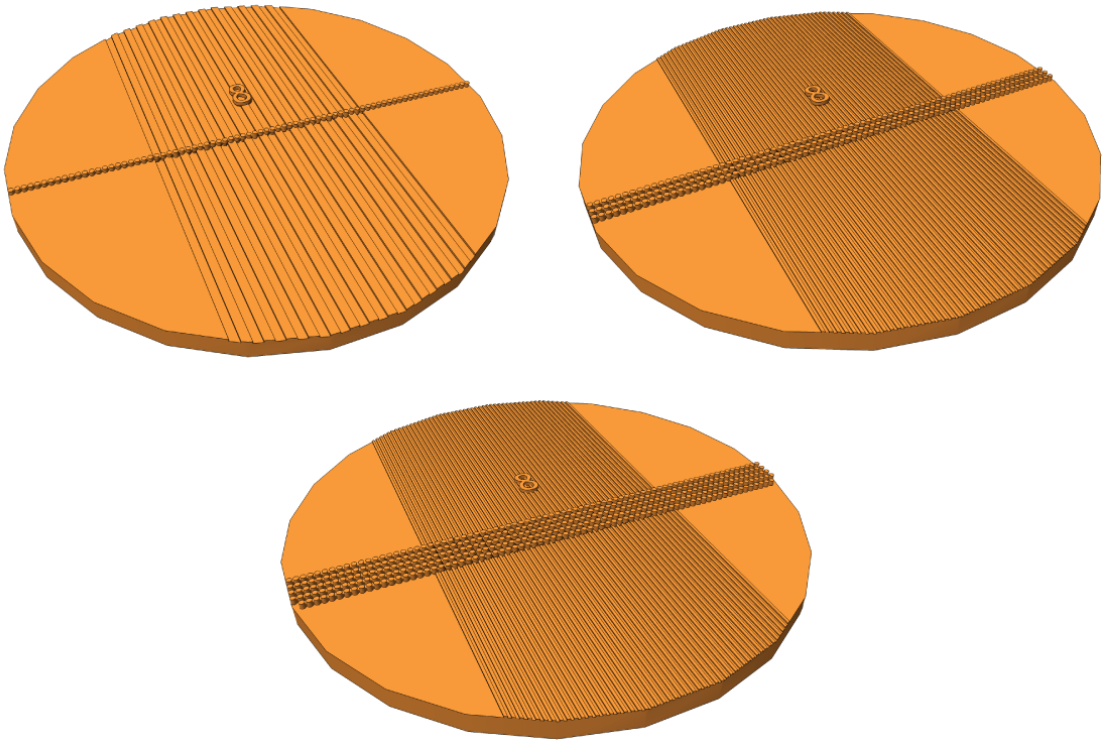

Figure 27: Sketch of the multi-pillar devices, showing the 1, 3 and 5 rows. Rows were spaced by 20 µm. The 8 indicates that all devices were of the 8 gap variant. Sketches are not to scale.

	Designed	Chrome	Ferric
Line Width	12.5	12.3 +/- 0.3	14.2 +/- 0.4
Space Width	12.5	12.7 +/- 0.5	10.4 +/- 0.5
Pit/Pillar Diameter	20	19.2 +/- 0.3	20.0 +/- 0.4
6 Gap	6	6.7 +/- 0.3	5.4 +/- 0.2
8 Gap	8	8.6 +/- 0.4	7.9 +/- 0.3
10 Gap	10	10.8 +/- 0.2	9.8 +/- 0.4
Row Spacing	20	21.0 +/- 0.3	19.9 +/- 0.4

Table 3: Dimensions of the chrome and ferric mask plates for the multi-pillar devices. The "designed" column shows the intended dimensions for the design. All measurements are shown in µm.

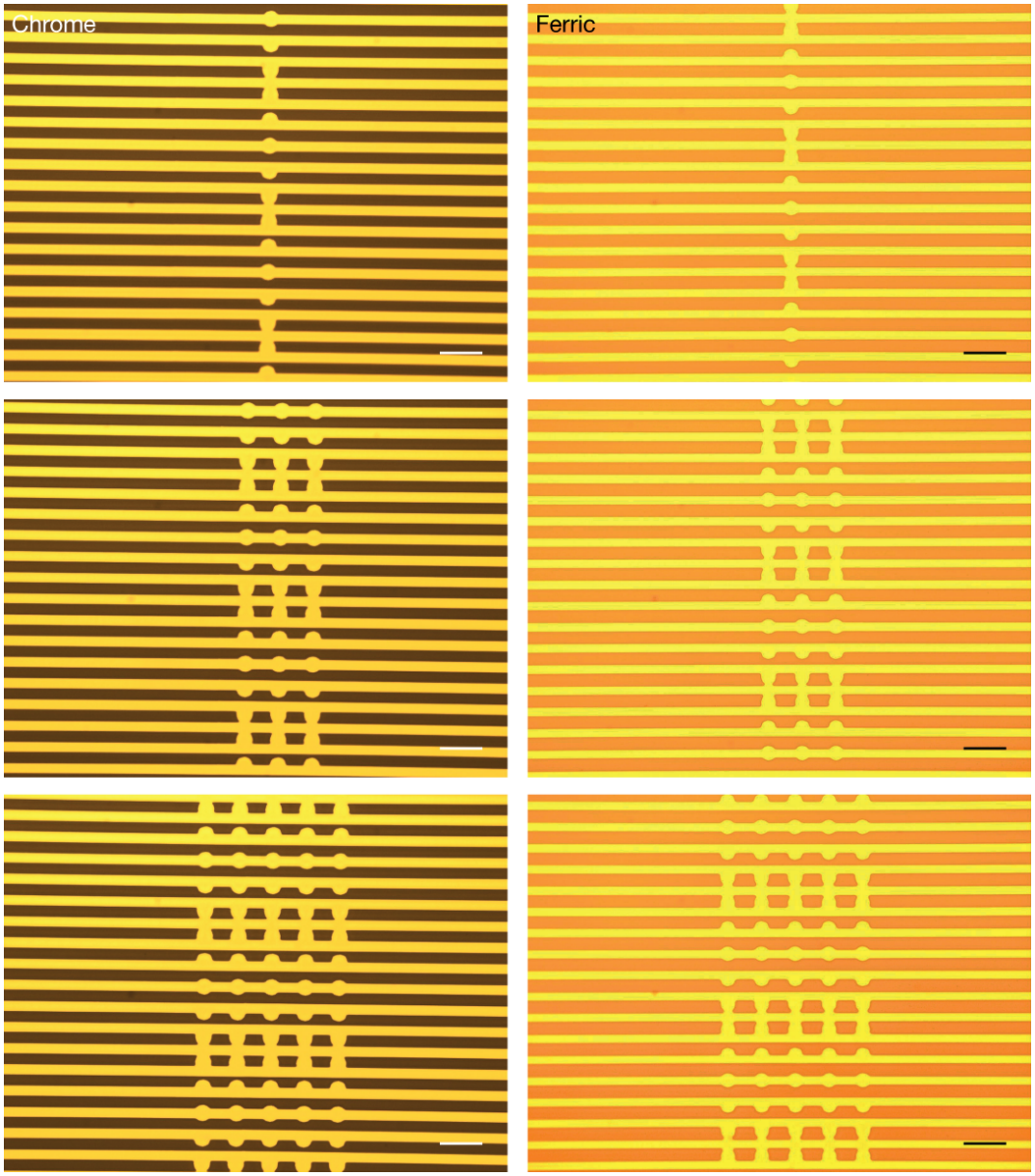

Figure 28: Chrome and ferric masks plates for the ridge layer of the multi-pillar dives. All pictures shown the 10 gap region of the mask. Scale bars are 50 µm. Gaps have been opened in the ridge layer to help reduce the distortion created by etching through the ridges to make pits. Due to the dimensions of the pits they align out of phase with the ridges.

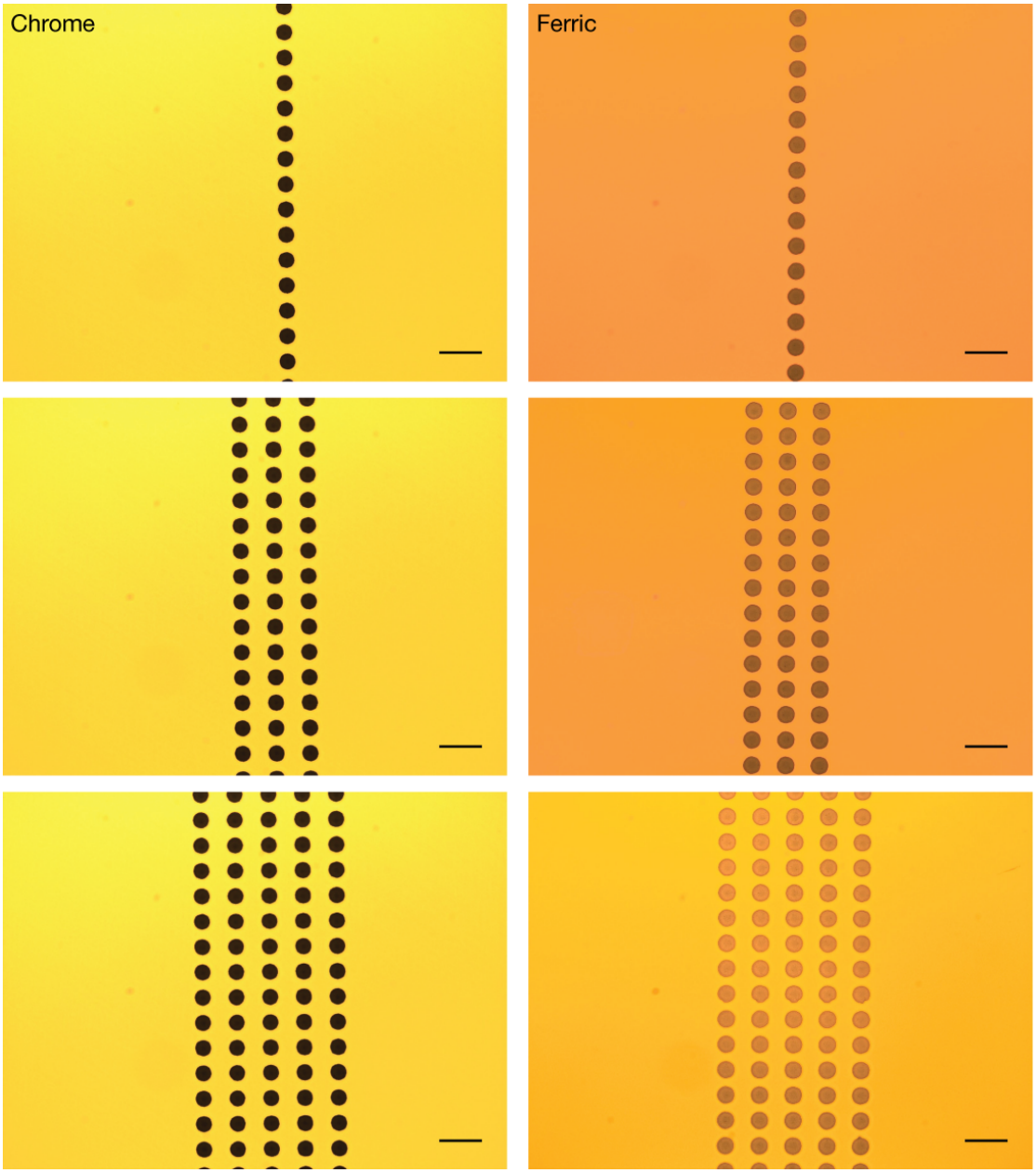

Figure 29: Chrome and ferric mask plates for the pit layer of the multi-pillar devices. All pictures show the 10 gap region of the mask. Scale bars are 50 µm.

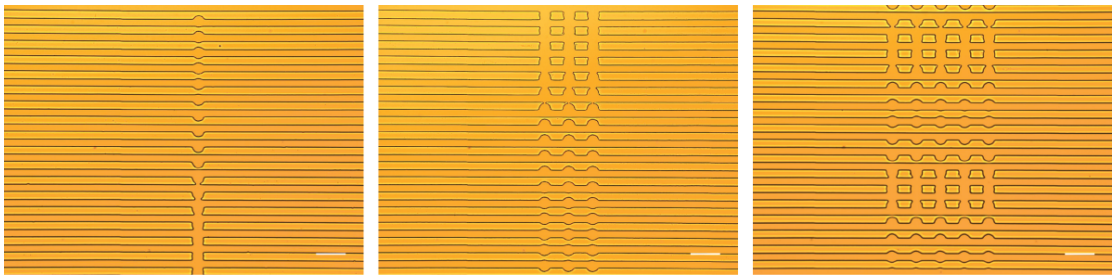

Figure 30: Etched ridge layer of the multi-pillar master. A 2.8 µm S1828 etch mask was used with the standard etch recipe described in the materials and methods section. Scale bars are 50 µm. All devices are of the 10 gap variety. A clean etch was obtained with only minor irregularities around the pit regions.

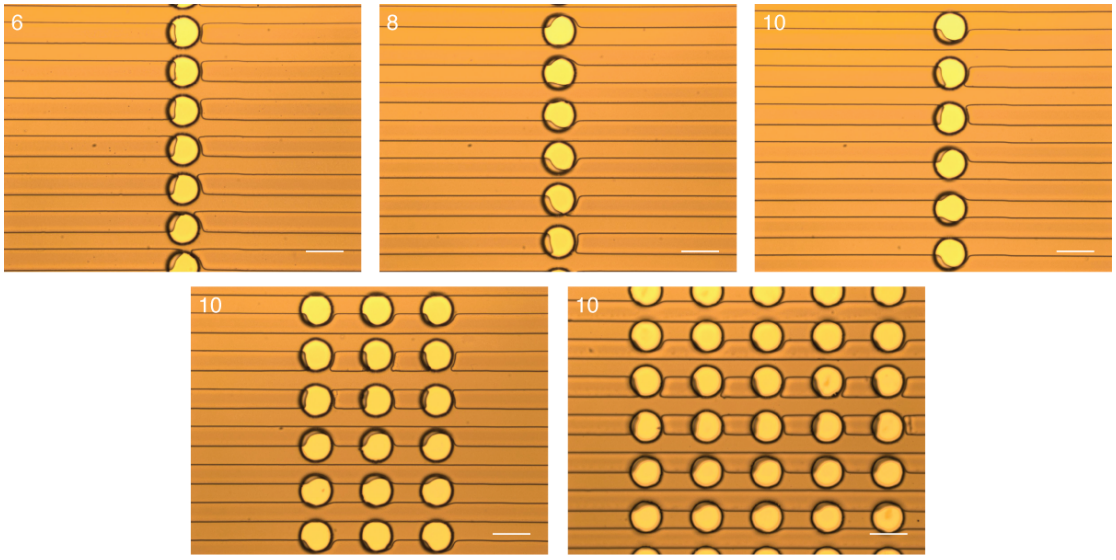

Figure 31: A 6µm thick AZ4562 etch mask for the pit layer of the multi-pillar master. The etch mask has been created on top of the ridge layer shown in Figure 30. Scale bars are 25 µm. The numbers show the intended gap size. A small error in alignment is present.

The etch, shown in Figure 32, resulted in some minor defects around the pit edges. However, these were well within tolerable limits. The finished master was then silanised and PDMS copies were cast. SEM images showing the pillars formed on the 3 and 5 row devices can be seen in Figure 33. Close up images of the differing gap dimensions are shown in Figure 34.

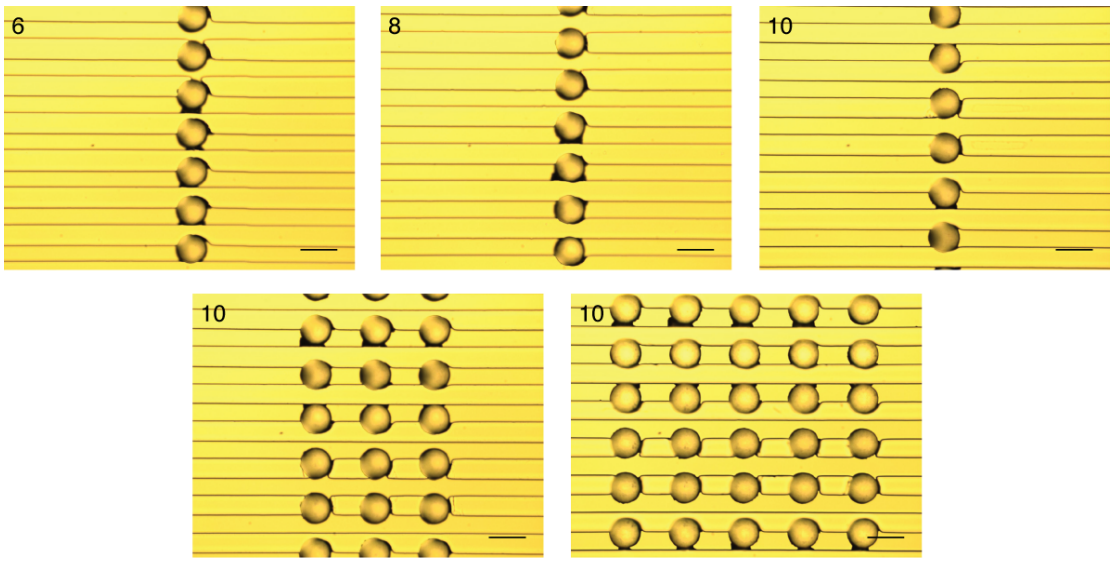

Figure 32: The completed multi-pillar Si master with pits etched through the ridge layer. Scale bars are 25 µm. The numbers show the intended gap size. Some minor defects can be seen around edges of the pits.

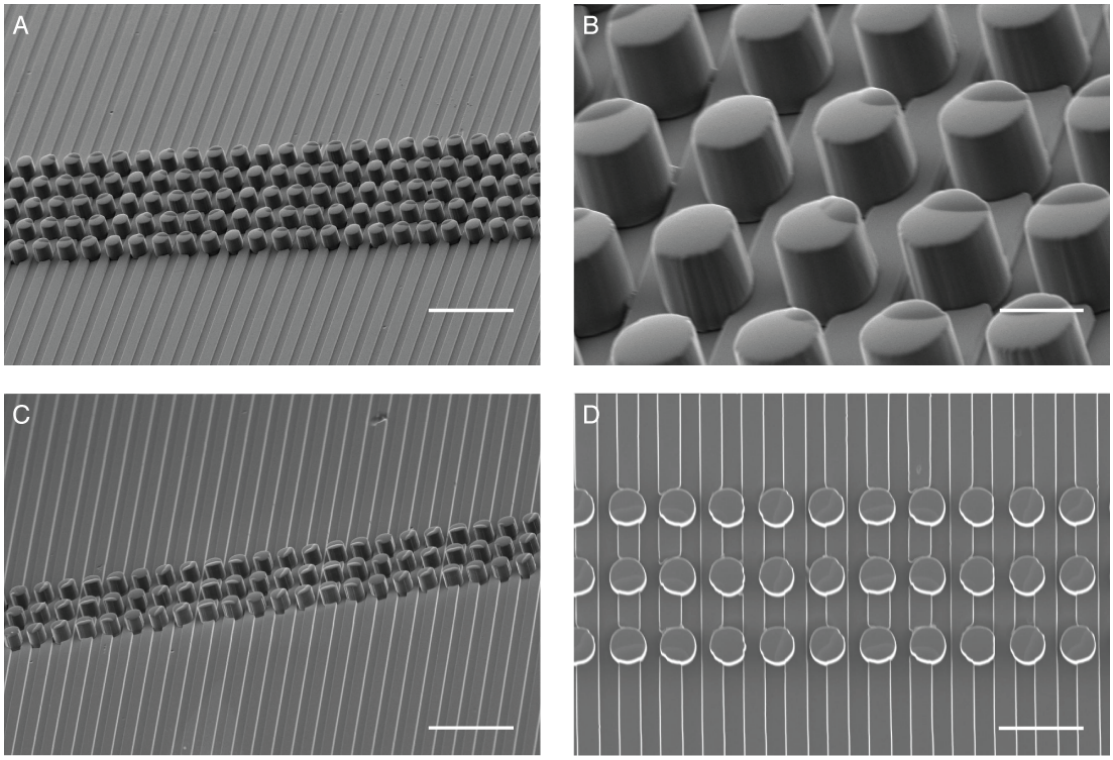

Figure 33: SEM images of PDMS devices cast from the master shown above. A) 5 row 10 gap (5-10) device shown at a 60° angle. Scale bar is 100 µm. B) A close up of the 5-10 device. Scale bar is 20 µm. Small nodules can be seen on top of some of the pillars. These were caused by the imperfect alignment of the pit and ridge layers. C) 3-10 device shown at 60°. Scale bar is 100 µm. D) 3-10 device shown from 0° angle. Scale bar is 50 µm.

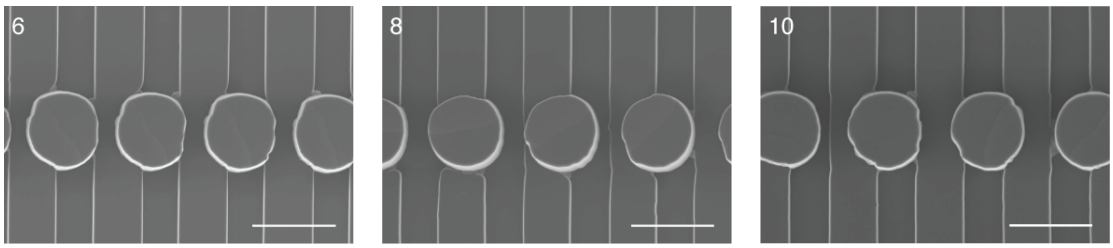

Figure 34: SEM images of the gap sizes on single row devices. The number in the top left indicated the designed gap size. Scale bars are 25 µm. Measured dimensions were as follows: 6 gap – 4.21 µm; 8 gap – 6.12 µm; 10 gap – 8.49 µm. The pillars formed were not completely rounded this is, again, likely due to the slight misalignment between the ridge and pit layers.

A summary of the measured dimension of the devices is shown in Figure 35. A comparison of these measurements to those of the ferric mask and the designed dimensions are shown in Table 4. The line pattern had transferred relatively well with an error of only ~ 0.5 µm compared to the ferric mask. However, the pillar dimensions had altered by up to 1.5 µm. To determine whether this was cause by the PDMS casting or the silicon master itself, the master

had to be measured. Once enough PDMS devices had been cast for biological experiments, the wafer was cleaved, sonicated in acetone to remove any PDMS and examined under an SEM.

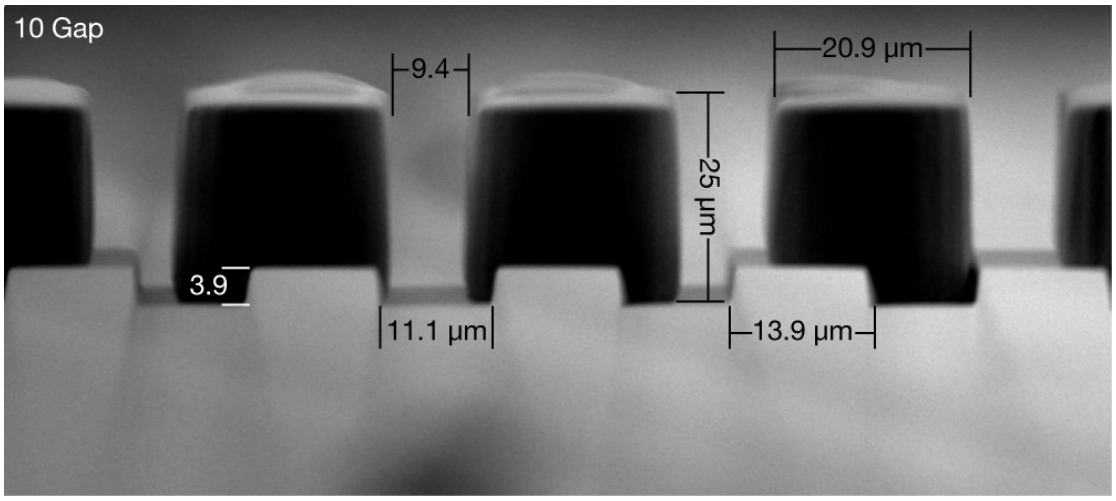

Figure 35: Dimensions of the PDMS multi-pillar devices. The SEM image shows the pillars and ridges along the length of the device. The device shown is of the 10 gap variant. One dimension not shown is that of the spacing between pillar rows; which was measured to be 18.9 µm.

	Designed	Ferric	PDMS
Line Width	12.5	14.2 +/- 0.4	13.9 +/- 0.4
Space Width	12.5	10.4 +/- 0.5	11.0 +/- 0.3
Pit/Pillar Diameter	20	20.0 +/- 0.4	21.6 +/- 0.7
6 Gap	6	5.4 +/- 0.2	5.1 +/- 0.2
8 Gap	8	7.9 +/- 0.3	7.3 +/- 0.2
10 Gap	10	9.8 +/- 0.4	9.0 +/- 0.6
Row Spacing	20	19.9 +/- 0.4	18.9 +/- 0.8
Ridge Height	5		4.2 +/- 0.2
Pillar Height	30		25.0 +/- 0.9

Table 4: Dimensions of the PDMS multi-pillar devices compared to those of the ferric mask and the designed dimensions.

SEM images of the silicon master are shown in Figure 36, the measured dimensions are shown in Table 5. It was apparent that the dimensions of the ridges had been retained throughout processing. However, the pits/pillars' diameter had expanded slightly during etching and

PDMS casting. This caused the row spacing and gaps to narrow somewhat but this was well within tolerable levels. A depth for the pits could not be accurately measured as the cleavages along the pit rows did not produce any clean breaks through a pit. As the difference in height between the silicon and PDMS ridges were negligible, it can be assumed the pits were ~ 25 µm deep. Also of note is that the etchs did not produce the depth as calculated. To produce depths closer to the desired size, optimisation of the etch would need to be performed. As time was at a premium and, as previously discussed, pillar height was not seen as a critical dimension, the etch depths obtained were deemed sufficient.

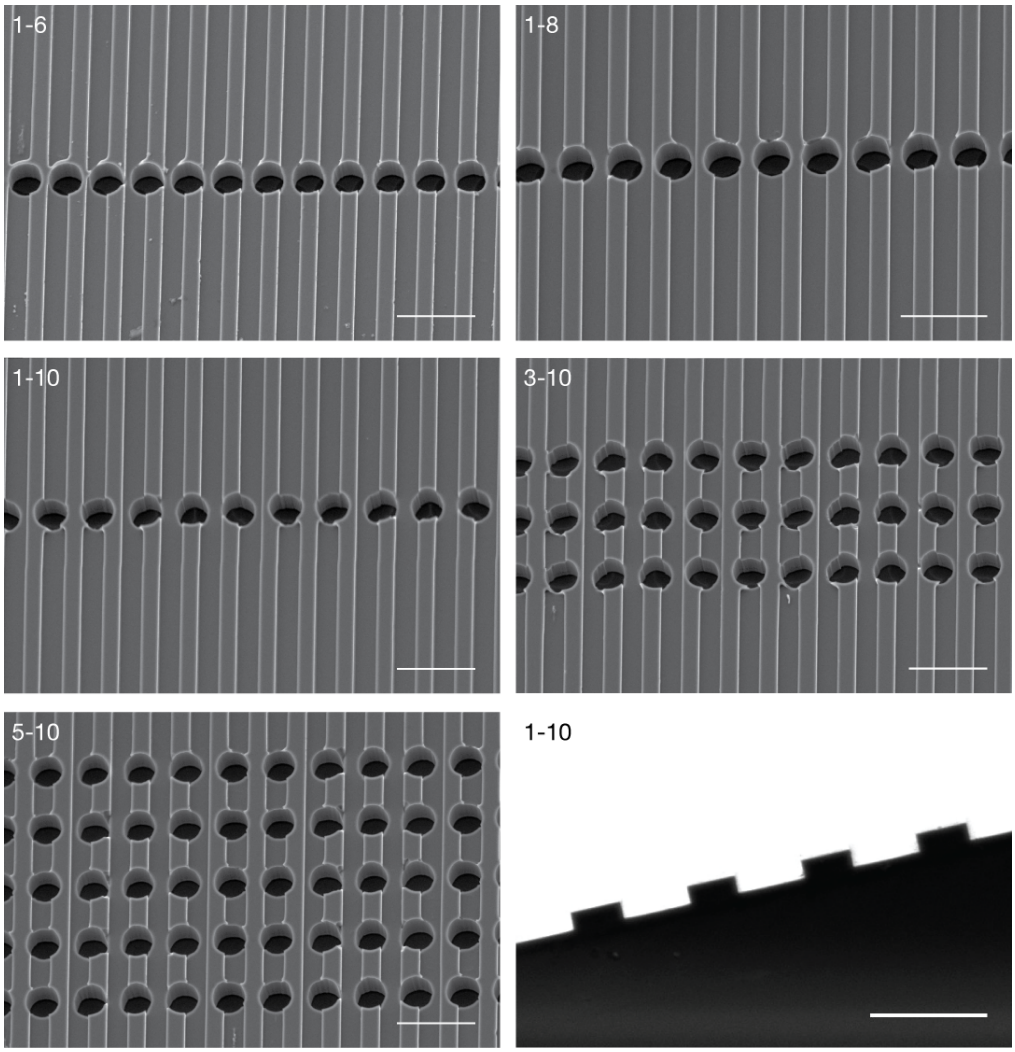

Figure 36: SEM images of the multi-pillar silicon master. All images were taken from a 30° angle except the bottom right image which was taken from 90°. Scale bars are 50 µm except the bottom right image which is 25 µm. Device type is shown in the top right in the form of "row-gap" i.e. 5-10 is 5 rows with 10 gap. Small defects were present around the edges of the pits where they joined onto the ridges. These did not appear to have any major affect on the PDMS copies as seen in Figure 33. The sidewalls of the ridges were straight with no visible under cutting. Small debris particles can be seen on some of the images, particularly 1-6. These are either pieces of PDMS that were not removed by the acetone wash or are fragments of silicon resulting from the cleaving of the wafer.

	Designed	Ferric	Si Master	PDMS
Line Width	12.5	14.2 +/- 0.4	13.9 +/- 0.2	13.9 +/- 0.4
Space Width	12.5	10.4 +/- 0.5	11.1 +/- 0.3	11.0 +/- 0.3
Pit/Pillar Diameter	20	20.0 +/- 0.4	20.9 +/- 0.3	21.6 +/- 0.7
6 Gap	6	5.4 +/- 0.2	5.0 +/- 0.1	5.1 +/- 0.2
8 Gap	8	7.9 +/- 0.3	7.2 +/- 0.5	7.3 +/- 0.2
10 Gap	10	9.8 +/- 0.4	9.4 +/- 0.4	9.0 +/- 0.6
Row Spacing	20	19.9 +/- 0.4	19.9 +/- 0.4	18.9 +/- 0.8
Ridge Height	5		3.9 +/- 0.1	4.2 +/- 0.2
Pillar Height	30			25.0 +/- 0.9

Table 5: Dimensions of the silicon master compared to those of the PDMS copies, ferric mask and the designed dimension.

2.3.7 Epoxy Mould

The silicon masters were very fragile and had to be handled with great care during PDMS casting. Even if handled properly it was not uncommon for one to crack during the oven curing of the PDMS or for the wafer to become stuck to the moulding jig and then shatter when being prised off. To help alleviate these problems an epoxy resin copy of the master was made.

This was achieved by first casting a PDMS copy of the silicon master. Epoxy resin was then mixed and spread across the inside of a large Petri dish lid. The PDMS sheet was then embossed into the epoxy resin. PDMS copies of the epoxy mould where then cast by pouring uncured polymer into the dish Petri dish lid containing the mould and then placing it in an 80° C oven for ~ 2 hours. Finally the epoxy mould and the PDMS copies were analysed under an SEM. Some of the acquired images are shown in Figure 37. Measured dimensions are shown in Table 6.

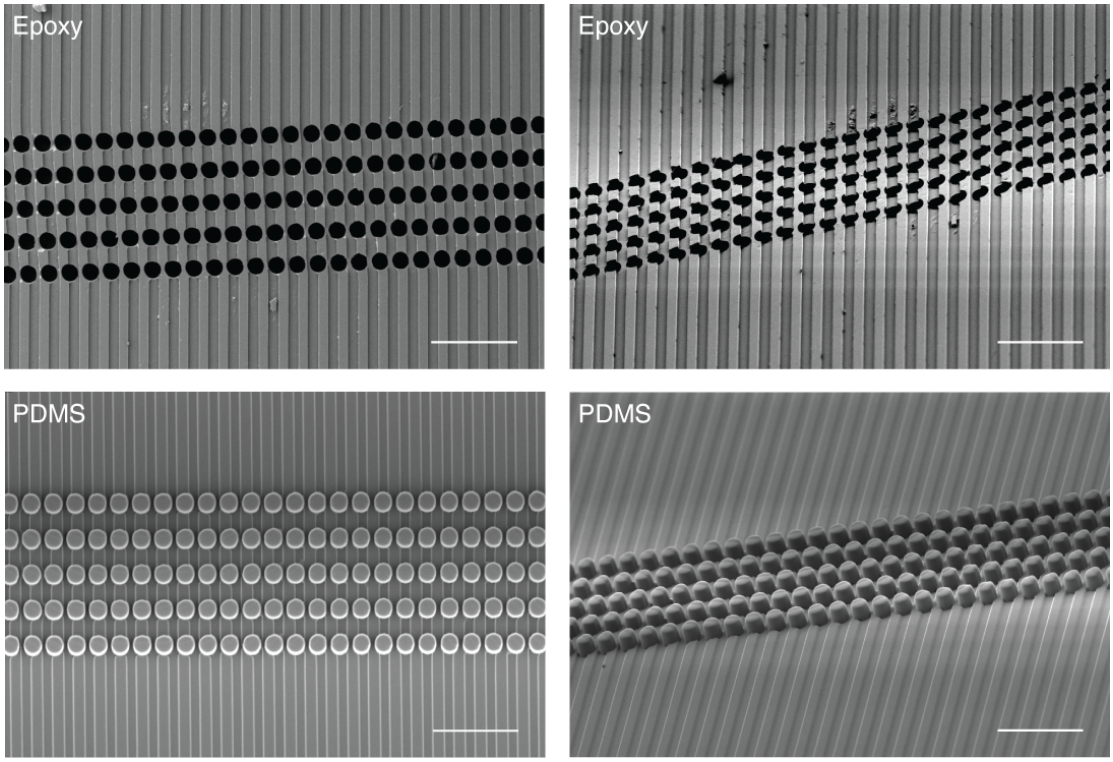

Figure 37: SEM images of the epoxy mould and its PDMS replicas. Scale bars are 100 µm. The left hand images were taken from a 0° angle while those on the right were taken from 60°. The debris on the epoxy moulds was a result of it being cut from the Petri dish lid.

	Designed	PDMS	Epoxy Mould	PDMS (Epoxy)
Line Width	12.5	13.9 +/- 0.4	13.0 +/- 0.6	15.1 +/- 0.2
Space Width	12.5	11.0 +/- 0.3	11.7 +/- 0.4	9.6 +/- 0.2
Pit/Pillar Diameter	20	21.6 +/- 0.7	19.6 +/- 0.3	21.6 +/- 0.2
6 Gap	6	5.1 +/- 0.2	4.7 +/- 0.2	4.4 +/- 0.3
Row Spacing	20	18.9 +/- 0.8	18.2 +/- 0.3	18.1 +/- 0.3
Ridge Height	5	4.2 +/- 0.2		2.7 +/- 0.1
Pillar Height	30	25.0 +/- 0.9		22.6 +/- 0.2

Table 6: Dimensions of the epoxy mould and its PDMS copies compared to the designed dimensions and those of the PDMS devices cast from the silicon mould.

There was only a small difference in pillar dimensions across the three stages. However, the ridge dimensions did not transfer well during epoxy embossing. A profile of the epoxy ridges could not be obtained as the edge of the topography was distorted when it was cut from the Petri dish. The PDMS (epoxy) devices give an indication that not enough pressure was

applied during embossing, which resulted in shorter pillars and ridges. This is also the likely cause of the rounded tops to the pillars and the non-straight sidewalls on the ridges.

These problems could easily be solved by either placing larger weights on top of the PDMS sheet during embossing or with the use of a hydraulic press.

2.3.8 Summary of Dimensions

A summary of the final dimensions for all stages of fabrication is presented in Table 7. The change in dimensions for each process is shown in Table 8.

	Designed	Chrome	Ferric	Si Master	PDMS	Epoxy Mould	PDMS (Epoxy)
Line Width	12.5	12.3 +/- 0.3	14.2 +/- 0.4	13.9 +/- 0.2	13.9 +/- 0.4	13.0 +/- 0.6	15.1 +/- 0.2
Space Width	12.5	12.7 +/- 0.5	10.4 +/- 0.5	11.1 +/- 0.3	11.0 +/- 0.3	11.7 +/- 0.4	9.6 +/- 0.2
Pit/Pillar Diameter	20	19.2 +/- 0.3	20.0 +/- 0.4	20.9 +/- 0.3	21.6 +/- 0.7	19.6 +/- 0.3	21.6 +/- 0.2
6 Gap	6	6.7 +/- 0.3	5.4 +/- 0.2	5.0 +/- 0.1	5.1 +/- 0.2	4.7 +/- 0.2	4.4 +/- 0.3
8 Gap	8	8.6 +/- 0.4	7.9 +/- 0.3	7.2 +/- 0.5	7.3 +/- 0.2		
10 Gap	10	10.8 +/- 0.2	9.8 +/- 0.4	9.4 +/- 0.4	9.0 +/- 0.6		
Row Spacing	20	21.0 +/- 0.3	19.9 +/- 0.4	19.9 +/- 0.4	18.9 +/- 0.8	18.2 +/- 0.3	18.1 +/- 0.3
Ridge Height	5			3.9 +/- 0.1	4.2 +/- 0.2		2.7 +/- 0.1
Pillar Height	30				25.0 +/- 0.9		22.6 +/- 0.2

Table 7: Dimensions of masks used during fabrication; the silicon master created; the PDMS devices cast from the master; the epoxy master and the PDMS copies made from it. All measurements are shown in µm.

Δ	Dsgn -> Chrome	Chrome -> Ferric	Ferric -> Si	Si -> PDMS	PDMS -> Epoxy	Epoxy -> PDMS (E)
Line Width	-0.2	1.9	-0.3	0.1	-0.9	2.1
Space Width	0.2	-2.4	0.7	0.0	0.6	-2.0
Pit/Pillar Diameter	-0.8	0.8	0.9	0.7	-2.0	2.0
6 Gap	0.7	-1.3	-0.5	0.2	-0.4	-0.3
8 Gap	0.6	-0.7	-0.8	0.1		
10 Gap	0.8	-1.0	-0.4	-0.4		
Row Spacing	1.0	-1.1	0.0	-1.1	-0.7	-0.1

Table 8: The change in dimensions throughout various stages of fabrication. All measurements are shown in µm. A negative numbers indicates a shrink in size while a positive number indicates an increase.

Chapter 3

Biology

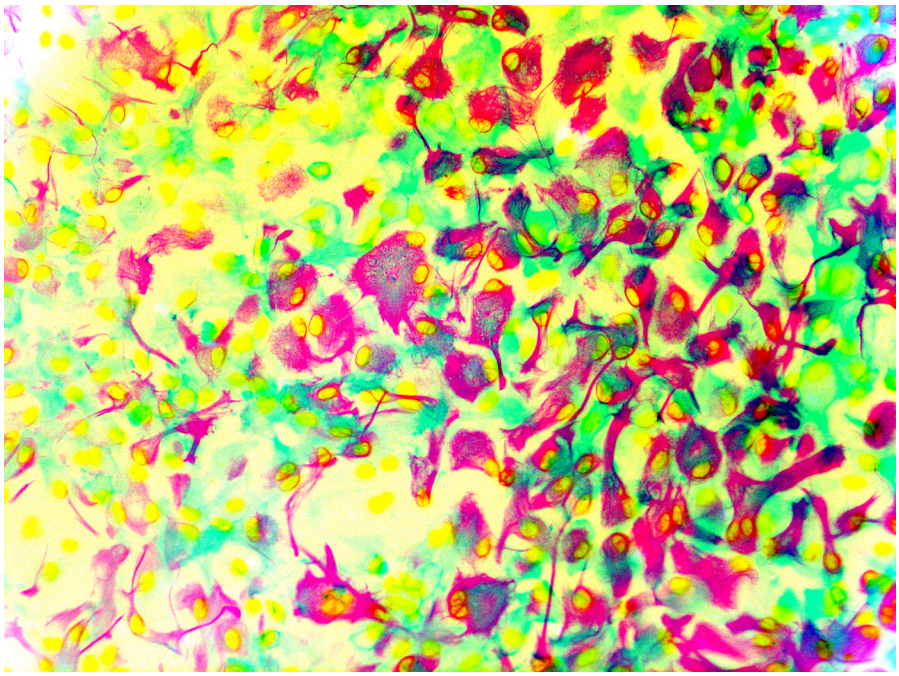

3.1 Materials and Methods

3.1.1 Astrocyte Cultures

Astrocyte cultures were prepared as in Boomkamp et al(Boomkamp et al., 2012). Striata were first obtained from postnatal day 1 Sprague Dawley (SD) rat pups. The striatum was dissected from the brain and then dissociated by trituration through a glass Pasteur pipette. The dissociated cells were then plated down into T75 flasks containing neurosphere media and epidermal growth factor. A confluent layer of cells was then allowed to form. The cells were then removed from the flask and triturated before being put into a new flask to form neurospheres overnight. The neurospheres were then spun down and resuspended in 10% FBS/DMEM before being plated down and allowed to differentiate into astrocytes. A confluent layer of cells was usually obtained in seven to ten days.

3.1.2 Myelinating Spinal Cord Cultures

Myelinating cultures were obtained as per the protocol in Boomkamp et al(Boomkamp et al., 2012). The spinal cords were dissected from E15 SD rat pups and stripped of their meninges. The cords were then finely chopped with a scalpel before disassociation with trypsin and collagenase. The cells were then triturated through a Pasteur pipette to form a cell suspension before being spun down, re-suspended in plating media and seeded onto devices or coverslips. The cultures were then fed with neurobasal media. Myelination started to occur after approximately 10 days. For myelin to form the cells had to be seeded on top of a confluent layer of astrocytes.

3.1.3 Device Sterilisation and Coating

Devices were sterilised in 70% ethanol for 30 minutes. They were then dried under nitrogen flow. The surface charge of the PDMS was altered using a Harrick Plasma PDC-002 Plasma Cleaner. The devices were treated for 1 min at 29.6 W; this rendered the surface hydrophilic,

see Figure 38. The devices were then submerged in a 13.3 µg/ml poly-l-lysine (PLL) solution over night. After coating, the devices were washed twice in sterile water to remove any excess PLL.

3.1.4 Seeding Onto Mk.2 Containment Devices

700 µl of media was pipetted into each well of a 24 well plate containing a device. The plate was then placed into an incubator for ~ 15 min to warm to 37 °C. A concentrated cell suspension was created and then placed into a fridge for ~ 15 mins to cool to ca. 4°C. 5 ml of suspension was slowly injected onto the device with the pipette tip suspended just above the device surface and pointing away from the pillar row. Care was taken to not disturb the devices after seeding as cells can be shaken onto the wrong side of the pillar row. The devices were left for ~ 30 minutes after seeding so that the cells could attach to the substrate.

The temperature differential between the media and the cell suspension stopped cells from floating in the media and thus helped to prevent unwanted crossing of the pillar row during seeding.

3.1.5 Micro Contact Printing of BSA

A modified version of von Philipsborn et al's protocol(Von Philipsborn et al., 2006) was used to contact print BSA on top of the pillars. A sheet of PDMS containment devices was prepared and PLL coated as described above; the devices were not cut from the sheet. A 1% BSA (Gibco, 10108) in sterile PBS solution was then prepared. A 100 mm silicon wafer was used as the stamp, which was sterilised and then plasma cleaned for 2 mins. The wafer was immersed in the BSA solution for 2 hours to allow the BSA to attach to the surface.

The stamp and the PDMS sheet were removed from their solutions, rinsed with sterile water and then dried under nitrogen flow. The PDMS sheet was placed onto a flat, sterile surface such as a petri dish and the stamp was gently placed on top of it. No pressure was applied to the stamp to prevent unwanted sagging of the PDMS and areas not on the top of pillars being coated. The stamp was left in place for several seconds before being removed carefully. The devices were then cut from the PDMS sheet.

3.1.6 Seeding Using Culture-Inserts

Culture-Inserts (Ibidi) were attached to devices so that one chamber was located as close as possible to the containment rows. 80 µl of cell suspension was then injected into the chamber, the plates were then placed in an incubator and the cells were left to attach over night. The inserts where then removed with tweezers and the well or petri dish filled with media as normal.

3.1.7 Cell Culture

Astrocytes, C2C12 and MG63 cells were fed with media consisting of DMEM (Sigma, D5671) with 10% FBS (Gibco, 10108), 0.02% antibiotic and 0.005% L-glutamine (Sigma, G7513). The antibiotic solutions consisted of 57% L-glutamine, 38% Penicillin-Streptomycin (Sigma, P0781) and 5% Fungizone (Gibco, 15290).

Cells cultured in T75 flasks were fed twice weekly with 10 ml of media. Cells in 24 well plates were fed three times a week. C2C12s and MG63s had all old media removed and were fed with 600 µl of media. Astrocytes had 500 µl of media removed and were fed with 600 µl.

Astrocytes were passaged once they became confluent; usually within 10 days. C2C12 and MG63s were passaged every 3 days with a splitting ratio of 1:10 to stop the cells becoming over confluent.

3.1.8 Statistical Analysis

Data were analysed in GraphPad Prism. One-way analysis of variance (ANOVA) tests were performed and, as comparisons of mutiple pairs of groups was required, Tukey's post test was used. Confidence intervals were set to 95 %. Tukey's post test uses the null hypothesis that all means come from the same population. Tukey's test was used in preference over Bonferroni's due to the wide confidence intervals of the latter. Similarly, Newman-Keuls' test was not used due to its increased likelihood of causing a Type I error, i.e. a false positive.

The formula for Tukey's post test is as follows:

$$q_s = \frac{Y_A - Y_B}{SE}$$

Where q_s is the q-value; Y_A is the larger mean value; Y_B is the smaller mean; and SE is the standard error. If q_s is larger than the q-value for the standardised range, the two means are significantly different.

3.1.9 Cell Growth Optimisation

The first stage in creating an environment conducive to cell growth was to alter the surface of the PDMS devices so they were more hydrophilic. This was achieved by exposing the devices to air plasma. To optimise the process, exposure time between 0 and 50 seconds were trialled.

Figure 38 shows the increasing hydrophilicity (decreasing contact angle) of the surface with increasing plasma exposure. During this process methyl groups on the surface are removed and the, now available, silicon atoms will bond to 3 or 4 oxygen atoms (Toth et al., 1994). This left a silica-like surface on the device.

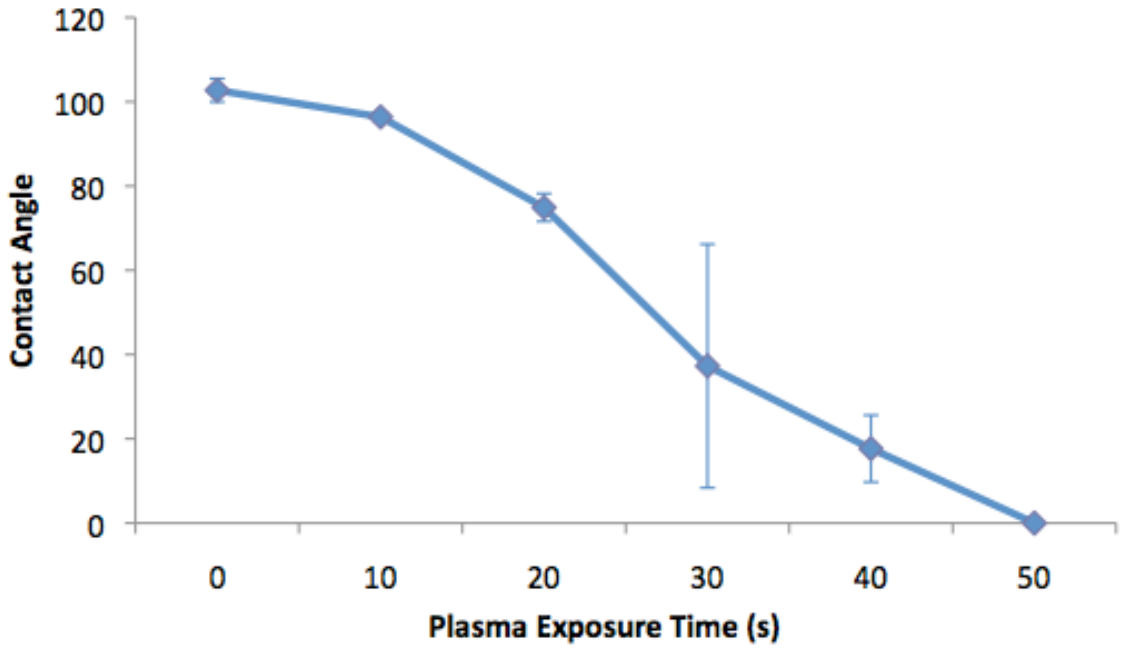

Figure 38: Contact angle against plasma exposure time for flat PDMS devices with a base to curing agent ratio of 10:1. 3 devices were tested for each time point and 3 measurements were made per device.

The region around 30 s had a large standard deviation associated with it. This was likely due to the variations in the surfaces' reaction to the plasma and the difficulty in precisely timing the exposure as the plasma cleaner had no automated timing system. An exposure time of 1 min was chosen for all further experiments as this avoided the problematic 30 to 40 s region and ensured that the devices were past the 50 s saturation point.

As hydrophobic recover could occur on the surface of the PDMS, a coating had to be applied to ensure the devices stayed hydrophilic. Fibronectin and poly-l-lysine (PLL) were trialled as they are relatively commonly used and were readily available. Devices were plasma treated and then left overnight in either a 1 μg/ml of fibronectin or 13.3 μg/ml PLL solution. The devices were rinsed in DI water and astrocytes then seeded onto them. After 10 days the cells were fixed and stained for DAPI and glial fibrillary acidic protein (GFAP), an astrocyte marker.

Figure 39 shows the comparison of astrocyte growth on alignment devices coated with either fibronectin or PLL. Confluent layers formed on the 12.5 and 25 μm devices, however, growth was patchy on the 50 μm devices. The type of coating did not appear to have any effect. The decision was taken to use PLL coatings in all further experiments, as it was more readily available in the lab than fibronectin.

The cause of the sparse growth on some of the devices was then investigated. It was postulated that this could be due to some of the silane coating being transferred from the master to the PDMS devices, which in turn could inhibit the cells' growth. To test this, sets of devices were cast from a silanised wafer and a non-silanised wafer. Astrocytes were grown on the two sets of devices for 10 days and then stained for GFAP, Figure 40 shows the results. The silanisation appeared to have no effect on cell growth and so the problems were due to some other cause.

Another possible cause of the patchy cell growth was that the PLL coating was either not attaching properly to the surface or being removed during culture. To ensure that the coating remained on the surface, 4 devices of each ridge width were coated with fluorescently-labelled PLL and were imaged after 10 days in culture with astrocytes.

Fluorescent images of the labelled devices are shown in Figure 41. The PLL coated the entire surfaces of the devices evenly and remained present on the surfaces even after 10 days in culture. Hydrophobic recovery of PDMS usually occurs between 1 and 7 days (Fritz and

Owen, 1995) if left exposed to air or, if stored in water, over a period of weeks (Kim et al., 2004). As the devices were kept immersed in an aqueous solution it was unlikely that the PLL coating was affected on devices that were cultured for more than 10 days. The astrocytes formed a confluent monolayer on these devices and so the previous growth problems were ascribed to imperfect device sterilisation and culture technique.

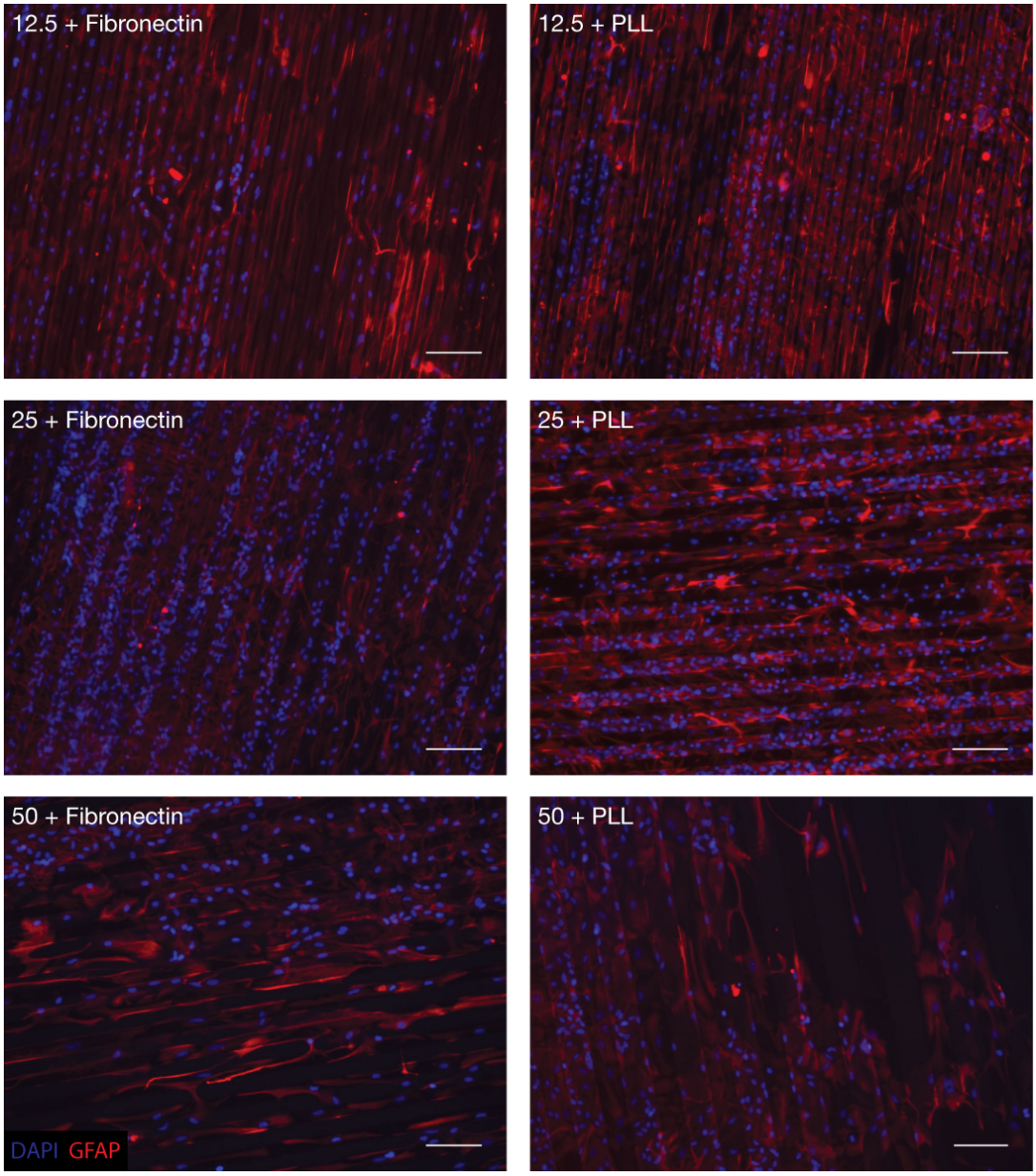

Figure 39: Astrocytes, after 10 days in culture, grown on PDMS alignment devices. The devices were coated with fibronectin (left images) or PLL (right images). The ridges were 5 µm high and their width in µm is noted on the images. The cells were stained red for glial fibrillary acidic protein (GFAP), a mature astrocyte marker, and blue with DAPI. The type of coating did not appear to effect cell growth. Scale bars are 100 µm.

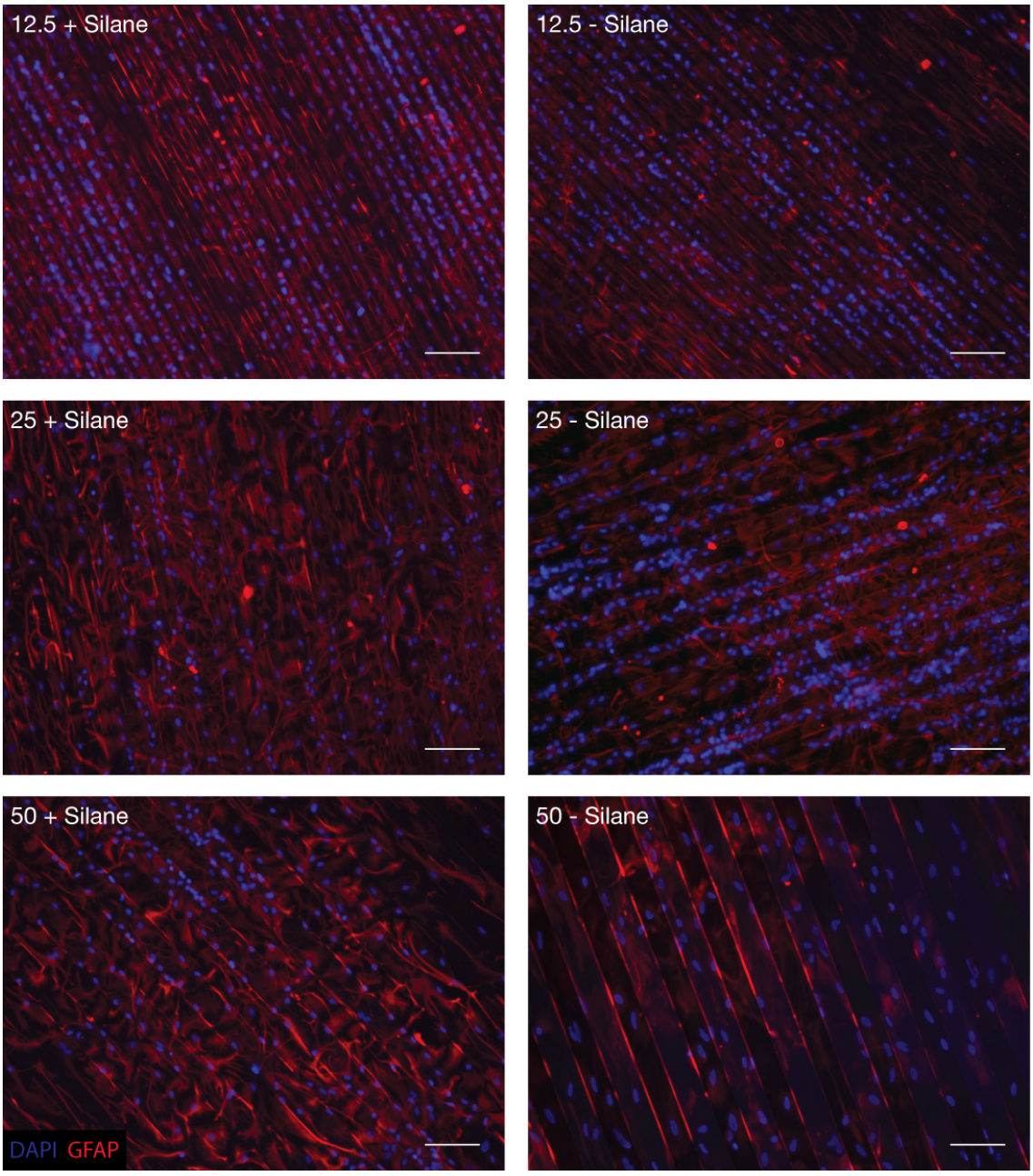

Figure 40: Astrocytes on alignment devices after 10 days in culture. Ridge height is 5 µm. Devices on the left were cast from a silanised wafer while the ones on the right were from a non-silanised wafer. The cells were stained red for GFAP, a mature astrocyte marker, and blue with DAPI. Scale bar is 100 µm. The silanisation appeared to have no adverse effect on cells growth but growth was still patchy on the 50 µm devices.

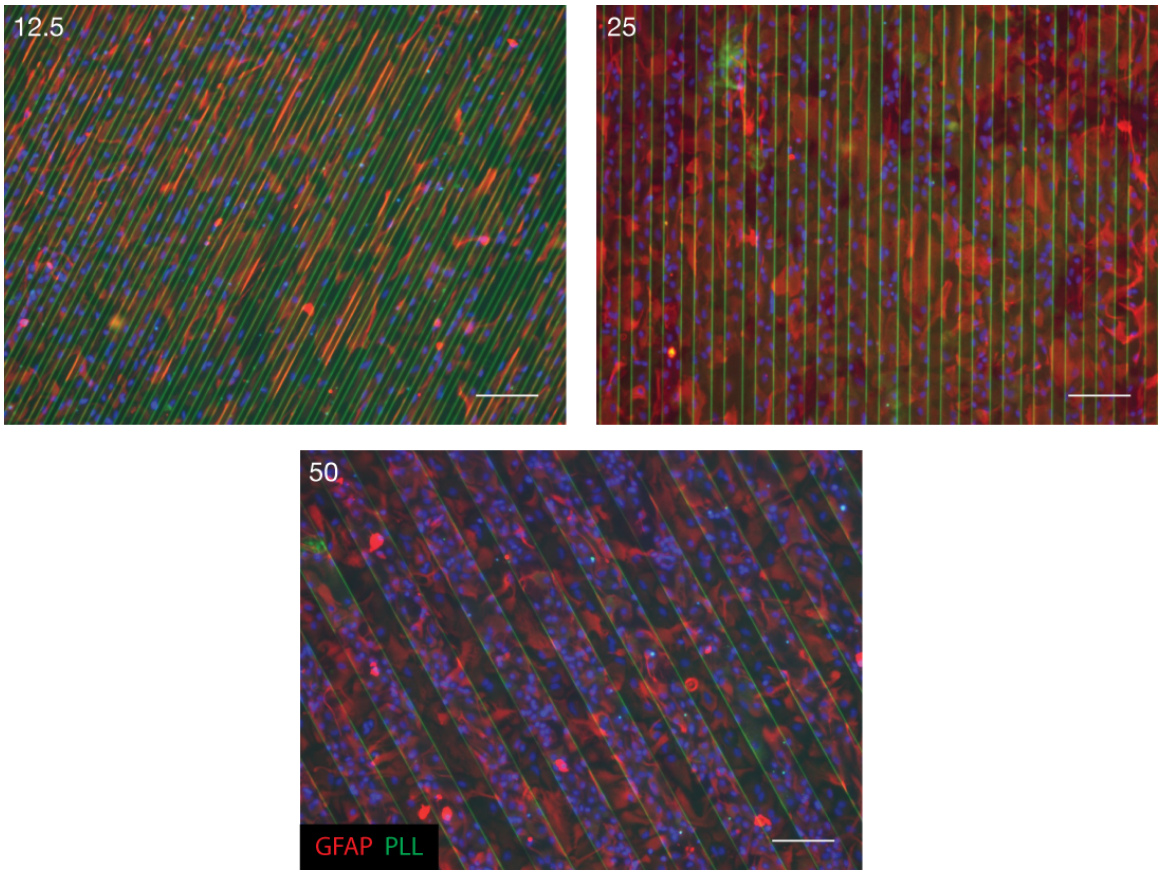

Figure 41: Astrocytes grown on alignment devices coated with fluorescently labelled PLL. Images were taken after 10 days in culture. Ridge height was 5 µm. Stains are DAPI (blue), GFAP (red) and PLL (green). Scale bars are 100 µm. The green lines visible in the images are where the PLL coated the ridge walls and thus resulted in a higher fluorescent intensity. The PLL was present across the entire surface of the device and a confluent layer of cells was obtained.

Experiments were then conducted to establish an optimal seeding density for the myelinating cultures and to assess the alignment of axons to the grooves. Alignment devices were cast and coated as per the, now established, protocol shown in the materials and methods section above. Flat 13 mm PDMS disks were used as controls. Astrocytes were seeded onto the devices and became confluent after ~ 10 days. At day 10, myelinating cultures were plated on top of the astrocytes, and seeded in densities of 150, 200, 250 or 300 x10^3 cells. After 28 days, the cells were stained for SMI-31, an axonal stain, and proteolipid protein (PLP), a myelin marker. Axonal density was quantified in ImageJ by comparison of the total image size against the area covered by the SMI-31 stain. Myelination was quantified by comparing the area covered by SMI-31 against the PLP area. For axon densities and myelination 4 devices were used per seeding density/groove width combination and 10 images were taken per device.

Samples of the images taken of the myelinating cultures are shown in Figure 42. The axons appeared to align well to the 12.5 µm grooves. The 25 and 50 µm groove also aligned the axons but to a lesser degree. The growth of the axons on the flat control appeared to be random and no long range alignment was evident.

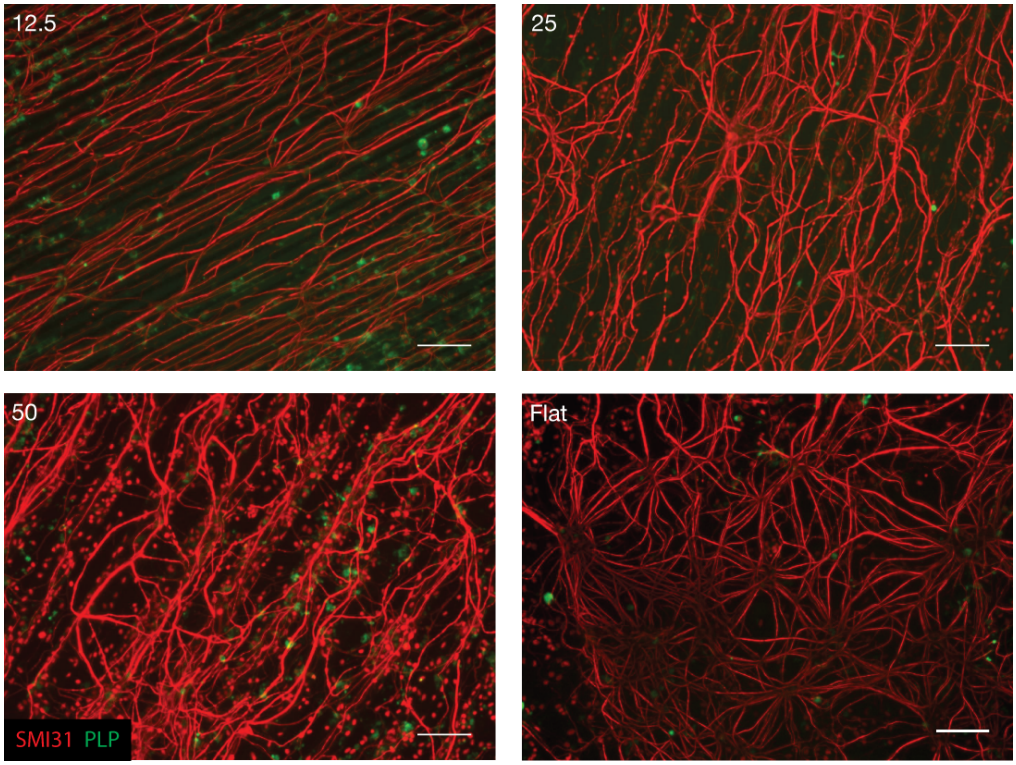

Figure 42: Myelinating cultures grown on alignment devices. The cultures were seeded on top of 10 day old astrocytes. Pictures were taken after 28 days in culture. The devices were seeded with 150x10^3 cells in 100 µl of media. Ridge height is 5µm and the width is indicated on the images. The image labelled "flat" was one of the control devices. The scale bar is 100 µm.

Quantification of the axonal densities against seeding density is shown in Figure 43. Generally, axonal density falls as seeding density increases. A seeding density of 150x10^3 cells provided the most consistent axonal density across the various ridge sizes and so was used for all further experiments.

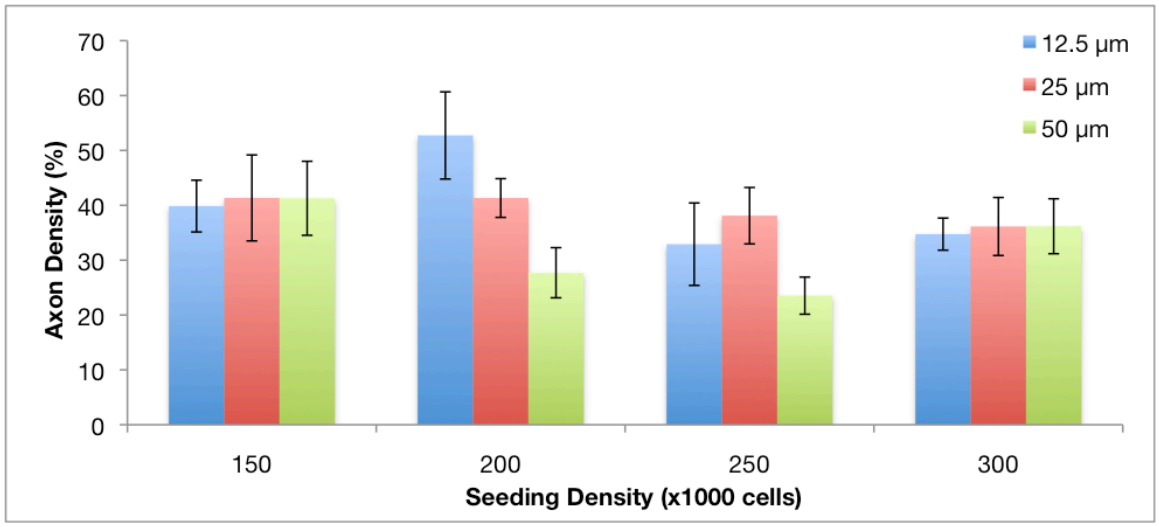

Figure 43: Percentile coverage of the ridged areas by axons against seeding density. Standard deviation was 7 at most. 4 devices were used for each variant and 10 images were quantified per device.

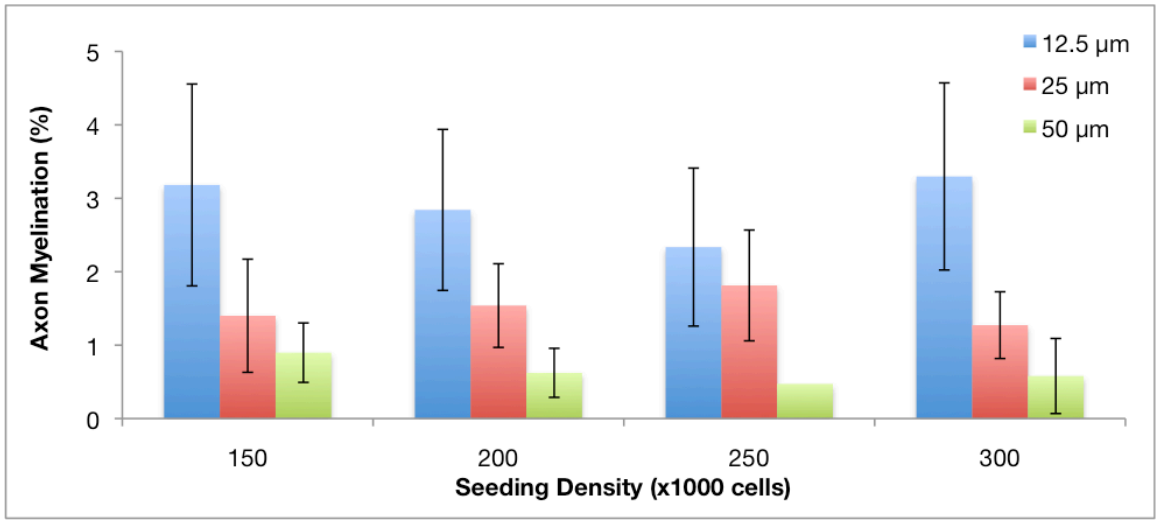

Figure 44: Axonal myelination on the ridged areas verses seeding density on guidance devices. Standard deviation was 1.3 at most. 4 devices were used for each variant and 10 images were quantified per device.

Myelination was poor on all devices, as shown in Figure 44, with a maximum coverage of only ~ 3%. This is possibly due to the topography causing the astrocytes to enter a reactive state (Eng and Ghirnikar, 1994) which would prevent the necessary growth factors for myelination being released.

3.1.10 Axon alignment

As seen in Figure 42, the axons appeared to align well to the grooves, however quantification was required so that a proper statistical analysis could be carried out. This was performed using a MATLAB script written by Dr. Thomas Endlein. The program identified the axons by thresholding the images and then fitting ellipses to each group of pixels using the least squares method. Controllable parameters allowed the program to be tuned to eliminate artefacts and background noise. The parameters were; maximum line length; maximum and minimum ellipse area; and threshold limit. Selected areas could also be excluded to remove known artefacts. After fittings the ellipses, the program measured the absolute value of the angle of the ellipse centre-line from the horizontal, outputting a value from 0° to 180°. To eliminate any variability between images cause by the pictures being taken off-axis, all images where rotated so that the ridges lay on the horizontal axis. The results where output to an Excel spreadsheet for analysis. A screenshot of the program is shown in Figure 45.

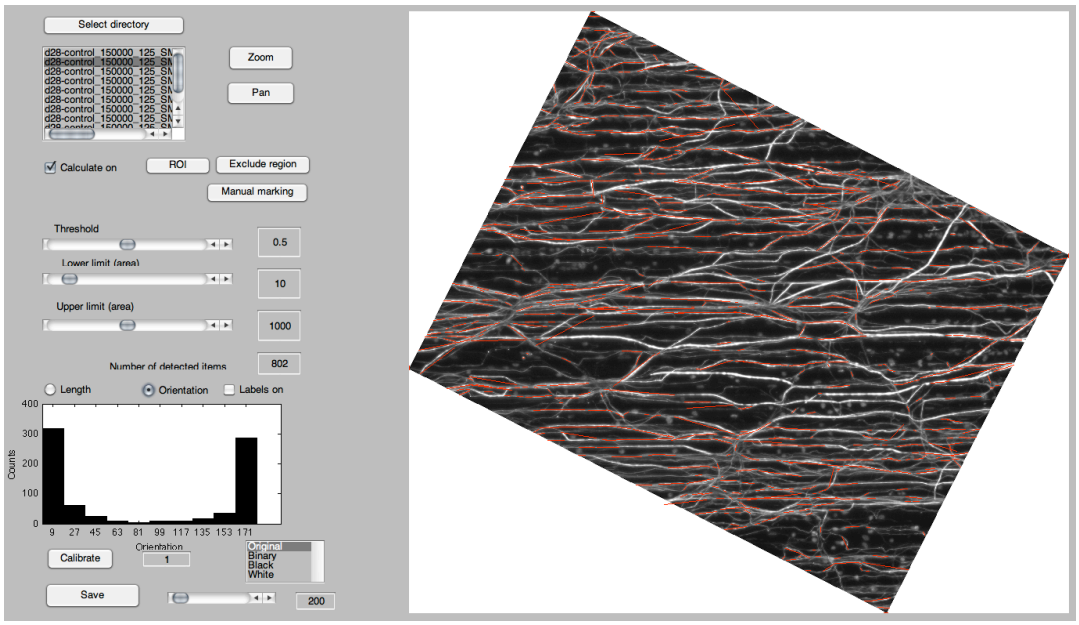

Figure 45: Screenshot of the MATLAB program used to quantify axonal alignment to the ridges. The program thresholds the image and then fits an ellipse to each identified pixel group. The angle of the centre line of each ellipse is then measured from the horizontal plane in absolute values.

To allow statistic methods to be performed, the results were transformed to obtain a normal distribution. This was achieved by rotating the values so that 90° correlated with alignment to the ridges. The data was analysed by creating bins of 20° (i.e. from 0 – 20, 20 – 40, etc) and then counting the number of segments in each bin. The percentage of the axons aligned within

each bin compared to the total for the image was then calculated. Axons that lay in the 80° to 100° bin were considered to be aligned parallel to the grooves while those in the 0° to 20° and 170° to 190° where perpendicular to the grooves. An average of three different data sets was used with three images from each set being analysed. A graph of the results is shown in Figure 46.

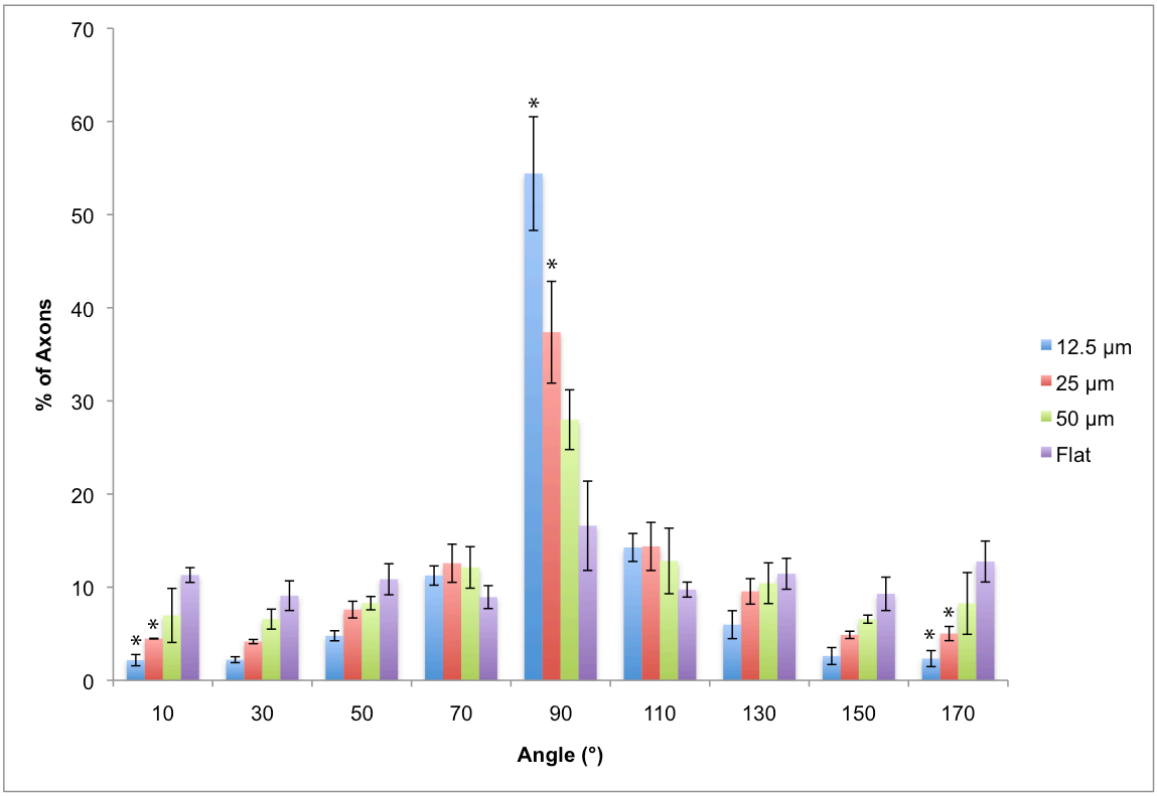

Figure 46: Quantification of the alignment of axons to PDMS devices with 12.5, 25, 50 µm wide and 5 µm high ridges or no ridges. The data is organised into 20° wide bins. Error bars show standard deviation, n = 3. Statistic analysis was performed on the parallel (80° - 100°) and perpendicular bins (0° - 20° & 160° - 180°). Asterisks show a significant difference (P ≤ 0.05) between a ridge type and the flat control. Within the parallel bin, there was a significant difference between all devices except 25/50 and 50/flat. Within the perpendicular bins there were significant differences between 12.5/50, 12.5/flat and 25/flat. The difference between the parallel and perpendicular bins was significant on all grooved devices but was not significant for flat devices.

The flat control showed an even distribution of angles, which correlates with a random alignment of the cells. The 25 µm devices showed a significant differences from the flat devices, however, the 12.5 µm ridges provided the best alignment with the majority of the axons falling into the 80 - 100° "aligned" bin and the fewest amount, compared to the other

devices, in bins corresponding to alignment perpendicular to the ridges. Therefore it was concluded that the 12.5 μm ridges would be used on the final device.

3.1.11 Cell Containment

As a hospitable environment had been created for the cells and the optimal ridge width for axonal alignment had been found, experiments then moved on to containing the soma to a specific area on the devices.

The first set of containment devices, know as Mk.1 containment devices, used two rows of pillars and two walls to create a rectangular containment area in the centre of the devices. A full description of the devices, including dimensions, can be found in Chapter 2.

To test the devices, 1 μl of astrocyte cell suspension was injected with a pipette into the containment area. The cells were given 20 minutes to attach to the devices before being imaged under a phase contrast microscope. A second set of micrographs was taken the morning after seeding.

Samples of the images acquired are shown in Figure 47. Only a small proportion of cells were successfully seeded and retained within the containment area. This probably resulted from the flow of the injection washing the cells over the pillars and walls. This "wash out" effect could even be observed in the 9 mm^2 devices which have a containment volume of ~ 1 μl. Several of the cells that were present inside the containment area 20 min after seeding were absent in day 2. This could possibly be due to the cells being dislodged during handling and floating outside of the area.

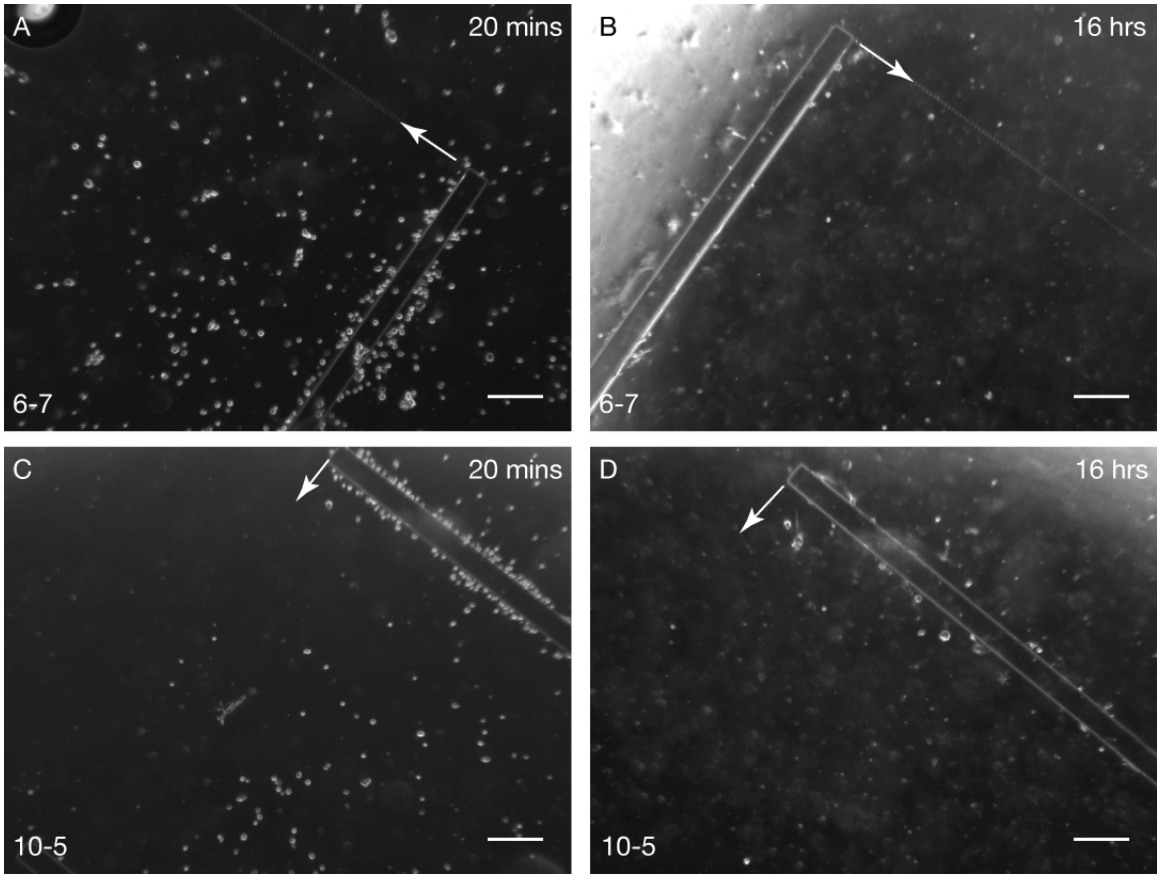

Figure 47: Micrographs of astrocytes seeded onto Mk.1 containment devices. A) & B) Devices with a gap size of 10 µm and area of 5 mm^2. C) & D) 6µm gap, 7 mm^2 area. A & C were taken 20 min after seeding; B & D were taken the morning after. The arrows point to the row of pillars. The astrocytes are the small white dots that are most noticeable near the walls on the left hand images. The cells have been washed outside of the containment area by the force of the injection and by day two some of the cells have either died or been displaced. Scale bars are 100 µm.

There were several practical problems associated with the Mk.1 design. Firstly, manually manoeuvring the pipette tip into the area was tricky and error prone. Secondly, a microscope was needed to easily see the smaller areas. Finally, the seeding was a slow process, requiring ~ 1 - 2 hours for 25 devices.

To eliminate these problems a new design, know as Mk.2, was created for the containment device. This design used only a single row of pillars to screen off a large section of the device. The containment area increased to 66.37 mm^2, compared to a maximum of 9 mm^2 in the previous devices; this was designed to prevent the "wash out" problem encountered during cell seeding. The larger area also made accurate pipette placement less critical and in turn removed the need for a microscope. Due to the increased area, larger volumes of cell

suspension could be used. The standard protocol was increased to 5 µl and thus eliminated the special pipette required to inject 1 µl accurately. Full details of the Mk.2 devices can be found in Chapter 2.

The larger containment area of the Mk.2 devices effectively eliminated the possibility of a misplaced seeding due to inaccurate pipette placement. However, it was still a concern that cells could be dislodged from the containment area by handling the plate after seeding or that cells might float over the containment row during seeding. Therefore a new protocol for seeding was developed. To reduce the amount of cells floating in the media during seeding, the cell suspensions were cooled to 4 °C while the media in the wells was warmed to 37 °C. The protocol was tested by injecting chilled or room temperature food dyes onto devices submerged in water. The effects of the temperature differential are shown in Appendix Figure 1 to Appendix Figure 4. The chilled dye solution showed laminar flow, and settled onto the device even if it had been injected just under the air/liquid interface. Dye solution of the same temperature as the liquid and injected just under the air/liquid interface showed hydrodynamic mixing, and took > 1min to sink to the bottom. This resulted in dye settling out with the containment areas of the device.

To reduce the likelihood of cells being dislodged just after seeding, the plates were left in the hood for 30 mins after seeding. This allowed the cells to settle onto the surface of the device and to begin attaching. They were then moved to an incubator with great care being taken to avoid jolting or tipping the plate.

To test the pillars ability to contain motile and proliferating cells, a culture of C2C12 cells was seeded onto one side of the containment row. C2C12 cells are mouse myoblasts and were chosen for this experiment as they move constantly, and grow very quickly, doubling every 13 hours (Bardouille et al., 2001) compared to the astrocytes' 4.5 days(Sasaki et al., 2004) doubling time, and so provide a method for quickly screening different designs. The cells were allowed to grow for 5 days; micrographs taken after this period are show in Figure 48.

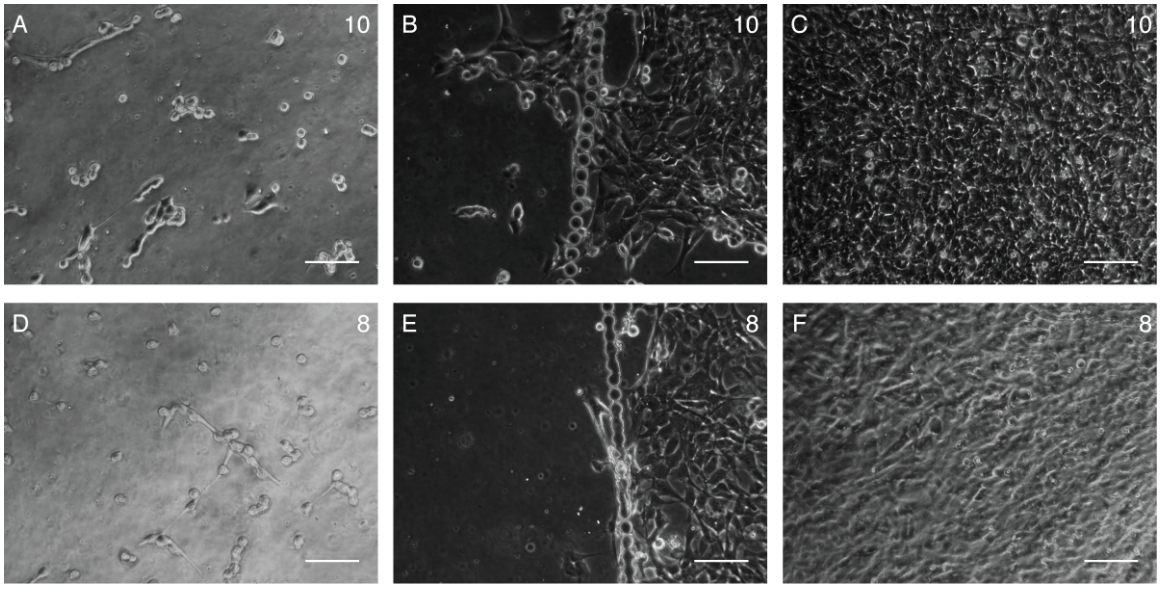

Figure 48: Micrographs of C2C12 cells after growing on Mk.2 containment devices for 5 days. A, B & C show a 10 gap device and D, E & F show an 8 gap device. Scale bars are 100 µm. A) The area of the device where cells were not seeded. The area shown is ~1 mm from the containment row. This image shows the highest density of cells in this area. B) The containment row. Cells can be seen breaching containment; it was not clear whether the cells were squeezing through the gaps or climbing over the pillars. C) The area where the cells were seeded. A highly confluent culture was present across the entirety of this side of the device. D) The non-seeded are of the 8 gap device. E) The containment row of a defective 8 gap device. In this area the pillars had fused together to form a wall. Cells could be observed breaching containment and thus must have been climbing over the pillars. F) A highly confluent cell layer on the seeded side of the 8 gap device.

As can be seen, cells were managing to climb over the 25 µm high pillars. One possibly solution to this problem was to create higher pillars. However, as shown in Chapter 2 performing deeper etches proved problematic. Drs Sun Tao and Peter Donoghue had also observed astrocytes climbing onto 80 µm high ridges so this potential solution was discarded. Another method was to print a chemical or protein, which the cells could not attach to, on top of the pillars. Bovine serum albumin (BSA) was chosen as a suitable protein as it was know to inhibit cell adhesion and could be easily stamped onto surfaces (Curtis, 1984, Lin et al., 2004). To test whether the protein could be printed onto the tops of the pillars only without also coating any of the "lower lying" ridges, a set of containment + alignment devices were trialled. It was not immediately evident whether the BSA would need to be printed before or after PLL coating so PDMS sheets were prepared with and without a PLL coating. The results of a test printing of BSA onto PLL coated and uncoated devices are shown in Figure 49.

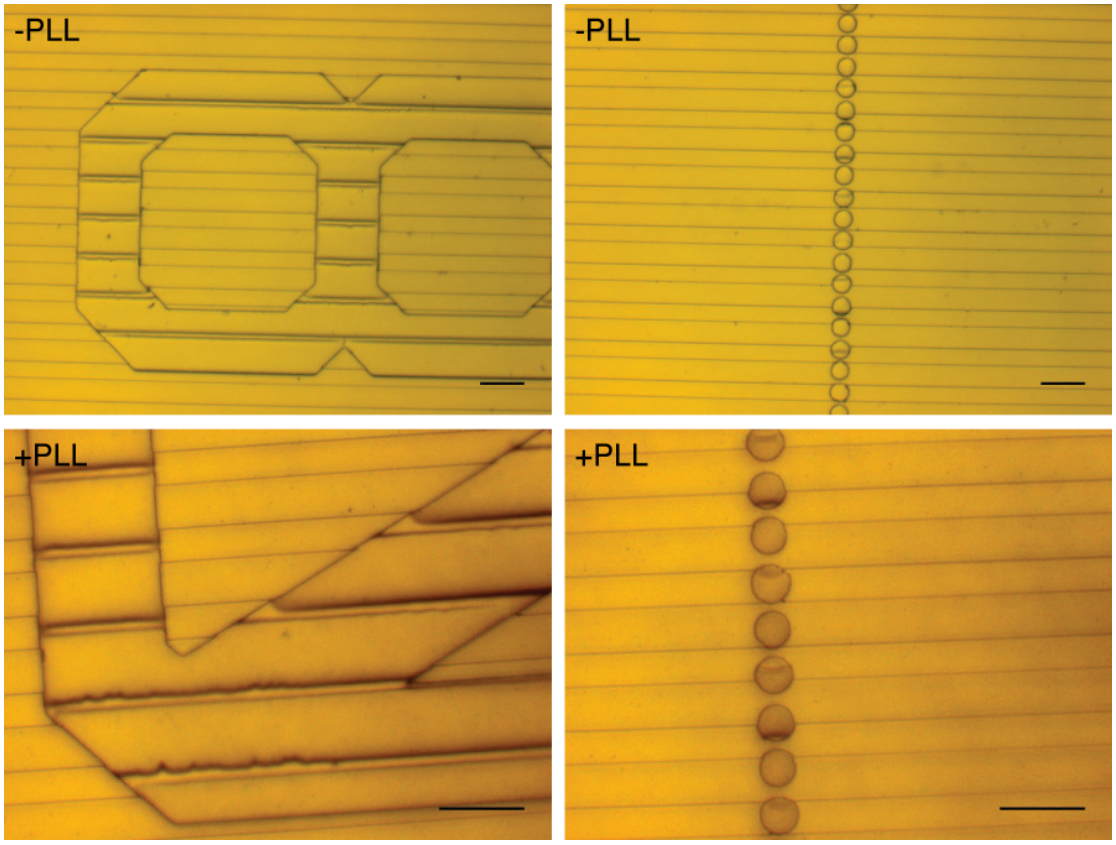

Figure 49: Micrographs of containment + alignment devices, which were either coated with poly-l-lysine (+PLL) or only plasma treated (-PLL). They were then stamped with a BSA coated silicon wafer. The images show the numerical indicator on the left and the pillar row on the right. The devices were treated with coomassie brilliant blue, which stained any protein present blue. The presence of BSA could be seen on the pillar tops and number indicators of the +PLL devices. This is evidenced by the mild blue/grey colouring in the +PLL pictures, which is absent on the –PLL devices. Scale bars are 50 µm.

Coating the devices with PLL prior to stamping allowed successful transfer of BSA to the pillars and the numerical indicators, which were the same height. The differential adhesion between the uncoated devices and the silicon wafer was not sufficient and so stamping was not successful. No BSA could be seen on the ridges of the +PLL devices.

Containment experiments with the BSA printing method were first conducted with MG63s, an osteoblast-like cell line, while new stocks of C2C12s were obtained. MG63s, similarly to C2C12, grow at a far faster rate than astrocytes and also provided another cell type for comparison. Cells were seeded on one side of the pillar row, which were then allowed to grow for 10 days. Results of this experiment can be seen in Figure 50.

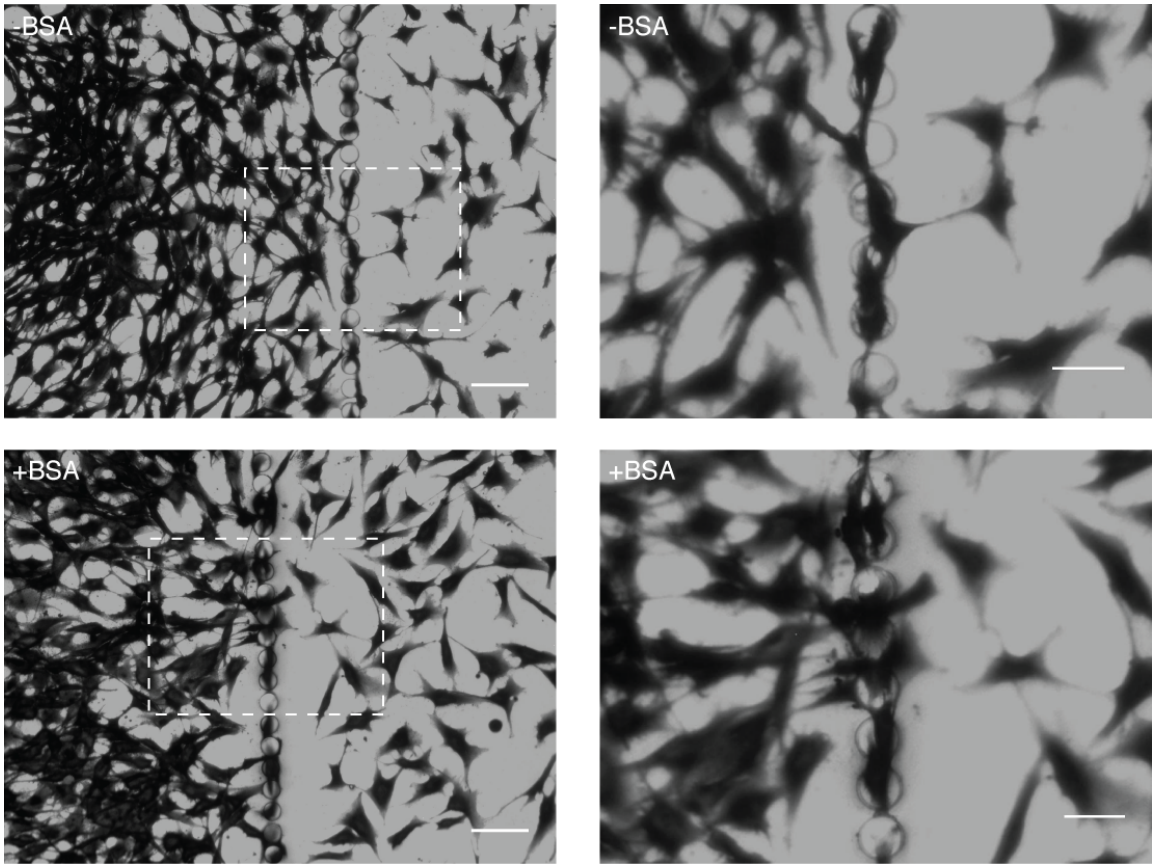

Figure 50: MG63s seeded on Mk.2 containment devices, which either had BSA stamped on top of the pillars (+BSA) or were left unstamped (-BSA). The cells were seeded on the left hand side of the devices and allowed to grow for 10 days. The cells were stained with Coomassie Brilliant Blue. The images on the right are enlargements of the area outlined in the left hand images. Scale bars are 100 µm on the left hand images and 50 µm on the right. Pillar dimension: diameter & height 25 µm, gap 4,5 µm.

Cells could be seen climbing over, and aligning to, the pillars in both the –BSA and +BSA devices. No coomassie staining could be seen on top of the pillars; unsuccessful stamping or the BSA dissolving during cell culture could have caused this. There was a greater density of cells on the seeded side than the un-seeded one, which suggested that the pillars were slowing the progress of the cells across the device. Cells were observed on top of the pillars and aligning to the row of pillars, they could also be seen making connections with cells on the flat areas next to the pillars. Cells could not be seen to successfully squeeze through the gaps between the pillars in any of the timelapse movies taken.

Further attempts at containing cells using BSA stamping were made with astrocytes. These experiments were conducted in the same manner as the MG63 experiments except that the astocytes were given 15 days to grow. Selected micrographs of one experiment are shown in Figure 51.

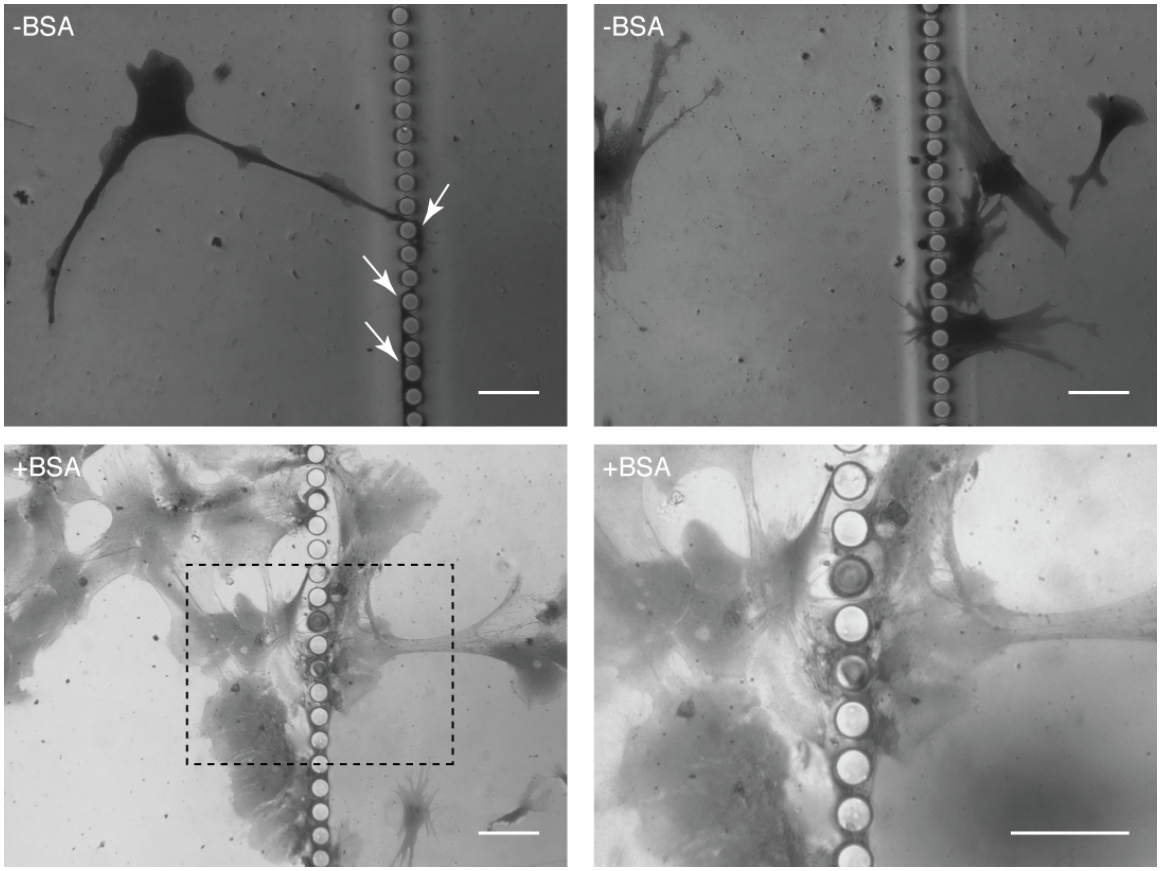

Figure 51: Astrocytes grown for 15 days on Mk.2 containment devices with or without BSA printing. The cells have been stained using Coomassie Brilliant Blue. The devices were prepared and seeded in the same manner as those shown in Figure 50. The bottom right image is an enlargement of the area shown in the image to its left. A thin projection can be seen to interact with the pillars in the top left image, its path is shown by the white arrows. Cells can be seen covering the top of a couple of the pillars in the +BSA images. Scale bars are 100 µm.

Once again, no evidence of BSA could be found on top of the stamped pillars. A lesser number of cells were observed on top of the pillars when compared to the MG63 cultures. However, many cells had managed to cross the containment row. Cells could be seen extending projections through the pillars; however, it appears that the cell bodies were unable to squeeze through the gaps. This was supported by a time-lapse video of C2C12 cells, shown in Appendix Figure 5. In the video cells could be seen attempting to squeeze through the gaps. Several cells wrapped a process round one of the pillars and then tried to pull themselves through the gaps; none of them were successful. Some cells could also be seen linking processes through the gaps.

From the above evidence it seemed that the cells were climbing over the pillars whether they were printed or not, in addition, stamping onto the pillars was time consuming. It was therefore decided that the BSA stamping method was not a viable option for preventing containment breaches and that a topographical solution should be sought. Evidence(Miyoshi et al., 2010) showed that multiple, interlaced grooves could cause cells to change the direction of movement and screen them from areas of a device. Multiple rows of pillars would form a similar topography and so efforts were made to create a new master with 1, 3 or 5 rows of pillars.

As there were some problems with the fabrication of multi-row devices, experiments were conducted with the defective multi-row devices, shown in Chapter 2 Figure 26, to establish whether multiple barriers would impede the movement of the cells. 3 devices of each type were seeded with C2C12 cells on one side of the pillars and allowed to grow for 8 days. They were then fixed, stained with Coomassie Brilliant Blue and images were taken across the length of the cell growth. Separate devices were also seeded for time-lapse recording.

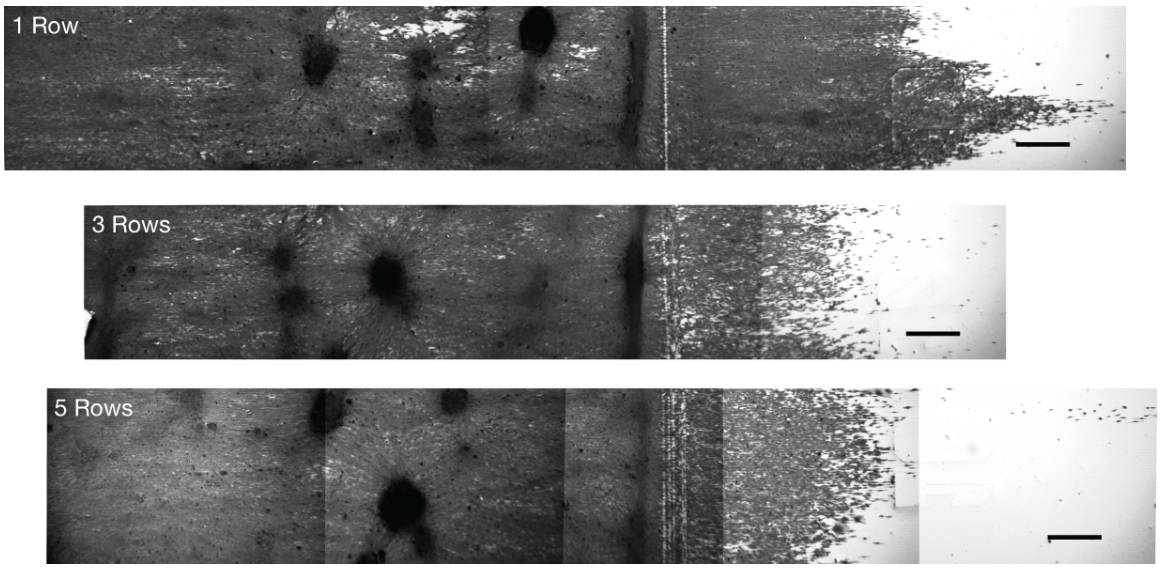

Figure 52: C2C12 cells grown on the defective multi-row devices for 8 days. A selection of the 1, 3 and 5 row devices are shown. A composite of 5 micrographs is shown in each image. The cells were seeded on the left hand side of the pillar rows and were stained with Coomassie Brilliant Blue. Scale bars are 500 µm. An area of high cell density formed just behind the pillar rows on all the devices. Cells had also formed aggregates on the seeded side of the pillars.

It was found that cells were crossing the barriers and that no difference could be seen between the different types of device. It was observed that a high density of cells built up behind the containment rows, this was particularly evident in the 5 row time-lapse movie. This suggested that pillar row topography had an effect on the cells analogous to that a 'speed bump' has on the flow of traffic. It was also of note that large cell aggregates formed on the devices and in some cases began to peel cells from the surface of the device. This was probably due to the very high cell density on the seeded side of the pillars after 8 days of growth.

One experiment, shown in Figure 53, highlighted two problems with the experimental method. Firstly, the cells could not be seeded the same distance from the pillars on every device. This lead to uncertainty as to whether cells had been successfully contained due to the topography or if they may have been seeded a long distance from the pillars and had only reached them when the experiment was concluded. It was thus hard to compare a device which had a distant seeding to one on which the seeding had been close to the pillars.

Secondly, in the time it took the cells to reach the pillars and begin to interact with them, large cell aggregates had formed on most of the devices and in some cases began to detach from the surface. Examples of this are shown in Figure 54. This lead to another uncertainty as aggregates could have been detaching from the surface, floating over the pillar rows and then settling onto the surface.

At this point the multi-row devices using the new mask were completed and experiments moved over to using them. A solution to the problem of cells being seeded too far from the containment rows was found in the form of Ibidi Culture-Inserts. These were small silicone devices measuring 9 mm x 9mm x 5 mm with two 0.22 cm^2 wells separated by a 500 µm thick spacer. By placing the Culture-Inserts so that the spacer lay on top of the containments rows, cells could be seeded very close to the pillars without any of them crossing the rows.

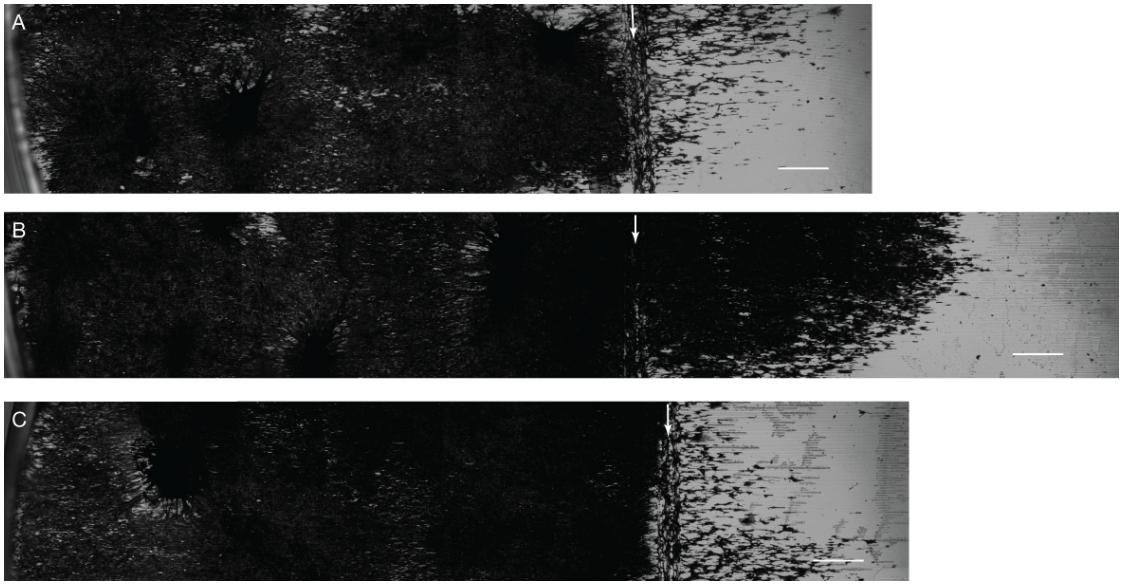

Figure 53: C2C12 cells stained with Coomassie Brilliant Blue after growing for 8 days on defective 5 row devices. The white arrows show the position of the middle of the containment rows. Scale bars are 500 µm. The cells on A) & C) appeared to be contained, with only a small number of cells appearing on the right hand side of the containment rows. However, the cells on B) had breached containment and formed a dense layer of cells to the right of the containment rows.

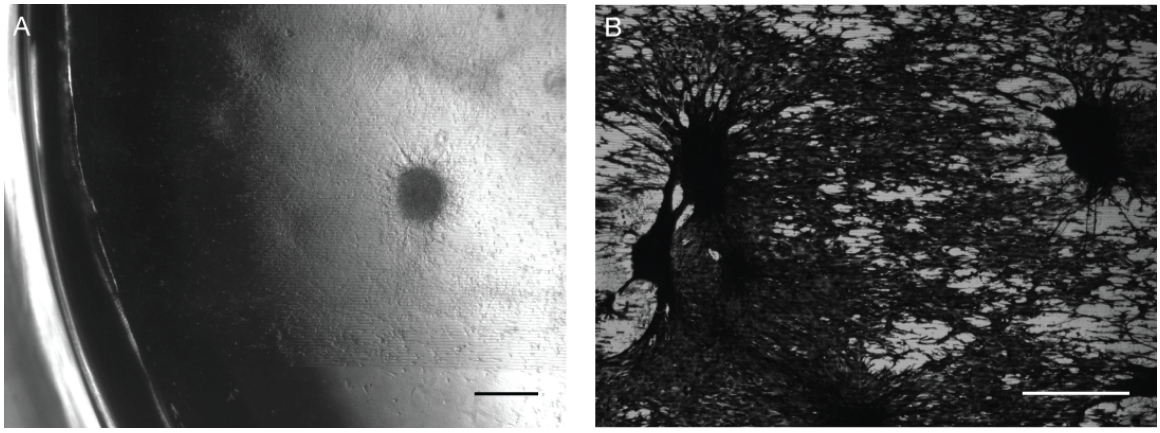

Figure 54: C2C12 cells aggregates on ridge and containment devices. A) An aggregate forming on day 5 of culture. At this point the cells had just reached the containment rows. B) Coomassie Brilliant Blue stained cells after 8 days in culture. The aggregates had peeled cells from the surface of the device and large gaps had opened up in the once confluent layer. Scale bars are 500 µm.

To eliminate the problems that the cell aggregates were causing, astrocytes were used for a long-term containment experiment. Previous experiments had shown that this cell type tended not to form aggregates on the devices even after 24 days in culture. For this experiment

cells were seeded onto containment devices using the Culture-Inserts. The devices were split into three sets, each containing either 6, 8 or 10 gaps devices with three devices each of the 1, 3 and 5 row variants. Three control devices that only had 12.5 µm ridges on them were included in each set. A small scratch was made on the control devices to indicate where the Culture-Insert's spacer had been located on the devices. Daily images were taken of the region around the pillars rows to allow the progress of the cells to be tracked. Due to the relatively slow growth of the astrocytes, the cells were observed over a period of 24 days. At the end of this period all the devices were fixed and stained with DAPI. Fluorescent images of the devices were then taken as shown in Figure 55.

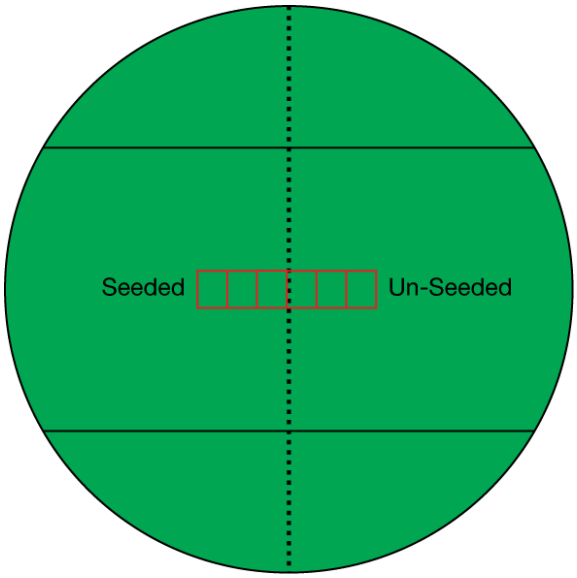

Figure 55: The area of the containment devices that was imaged for analysis. The dashed line represents the containment rows, the solid lines denote the ridged area and the red boxes shown the field of view for the microscope using a 10x objective. Images were taken as close to the vertical centre of the ridged area as possible. For devices with no containment rows, the scratch mark that showed the position of the Culture-Insert's spacer was used as the centre line.

The images were imported into Adobe Photoshop and each set of 6 images was aligned and then combined into one image. The images were transferred to ImageJ where they were rotated so that the ridges lay on the horizontal axis. The images were then thresholded and a particle analysis was performed. The x and y coordinates of all the detected particles and the position of the containment rows, or the centre position of the image for control devices, were exported to Excel. The coordinates were then used to count the number of particles within

the seeded, un-seeded and pillar regions. Images comparing the effects of the differing number of rows are shown in Figure 56, while the effects of gap size are shown in Figure 57.

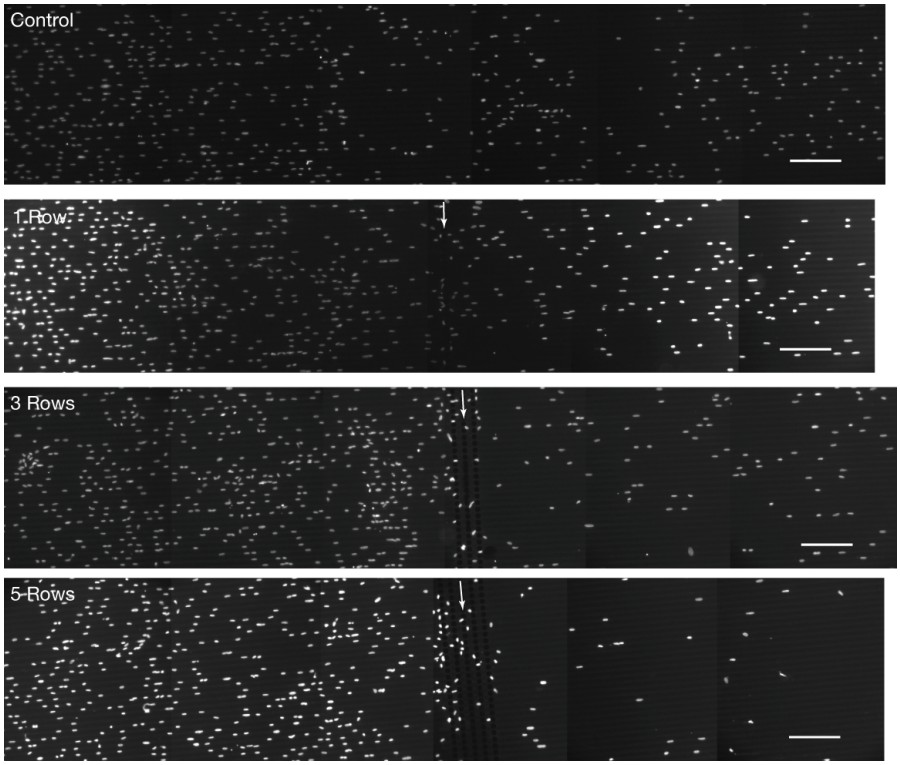

Figure 56: Astrocytes grown on 6 gap containment devices for 24 days stained with DAPI. The number of containment rows is shown in the top left of each image, the control device had no containment rows. The white arrows show the centre position of the rows. Scale bars are 200 µm.

The containment ratio was calculated for each device. This was defined as the number of nuclei on the seeded side of the pillar rows plus those within the pillar rows divided by the number of cells on the unseeded side. A graph of the results is shown in Figure 58. All of the 1 and 3 row devices did not contain the cells any better than the control devices that lacked pillar rows. The 5 row 10 gap (5-10) devices also appeared to perform no better than the controls. The 5-6 and 5-8 devices gave higher containment ratios than the controls. However, due to the variability these results were not significant. It should be noted that in both cases a single outlier caused the large deviation, for the 5-6 devices this was a high outlier at 11.02 and a low outlier at 2.98 for the 5-8 devices. Further experiments would help to smooth out this problem.

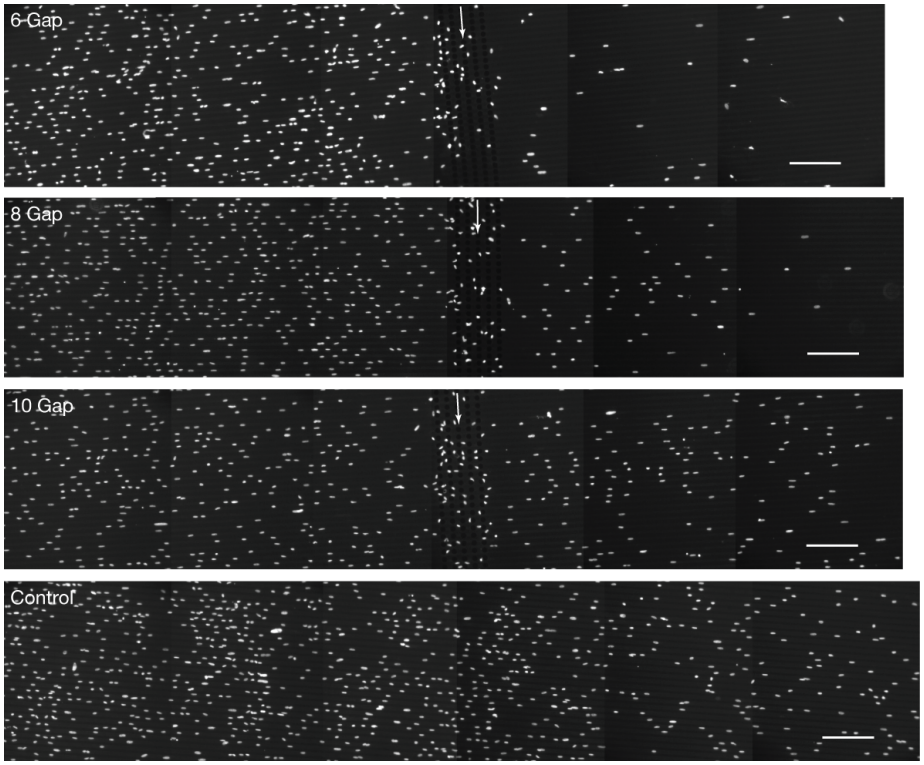

Figure 57: Astrocytes grown on 5 row containment devices for 24 days stained with DAPI. The gap size is shown in the top left of each image, the control device consisted of ridges only. White arrows indicate the centre of the containment rows. Scale bars are 200 µm.

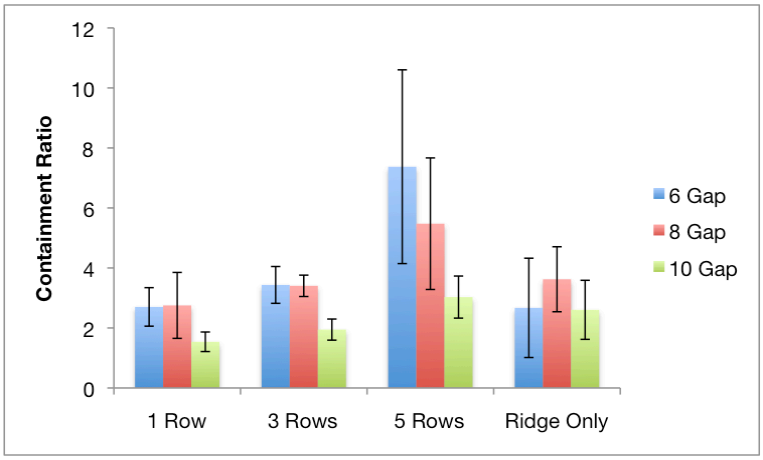

Figure 58: The containment ratios, number of cells on seeded side plus those within the pillar rows divided by number of cells on the unseeded side, of the multi-row containment devices. Devices had either 1, 3 or 5 rows of pillars with gap sizes of 6, 8 or 10. The ridge only columns show the pillar-less control devices for each set of devices. Three devices were analysed for each pillar varient.

Experiments were also conducted using the Culture-Inserts with C2C12s. Time-lapse videos were taken of every combination of the 1, 3 and 5 rows; and the 6, 8 and 10 gaps. In these videos cells could be seen easily passing through the 10 gaps and squeezing through the 8 gaps with a small slowing in movement. The 6 gap devices slowed the cells down far more as they had to exert some effort to climb over the pillars or, possibly in some cases, squeeze through the gaps.

Upon approaching the pillars some cells began to move parallel to the row or to turn back and head in the opposite direction to their previous movement. Cells were also observed climbing/squeezing into the area between pillar rows and the moving parallel to the rows.

The result of the astrocyte experiment, above, could be explained by probabilities associated with the climbing, squeezing, turning parallel and about turn movements. If a cell has a certain probability associated with each of these actions then the presence of multiple pillar rows would raise the likelihood of a cell being contained. Similarly, the smaller gap size could reduce or eliminate the chance of a squeeze movement and thus further reduce the chance of a containment breech. Hence the 5 row, 6 gap devices providing the best containment. However, more data would be required to properly quantify these probabilities.

3.1.12 Neuronal Containment

While attempts were being made to resolve the problems associated with C2C12 containment, experiments were conducted using myelinating cultures. Initial experiments were unsuccessful as the cell density was abnormally low. It was first thought that the cells might have been dying for some unknown reason. However, this seemed unlikely as the cultures grew normally on the control (flat) PDMS devices. As the myelinating cultures had to be grown in small petri dishes, unlike the MG63, C2C12s and astrocytes, which were grown in 24-well plates, it was hypothesized that the temperature differential seeding protocol might be causing the cells to wash off the side of the devices. To test this several devices in 50 mm petri dishes were seeded with MG63s using the chilled suspension protocol. The results are shown in Figure 59.

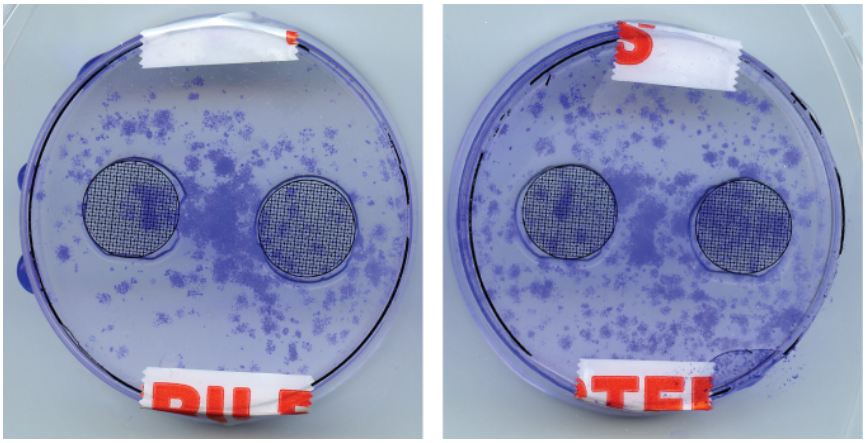

Figure 59: MG63s seeded into 50 mm detri dishes using the chilled suspension protocol. The cells were stained with Coomassie after 5 days of growth. The devices are located above the circular grids. The majority of the cells were washed off the side of the devices and were growing in the bottom of the petri dish.

The chilled suspension seeding method was developed to shorten the time required for the cells to attach to the surfaces and to reduce the amount of missed containment seedings caused by placing the pipette tip too high in the solution. However, the temperature differential was causing the majority of the cells to wash off the top of the devices in the Petri dishes. To prevent this all future seeding were conducted with the cell suspension and the media in the dish heated to 37 °C.

After the seeding problem was solved, experiments could be performed with the myelinating cultures. Several containment devices were seeded with astrocytes across their entire surface. After 10 days, myelinating cultures were seeded on one side of the containment pillars and allowed to grow for 15 days. They were then fixed and stained for SMI31, and axonal marker, and NeuN(Mullen et al., 1992), and marker of somata. Micrographs of the results are shown in Figure 60.

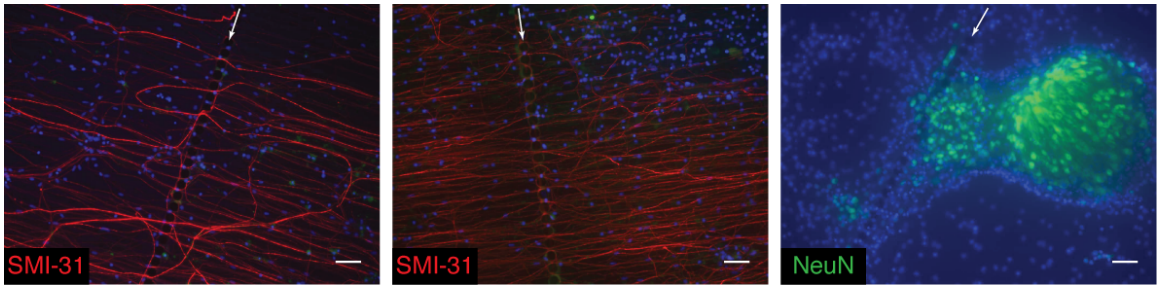

Figure 60: Myelinating cultures after 25 days in culture on containment devices. The cultures were seeded on the right hand side of the pillars. The cultures were stained for SMI-31, an axonal marker; or NeuN, a soma specific marker. Faint traces of green PLP staining can be seen in the SMI-31 pictures. White arrows show the location of the containment pillars. Scale bars are 100 µm. Axons were freely able to navigate through the pillars and maintain their alignment with the ridges. The majority of the soma appeared to remain on the seeded side of the pillars.

The majority of the neurons were successfully contained and the axons were aligned to the ridges and able to pass through the containment row without much hindrance. Some axons were observed looping round after passing through the pillars and then returning to the seeded side. Other axons could be seen turning perpendicular to the ridges and aligning to the pillar row. Some soma had breached the containment but it was unclear if this was caused by them climbing over the pillars or if it had occurred during seeding. Once again, it was also uncertain whether the soma had successfully been contained due to the pillars or if they had only come into contact with them just before the experiment ended.

To ascertain the cause for the cell containment Ibidi Culture-Inserts were used to seed the myelinating cultures on top of astrocyte layers which where grown on 6 gap multi-row devices and ridge only devices. The use of the culture inserts had been avoided in previous experiments as it was thought they would damage the astrocyte layer and effect the axonal outgrowth. However, after the Culture-Inserts were removed, astrocytes moved back into the affected regions and appeared to not inhibit axonal growth. Images showing the cultures 12 days after the seeding of the myelinating cultures are shown in Figure 61.

As can be seen in the ridge only images, the majority of the somata appeared to not move from the position they were seeded in and the overall distribution of the neurons still maintained the shape of the Culture-Insert wells. Some somata moved away from the seeded area but this was only a small minority. It appeared that the pillars were unnecessary for the containment of the somata and that Culture-Inserts could be used to confine the seeding of the myelinating

cultures to a desired area. However, the pillars could potentially be used to isolate two types of cultures to create, for example, a model of interaction between the CNS and PNS. This is discussed more in Chapter 5. It was also noticed on the ridge only images that axons appreared to cross the ridges more regularly close to the soma. While a small distance from the soma the ridge cross-over was infrequent.

It was noticed that additional rows of pillars seemed to cause axons to turn and move perpendicular to the ridges. To quantify this effect the program used in 3.1.10 was employed. Axon alignment was first quantified across the entire frame of 3 images per device. A region, centred on the pillars, measuring 234 x 1071 μm was then cropped from the images and analysed. This area was chosen as it covered the width of 5 rows of pillars, plus a small region either side of the rows, and the height of a frame when rotated for alignment quantification. The results of the full frame analysis are shown in Figure 62 and the pillar regions are shown in Figure 63.

When compared to the control devices, the presence of any pillars caused a reduction in the number of axons falling within the 80 - 100° aligned bin. Across the entire frame, the difference between the control and 1 row devices was minor apart from in the 100 - 120° bin. When looking at only the pillar region, there was a large difference between the control and 1 row devices in the aligned bin. However, there was still only a small difference in the 0 - 20° and 160 - 180° parallel bins.

There was not a large difference between the 3 and 5 row devices across the entire frame or within the pillar region. However, when compared to the 1 row devices in the pillar region, the multi-row devices had half the amount of axons in the aligned bin and triple the amount in the parallel bins. When compared to the control devices this became a quarter of the amount in the aligned bin and 20 times the amount in the parallel bins.

It was clear that multiple rows of pillars were causing the axons to deviate from their course. This effect could potentially be used to create turning points on devices to allow complex axonal paths. This concept is discussed more in chapter 5.

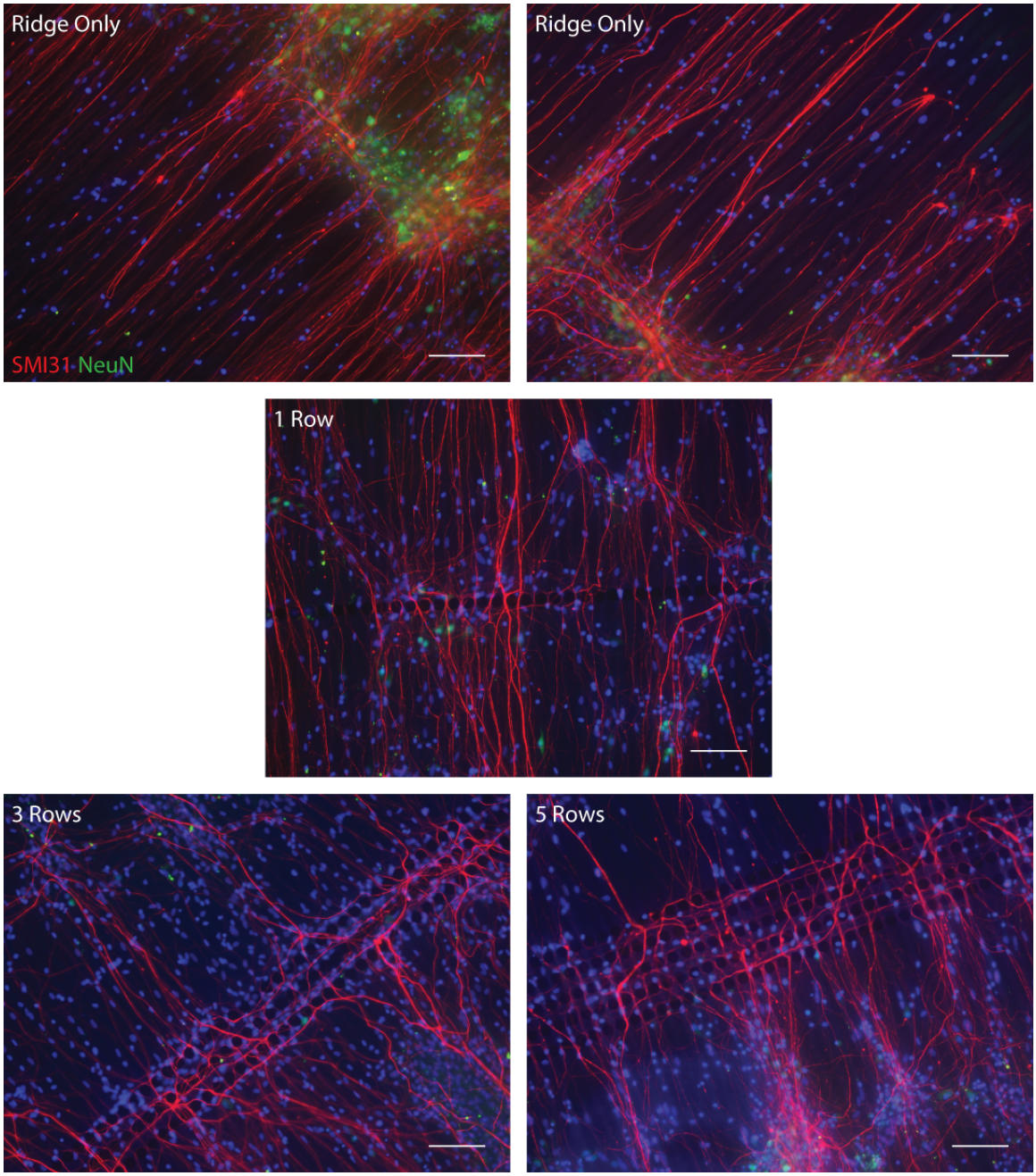

Figure 61: Myelinating cultures grown for 12 days on multi-row containment devices and ridge only control devices. Cells were seeded using Ibidi Culture-Inserts. Axons were stained for SMI31, red, while somata were stained with NeuN, green. The soma did not move far from their initial seeding positions. Multiple rows of pillars appeared to cause axons to align to the pillar rows. Note that in the ridge only images the majority of axons crossing the ridges appeared to be concentrated near the soma. As the axons extend away from the soma they followed a straighter course. Scale bars are 100 µm.

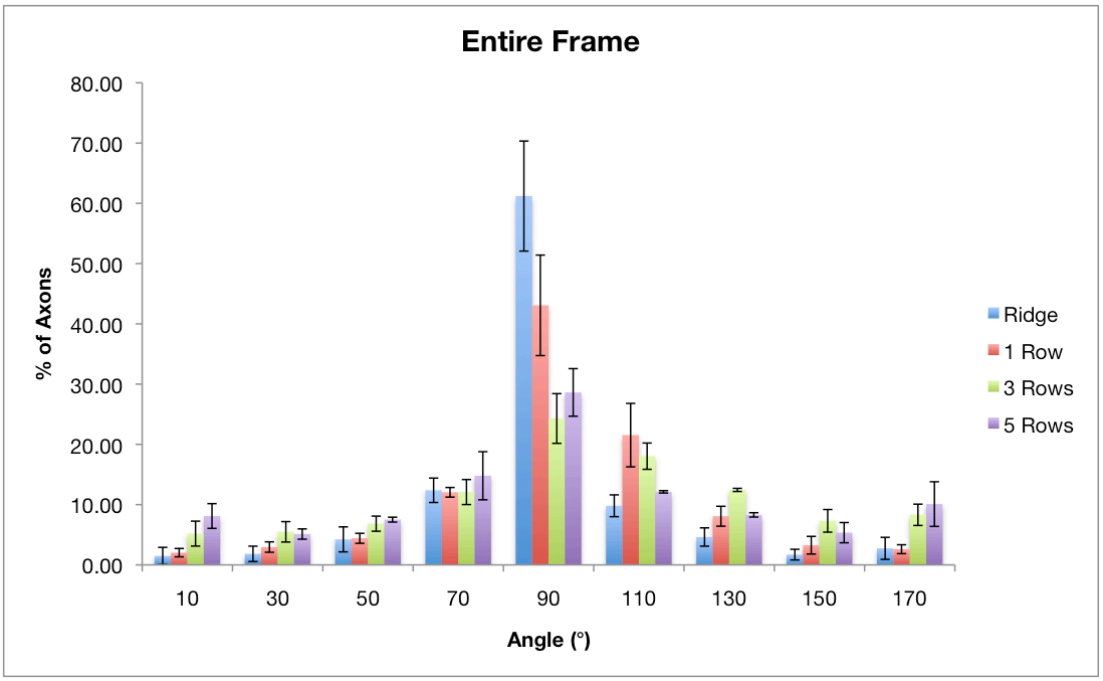

Figure 62: Graph showing the alignment of axons on the multi-row and ridge only devices. The percentage of the detected axon elements in each bin compared to the total axon elements detected is shown on the vertical axis. Bins 20° wide are shown on the horizontal axis. "Ridge" was the pillar free control devices. This graph shows the alignment across an entire frame, as shown in the figure above. Four images were analysed per device type.

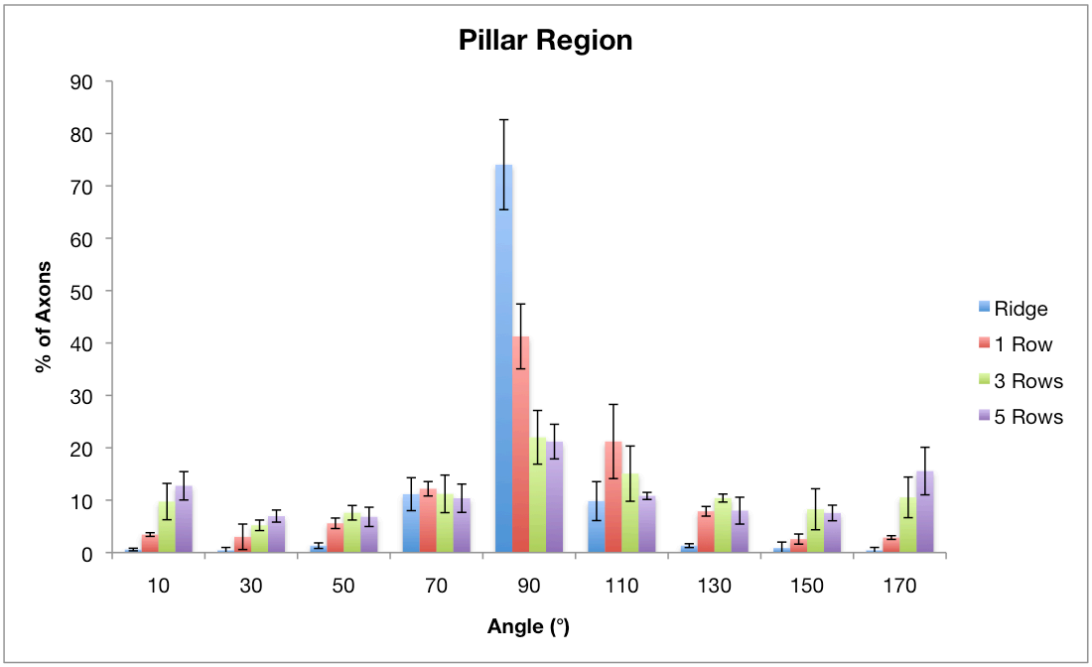

Figure 63: Alignment of axons within the pillar region. This was an area of 234 x 1071 µm centred on the middle of the pillar rows. Data is shown in the same format as the graph above.

Chapter 4

Cell Wounding

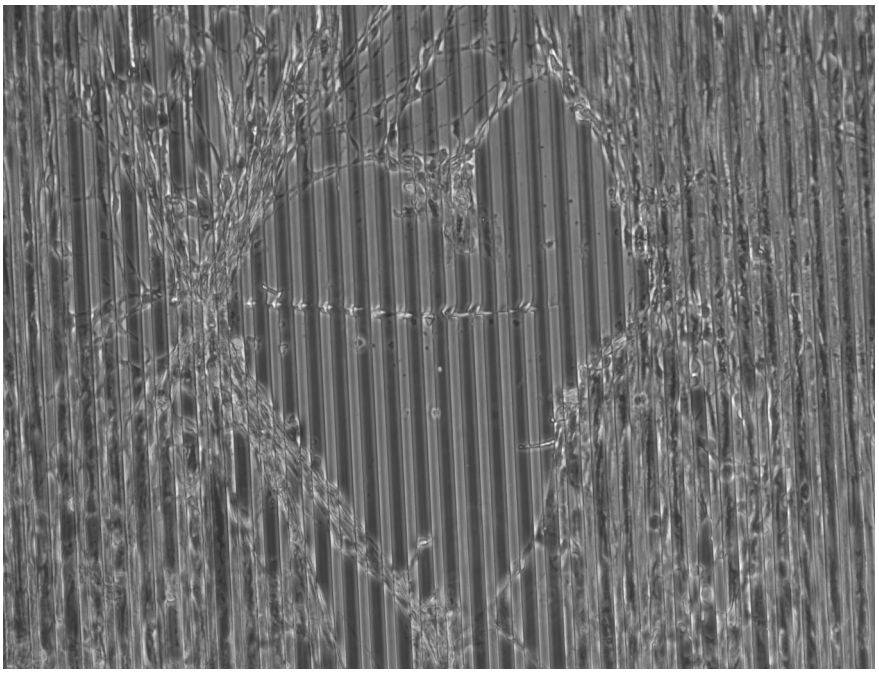

4.1 Materials and Methods

4.1.1 Cutting of Devices

For testing how the devices were damaged and changed, they were cut by hand using either a Feather No. 11 blade or a Fine Science Tools (FST) ultra fine micro knife. The cuts were made as follows: by slicing off sections of the device to expose the inner surface (cut), dragging the blade across the surface (slash) or vertically inserting the blade into the device (stab). The devices were then sputter coated with an 18 nm layer of gold and analysed with a Hitachi S-3000H SEM.

4.1.2 Cutting of Cells

Astrocytes and MG63s were grown on PMDS alignment devices as per the protocol shown in Chapter 3. To allow automated cutting of cells, the blades were clamped into an Eppendorf InjectMan NI 2 micromanipulator mounted on a Zeiss Axiovert 200M microscope. The microscope was equipped with a heated stage to provide a hospitable environment for the cells. This stage was heated to 37 °C prior to cutting. For the cutting experiments the devices were individually transferred into 50 mm Petri dishes, which were then filled with enough CO_2 independent media to cover the devices.

The micromanipulator was programmed to make a unidirectional cut 700 µm long, 30 µm deep, with a blade angle of 30° to the device and at a speed of 120 µm/s. A calibration cut was made on each device before recorded cuts were made. This allowed the height of the device to be established and the correct cut depth to be set.

4.1.3 Manual Wounding of Cells

Cells were grown on alignment devices as per the usual protocol in Chapter 3.They were then transferred to 50 mm Perti dishes and immersed in CO_2 independent media. During cutting

the dishes were placed on the heated stage of the microscope so that they would experience the same environmental conditions as the cells cut with the micromanipulator. The cells were then cut by hand with the same blade used for the automated cuts. After cutting images of the resultant wounds were taken on the Axiovert 200M.

4.1.4 Quantification of Wound Dimensions

Adobe Photoshop CS4 was used to interactively define the area of the wound from the micrographs. The wound images were then imported into ImageJ and scaled. The image was then thresholded so that the entire wound area could be selected. For hand made cuts the image was rotated so that the direction of the cut lay along the x-axis. Wound dimensions were then quantified by fitting a bounding rectangle to the wound; the width of the wound was defined as the *y*-axis distance and the length as the x-axis. The area and was also measured. The data were then imported to Microsoft Excel so that analysis could be performed.

4.1.5 Statistical Analysis

Statistical analysis of data was performed in the same manner as described in Chapter 3.

4.2 Results and Discussion

4.2.1 Cutting of Devices/Astrocytes

The first stage in developing a cutting method was to choose a suitable blade. Several standard lab scalpels were available; the Swann-Morton No.11 blade was selected as it had a fine, straight blade. A second scalpel, the Fine Science Tools (FST) ultra fine micro knife, was also chosen. It featured a finer blade than the No.11, as can be seen in Figure 64.

To establish what damage cutting could cause to the surface of the PDMS devices; several different incisions were made on alignment devices with both blades. The blades and the devices were then inspected with an SEM. Selected images are shown in Figure 64.

The No.11 blade had a far rougher cutting edge and a greater thickness than the micro knife. The blade roughness resulted in ragged lacerations on the devices and, which probably contributed to the shear force that distorted the topography. The blade's thickness and roughness was sufficient to create the large fissures in the surface. The micro knife caused a much smaller amount of debris and barely distorted the topography.

Based on these results it was decided that the micro knife would be the better candidate for performing further experiments. However, to make sure the blade choice would not have unexpected consequences, both blades were trialled on monolayers of astrocytes. This experiment was performed on flat PDMS devices to reduce complications while the cutting method was being developed. Selected images of the resultant wounds are shown in Figure 65. Quantification of the length, width and area of the wounds are shown in Figure 66.

As the blade was drawn across the surface it accumulated cell debris on the leading edge, which then pulled neighbouring cells out of position. This effect propagated along the blade's course and resulted in a flap of cells being torn off the surface. The variability in wound area, see Figure 66, was probably due to different amounts of tension in the cell layers causing varying amounts of cells to be pulled from their original position, this hypothesis was tested using cytoskeletal poisons.

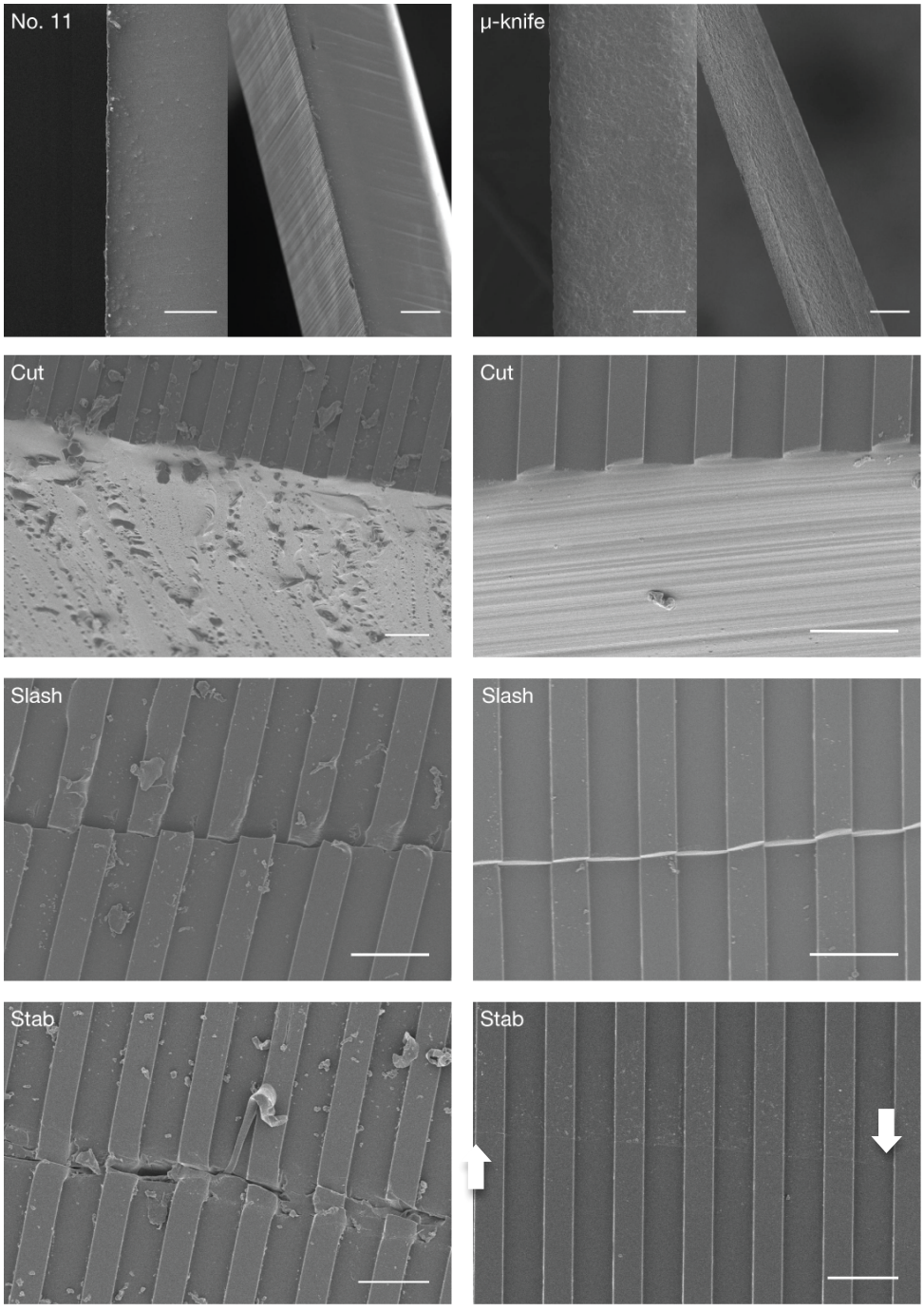

Figure 64: SEM micrographs of blade edges and the damaged they caused to PDMS alignment devices. A Feather No.11 blade, shown in the left hand images, and a FST ultra fine micro knife, shown on the right, were tested. The top two images show the blades from a 90° and 30° tilt angle. The No.11 blade caused extensive damage around the incision, creating a fissure 1 - 10 μm wide, leaving debris up to 20 μm in size and distorting the topography. The micro knife caused less damage to the structures. The slash left a fissure between 1 and 5 μm. The stab left a barely detectable scar (see faint line between white arrows) << 1 μm wide with only minor debris. Scale bars are 100 μm in the top two images and 50 μm in all other images.

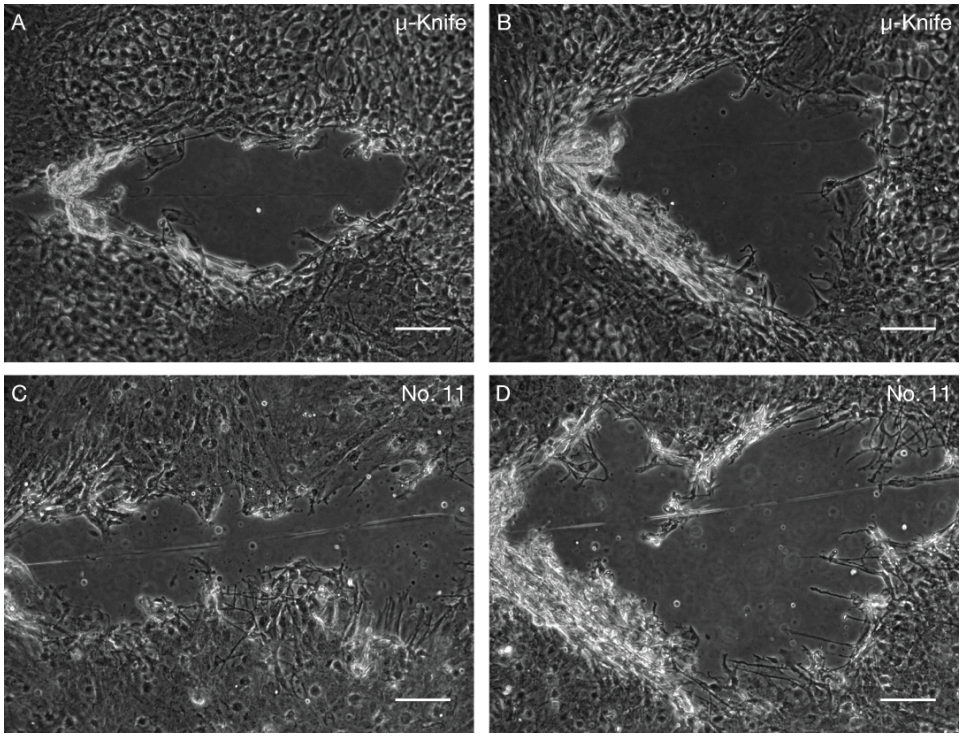

Figure 65: Micrographs of cuts made with the two types of blade to a 10 day old monolayers of astrocytes grown on flat PDMS devices. A) and B) show two of the wounds created by cuts made with an FST micro knife. C) and D) show the wounds resulting from cuts by a Swann-Morton No.11 blade. Cut direction was right to left. The micromanipulator was set to make cuts 700 μm long and 30 μm deep, with a blade angle of 30° and speed of 120 μm/s. As the blade was drawn across the devices surface, cells snagged on the leading edge of the blade and dragged neighbouring cells that, in turn, displaced other cells. This resulted in a wound that resembled a tear rather than a cut. A flap of cells that were detached from the substrate can be seen at the leftmost edge of the cut. Scale bars are 100 μm.

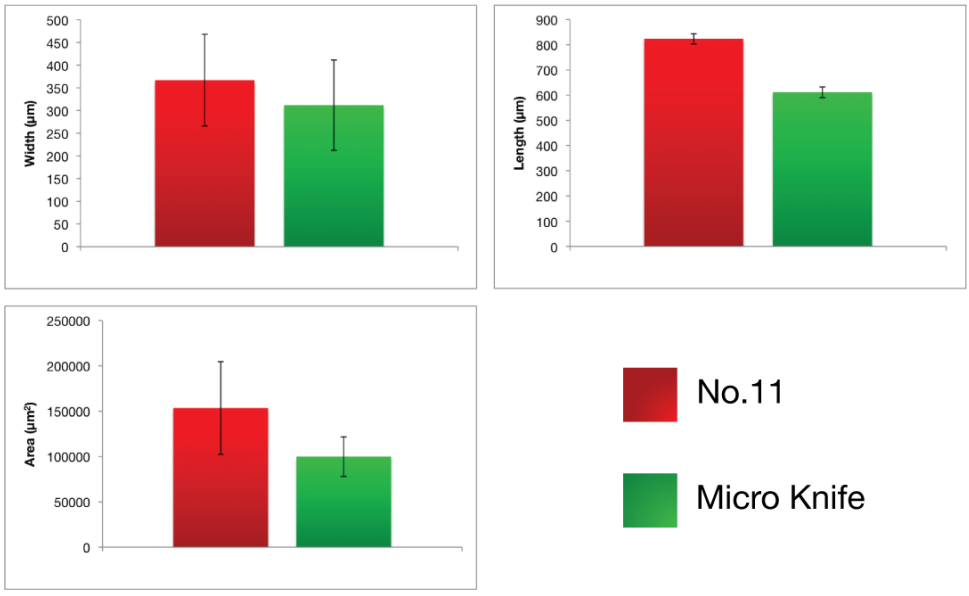

Figure 66: Analysis of cuts made with a Swann-Morton No.11 blade and a FST micro knife to 10 day old monolayers of astrocytes. Graphs show the width, length and area of the resultant wounds. Error bars show the standard deviation. n=3

The No.11 blade created slightly longer wounds than the micro knife; the micromanipulator was programmed to move the blade 700 μm, with the blade tip as the start point, in both cases. However, the no.11 had a slightly different blade angle to the surface, which accounts for the increased wound length. There was only a small amount of variability in the wound length. Both blades caused wounds of a similar width with almost the same standard deviation.

The blades caused similar wounds in the astrocyte layers; however, the No.11 blade had been shown to cause considerable damage to the topography and so the FST micro knife was selected for all further experiments.

4.2.2 Wound Formation on Topography

It needed to be established what affect the alignment of cells by linear groove/ridge topography had on wound formation. To investigate this, monolayers of astrocytes were grown on alignment devices and then cut using a FST micro knife. Cuts were performed on the flat areas of the devices and perpendicular or parallel to the grooves. A sample of the resultant wounds can be seen in Figure 67. Quantification of the wound dimensions is shown in Figure 68.

The length of the wounds was consistent across the different cut directions; this was due to the micromanipulator allowing very accurate movement of the blade. The main variable was the width of the wounds. The width of the parallel cuts was barely larger than the width of the blade whereas perpendicular cuts caused relatively large tears in the cell layer. Due to this the wound areas and aspect ratios were noticeably different between the flat, parallel and perpendicular cuts. Perpendicular cuts caused low aspect ratio, relatively large wounds. Flat cuts created wounds similar to the perpendicular cuts; however, they were slightly smaller on average. Parallel cuts created small, high aspect ratio wounds.

To find out whether the wound shapes were caused solely by the topography or if it was a cell specific effect, monolayers of MG63 cells were cut using the same method. Images of the wounds formed are shown in Figure 69. The analysis of these cuts is shown in Figure 70.

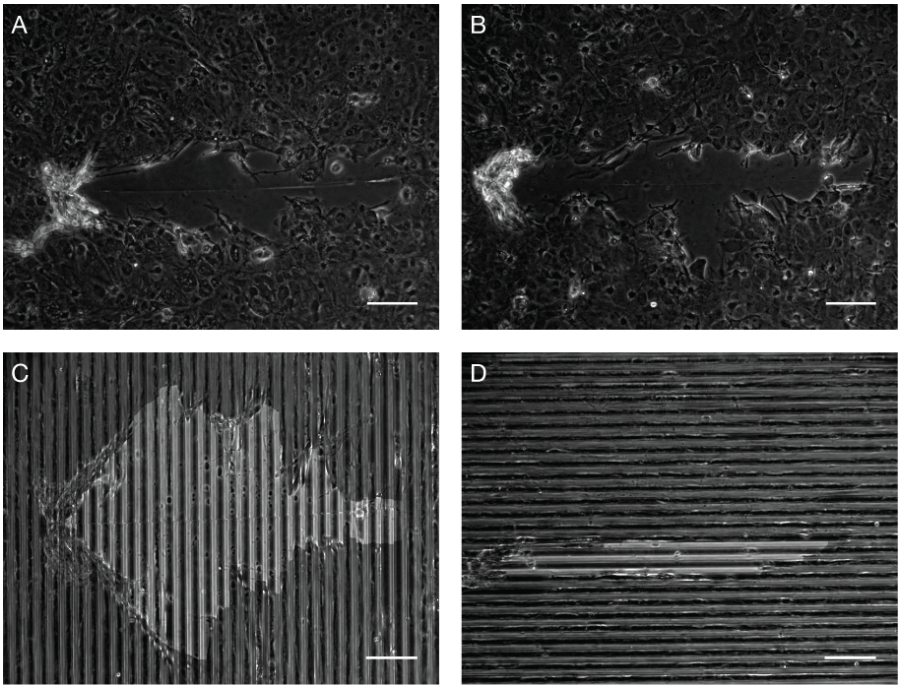

Figure 67: Wounds resulting from automated cutting, with an FST micro knife, of 10 day old astrocyte cultures grown on PDMS alignment devices. A) & B) Cuts on the flat areas of the devices. C) Parallel to the ridges. D) Perpendicular to the ridges. Cut direction was right to left. The wound areas have been highlighted in C & D. Scale bars are 100 µm.

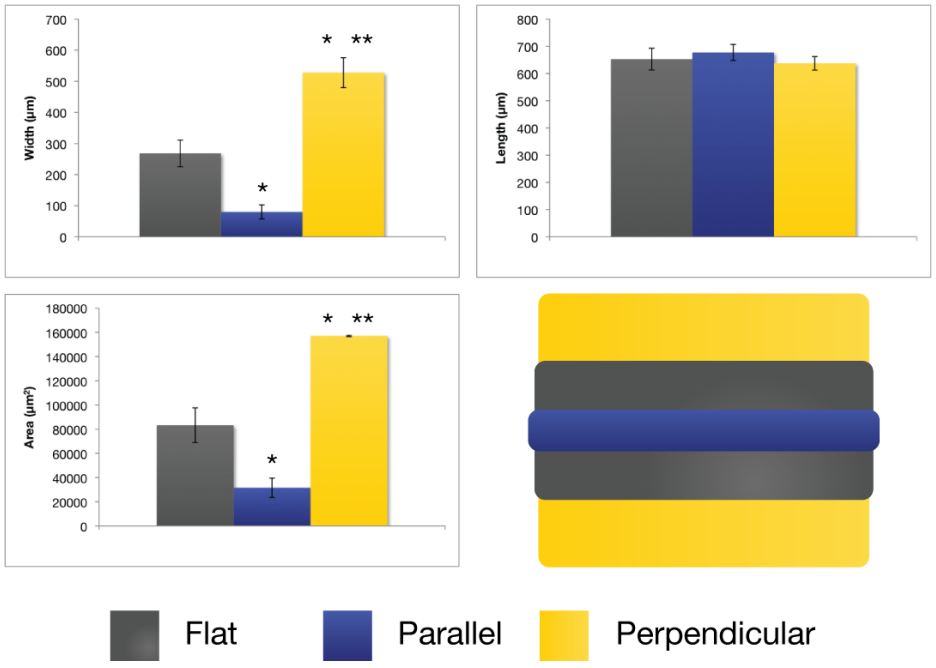

Figure 68: Analysis of wounds made to monolayers of astrocytes. Cuts were made as shown in Figure 67. The graphs show the width, length and area of the wounds formed by the different types of cut (n=3). Error bars show the standard deviation. An asterisk denotes significant difference ($P < 0.01$) from the flat control, a double asterisk show significant difference from the parallel cut. There was no significant difference between the lengths ($P > 0.05$). The graphic shows the relative average width and length of the wounds. The average aspect ratios were: Flat = 2.5:1, Parallel = 9:1, Perpendicular = 1.2:1.

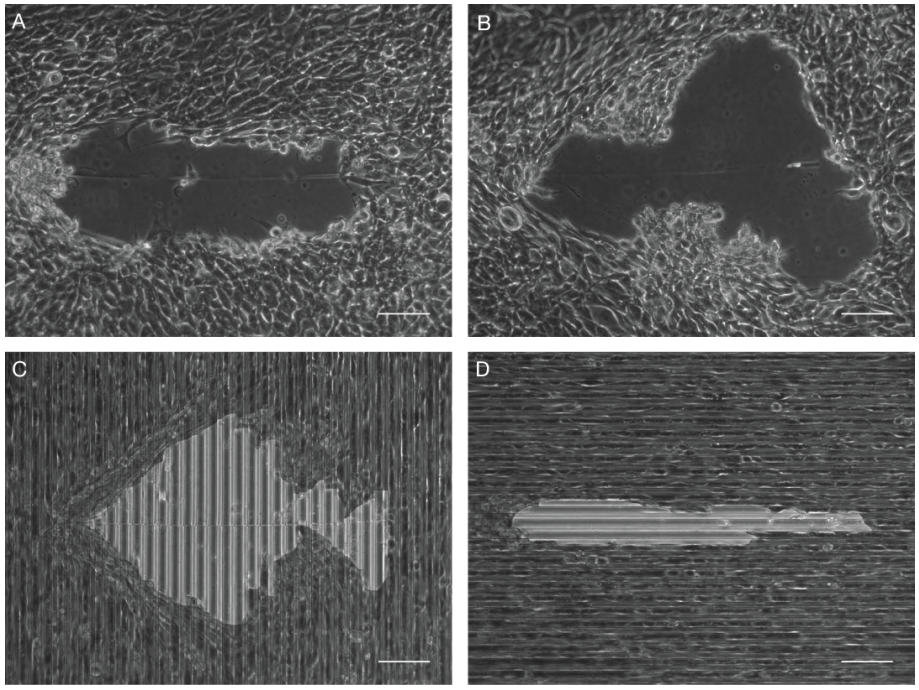

Figure 69: Cuts made to a confluent layer of M63 cells grown for 4 days on PDMS alignment devices. Cuts were made with an FST micro knife and the direction was right to left. A) & B) Cuts made to flat areas of the device. C) Cut made perpendicular to the ridges. D) Cut made parallel to the ridges. The wounds have been highlighted in C) & D). Scale bar are 100 µm.

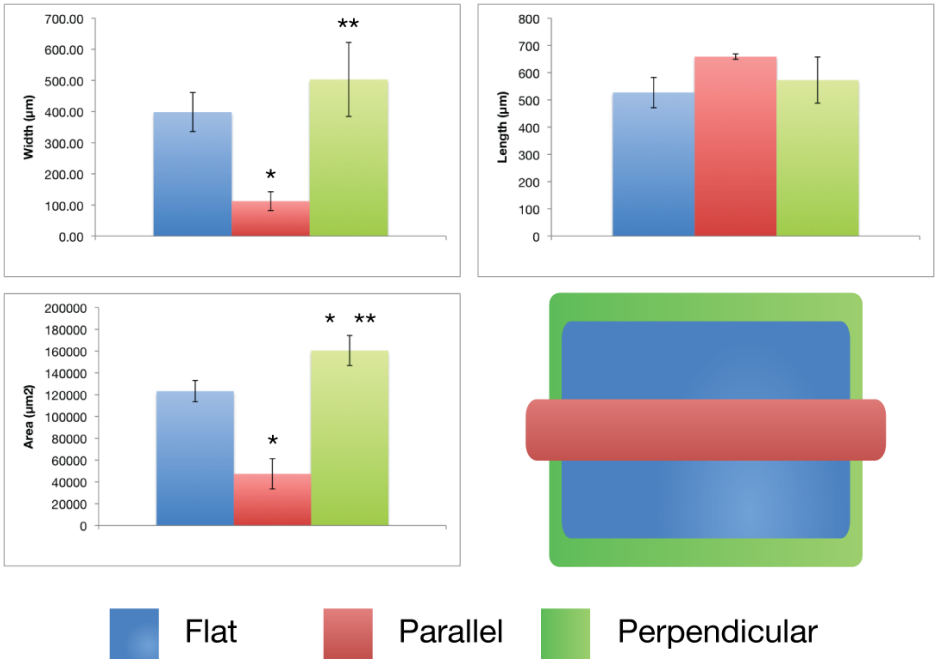

Figure 70: Analysis of wounds made to monolayers of MG63 cells. Cuts were made using the same method as the astrocytes, above. The graph shows the area, length and width of the wounds formed by the different types of cut (n=3). Error bars show the standard deviation. An asterisk denotes significant difference (P < 0.05) from the flat control, a double asterisk show significant difference from the parallel cut. The differnce in cut lengths was not significant (P > 0.05). The graphic shows the relative average length and width of the wounds. The average aspect ratios were: Flat = 1.4:1, Parallel = 6.2:1, Perpendicular = 1.6:1.

The MG63s and astrocytes formed very similar wound sizes and shapes. Full comparisons of the wounds are shown in Figure 71 and Figure 72. The only significant difference between the MG63s and the astrocytes was the area of the wounds on the flat regions of the devices. This was due to the MG63s developing a slightly wider wound whilst it stayed slightly shorter than those in astrocyte monolayers. However, the differences in length and width were not significant themselves. The length difference could be explained by 'pull back', an effect observed when the blade was withdrawn after cutting: after all cuts ~ 1 minutes was allowed for the cells to settle into place before images were acquired. During this period the displaced flap of cells on the leading edge of the wounds would slowly be pulled back into the cell free area. This was also observed in the astocyte layer but to a lesser extent. The difference is possibly due to higher tension in the MG63 layer when compared to the astrocytes. This would also explain the larger width of MG63 wounds, as a higher tension would cause more cells to be displaced by the blade. However, the ridges appeared to be countering this difference, as there was no significant difference in area for the parallel and perpendicular cuts. These findings led to the hypothesis that the cells were forming preferential mechanical connections longitudinally along the ridges. This would explain the large sheets of cells being torn from the substrate when cuts were performed perpendicular to the ridges.

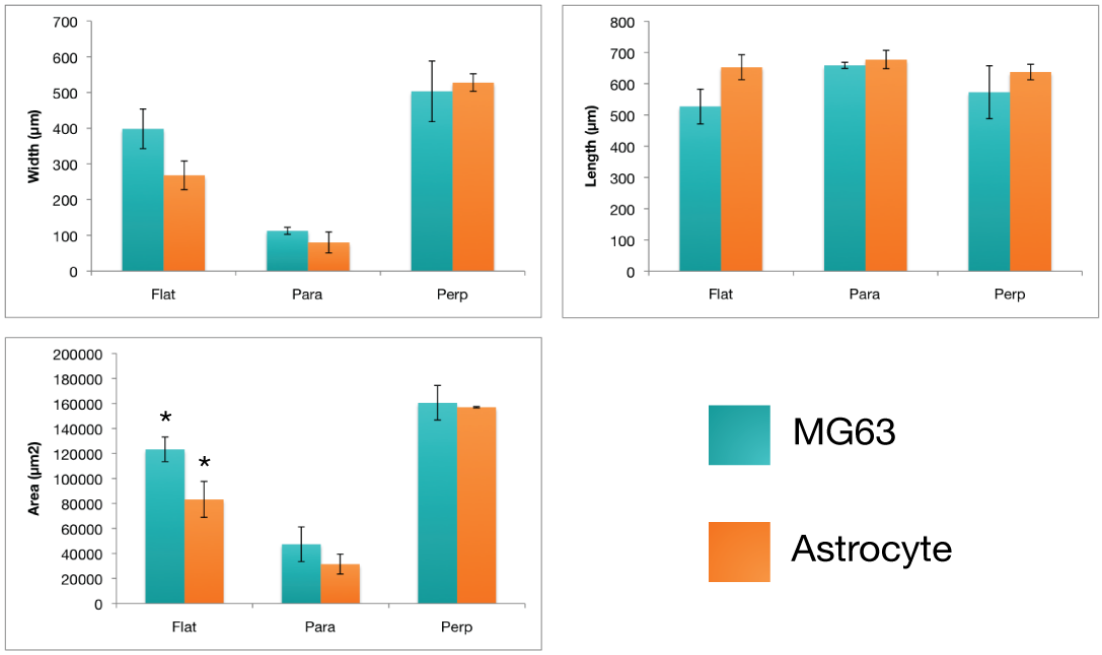

Figure 71: Graphs showing a comparison of wounds formed in layer of MG63 cells and astrocytes (n=3). The cells were grown on PDMS alignment devices. The length, width and area of the different wound types are shown. Error bars show the standard deviation. The only significant difference ($P < 0.05$), shown with an asterisk, was the area of the flat cuts. All other differences between the cell types were not statistically significant ($P > 0.05$).

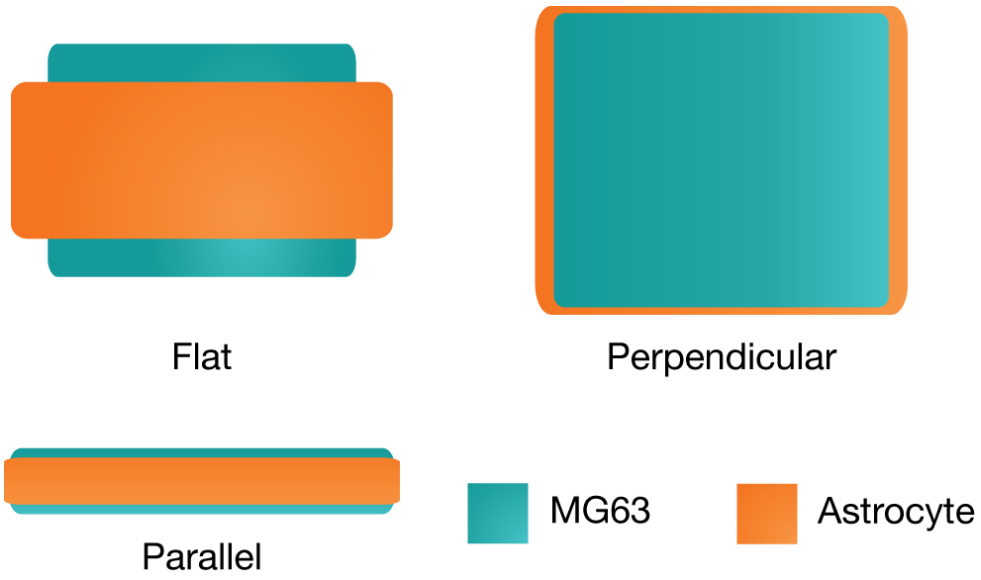

Figure 72: Graphics showing the relative average length and width of wounds made to MG63 cells and astrocytes grown on PDMS alignment devices.

4.2.3 Cytoskeleton Poisoning

To further develop this hypothesis, experiments were planned to investigate the role of connexins, cadherins and cytoskeletal elements in the establishment of the cell-to-cell connections on the ridges; and whether there were stronger connections along one axis of the cells when compared to the other. Actin was first investigated, as it is responsible for some of the mechanical stability of the cells. Glial fibrillary acidic protein (GFAP), vimentin and nestin were also of interest as they are intermediate filaments and play important roles in maintaining the mechanical stability of the cell.

Acrylamide destabilises the micro and intermediate filament network(Sager, 1989) and so provided a means to investigate how GFAP and actin were involved in the wound formation. The cells were to be treated with acrylamide and then cut to see if the wound shape changed. If similar wounds were formed after destabilisation of the filament network then it would be unlikely these networks were the cause of the asymmetrical connection strength.

To establish the required acrylamide concentration, monolayers of astrocytes were grown on PDMS alignment devices. They were then treated with acrylamide in their growth media for one hour at a concentration of 2, 4, 6, 8 or 10 mM. The cells were then stained for GFAP and actin. Micrographs of the stained cells are shown in Figure 73.

No difference could be seen in the GFAP and actin networks between the different treatments. It appeared that the treatment time was not sufficient and so a time course experiment was conducted. In addition to immunostaining, the treated cells were also cut with the micro knife to establish whether the treatment was affecting the wound formation.

Seven devices were immersed in growth media with 10 mM acrylamide. A control device was left untreated. Every half hour one devices was removed from the solution and transferred to CO_2 independent media. Flat, parallel and perpendicular cuts were then performed. The device was then transferred to fresh growth media while the other devices were cut. Once all devices had been cut, they were fixed and stained for GFAP. Graphs showing the wound areas and aspect ratios compared to the treatment time are shown in
Figure 74.

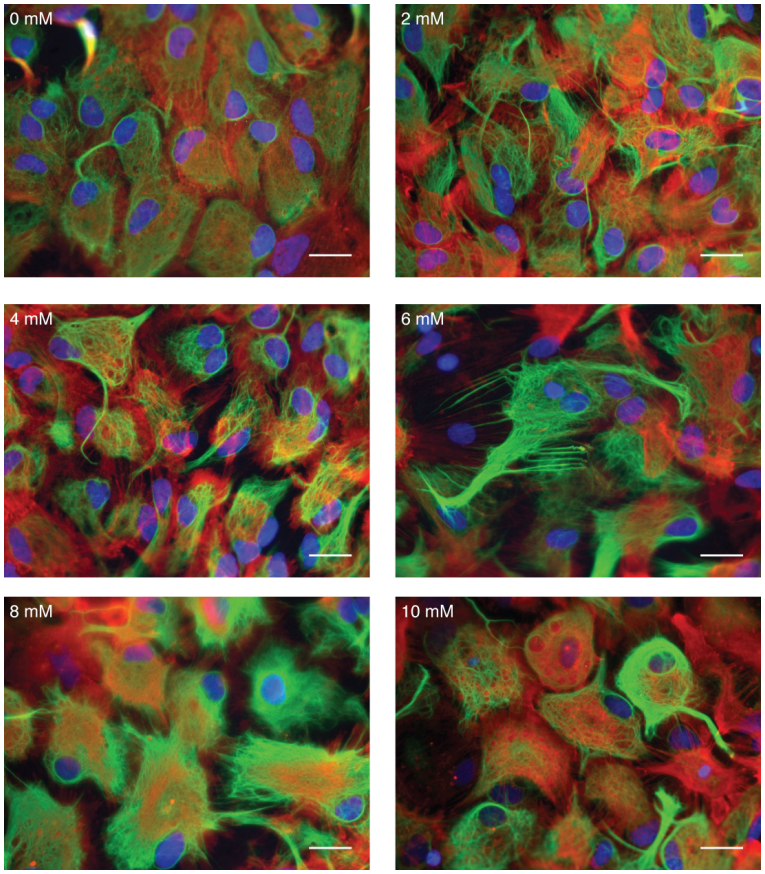

Figure 73: Astrocytes treated with different concentrations of acrylamide in their growth media and then stained for GFPA (green) and F-actin (red). The cells were grown for 10 days on PDMS alignment devices and were treated for one hour at the concentration indicated on each image. Scale bars are 25 µm. The treatment appeared to not affect the GFAP or actin filaments.

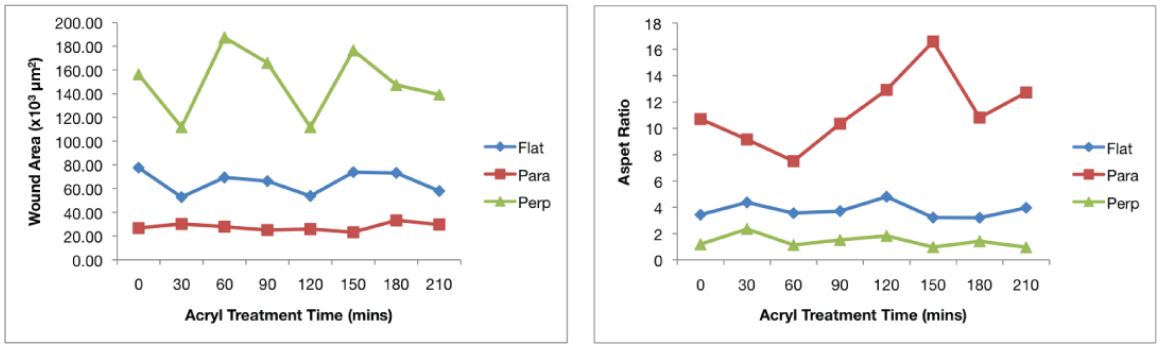

Figure 74: Area and aspect ratios of wounds formed in astrocyte monolayers vs. the treatment time in 10 mM acrylamide. The '0' time point corresponds to the control device. The acrylamide appeared to have no effect on the wounds formed in the astrocyte layers. n=1

The acrylamide treatment, appeared to cause no changes to the cells. In 2007 Holden et al (Holden and Coleman, 2007) showed that exposing astrocytoma cells to 10 mM of acrylamide for 4 hours significantly reduced GFAP expression. The 210 min treatment was close to this and so it appeared that some difference should have been seen at this time point. However, Holden et al had used 3 astrocytoma cell lines and only 2 of them had shown a difference at the 4 hour time point. Thus it was probable that a longer treatment time was required to have the desired effect.

4.2.4 Mathematical Model

It was proposed that the difference in connection strength between the two axes could be due to a difference in contact area between the cells. To test this hypothesis an idealised model of the cells was constructed.

From images such as those from Chapter 3 Figure 56 it could be seen that the nuclei tended to sit within the grooves between the ridges. It could also be seen from other images, such as those in Figure 69, that the cells formed confluent layers on the devices. From these observations the model of cells growing on ridges was created, shown in Figure 75 and Figure 76. Using the idealised cell model the following terms were defined:

A_f = Area of the face of the cell that can connect to another cell.
A_s = Area of the side of the cell that sits above the ridges and can connect to another cell.
W_c = Width of the cell including the portions above the ridges.

W_r = Width of the ridges and thus the width of the lower portion of the cell.

h_c = Total height of the cell.

h_r = Height of the ridges.

h_a = Height of the cell above the ridges.

L_c = Length of the cell.

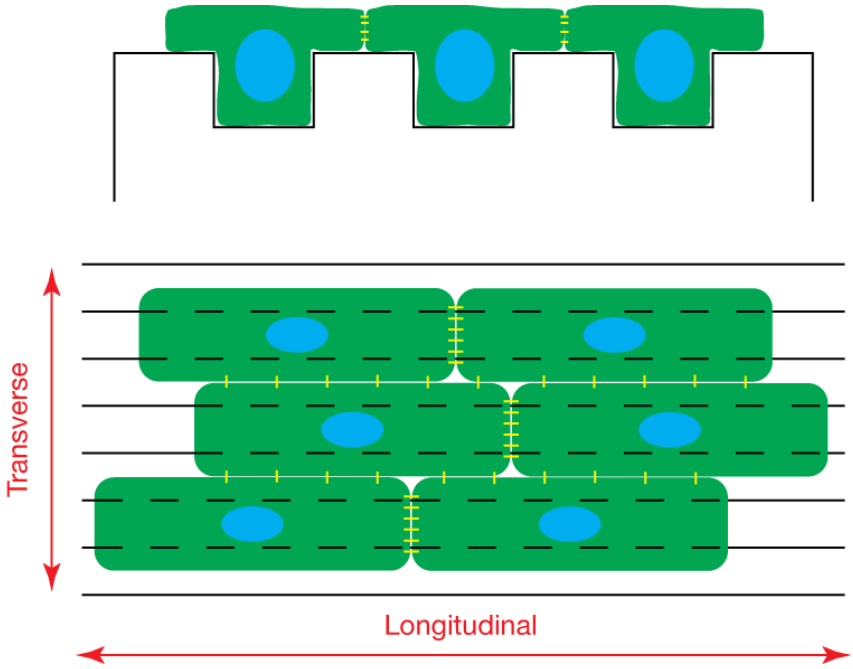

Figure 75: Sketch showing the top and side view of idealised cells sitting in the troughs between ridges and forming connections over the ridges. Blue ellipses represent the nuclei; green boxes are the cell bodies; yellow lines are cell-cell connections and dashed lines show where the ridges and grooves lie under the cell bodies. All cells were assumed to have the same dimensions.

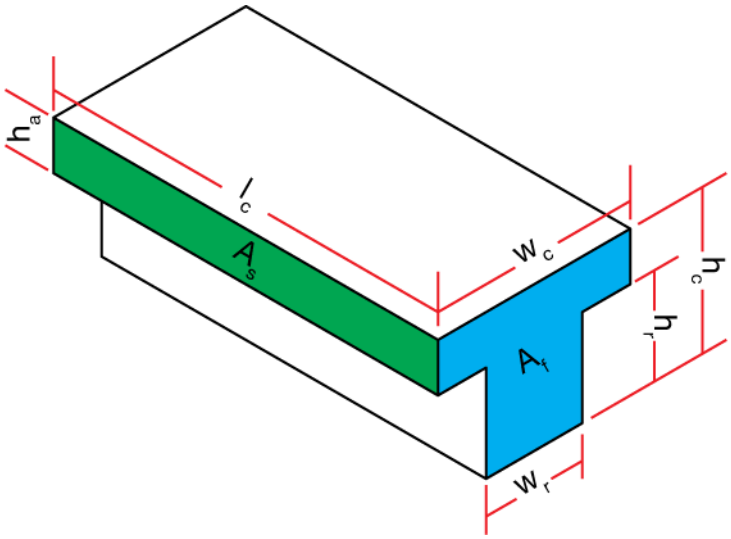

Figure 76: Model of idealised cell sitting in a trough between two ridges, showing the dimension defined above. The cell is shown in isometric view without the ridges.

From these it can be stipulated that:

$$A_s = h_a \times l_c$$
$$A_f = (W_r \times h_r) + (h_a \times W_c)$$

From the measurements discussed in Chapter 2 it is known that:

$$h_r = 4.2\ \mu m$$
$$W_r = 11\ \mu m$$

Assuming that the cells will evenly cover half of the width of the ridges then:

$$W_c = W_r + 13.9 = 24.9\ \mu m$$

To find a value for l_c some of the images shown in Chapter 3 Figure 56 where reanalysed. Images from the seeded side were imported into ImageJ, rotated so that the ridges aligned to the y plane and thresholded to highlight the nuclei. Individual troughs were then selected as regions of interest (ROI) and the x and y coordinates of the centre of each nucleus in the ROI were exported to Excel. The distance between each nucleus in the y plane was then calculated. 3 images were used and 5 readings were taken per images. Assuming that the cells evenly fill the spaces between nuclei gave the following result for MG63 cells:

$$l_c = 68.7 \pm 4.82\ \mu m$$

Substituting these known and calculated values in the area formulas gives:

$$A_s = 68.7\, h_a$$
$$A_f = 24.9\, h_a + 46.2$$

The value of h_a was unknown so final area values could not be calculated. However, to establish whether there was a likelihood of A_f being larger than A_s the following calculations were made.

$$\text{for } A_s = A_f$$
$$68.7\,h_a = 24.9\,h_a + 46.2$$
$$\therefore h_a = 1.05\ \mu m$$
$$\text{Thus}$$
$$\text{if } h_a > 1.05 \rightarrow A_s > A_f$$
$$\text{if } h_a < 1.05 \rightarrow A_f > A_s$$

As the average height for an MG63 cell on a flat surface is 20 μm (Shin and Athanasiou, 1999), it seems likely that h_a would be greater than 1.05 μm and thus A_s would be larger than A_f.

However this assumes that the cells would only contact one other cell on its longitudinal axis. This would be unlikely and it is probable that the cells have differing amounts of contact with neighbouring cells, as shown in Figure 75. This configuration could result in different contact strength between cells along the longitudinal axis. To ascertain whether this could result in a larger contact area per cell on the transverse axis than the longitudinal axis the following calculations where made. For any given cell (cell A) to be in contact with at least two other cells (cells B & C) and to have the minimum contact with each cell, and still form a confluent layer, then 50% of cell A's longitudinal side must be in contact with cell B and 50% of it must be in contact with cell C. Taking this into consideration and once again equating A_s to A_f, we obtain.

$$l_c = 34.35\ \mu m$$
$$\text{and thus}$$
$$h_a = 4.89\ \mu m$$

Once again, this number lies within the potential height of the cells above the ridge. This indicates that the strength of the cell – cell bonds is not due to a greater contact area on the cells' transverse axis. This still leaves two possible hypothesises; that the cells have a greater number of cadherin complexes on its transverse axis; or that there are a similar number cadherin complexes on both axis but they cluster closer together on the transverse axis compared to the longitudinal axis. These hypothesise and potential experiments to test these hypotheses are further discussed in Chapter 5.

4.2.5 Manual Vs. Automated Cuts

The automated cutting method was developed to minimise potential variability in the wounds created by manual cutting. To compare the reproducibility of the two cutting methods, MG63 cells were grown on paired sets of alignment devices. One set was cut with the micromanipulator while the other was cut by hand. Three paired sets were cut in total. Images comparing the resultant wounds from automated and hand made cuts are shown in Figure 77; analysis of the wounds is shown in Figure 78; and graphics showing the relative sizes of the wounds are shown in Figure 79.

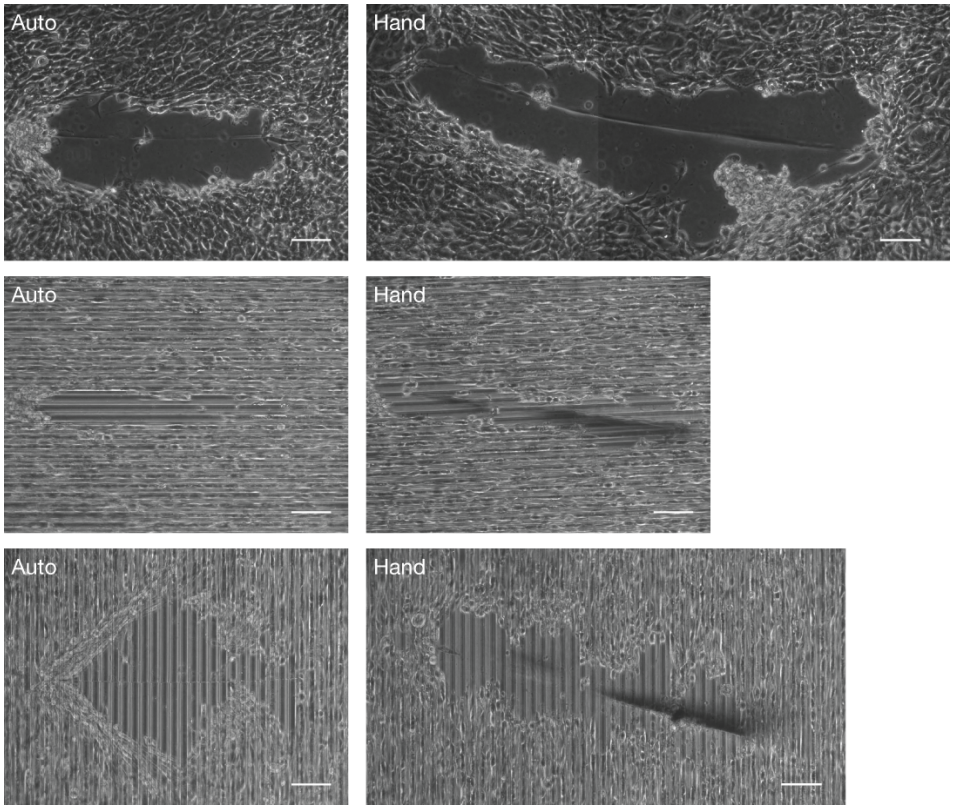

Figure 77: Wounds formed in layers of MG63s after cutting by the automated method and by hand. The cells were grown on PDMS alignment devices. Cuts were made on flat areas of the devices (top), parallel to the ridges (middle) or perpendicular to the ridges (bottom). Scale bars are 100 µm.

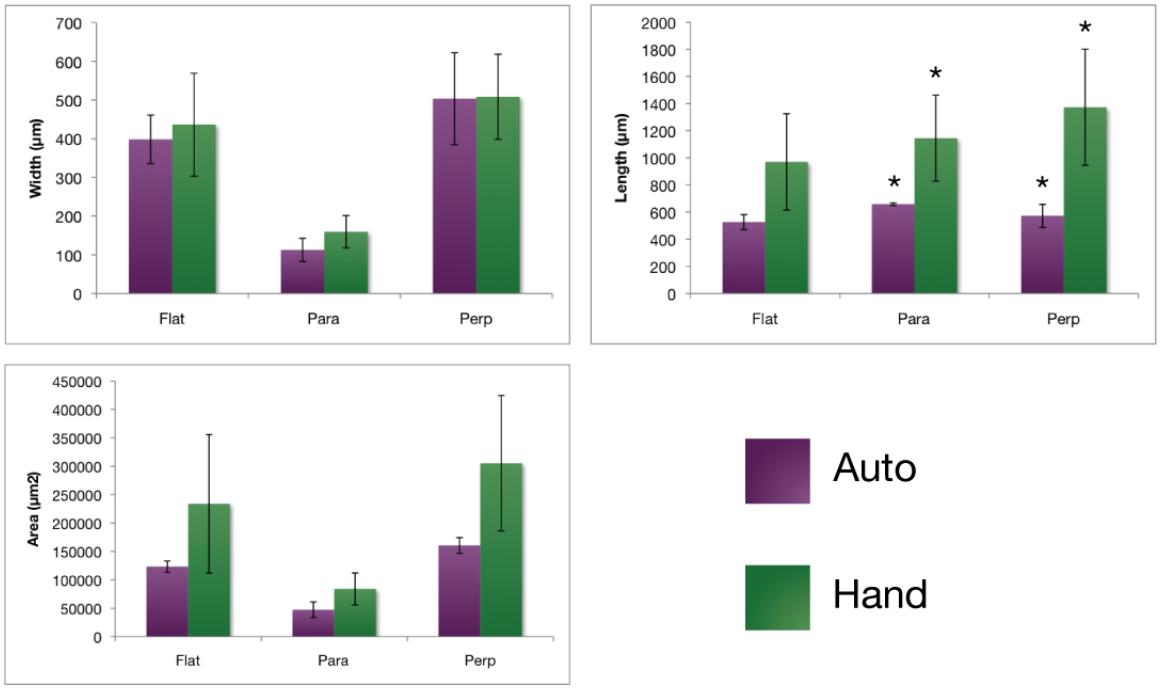

Figure 78: Analysis of wounds made with the automated cutting method or by hand to confluent layers of MG63s (n=3). The cells were grown on PDMS alignment devices and were cut perpendicular or parallel to the ridges, or on the flat regions of the devices. Error bars show the standard deviation. Significant differences (P < 0.05) between the hand and auto cuts are shown with an asterisk.

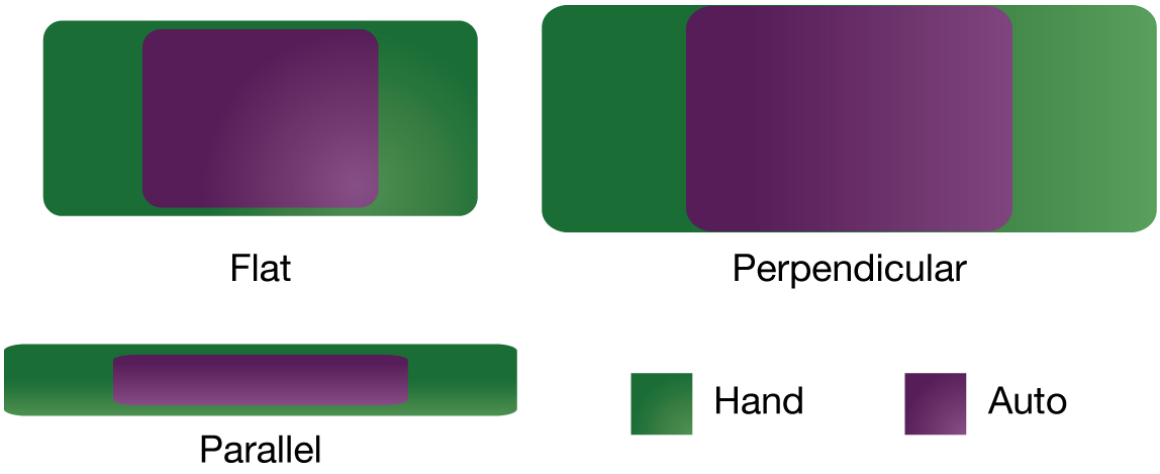

Figure 79: Graphics showing the relative average length and width of wounds formed by cuts made by hand or with the automated method to layers of MG63s.

Wounds created by hand were both longer on average and more variable than those caused by automated cutting. This is a result of the difficulty in controlling the cut length by hand. There was similar difficulty in making the cuts exactly parallel or perpendicular to the ridges. However, the width of the hand made wounds was consistent with those caused by automated cutting. This suggested that there was a maximum wound width that was

independent of the length. It is also worth noting that, like the automated cuts, the manual cuts had a significant difference ($P < 0.05$) between the width of the parallel wounds and the flat and perpendicular one, but the was no significant difference ($P > 0.05$) between the flat and perpendicular wounds.

This system of automated cutting provided several advantages when compared to manual cuts. It created wounds of a consistent area and aspect ratio. The cuts could be performed concurrently with microscopy so live images of the wound formation could be obtained. The micromanipulator allowed the blade to be manoeuvred with an accuracy of 1 μm and all aspects of the blades positioning (speed, angle, etc.) could be controlled. This accuracy allowed very small wounds to be easily created. With practice up to 3 cuts could be performed and imaged within 15 minutes.

However, the automated method did have a couple of disadvantages. Firstly, the cells had to be moved out of their normal culture media and placed into CO_2 independent media during cutting. This may have affected their response to wounding. However, on average the cells only spent ~ 20 mins in the media and during this time were on a heated stage. Secondly, the cuts were performed in a non-sterile environment, as the microscope stage did not have an environmental control unit. Despite this, no signs of infection were seen when the cells were put back into culture after wounding.

4.2.6 Neuronal Cutting

The cutting method was further developed by the cutting of neuronal cultures, in collaboration with Paul Turko (supervised by Prof. Stuart Cobb). Hippocampal neuronal cultures were obtained from p0-2 male and female Wistar rat pups. Cultures of neurons were seeded on a glass slide either side of a ~ 2 mm thick piece of PDMS. After allowing the cells to attach to the surface the PDMS was peeled from the surface, leaving a gap between the two cultures. The cultures were then allowed to grow for 10 – 12 days. During this time a dense field of axons formed in the gap. Some soma and glial cells also migrated into the gap, however, areas were still present that allowed cutting of only the axons. Cuts were then performed on three devices and wounds were made to the soma and the axons, the results of which are shown in Figure 80. A comparison of the results with the cuts performed on flat areas with the MG63 and astrocyte cultures is shown in Figure 81.

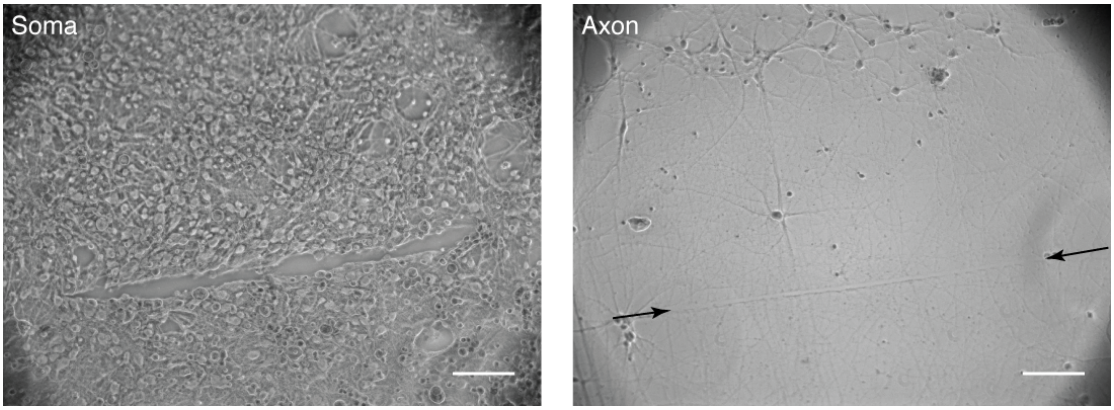

Figure 80: Wounds resulting from automated cutting, with an FST micro knife, of neuronal cultures grown on glass slides. The left-hand image shows a cut made to the soma. The right-hand image shows a cut made to the axon field, which was mainly clear of cell bodies. The arrows on the right-hand image indicate the wound area. Both cuts resulted in a wound comparable to the width of the blade. Cut direction was right to left. Scale bars are 100 µm. Cultures kindly supplied by Paul Turko.

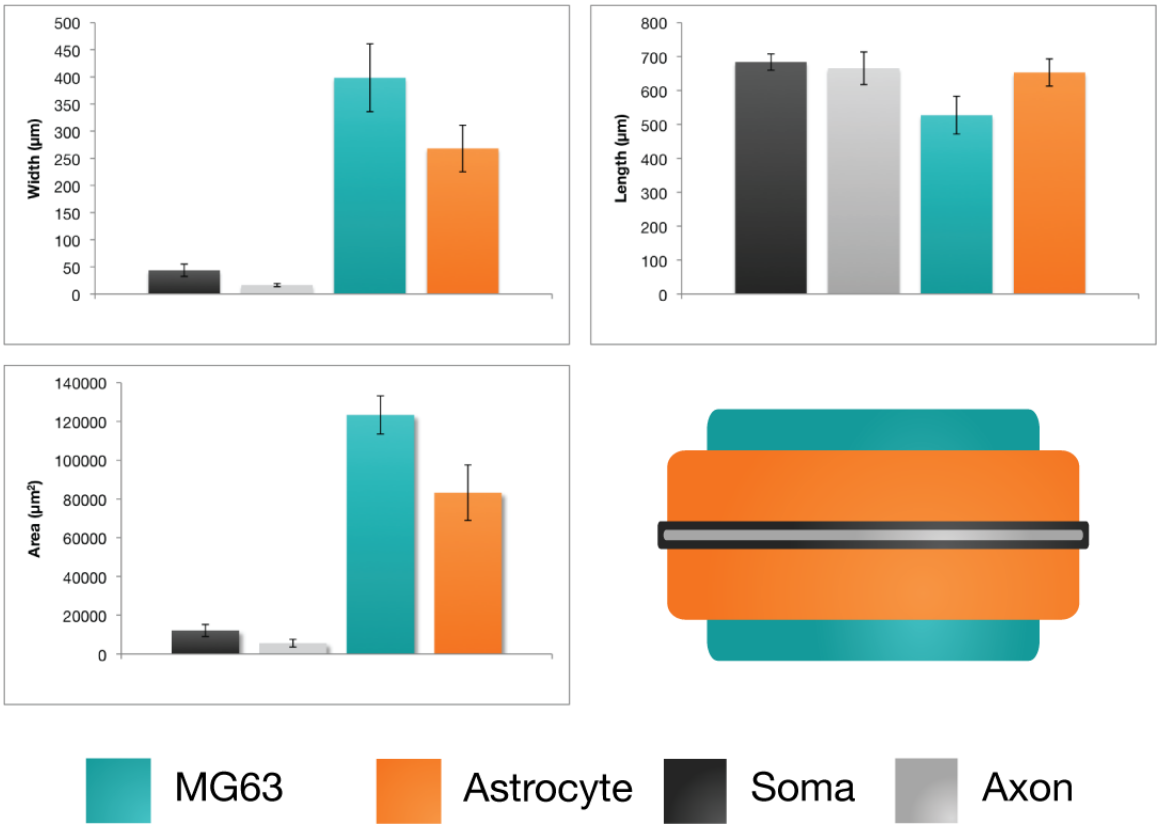

Figure 81: Comparison of wounds made to the soma and axons of neurons, monolayers of astrocytes and MG63. The graph shows the length, width and area of the wounds formed in the different cell types (n=3 for MG63 and astrocytes, n=1 for neurons). Error bars show the standard deviation. The graphic shows the relative average area and aspect ratio of the wounds. The average aspect ratios were: Soma = 32:1, Axon = 65:1, MG63 = 3:1, Astrocyte = 2:1.

These results suggested that the connections between somata are a lot weaker than those between MG63s or astrocytes. Thus wounds caused to astrocyte monolayers could result in significantly larger damage area when compared to neurons. This could mean that large amounts of damage caused to the CNS are actually due to secondary tearing effects within the astrocytes causing additional damage to the neurons around them. However, more research is required to further investigate this.

Chapter 5

General Discussion

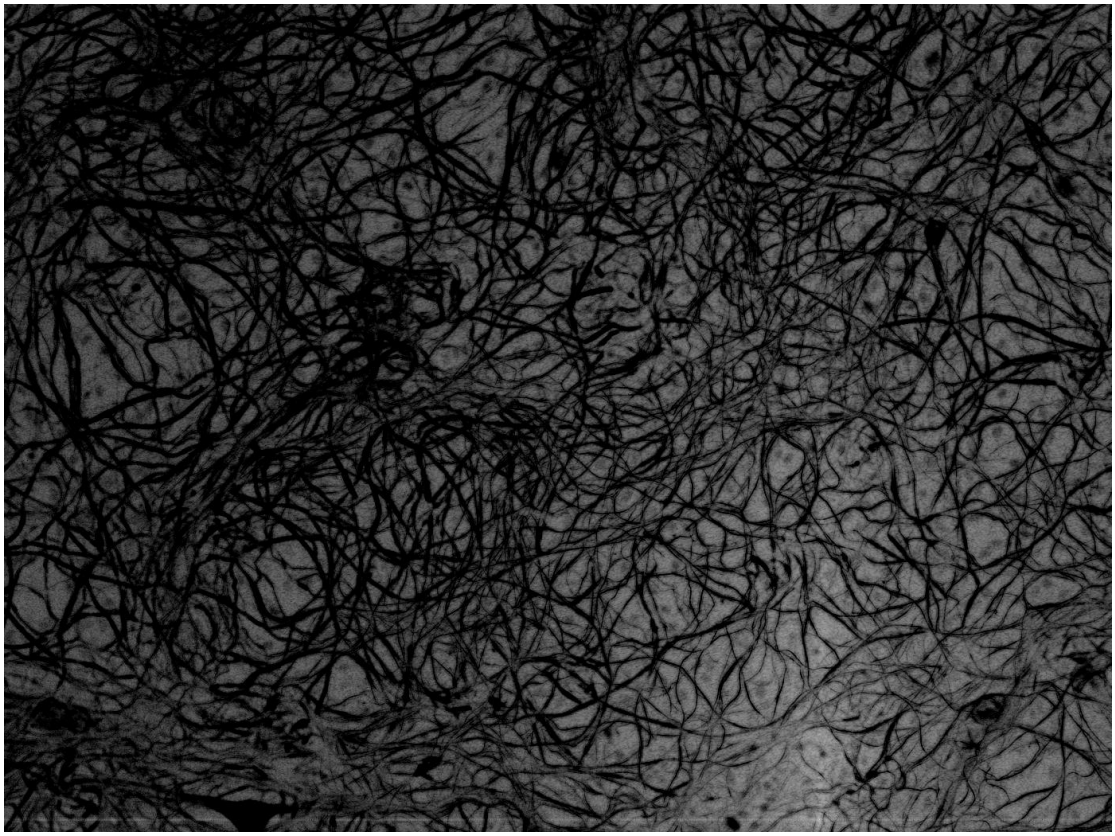

5.1 Project Goals

The project had two main goals, to create a device that could align and contain neuronal cells; and to develop a method of creating reproducible wounds within a cell layer. The first goal was further divided into three sub-goals; to create a hospitable environment for the cells; to align the axons into parallel lines; and to contained the soma to a predefined area. These goals were broadly met but each merits discussion in its own right.

Ensuring biocompatibility of the device was a fundamental goal of the project, as a lack of viable cells would clearly negate any further use of the device. Treating the device surfaces with PLL allowed cultures to grow for more than 28 days. Myelination on the devices was poor even after 40+ days, a time when the effect of other materials that delay myelination can be overcome (Donoghue et al. accepted in Tissue Eng and Regen Med). It is probable that the astrocytes were entering a reactive state, preventing full myelination from occurring.

One of the most important roles of the device was to pattern out the axons into parallel lines to resemble their arrangement in the spinal cord. The 12.5 µm grooves caused the greatest alignment of axons to the topography and were used in the final device. In comparison to Sorensen et al. (Sorensen et al., 2007), on which this work was based, significant differences were found between the 12.5 µm grooves and 25/50; whereas Sorensen et al. did not see significant differences between these groups. This may have been caused by the use of a different material, PDMS vs. PCL, or could have been due to the difference in the method of analysis used. Sorensen et al used a subjective method of volunteers assigning an alignment score based on their judgment whereas a computational method based on a MATLAB program that identified axons and calculated their alignment, using a least squares ellipse fit method, was used here.

The data presented here is in opposition to the work of Lietz et al.'s (Lietz et al., 2006), who found no difference in dorsal root ganglion neurite alignment on grooves with widths ranging from 2 – 100 µm. As a different substrate material and the same culture system as Sorensen et al. was used, this supports their conclusion about Lietz et al., that the origin of the neuronal cells can have an affect on their alignment abilities/conditions. Additionally it is also worth noting that culture time could also play a factor in this discrepancy, as a 28 day time-point

was used here and Sorensen et al. used a first time-point of 7 days, while Lietz et al. measured alignment after 2 days.

A wide variety of groove dimensions have also been reported to align neurites (Hoffman-Kim et al., 2010). We will look at a couple here that highlight the complex nature of the variables involved in neurite alignment. Yao et al. (Yao et al., 2009) grew PC12 cells for 7 days on PLGA surfaces with 5 or 10 μm wide, 2-3 μm deep grooved topographies. They found that the 5 μm wide grooves produced the greatest alignment. Sun et al. (Sun et al., 2010) used PCL films with 5, 10 or 20 μm wide, 3 μm deep grooves. They grew NG108-15 cells on these microtopographies for 6 days and did not find a significant difference between the 5 and 10 μm ridge but did find one between these and the 20 μm ridges. Even though both studies used highly similar structures they found different degrees of alignment. It is likely, as with Sorensen discussed above, that the cell lines have different responses to the topographies. This also shows that even if the alignment properties are know for a certain cell line/device combination, if the parameters are changed then a new alignment test may be required.

It is also worth noting that all of the studies mentioned here used different techniques to quantify alignment, which makes direct comparison of alignment scores impossible. A widely accepted method of scoring would help to unify the data from different groups and aid in discussion.

One aspect of axon alignment noticed in this project was that it appeared that the majority of ridge crossover by axons occurred near clusters of cell bodies. This was likely due to axons sprouting from the soma at an oblique angle to the ridges and growing in its original direction for a short period of time before turning to align to the ridges. These are similar to the observations of Rajnicek et al (Rajnicek et al., 1997). In their study they recorded xenopus spinal neurites turning to grow perpendicular to 130 nm deep and 1 μm wide grooves; 46% of neurites turned to align perpendicular to the grooves, while 16 % turned to align parallel and the remaining neurites did not turn from their original course. It should be noted that xenopus neurites preferentially aligned perpendicular to the ridges unlike the rat spinal neurons used in this project. As can be seen in ridge only images of Figure 61, the majority of axons appeared to turn to align to the ridges, although this was not quantified. This supports the desire to make sure the soma were contained to a predefined area so that they would not confuse experimental data e.g. quantifying alignment of axons around a wound site would be

complicated by axons sprouting perpendicular to the ridges. Ridge crossover was also seen around the pillars, which is discussed later in this section.

The use of pillars to contain individual neurons was developed by Zeck and Fromherz(Zeck and Fromherz, 2001), an adaptation of this method to contain large groups of soma was trialled in this project. Placing the cells in a square 'corral', which had two solid walls and two pillar rows, was first attempted. It became apparent that seeding the cells into the corral would be impractical and so using single and multiple rows of pillars bisecting the device was investigated. This alleviated the seeding problems, however, it was shown that rows of pillars were not required to contain the soma. Seeding the cells into Ibidi Culture Inserts allowed them to be placed on a predetermined area on the device surface from which they did not stray.

However, the pillars had an effect on the movement of other cell types. The 5 row 6 gap provided the best containment for astrocytes and suggested that smaller gap sizes may improve containment further. Several experiments (Irimia et al., 2007, Fu et al., 2012) have show that small numbers of cancer cells can squeeze through channels 4 μm wide by deforming their nucleus a small amount. Cancer cells are known to be softer than normal cells (Guck et al., 2005) so it is possible that gaps of ~ 4 μm may stop astrocytes or MG63s from crossing.

Another factor that might affect cell containment is the spacing between rows of pillars. Several studies have looked into the influence of pillar dimensions and spacing on cell attachment and proliferation (Kolind et al., 2010, Turner et al., 2000). It was found that pillar dimensions had no significant affect on proliferation while spacing was significant. However, these studies used far smaller pillars and spacings than those used in this project, with maximums at 6 μm each.

Miyoshi et al. (Miyoshi et al., 2010) used interlacing grooves to create pillar-like structures which discouraged cells from crossing them. In their paper, epidermal keratocytes approached the interlacing grooves from a flat surface and would turn back on their course once they encountered the structures. This was most effective on 1.5 μm wide, 20 μm deep grooves with a 5 μm spacing. This arrangement effectively created 5 μm wide square pillars with 1.5 μm gaps between them. This suggests smaller spacing between the pillars would not only help to prevent cells from squeezing between the pillars but would also dissuade cells that had climbed on top of the pillars from proceeding further.

Although the pillar rows were not required for the containment of the soma they showed potential in slowing the spread of other cell types. Using this property, the device could be used to model cell interactions without allowing direct contact between the different cell types. For example, this would allow modelling of interactions between the CNS and PNS without having to model the complex arrangement of meninges that surround the CNS.

Even thought the pillars were not necessary for soma containment, they had a significant effect on axon alignment. The presence of even a single row of pillars caused a decrease in alignment to the ridges as the axons turned when they encountered the pillars or weaved through them. There was a greater decrease in alignment as the number of pillar rows increased. This is likely due to the increased probability of an axon coming into contact with a competing guidance cue to the ridges and deciding to turn. This effect is comparable to that observed by Dowell-Mesfin et al. (Dowell-Mesfin et al., 2004), where arrays of square pillars with different gap sizes were used to affect axon alignment. The neurons were seeded onto the pillar arrays and it was found that smaller gaps size cause the cells to turn and align to the pillars. An example of this is shown in Figure 82. The devices used in this project did not have as pronounced an effect possibly due to competing guidance cues from the ridges, pillar shape or the larger gaps sizes. Potential uses for the turning effect and combined ridge and pillar structures are discussed later in this chapter.

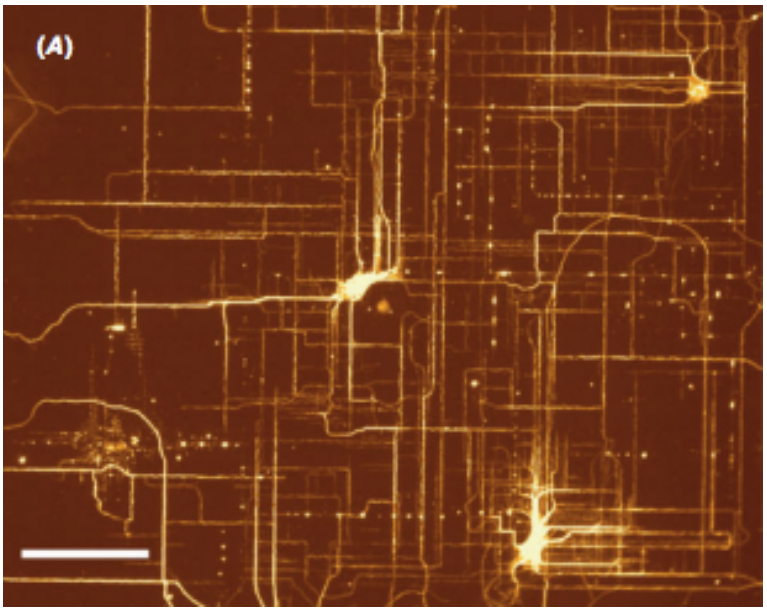

Figure 82: Dowell-Mesfin et al.'s pillar array (Dowell-Mesfin et al., 2004) causing axons to align to the pillars and perform 90° turns. The pillars were 2 µm wide and had gaps between them of 1.5 µm. The cells are stained for βm-tubulin and the scale bar is 100 µm.

5.1.1 Cell Wounding

A reproducible and precise wounding method was developed to allow the instantaneous effects of incisions to be studied. The method allowed a wide variety of parameters to be controlled including blade angle, cutting speed and cut depth. The use of a micromanipulator allowed the blade to be positioned with an accuracy of 1 μm and for the cut to be made in the exact same fashion every time. A full comparison of this method to other existing methods can be found in the section below.

The majority of literature on CNS wounding deals with the die back of the cell layer post wounding, or the regrowth of cells into the wound site. There is very little literature that deals with the instantaneous effects of the wounding e.g. how the cells are removed from the surface e.g. by being pulled by their neighbours. The cutting method developed here allowed these instantaneous effects to be studied. It also allowed the effects of different blades, topographies and cells types on the wound dimensions to be investigated.

5.2 *In vitro* SCI models and Wounding Method Comparisons

5.2.1 Comparison to Other *In Vitro* Models

In their 2010 review paper Leach et al (2010) defined three key criteria for *in vitro* models of spinal cord injury. These were: "(1) biologically-relevant scaffolding materials; (2) presence of most or all of the relevant cell types, namely neurons, astrocytes, microglia, endothelial cells and meningeal fibroblasts; and (3) appropriate spatial arrangement of the scaffolding materials and cells."

The device developed during this project meets all of these criteria as follows. (1) PDMS was modified to allow PLL to bond to the surface and create a hospitable environment for the spinal cord cells. PLL is a commonly used surface coating within biological research. It was also shown that this coating would remain on the device surface over extended culture periods. Various other surface coating could be applied to the PDMS if required. (2) The culture system developed by Prof. Sue Barnett's group (Sorensen et al., 2008) was grown on the devices and provided every cell type present within the spinal cord. (3) The devices patterned the axons in parallel lines while the soma remained within a pre-defined area. This gave a spatial arrangement similar to that of a spinal cord.

As discussed in Chapter 1, there are multiple existing *in vitro* models of spinal cord tissue (Abu-Rub et al., 2010, Robins and Fehlings, 2008), or SCI, which have various advantages and disadvantages. To reduce the number of models to analyse, and as they are most relevant to this project, we will only concern ourselves with the model described in the "devices" category in Chapter 1. These models are compared to the model developed in this project using the criteria laid out by Leach et al. (Leach et al., 2010).

First we will look at East et al.'s (2010) 3D gel model. This model meets all of Leach's criteria. (1) It uses collagen as a scaffolding material, which is a major component of the ECM. However, it should be noted that collagen does not comprise the majority of the environment

within the spinal cord, as it does here. (2) Neurons, astrocytes, microglia and fibroblasts are all present. (3) The stretched collagen gels provide alignment for the astrocytes and thus the axons too, the 3D nature of the gels also allows a greater mimicry of the *in vivo* environment. However, this model has several drawbacks related to the cellular and physical aspects. Firstly, there is no mention of oligodendrocytes or myelin so it is unclear whether myelination is possible within this model. Secondly, due to the model being 3D, a confocal microscope is required to acquire images of anything but the very surface of the gel. Thirdly, alignment varies throughout the gel, with cells in the middle of the collagen being more aligned that those towards the edges. Finally, each gel requires its own mould; this means that a great number of moulds or ample preparation time would be required to produce gels for a large experiment. This model creates a complex 3D culture that comes closer to mimicking the *in vivo* environment, however, it cannot match the ease of production and analysis of the model presented in this thesis.

Taylor et al.'s (2005) microfluidic device broadly meets Leach's criteria: (1) the device is made of PDMS and it is bound to a PLL coated coverslip, on which the cells grow; (2) only neurons and oligodendrocytes were present in the work presented, however, other cells types could be introduced into the chambers; (3) the device isolates the soma and patterns out the axons within the guidance tunnel. This model allows rapid testing of drug compounds and their effects on neurite outgrowth. However, axons are only aligned when they are within the channel between chambers as no guidance cues are present within the chambers themselves. This design is also not as suitability for injury testing when compared to the device presented in this thesis. Taylor et al's device only aligns the axons within the tunnels and their injury method, vacuum aspiration, appears to only injure the unaligned axons within the axon chamber. The sealed nature of the tunnel also prevents any mechanical injury being inflicted upon the aligned axons. It is also not clear whether the oligodendrocytes could migrate into the tunnel and myelinate the axons within.

Finally Delivopoulos et al.'s (2009) chemically patterned Si chips. Once again, this model meets the key criteria for an *in vitro* model. (1) Various methods were used to analyse the surface of the parylene and it was concluded that vitronectin was most likely responsible for the biocompatibility and differential adhesion. Vitronectin is a common ECM protein and so can be said to be biologically relevant. (2) Dissociated hippocampal cells were cultered on the chips so it is probably that most of, if not all, required cell types were present. (3) The chips

patterned the cells into strips creating a parallel architecture similar to that of the spinal cord. The technique used to fabricate the chips could easily be combined with other microfabrication method and the authors specifically state that electrodes could be incorporated into the surface of the chips to allow electrical readings to be made. As the chips are flat, open-faced devices they allow easy access to the cells for wounding/treatment and analysis. However, the chips are made of silicon and thus opaque which limits their flexibility with regards to microscopy. The chips are not described as reusable and so new chips would have to be fabricated for each experiment. This would greatly increase the cost and preparation time when compared to the soft-lithography technique used in this thesis. The striped patterning isolates each strip from the next by a relatively large distance (≥ 100 μm). This would likely cause changes in tension within the cell layer when compared to a monolayer of cells; the tension, as discussed earlier, plays an imported role in wound formation (LaPlaca et al., 2007).

It is also worth discussing the suitability of these models, and the PDMS device developed in this project, for testing the various treatments currently being developed to treat SCI. All of the devices could easily be used to test neural cell transplants apart from East et al.'s model. This is due to the fact that the cells must be implanted in the 3D during its creation. This would preclude cells from being introduced after a wound had bee inflicted. Ibidi Culture Inserts could be used with the PDMS model to seed transplanted cells directly around the wound site. This method would probably also work with Delivopoulos et al.'s model but it is unknown if this would affect the chemical patterning. Cells could be seeded into the chambers of Taylor et al.'s microfluidic device, however, the transplanted cells might not be able to reach the uninjured aspects of the axons confined in the connecting channels.

Testing of neurotrophic factors and the suppressions of growth inhibitors is possible on all of the models, with the microfludic device being designed specifically for this type of treatment. Although the 3D gel's permeability to compounds is not specifically mentioned it can be assumed that this would not be too much of a problem as nutrients from the media and the various compounds used in immunocytochemistry were capable of reaching the cells. Both the PDMS and chemically patterned devices allow ready access to the cells and thus easy treatment of them.

Axonal guidance techniques for wound healing are somewhat more difficult to use with these models as a lot of the techniques required topographical or chemical patterning of a substrate,

which two of these model already have. However, the optical and electrical guidance methods can be applied to most of these models. Electrodes could be added to the surface of any of the devices or inserted into the gel to allow testing of electrical fields ability to aid regeneration. Optical guidance should be possible on the PDMS, microfluid and chemically patterned devices as they are all capable of fitting under a microscope. However, it is unclear whether focusing a laser onto growth cones within a 3D gel would be possible.

In conclusion, when compared to other *in vitro* models of spinal cord tissue, the device presented in this thesis does not create as complex an environment as some and lacks chemical isolation. However, this lack of complexity allows the device to be inexpensively and rapidly manufactured. The device also allows ready access to the cell layer for manipulation and analysis; the analysis also does not require any specialised instruments. In addition, minimal training is needed to allow fabrication of the device once a master is obtained. The PDMS device is also suitable for testing all of the current treatments for SCI being trialled.

5.2.2 Comparison of Wounding Methods

As discussed in Chapter 1, there are a great number of methods available to induce injury both *in vivo* and *in vitro*. We will compare the method developed here to the five *in vitro* methods previously described in the models section of Chapter 1. A direct comparison of the wounds formed is impossible as there is no universal system of wound characterisation used across all the literature so the methods will be compared by looking at four criteria: (1) reproducibility, (2) ease of use, and (3) ability to view the cell layer during wounding. The last criterion is included as one of the aims of the project was to study the instantaneous effects of wound formation.

First we will compare the automated cutting method with the criteria laid out above. (1) As shown in chapter 4, reproducible wounds were created. The length of the wounds was very precise, while there was a small amount of variability in their width. (2) The control system for the micromanipulator consisted of a joystick and a few buttons. Moving the manipulator was intuitive and adjusting variables was a simple process. (3) As the micromanipulator was attached to the microscope, all stages of the wounding process could be observed. With the use of the microknife, only a very small area under the blade was not visible and image distortions around the edges of the blade were minimal.

Fayaz and Tator's (2000) impactor method: (1) The impactor produced wounds with a width comparable to that of the impactor tip 100s of μm with an SEM of ± 15 μm, which can easily be classed as reproducible. (2) To inflict injury all that was required was for the culture dish to be placed under the impactor and for it to be turned on. (3) The impactor needed ample room above the culture dishes to operate; this would make it difficult to integrate into a standard microscope setup. Even if a scaled down microscope friendly version was produced, it is likely that the impactor would obscure the cells and the jarring of the impact may knock the image out of focus. Additionally, this method lacks precision and could only be used to inflict injury to entire sections of a culture. In summary this is a cheap and easy method of inflicting contusion injuries to large areas of a culture but lack precision and would be unlikely to be suitable for mid-injury viewing.

Magou et al.'s (2011) stretch injury method: (1) Reproducibility was good at low pressures but became poor at high pressures. They concluded that this was due to inconsistencies in membrane thickness. Homogeneity within a material will be an important factor for consistent results when dealing with and substrate deformation based injury model. (2) The set up of the pressure regulation system is relatively complex when compared to other injury methods discussed here. However, inflicting the injury itself only required the plate to be mounted on the rig and the appropriate setting to be entered into the LabVIEW control program. (3) Due to the nature of a stretch injury it would be hard to keep individual cells or groups of cells in focus during the injury as the substrate has to move. Although such an injury method would prove unsuitable for the project described in this thesis, Magou et al's method allows up to 24 cultures to be wounded at the same time, while all of the other methods discussed here can only be used on one culture at a time. This represents a significant advantage for studies that use a large number of samples.

Que et al.'s (2011) simple incision method: (1) They reported consistent and reproducible cut lengths although exact dimensions were not discussed. (2) The model is very easy to use as all that is required is cardboard and a sterile knife. (3) The use of cardboard would negate the use of inverted microscopes to observe the wounding process. The grids could be printed onto acetate to allow light to pass through them. However, experience during this project showed that the printed areas cause distortions in the microscope image and make accurate observation difficult. This incision model is elegantly simple and does not require any

specialist material, however, as discussed in chapter 4, creating accurate cuts requires a very steady hand and cannot match the precision of a micromanipulator.

Hellman et al.'s (2010) laser axotomy method: (1) The system was precise and reproducible due to ability to control the positioning of the laser, via the microscope, and all of the variables associated with the laser. (2) The setup of the laser apparatus was somewhat complex. However, the injury process should only involved inputting the correct settings and then aligning the laser to its target. (3) Due to the laser being mounted on an inverted microscope, observations could be made during the wounding process. In their paper they even show images of the immediate effects of the laser in the nanoseconds afters it firing. However, this method of injury is unlikely to be encountered by neurons in anything other than the lab environment. The damage is created by plasma causing heat damage to the axons and stress from a shockwave induced in the media. The heat could also cause damage to the substrate.

Stretavan et al.'s (2005) micro-scale knives: (1) The knife can create precise and reproducible wounds by mounting it on a micromanipulator. (2) Once the knife has been fabricated, its use only requires positioning via a micromanipulator and microscope. (3) The forms part of a silicon nitride membrane, which is transparent, and so allows observation of the axon during cutting. However, the creation of the blades and its support frame is not a simple method or particularly cheap when compared to the other methods discussed here. The small length and height of the blade could also cause problems when larger wounds or multi-layered cultures, like the ones used in this project, are required.

In comparison to the other wound methods discussed here, only the laser and micro-scale knife can offer precision comparable to the automated cutting method. However, the laser system has a far more complex setup and inflicts damage via heat, which is unlikely to be the cause of SCI, and the micro-scale knife doesn't have the versatility of the automated method. Que et al.'s incision model relied on human control of the blade, which cannot match the precision of the micromanipulator, as shown in Chapter 4. The automated method cannot match the simplicity of Fayaz and Tator's impactor or the high throughput of Magou et al.'s stretch method. On the other hand, the automated cutting method allows observation throughout the wounding process and could aid in the understanding of tension within the cell layers. All of the methods create different types of injury that allow the various forms of SCI to be investigated. The stretch model represents the types of injury than can be caused by

the twisting of the body in a car crash; the contusion injury model can represent any number of impact injuries such as falling back first onto an object; while the automated cutting method represent any severing of the cord or the type of wounding that would occur during surgery on the spinal cord.

5.3 Microfabrication

5.3.1 Adherence to Design Principles

Throughout the project steps were taken to limit the complexity of the device design and manufacturing process. This served two purposes, firstly it limited manufacturing costs and, secondly, it ensured that potential end users would only require limited engineering knowledge. One example of this was during the initial problems with cells washing out of the containment area during seeding. A possible solution to this problem would be to enclose the containment area in a microfluidic (Beebe et al., 2002) device so that the contained area was a chamber that the cells would be trapped in by the row of pillars. However, this solution would add several design complexities such as ensuring that the flow would spread cells evenly across the chamber. The end user would also be required to be proficient in the use of microfluidic devices. Although the use of such a design would provide an elegant solution, the additional complexities it would add to the design and use of the device were deemed too great a drawback and so this solution was discarded.

Another example of the simplicity design principle was that of the repeated attempts to create the containment devices in SU-8. This was due to the desire to avoid adding etching steps to the microfabrications process as these additional steps increased the duration of the process and also added more potential causes of defects.

5.3.2 Design Evolution

The design of the full containment and alignment device went through several stages of evolution during the project; these are shown in Figure 83. The initial design featured a containment structure that resembled the Coliseum. This structure consisted of a semi-circle of pillars, a solid wall closing off the circle and an upper capping ring. Ridges stretched from the gaps between the pillars. A circular containment area was used as it was envisioned that it could be easily modified to allow axons to project in any direction. The capping ring was intended to stop and cells climbing over the pillars and also provided an area with a larger volume thus aiding the seeding process.

The initial coliseum design was quickly discarded as the obstacles arising from the practicalities of implementing the design were realised. A rectangular area replaced the circular containment area, as it was unlikely that the cells would be needed to grow in anything other than parallel lines. The capping ring was removed as removing photoresist from under the ring would likely add time to the development process and making the pillars and containment wall taller would create the required height. This 2nd generation design is shown below as B.

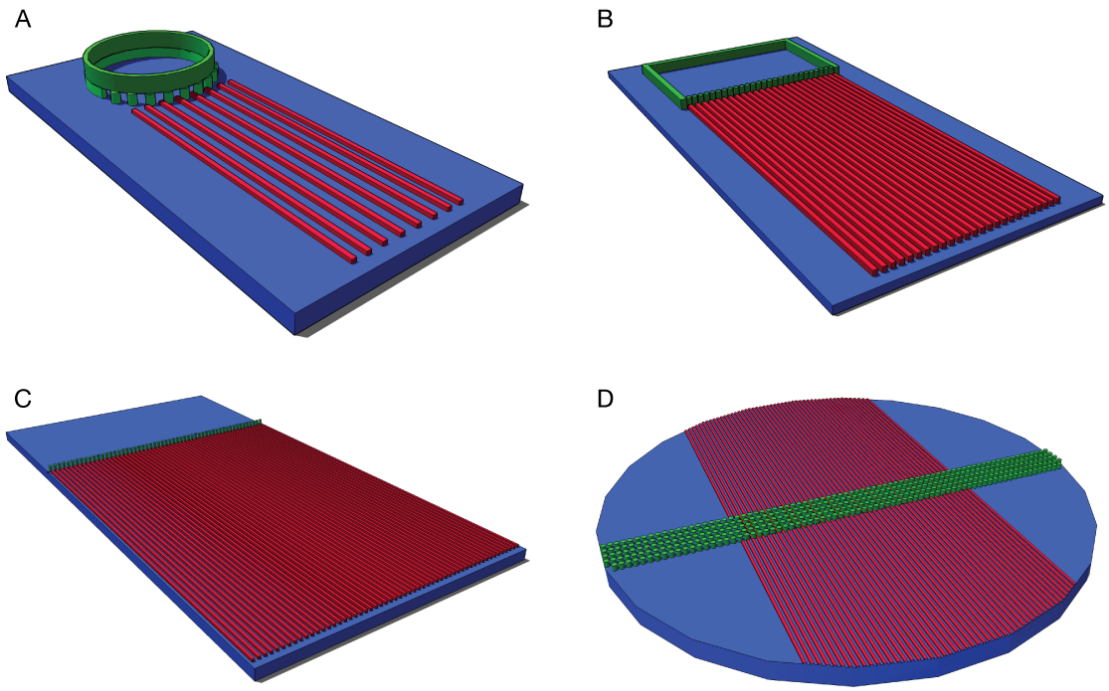

Figure 83: Sketches showing the evolution of the device design. A) Initial design with circular seeding area and capping ring. B) Revised design with rectangular containment area and removal of the capping ring. C) 3rd design with a row of pillars to form the containment area and ridges covering the width of the device. D) Final design with multiple pillar rows, ridges covering the length of the device, flat control areas and circular shape allowing it to easily fit into 24 well culture plates. In all sketches red shows the ridges, the pillars are green and blue is the flat surface of the device. N.B. Sketches are not to scale.

After the containment experiments showed that a fenced off containment area was impractical the design was revised once again to create the 3rd generation device shown in C. This design had a row of pillars that ran across the device that cut off the ridges from the flat seeding area. Also of note was that this design had the ridges covering the width of the device.

A single row of pillars was discovered to be insufficient to contain the cells and so the device was redesigned into its final form shown in D. This design had 5 rows of pillars and flat areas to either side of the ridges to create a built in control if required. Also of note is that the device is circular as this shape was the easiest to cut from the sheet of PDMS with the use of a cork borer.

5.3.3 Manufacturing Tolerances

During device fabrication the largest changes in dimensions occurred during the transfer of the mask design from chrome to ferric, with line and space width changing by up to 2.5 µm. Clean room staff conducted this process and so it could not be as tightly control as later stages of processing. Using the chrome masks for lithography could circumvent these changes in dimension. However, this would risk damaging the expensive masks and would make multi-layer alignment more difficult. A less problematic solution would be to change the design of the chrome masks to take into account the changes that occur during the transfer to ferric.

The other large change in dimensions came when PDMS devices were cast from the epoxy mould. This may have been due to reduced pit depth and ridge height on the epoxy mould. Another contributing factor could have been air trapped between the ridges or in the pits during casting. These devices were cast by pouring PDMS into the Petri dish lid as opposed to the usual casting jig method. Using the jig for future castings could help to eliminate trapped air as it tends to be pushed to the jig's outlet during PDMS injection.

5.4 Further Experiments

5.4.1 Pillar Shape

Throughout this project circular pillars were used. Different shapes of pillar could affect the probability of cells crossing the rows or turning parallel to them. For example a rectangular column may cause more cells to turn than the circular pillars, as cells would not be funnelled into the gaps. Diamond shaped columns would provide an even greater degree of funnelling than the circular pillars and could increase crossover. Triangular pillars would combine the properties of the square and diamond columns, this could potentially be used to encourage crossover from one direction only.

Hallstrom et al (Hallstrom et al., 2009) have shown that nano-wires patterned into echelons provide uni-directional guidance to axons. Similar structures made through conventional microfabrication could effect cell migration, for example, a series of echelons running across a device surface like the pillar rows could create a greater probability of turning than the pillars. Echelons could also be incorporated into a wall like structure to provide gateways in the structure that would only allow passage from one side of the device.

5.4.2 Effect of Pillars on Alignment

As previously discussed in Chapter 3, the pillar rows caused some axons to turn and align parallel to the rows. This effect could be utilised to create turning points on a device's surface. A potential device design is shown in Figure 84. In this design the cell would be seeded at the top of the device and the axons would grow along the ridges until they contacted the pillars. The pillars would then cause the axons to turn and grow along a new set of ridges aligned perpendicular to the set above the pillar row. The pillars would provide a turning post so that the axons would not be pulled off course once they had made the 90° turn. A visual representation of this effect is shown in Figure 85. Although the device below only shows one row of pillar, the addition of multiple rows would encourage more axons to change course. More complex designs could also be produced where axons could be directed off from the sides of a larger group of axons.

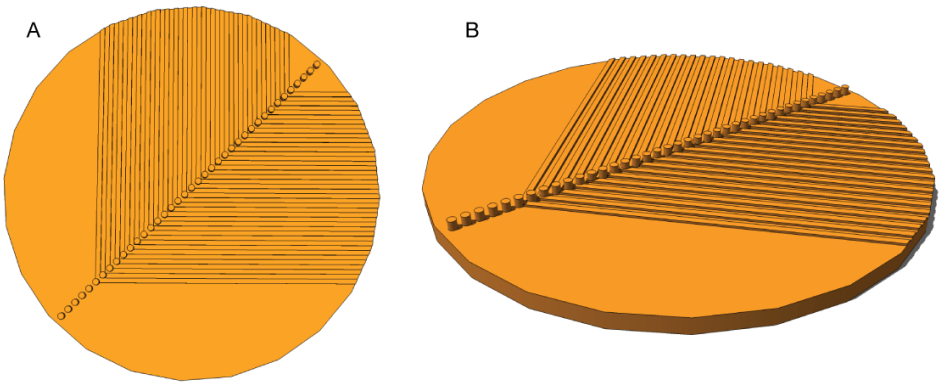

Figure 84: Sketches of a potential design for a device to cause turns in an axons path. The axons would potential grow along the ridges before contacting the pillars, turning 90° and continuing to grow perpendicular to their original path. A) Device shown in plan view. B) Device shown from an oblique angle.

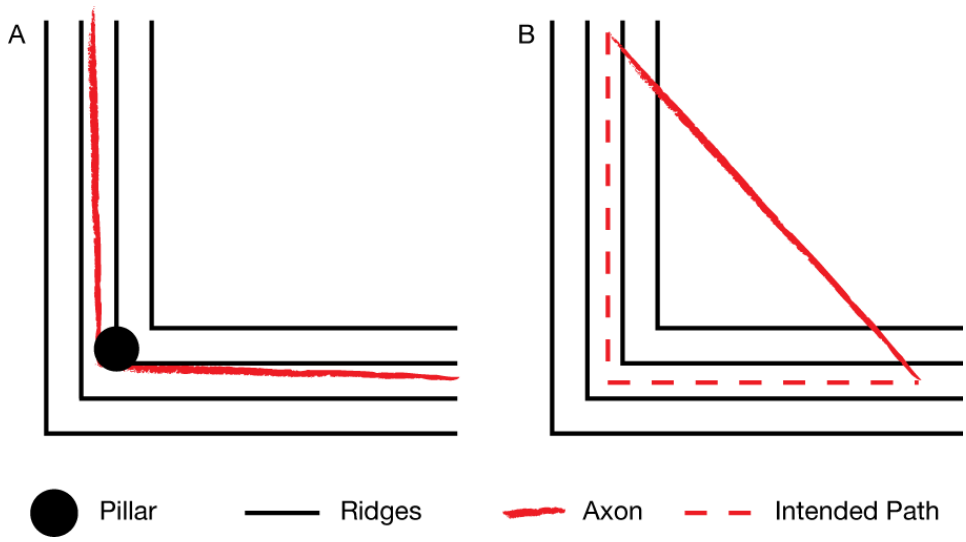

Figure 85: The potential 'turning post' effect a pillar would have upon an axon's path. A) The path of an axon growing from the top of the image, using the pillar as a turning post and then growing perpendicular to its original path. B) An axon growing along the ridges without the aid of a pillar turning post. As the growth cone moves along the horizontal ridges it will pull the axon off course, which results in the axon lying at an angle to the ridges.

5.4.3 Cytoskeleton

Further investigation into the distribution and role of various cell-cell connections would help to establish the causes of the wound shapes formed by the parallel and perpendicular cuts. For astrocytes, one proteins of particular interest would be CDH2, also know as neural cadherin, which plays a major role in cell to cell attachment (Boda-Heggemann et al., 2009). Clustering of cadherin attachments on the transverse axis could account for the differences in wounds size upon topography. CDH2 connects to the actin filaments through α- & β-catenin (Nelson, 2008), making these other potential targets for study. Another protein of interest would be CX43 (Olk et al., 2009), a connexin present in astrocytes which forms gap junctions between the cells. Vinculin is known to link e-cadherin to the actin network (Hazan et al., 1997), however it is currently not know as an interaction partner of n-cadherin and so is unlikely to be present in the astrocyte cadherin adhesion complex. Nonetheless, vinculin would be a worthy target for study as it is associated with focal adhesion plaques whose distribution can be effected by surface topography (Turner et al., 2000). A MG63 specific target would be CDH5 (Zhang et al., 2010), also called VE-cadherin, which plays a similar role to CDH2.

Cytochalasine (Cooper, 1987) and latrunculin (Peterson and Mitchison, 2002) provide methods of destabilising the actin network and so could be used to investigate its role in wound formation. Similarly, drug based inhibitors or knockouts could be used to study the proteins discussed above.

5.4.4 Extent of Damage

To study the extent of damage around the wound site, fluorescently labelled dextrans could be introduced into the culture media during or immediately following wounding. If molecules of the correct molecular weight are used, the cytoplasm will be impermeable to them. When a cell's membrane is compromised during wounding the dextran molecules will be able to enter; if the cytoplasm subsequently heals, the dextrans will be retained within the cell (Stroetz et al., 2001). This technique could be combined with a standard live/dead stain to determine which cells were unwounded; wounded and died; or wounded and survived. This method would also show whether cell damage is limited to the periphery of the wound site or if it spreads deeper into the cell layer.

5.4.5 Additional Wounding Parameters

During this project the main variables studied were blade & cell type, cut direction and cutting method. The parameters used for wounding were kept constant. Varying these parameters could provide additional data on wound formation. For example cut speed may affect the wound size. Other parameters of interest would be blade angle to the surface and cut depth.

5.5 Conclusions

A device, to be used in conjunction with myelination cell cultures, was developed that provide a hospitable environment for the cells, align axons and contain soma to a pre-defined area. In addition, an automated method of wounding cell layers was developed and investigations were made into the affect topography had upon wound formation.

Myelination spinal cord cultures and pure astorcyte cultures were able to survive on the devices past 28 days. However, myelination on the devices was not as abundant as on a glass coverslip.

Axons were patterned into parallel lines via the use of ridged surface topographies. It was found that 12.5 μm wide ridges provided the best degree of alignment. The rows of pillars adversely affected axon alignment, cause axons to turn perpendicular to the ridges or weave back and forth through multiple pillar rows.

The ability of rows of pillars to contain large populations of cells was investigated. It was found that five rows of pillars with 5 μm between the pillars provided the best containment for astrocyte cultures. However, the pillars were not required to contain the neuronal soma. Seeding the myelination cultures using Ibidi Culture Inserts resulted in the soma not straying from their original seeding area.

A wounding method was developed that used a micromanipulator to make automated cuts in cell layers. This method created highly precise, reproducible wounds and also allowed observations to be made during the wounding process. It was found that ridged topographies caused significant differences in wound size when the cut direction was altered. Cuts made parallel to the ridges resulted in small, high aspect ratio wounds; while perpendicular cuts created large, low aspect ratio wounds. There was also a significant difference between the wound sizes on topographies and those of flat PDMS.

Appendix

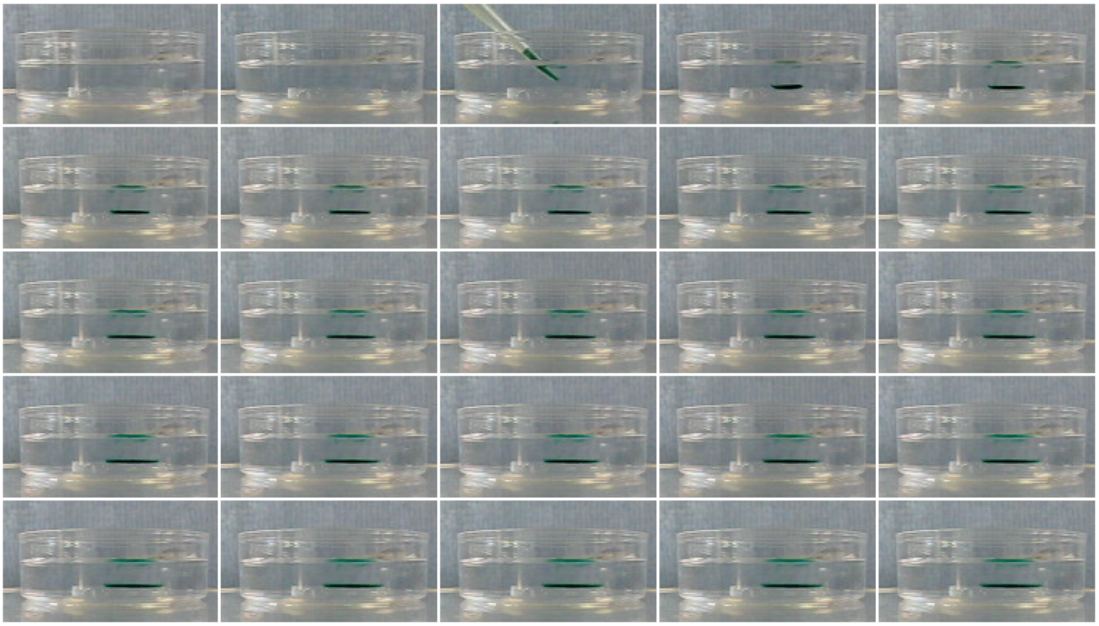

Appendix Figure 1: Room temperature dye being injected onto a device mounted in the bottom of a 50 mm petri dish. The dish was filled with RO water heated to 37 °C. The dye settled onto the surface of the device with only small amounts flowing off the side. A small amount of dye can be seen on the surface of the water. This was dye that was coating the outside of the pipette tip, which washed off as the tip was lowered into the water.

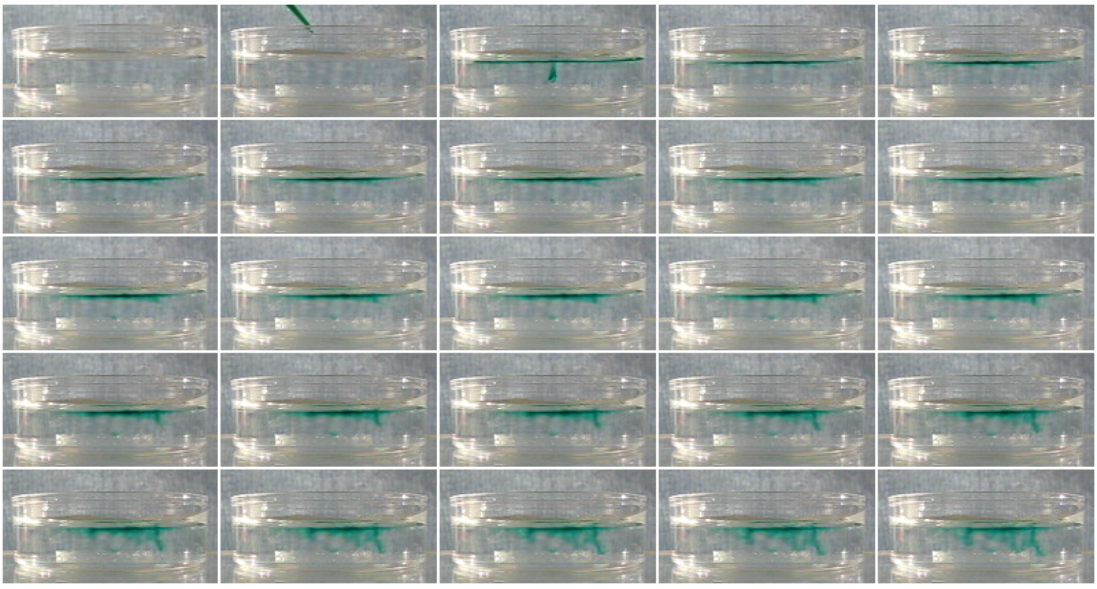

Appendix Figure 2: Room temperature dye injected just under the surface of the water filling a 50 mm petri dish. A device was mounted at the bottom of the dish. The dish was filled with RO water heated to 37 °C. The dye remained at the surface of the water, began to diffuse out, and after ~ 1 min began to sink.

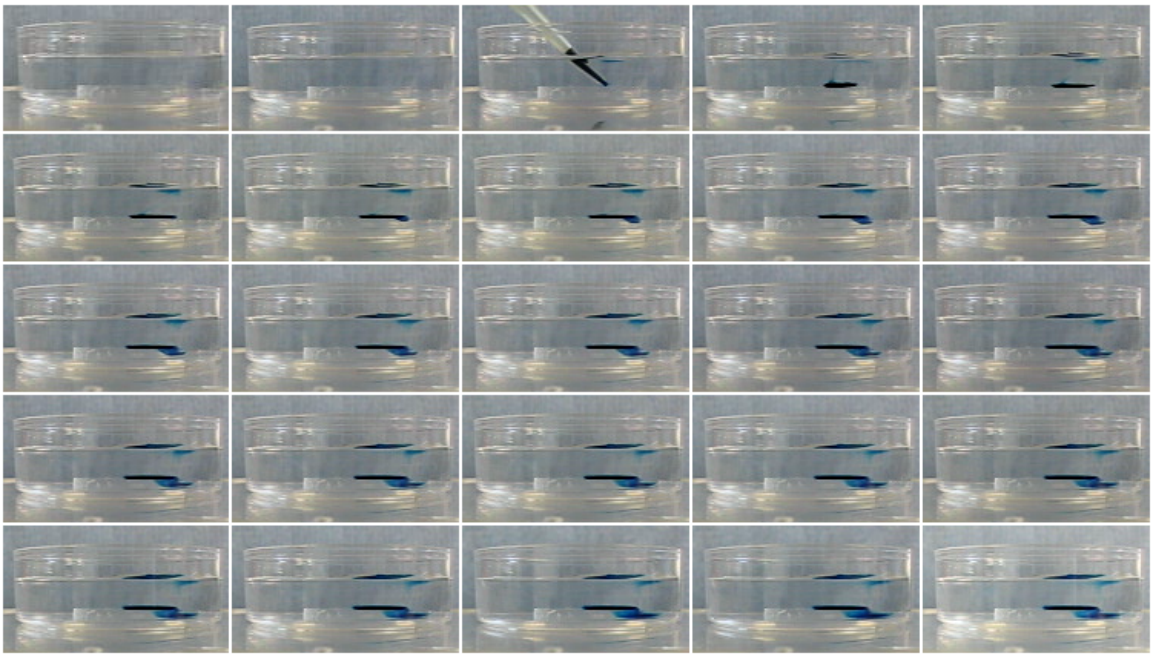

Appendix Figure 3: Dye cooled to 4 °C being injected onto a device mounted in the bottom of a 50 mm petri dish. The dish was filled with RO water heated to 37 °C. In a similar manner to the room temperature dye injected onto the device, the dye settled onto the device with small amounts flowing off the side.

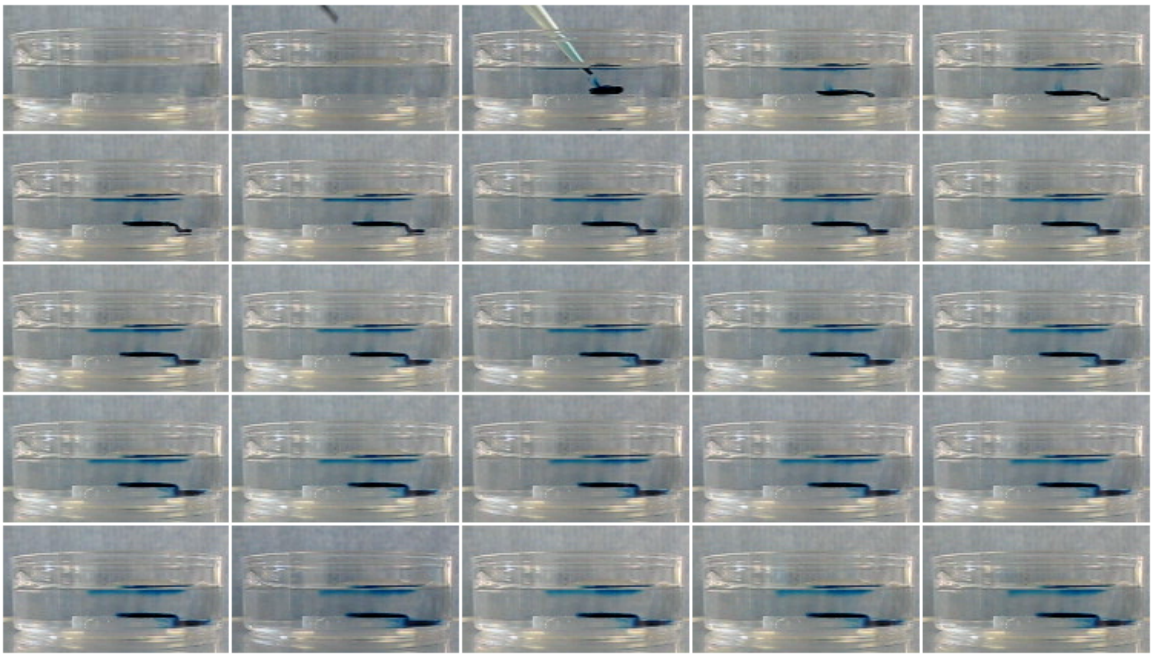

Appendix Figure 4: Dye chilled to 4 °C injected just under the surface of the water filling a 50 mm petri dish. The dye instantly sank to the bottom of the dish and settled onto the device. When compared to the 4 °C and room temperature injections onto the device; slightly more dye flowed over the side of the device.

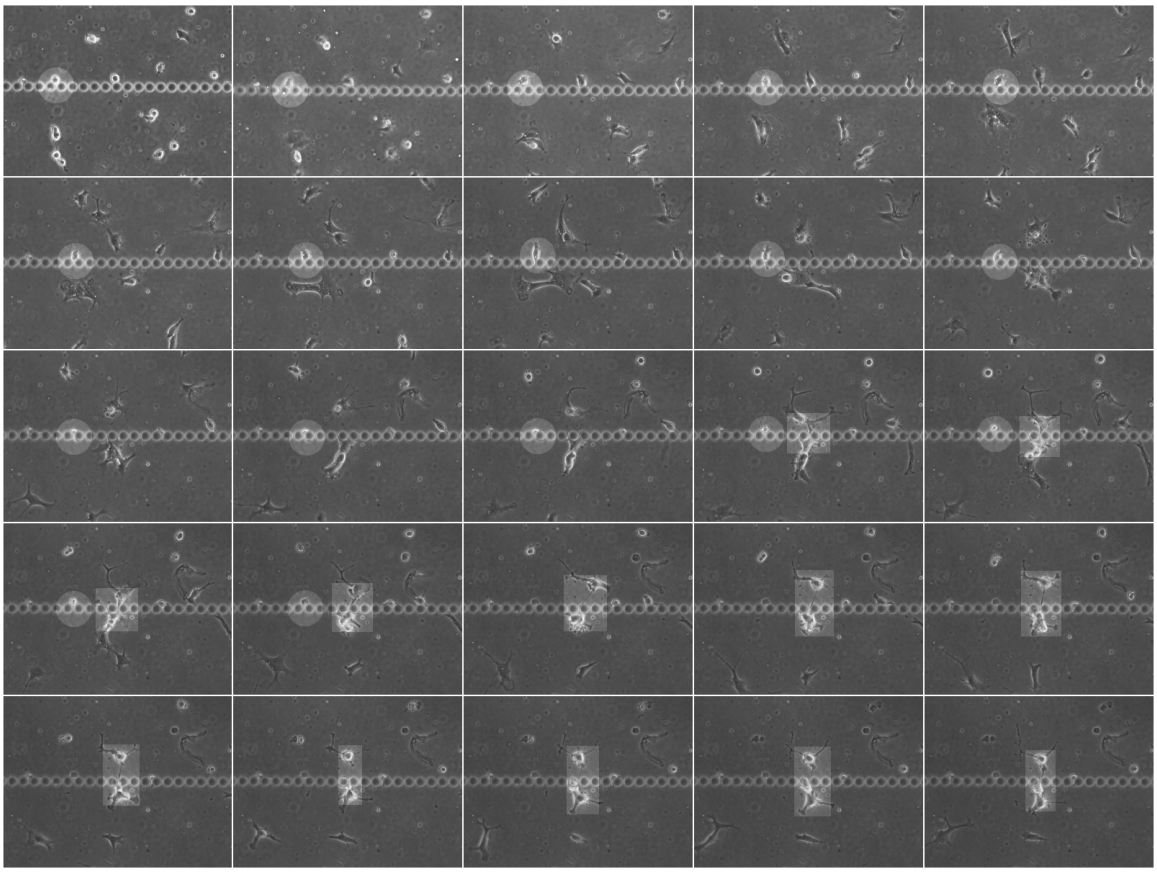

Appendix Figure 5: C2C12 cells attempting to squeeze through 4.5 µm gaps in a pillar wall. Diameter and height of the pillars was 25 µm. The cells were imaged every 2 mins over a 22 hour period, a selection of these images is shown. One cell, highlighted by the circle, could be seen extending a process through a gap and wrapping it around one of the pillars. It then tried to pull itself through the gap but could not fit. Eventually it either kills itself through effort or died due to environmental conditions. Two larger cells, highlighted by the rectangle, were observed extending multiple large processes through the gaps and linking up with each other. A further two cells on the right were seen failing to squeeze through the gaps.

References

ABU-RUB, M., MCMAHON, S., ZEUGOLIS, D. I., WINDEBANK, A. & PANDIT, A. 2010. Spinal cord injury in vitro: modelling axon growth inhibition. *Drug Discovery Today,* 15**,** 436-443.

ALBERT, D. J. 1969. A simple method of making cuts in brain tissue. *Physiology & Behavior,* 4**,** 863-864.

ALVARO, M., AARON, J. F. & SHUVO, R. 2006. Fabrication of multi-layer SU-8 microstructures. *Journal of Micromechanics and Microengineering***,** 276.

AZEVEDO, F. A. C., CARVALHO, L. R. B., GRINBERG, L. T., FARFEL, J. M., FERRETTI, R. E. L., LEITE, R. E. P., FILHO, W. J., LENT, R. & HERCULANO-HOUZEL, S. 2009. Equal numbers of neuronal and nonneuronal cells make the human brain an isometrically scaled-up primate brain. *The Journal of Comparative Neurology,* 513**,** 532-541.

BARDOUILLE, C., LEHMANN, J., HEIMANN, P. & JOCKUSCH, H. 2001. Growth and differentiation of permanent and secondary mouse myogenic cell lines on microcarriers. *Applied Microbiology and Biotechnology,* 55**,** 556-562.

BARNETT, S. C. & RIDDELL, J. S. 2004. Olfactory ensheathing cells (OECs) and the treatment of CNS injury: advantages and possible caveats. *Journal of Anatomy,* 204**,** 57-67.

BARNETT, S. C. & RIDDELL, J. S. 2007. Olfactory ensheathing cell transplantation as a strategy for spinal cord repair - what can it achieve? *Nature Clinical Practice Neurology,* 3**,** 152-161.

BEEBE, D. J., MENSING, G. A. & WALKER, G. M. 2002. Physics and applications of microfluidics in biology. *Annual Review of Biomedical Engineering,* 4**,** 261-286.

BODA-HEGGEMANN, J., REGNIER-VIGOUROUX, A. & FRANKE, W. W. 2009. Beyond vessels: occurrence and regional clustering of vascular endothelial (VE-)cadherin-containing junctions in non-endothelial cells. *Cell and Tissue Research,* 335**,** 49-65.

BOOMKAMP, S. D., RIEHLE, M. O., WOOD, J., OLSON, M. F. & BARNETT, S. C. 2012. The development of a rat in vitro model of spinal cord injury demonstrating the additive effects of rho and ROCK inhibitors on neurite outgrowth and myelination. *Glia,* 60**,** 441-456.

BRITLAND, S., MORGAN, H., WOJIAKSTODART, B., RIEHLE, M., CURTIS, A. & WILKINSON, C. 1996. Synergistic and hierarchical adhesive and topographic guidance of BHK cells. *Experimental Cell Research,* 228**,** 313-325.

CARNEGIE, D. J., STEVENSON, D. J., MAZILU, M., GUNN-MOORE, F. & DHOLAKIA, K. 2008. Guided neuronal growth using optical line traps. *Optics Express,* 16**,** 10507-10517.

CHOI, Y., POWERS, R., VERNEKAR, V., FRAZIER, A. B., LAPLACA, M. C., ALLEN, M. G. & ASME. Year. High aspect ratio SU-8 structures for 3-D culturing of neurons. *In:* ASME International Mechanical Engineering Congress, Nov 15-21 2003 Washington, DC. Amer Soc Mechanical Engineers, 651-654.

CLARK, P., CONNOLLY, P., CURTIS, A. S. G., DOW, J. A. T. & WILKINSON, C. D. W. 1987. TOPOGRAPHICAL CONTROL OF CELL BEHAVIOR .1. SIMPLE STEP CUES. *Development,* 99**,** 439-448.

CLARK, P., CONNOLLY, P., CURTIS, A. S. G., DOW, J. A. T. & WILKINSON, C. D. W. 1990. TOPOGRAPHICAL CONTROL OF CELL BEHAVIOR .2. MULTIPLE GROOVED SUBSTRATA. *Development,* 108**,** 635-644.
COOPER, J. A. 1987. Effects of cytochalasin and phalloidin on actin. *Journal of Cell Biology,* 105**,** 1473-1478.
CURTIS, A. & WILKINSON, C. 1997. Topographical control of cells. *Biomaterials,* 18**,** 1573-1583.
CURTIS, A. S. G. 1984. The competitive effects of serum-proteins on cell-adhesion. *Journal of Cell Science,* 71**,** 17-35.
CURTIS, A. S. G. & VARDE, M. 1964. CONTROL OF CELL BEHAVIOR - TOPOLOGICAL FACTORS. *Journal of the National Cancer Institute,* 33**,** 15-&.
CURTIS, A. S. G. & WILKINSON, C. D. 1998. Reactions of cells to topography. *Journal of Biomaterials Science-Polymer Edition,* 9**,** 1313-1329.
DEL CAMPO, A. & GREINER, C. 2007. SU-8: a photoresist for high-aspect-ratio and 3D submicron lithography. *Journal of Micromechanics and Microengineering,* 17**,** R81-R95.
DELIVOPOULOS, E., MURRAY, A. F., MACLEOD, N. K. & CURTIS, J. C. 2009. Guided growth of neurons and glia using microfabricated patterns of parylene-C on a SiO2 background. *Biomaterials,* 30**,** 2048-58.
DOLAN, E. J. & TATOR, C. H. 1979. A new method for testing the force of clips for aneurysms or experimental spinal cord compression. *Journal of Neurosurgery,* 51**,** 229-233.
DOUCETTE, R. 1990. Glial influences on axonal growth in the primary olfactory system. *Glia,* 3**,** 433-449.
DOWELL-MESFIN, N. M., ABDUL-KARIM, M. A., TURNER, A. M. P., SCHANZ, S., CRAIGHEAD, H. G., ROYSAM, B., TURNER, J. N. & SHAIN, W. 2004. Topographically modified surfaces affect orientation and growth of hippocampal neurons. *Journal of neural engineering,* 1**,** 78-90.
EAST, E., DE OLIVEIRA, D. B., GOLDING, J. P. & PHILLIPS, J. B. 2010. Alignment of Astrocytes Increases Neuronal Growth in Three-Dimensional Collagen Gels and Is Maintained Following Plastic Compression to Form a Spinal Cord Repair Conduit. *Tissue Engineering Part A,* 16**,** 3173-3184.
ENG, L. F. & GHIRNIKAR, R. S. 1994. GFAP and astrogliosis. *Brain Pathology,* 4**,** 229-237.
FARBMAN, A. I. 1990. Olfactory neurogenesis - genetic or environmental controls. *Trends in Neurosciences,* 13**,** 362-365.
FAULKNER, J. R., HERRMANN, J. E., WOO, M. J., TANSEY, K. E., DOAN, N. B. & SOFRONIEW, M. V. 2004. Reactive astrocytes protect tissue and preserve function after spinal cord injury. *Journal of Neuroscience,* 24**,** 2143-2155.
FAYAZ, I. & TATOR, C. H. 2000. Modeling axonal injury in vitro: injury and regeneration following acute neuritic trauma. *Journal of Neuroscience Methods,* 102**,** 69-79.
FELLER, L., BEARINGER, J. P., WU, L., HUBBELL, J. A., TEXTOR, M. & TOSATTI, S. 2008. Micropatterning of gold substrates based on poly(propylene sulfide-bl-ethylene glycol), (PPS-PEG) background passivation and the molecular-assembly patterning by lift-off (MAPL) technique. *Surface Science,* 602**,** 2305-2310.
FRIESEL, R. E. & MACIAG, T. 1995. Molecular mechanisms of angiogenesis - fibroblast growth-factor signal-transduction. *Faseb Journal,* 9**,** 919-925.
FRITZ, J. L. & OWEN, M. J. 1995. Hydrophobic recovery of plasma-treated polydimethylsiloxane. *Journal of Adhesion,* 54**,** 33-45.
FU, Y., CHIN, L. K., BOUROUINA, T., LIU, A. Q. & VANDONGEN, A. M. J. 2012. Nuclear deformation during breast cancer cell transmigration. *Lab on a Chip,* 12**,** 3774-3778.

GORDON-WEEKS, P. R. 2008. *Neuronal Growth Cones,* Cambridge, Cambridge University Press.

GUCK, J., SCHINKINGER, S., LINCOLN, B., WOTTAWAH, F., EBERT, S., ROMEYKE, M., LENZ, D., ERICKSON, H. M., ANANTHAKRISHNAN, R., MITCHELL, D., KAS, J., ULVICK, S. & BILBY, C. 2005. Optical deformability as an inherent cell marker for testing malignant transformation and metastatic competence. *Biophysical Journal,* 88**,** 3689-3698.

HALLSTROM, W., PRINZ, C. N., SUYATIN, D., SAMUELSON, L., MONTELIUS, L. & KANJE, M. 2009. Rectifying and Sorting of Regenerating Axons by Free-Standing Nanowire Patterns: A Highway for Nerve Fibers. *Langmuir,* 0.

HARRISON, R. G. 1914. The reaction of embryonic cells to solid structures. *Journal of Experimental Zoology,* 17**,** 521-544.

HAZAN, R. B., KANG, L., ROE, S., BORGEN, P. I. & RIMM, D. L. 1997. Vinculin is associated with the E-cadherin adhesion complex. *Journal of Biological Chemistry,* 272**,** 32448-32453.

HE, Z. G. & KOPRIVICA, V. 2004. The Nogo signaling pathway for regeneration block. *Annual Review of Neuroscience,* 27**,** 341-368.

HELLMAN, A. N., VAHIDI, B., KIM, H. J., MISMAR, W., STEWARD, O., JEON, N. L. & VENUGOPALAN, V. 2010. Examination of axonal injury and regeneration in micropatterned neuronal culture using pulsed laser microbeam dissection. *Lab on a Chip,* 10**,** 2083-2092.

HILLBORG, H. & GEDDE, U. W. 1999. Hydrophobicity changes in silicone rubbers. *Ieee Transactions on Dielectrics and Electrical Insulation,* 6**,** 703-717.

HOFFMAN-KIM, D., MITCHEL, J. A. & BELLAMKONDA, R. V. 2010. Topography, Cell Response, and Nerve Regeneration. *In:* YARMUSH, M. L., DUNCAN, J. S. & GRAY, M. L. (eds.) *Annual Review of Biomedical Engineering, Vol 12.* Palo Alto: Annual Reviews.

HOLDEN, L. J. & COLEMAN, M. D. 2007. Assessment of the astrogliotic responses of three human astrocytoma cell, lines to ethanol, trimethyltin chloride and acrylamide. *Toxicology,* 241**,** 75-83.

HUGHES, P. M., ANTHONY, D. C., RUDDIN, M., BOTHAM, M. S., RANKINE, E. L., SABLONE, M., BAUMANN, D., MIR, A. K. & PERRY, V. H. 2003. Focal lesions in the rat central nervous system induced by endothelin-1. *Journal of Neuropathology and Experimental Neurology,* 62**,** 1276-1286.

IRIMIA, D., CHARRAS, G., AGRAWAL, N., MITCHISON, T. & TONER, M. 2007. Polar stimulation and constrained cell migration in microfluidic channels. *Lab on a Chip,* 7**,** 1783-1790.

KASLIN, J., GANZ, J. & BRAND, M. 2008. Proliferation, neurogenesis and regeneration in the non-mammalian vertebrate brain. *Philosophical Transactions of the Royal Society B-Biological Sciences,* 363**,** 101-122.

KELLEHER, M. O., MYLES, L. M., AL-ABRI, R. K. & GLASBY, M. A. 2006. The use of ciliary neurotrophic factor to promote recovery after peripheral nerve injury by delivering it at the site of the cell body. *Acta Neurochirurgica,* 148**,** 55-61.

KIM, B., PETERSON, E. T. K., PAPAUTSKY, I. & IEEE 2004. Long-term stability of plasma oxidized PDMS surfaces. *Proceedings of the 26th Annual International Conference of the Ieee Engineering in Medicine and Biology Society, Vols 1-7.* New York: Ieee.

KOLIND, K., DOLATSHAHI-PIROUZ, A., LOVMAND, J., PEDERSEN, F. S., FOSS, M. & BESENBACHER, F. 2010. A combinatorial screening of human fibroblast responses on micro-structured surfaces. *Biomaterials,* 31**,** 9182-9191.

KRASSIOUKOV, A. V., ACKERY, A., SCHWARTZ, G., ADAMCHIK, Y., LIU, Y. & FEHLINGS, M. G. 2002. An in vitro model of neurotrauma in organotypic spinal cord cultures from adult mice. *Brain Research Protocols,* 10**,** 60-68.

LAKATOS, A., FRANKLIN, R. J. M. & BARNETT, S. C. 2000. Olfactory ensheathing cells and Schwann cells differ in their in vitro interactions with astrocytes. *Glia,* 32**,** 214-225.

LAPLACA, M. C., SIMON, C. M., PRADO, G. R. & CULLEN, D. K. 2007. CNS injury biomechanics and experimental models. *In:* WEBER, J. T. & MAAS, A. I. R. (eds.) *Neurotrauma: New Insights into Pathology and Treatment.* Amsterdam: Elsevier Science Bv.

LEACH, J. B., ACHYUTA, A. K. H. & MURTHY, S. K. 2010. Bridging the Divide between Neuroprosthetic Design, Tissue Engineering and Neurobiology. *Frontiers in neuroengineering,* 2**,** 18.

LEE, J. W., LEE, K. S., CHO, N., JU, B. K., LEE, K. B. & LEE, S. H. 2007. Topographical guidance of mouse neuronal cell onSiO(2) microtracks. *Sensors and Actuators B-Chemical,* 128**,** 252-257.

LEE, K. Y., LABIANCA, N., RISHTON, S. A., ZOLGHARNAIN, S., GELORME, J. D., SHAW, J. & CHANG, T. H.-P. Year. Micromachining applications of a high resolution ultrathick photoresist. *In*, 1995. AVS, 3012-3016.

LEVISON, D. 2008. *Muir's Textbook of Pathology,* London, Arnold.

LIETZ, M., DREESMANN, L., HOSS, M., OBERHOFFNER, S. & SCHLOSSHAUER, B. 2006. Neuro tissue engineering of glial nerve guides and the impact of different cell types. *Biomaterials,* 27**,** 1425-1436.

LIN, S.-P., CHUANG, T.-L., CHEN, J.-J. J. & TZENG, S.-F. 2004. Design of Microscopy-based Microcontact Printing Stamp and Alignment Device for Patterned Neuronal Growth. *Journal of Medical and Biological Engineering,* 24**,** 45-50.

LU, P., BLESCH, A., GRAHAM, L., WANG, Y. Z., SAMARA, R., BANOS, K., HARINGER, V., HAVTON, L., WEISHAUPT, N., BENNETT, D., FOUAD, K. & TUSZYNSKI, M. H. 2012. Motor Axonal Regeneration after Partial and Complete Spinal Cord Transection. *Journal of Neuroscience,* 32**,** 8208-8218.

LUSSI, J. W., FALCONNET, D., HUBBELL, J. A., TEXTOR, M. & CSUCS, G. 2006. Pattern stability under cell culture conditions - A comparative study of patterning methods based on PLL-g-PEG background passivation. *Biomaterials,* 27**,** 2534-2541.

MADOU, M. J. 2002. *Fundamentals of Microfabrication: The Science of Miniaturization,* London, CRC Press.

MAGOU, G. C., GUO, Y., CHOUDHURY, M., CHEN, L., HUSUSAN, N., MASOTTI, S. & PFISTER, B. J. 2011. Engineering a High Throughput Axon Injury System. *Journal of Neurotrauma,* 28**,** 2203-2218.

MCCAIG, C. D., RAJNICEK, A. M., SONG, B. & ZHAO, M. 2005. Controlling Cell Behavior Electrically: Current Views and Future Potential. *Physiol. Rev.,* 85**,** 943-978.

MICHEL, R., LUSSI, J. W., CSUCS, G., REVIAKINE, I., DANUSER, G., KETTERER, B., HUBBELL, J. A., TEXTOR, M. & SPENCER, N. D. 2002. Selective molecular assembly patterning: A new approach to micro- and nanochemical patterning of surfaces for biological applications. *Langmuir,* 18**,** 3281-3287.

MICROCHEMICALS. 2010. *Exposure of Photoresists* [Online]. Available: http://www.microchemicals.eu/technical_information/ [Accessed 11-02 2012].

MILNER, R., HUANG, X., WU, J., NISHIMURA, S., PYTELA, R., SHEPPARD, D. & FFRENCH-CONSTANT, C. 1999. Distinct roles for astrocyte alphavbeta5 and alphavbeta8 integrins in adhesion and migration. *Journal of Cell Science,* 112**,** 4271-4279.

MIYOSHI, H., JU, J. M., LEE, S. M., CHO, D. J., KO, J. S., YAMAGATA, Y. & ADACHI, T. 2010. Control of highly migratory cells by microstructured surface based on transient change in cell behavior. *Biomaterials,* 31**,** 8539-8545.

MOORE, J. W. & COLE, K. S. 1960. Resting and action potentials of the squid giant axon in-vivo. *Journal of General Physiology,* 43**,** 961-970.

MUKHIN, A. G., IVANOVA, S. A., KNOBLACH, S. M. & FADEN, A. I. 1997. New in vitro model of traumatic neuronal injury evaluation of secondary injury and glutamate receptor-mediated neurotoxicity. *Journal of Neurotrauma,* 14**,** 651-663.

MULLEN, R. J., BUCK, C. R. & SMITH, A. M. 1992. Neun, a neuronal specific nuclear-protein in vertebrates. *Development,* 116**,** 201-211.

MURINSON, B. B., ARCHER, D. R., LI, Y. B. & GRIFFIN, J. W. 2005. Degeneration of myelinated efferent fibers prompts mitosis in Remak Schwann cells of uninjured C-fiber afferents. *Journal of Neuroscience,* 25**,** 1179-1187.

NAGY, J. I., DUDEK, F. E. & RASH, J. E. 2004. Update on connexins and gap junctions in neurons and glia in the mammalian nervous system. *Brain Research Reviews,* 47**,** 191-215.

NAGY, J. I. & RASH, J. E. 2003. Astrocyte and oligodendrocyte connexins of the glial syncytium in relation to astrocyte anatomical domains and spatial buffering. *Cell Communication and Adhesion,* 10**,** 401-406.

NAKAHARA, Y., GAGE, F. H. & TUSZYNSKI, M. H. Year. Grafts of fibroblasts genetically modified to secrete NGF, BDNF, NT-3, or basic FGF elicit differential responses in the adult spinal cord. *In:* 2nd Annual Meeting of the American-Society-for-Neural-Transplantation, Apr 27-29 1995 Clearwater, Fl. Pergamon-Elsevier Science Ltd, 191-204.

NELSON, W. J. 2008. Regulation of cell-cell adhesion by the cadherin-catenin complex. *Biochemical Society Transactions,* 36**,** 149-155.

NEWMAN, E. A. 2001. Propagation of Intercellular Calcium Waves in Retinal Astrocytes and Müller Cells. *Journal of Neuroscience,* 21**,** 2215-2223.

NI, M., TONG, W. H., CHOUDHURY, D., RAHIM, N. A. A., ILIESCU, C. & YU, H. 2009. Cell Culture on MEMS Platforms: A Review. *International Journal of Molecular Sciences,* 10**,** 5411-5441.

NORENBERG, M. D., SMITH, J. & MARCILLO, A. 2004. The pathology of human spinal cord injury: Defining the problems. *Journal of Neurotrauma,* 21**,** 429-440.

NSCISC. 2012. *Spinal Cord Injury Facts and Figures at a Glance* [Online]. Available: https://www.nscisc.uab.edu/PublicDocuments/fact_figures_docs/Facts%202012%20Feb%20Final.pdf [Accessed 25/08/2012 2012].

OFFENHAUSSER, A., BOCKER-MEFFERT, S., DECKER, T., HELPENSTEIN, R., GASTEIER, P., GROLL, J., MOLLER, M., RESKA, A., SCHAFER, S., SCHULTE, P. & VOGT-EISELE, A. 2007. Microcontact printing of proteins for neuronal cell guidance. *Soft Matter,* 3**,** 290-298.

OLK, S., ZOIDL, G. & DERMIETZEL, R. 2009. Connexins, Cell Motility, and the Cytoskeleton. *Cell Motility and the Cytoskeleton,* 66**,** 1000-1016.

ONIFER, S. M., RABCHEVSKY, A. G. & SCHEFF, S. W. 2007. Rat models of traumatic spinal cord injury to assess motor recovery. *Ilar Journal,* 48**,** 385-395.

OUDEGA, M. & HAGG, T. 1996. Nerve growth factor promotes regeneration of sensory axons into adult rat spinal cord. *Experimental Neurology,* 140**,** 218-229.

OYESIKU, N. M., WILCOX, J. N. & WIGSTON, D. J. 1997. Changes in expression of ciliary neurotrophic factor (CNTF) and CNTF-receptor alpha after spinal cord injury. *Journal of Neurobiology,* 32**,** 251-261.

PARKIN, S., KNONER, G., SINGER, W., NIEMINEN, T. A., HECKENBERG, N. R. & RUBINSZTEIN-DUNLOP, H. 2007. Optical torque on microscopic objects. *In:*

BERNS, M. W. & GREULICH, K. O. (eds.) *Laser Manipulation of Cells and Tissues.* San Diego: Elsevier Academic Press Inc.
PENG, H., SHAH, W., HOLLAND, P. & CARBONETTO, S. 2008. Integrins and dystroglycan regulate astrocyte wound healing: The integrin beta 1 subunit is necessary for process extension and orienting the microtubular network. *Developmental Neurobiology,* 68**,** 559-574.
PETERSON, J. R. & MITCHISON, T. J. 2002. Small molecules, big impact: A history of chemical inhibitors and the cytoskeleton. *Chemistry & Biology,* 9**,** 1275-1285.
PURVES, D. 2008. *Neuroscience,* Sunderland, Sinauer Associates.
QUE, H. P., LIU, Y., JIA, Y. F. & LIU, S. J. 2011. Establishment and assessment of a simple and easily reproducible incision model of spinal cord neuron cells in vitro. *In Vitro Cellular & Developmental Biology-Animal,* 47**,** 558-564.
RABCHEVSKY, A. G. 2006. Segmental organization of spinal reflexes mediating autonomic dysreflexia after spinal cord injury. *Autonomic Dysfunction after Spinal Cord Injury,* 152**,** 265-274.
RAJNICEK, A. M., BRITLAND, S. & MCCAIG, C. D. 1997. Contact guidance of CNS neurites on grooved quartz: influence of groove dimensions, neuronal age and cell type. *Journal of Cell Science,* 110**,** 2905-2913.
RAJNICEK, A. M. & MCCAIG, C. D. 1997. Guidance of CNS growth cones by substratum grooves and ridges: effects of inhibitors of the cytoskeleton, calcium channels and signal transduction pathways. *Journal of Cell Science,* 110**,** 2915-2924.
RAMON-CUETO, A., CORDERO, M. I., SANTOS-BENITO, F. F. & AVILA, J. 2000. Functional recovery of paraplegic rats and motor axon regeneration in their spinal cords by olfactory ensheathing glia. *Neuron,* 25**,** 425-435.
RECKNOR, J. B., RECKNOR, J. C., SAKAGUCHI, D. S. & MALLAPRAGADAA, S. K. 2004. Oriented astroglial cell growth on micropatterned polystyrene substrates. *Biomaterials,* 25**,** 2753-2767.
REID, R. & ROBERTS, F. 2005. *Pathology Illustrated,* Edinburgh, Elsevier/Chruchill Livingstone.
ROBINS, S. L. & FEHLINGS, M. G. 2008. Models of experimental spinal cord injury: Translational relevance and impact. *Drug Discovery Today: Disease Models,* 5**,** 5-11.
ROBINSON, K. R. & CORMIE, P. 2008. Electric field effects on human spinal injury: Is there a basis in the in vitro studies? *Developmental Neurobiology,* 68**,** 274-280.
ROMERO, M. I., RANGAPPA, N., GARRY, M. G. & SMITH, G. M. 2001. Functional regeneration of chronically injured sensory afferents into adult spinal cord after neurotrophin gene therapy. *Journal of Neuroscience,* 21**,** 8408-8416.
SAGER, P. R. 1989. Cytoskeletal Effects Of Acrylamide And 2,5-Hexanedione - Selective Aggregation Of Vimentin Filaments. *Toxicology and Applied Pharmacology,* 97**,** 141-155.
SASAKI, T., HIRABAYASHI, J., MANYA, H., KASAI, K.-I. & ENDO, T. 2004. Galectin-1 induces astrocyte differentiation, which leads to production of brain-derived neurotrophic factor. *Glycobiology,* 14**,** 357-363.
SCHEFF, S. W., RABCHEVSKY, A. G., FUGACCIA, I., MAIN, J. A. & LUMPP, J. E. 2003. Experimental modeling of spinal cord injury: Characterization of a force-defined injury device. *Journal of Neurotrauma,* 20**,** 179-193.
SCHMIDT, C. E. & LEACH, J. B. 2003. Neural tissue engineering: Strategies for repair and regeneration. *Annual Review of Biomedical Engineering,* 5**,** 293-347.
SCHRIMSHER, G. W. & REIER, P. J. 1993. Forelimb Motor-Performance Following Dorsal Column, Dorsolateral Funiculi, Or Ventrolateral Funiculi Lesions Of The Cervical Spinal-Cord In The Rat. *Experimental Neurology,* 120**,** 264-276.

SHIN, D. & ATHANASIOU, K. 1999. Cytoindentation for obtaining cell biomechanical properties. *Journal of Orthopaedic Research,* 17**,** 880-890.
SILVER, J. & MILLER, J. H. 2004. Regeneration beyond the glial scar. *Nature Reviews Neuroscience,* 5**,** 146-156.
SORENSEN, A., ALEKSEEVA, T., KATECHIA, K., ROBERTSON, M., RIEHLE, M. O. & BARNETT, S. C. 2007. Long-term neurite orientation on astrocyte monolayers. aligned by microtopography. *Biomaterials,* 28**,** 5498-5508.
SORENSEN, A., MOFFAT, K., THOMSON, C. & BARNETT, S. C. 2008. Astrocytes, but not olfactory ensheathing cells or Schwann cells, promote myelination of CNS axons in vitro. *Glia,* 56**,** 750-763.
SRETAVAN, D. W., CHANG, W., HAWKES, E., KELLER, C. & KLIOT, M. 2005. Microscale surgery on single axons. *Neurosurgery,* 57**,** 635-645.
STEPIEN, E., STANISZ, J. & KOROHODA, W. 1999. Contact guidance of chick embryo neurons on single scratches in glass and on underlying aligned human skin fibroblasts. *Cell Biology International,* 23**,** 105-116.
STEWARD, O., SHARP, K., SELVAN, G., HADDEN, A., HOFSTADTER, M., AU, E. & ROSKAMS, J. 2006. A re-assessment of the consequences of delayed transplantation of olfactory lamina propria following complete spinal cord transection in rats. *Experimental Neurology,* 198**,** 483-499.
STOLL, G., GRIFFIN, J. W., LI, C. Y. & TRAPP, B. D. 1989. Wallerian degeneration in the peripheral nervous-system - participation of both schwann-cells and macrophages in myelin degradation. *Journal of Neurocytology,* 18**,** 671-683.
STROETZ, R. W., VLAHAKIS, N. E., WALTERS, B. J., SCHROEDER, M. A. & HUBMAYR, R. D. 2001. Validation of a new live cell strain system: characterization of plasma membrane stress failure. *Journal of Applied Physiology,* 90**,** 2361-2370.
SUN, M. Z., MCGOWAN, M., KINGHAM, P. J., TERENGHI, G. & DOWNES, S. 2010. Novel thin-walled nerve conduit with microgrooved surface patterns for enhanced peripheral nerve repair. *Journal of Materials Science-Materials in Medicine,* 21**,** 2765-2774.
TAO, S. L., POPAT, K. C., NORMAN, J. J. & DESAI, T. A. 2008. Surface modification of SU-8 for enhanced biofunctionality and nonfouling properties. *Langmuir,* 24**,** 2631-2636.
TAYLOR, A. M., BLURTON-JONES, M., RHEE, S. W., CRIBBS, D. H., COTMAN, C. W. & JEON, N. L. 2005. A microfluidic culture platform for CNS axonal injury, regeneration and transport. *Nature Methods,* 2**,** 599-605.
TOBIAS, C. A., SHUMSKY, J. S., SHIBATA, M., TUSZYNSKI, M. H., FISCHER, I., TESSLER, A. & MURRAY, M. 2003. Delayed grafting of BDNF and NT-3 producing fibroblasts into the injured spinal cord stimulates sprouting, partially rescues axotornized red nucleus neurons from loss and atrophy, and provides limited regeneration. *Experimental Neurology,* 184**,** 97-113.
TOFT, A., SCOTT, D. T., BARNETT, S. C. & RIDDELL, J. S. 2007. Electrophysiological evidence that olfactory cell transplants improve function after spinal cord injury. *Brain,* 130**,** 970-984.
TOMASELLI, K. J., NEUGEBAUER, K. M., BIXBY, J. L., LILIEN, J. & REICHARDT, L. F. 1988. N-cadherin and integrins - 2 receptor systems that mediate neuronal process outgrowth on astrocyte surfaces. *Neuron,* 1**,** 33-43.
TOTH, A., BERTOTI, I., BLAZSO, M., BANHEGYI, G., BOGNAR, A. & SZAPLONCZAY, P. 1994. Oxidative damage and recovery of silicone-rubber surfaces .1. X-ray photoelectron spectroscopic study. *Journal of Applied Polymer Science,* 52**,** 1293-1307.
TSONIS, P. A. 2000. Regeneration in vertebrates. *Developmental Biology,* 221**,** 273-284.

TURNER, A. M. P., DOWELL, N., TURNER, S. W. P., KAM, L., ISAACSON, M., TURNER, J. N., CRAIGHEAD, H. G. & SHAIN, W. 2000. Attachment of astroglial cells to microfabricated pillar arrays of different geometries. *Journal of Biomedical Materials Research,* 51**,** 430-441.

VARGAS, M. E. & BARRES, B. A. 2007. Why is Wallerian degeneration in the CNS so slow? *Annual Review of Neuroscience,* 30**,** 153-179.

VAUGHN, J. E. & PEASE, D. C. 1970. Electron microscopic studies of wallerian degeneration in rat optic nerves .2. astrocytes, oligodendrocytes and adventitial cells. *Journal of Comparative Neurology,* 140**,** 207-&.

VIRCHOW, R. 1846. Ueber das granulirte Aussehen der Wandungen der Gehirnventrikel. *Allg Z Psychiat***,** 242-250.

VON PHILIPSBORN, A. C., LANG, S., BERNARD, A., LOESCHINGER, J., DAVID, C., LEHNERT, D., BASTMEYER, M. & BONHOEFFER, F. 2006. Microcontact printing of axon guidance molecules for generation of graded patterns. *Nature Protocols,* 1**,** 1322-1328.

WALBOOMERS, X. F., CROES, H. J. E., GINSEL, L. A. & JANSEN, J. A. 1999. Contact guidance of rat fibroblasts on various implant materials. *Journal of Biomedical Materials Research,* 47**,** 204-212.

WALZ, W. 2000. Role of astrocytes in the clearance of excess extracellular potassium. *Neurochemistry International,* 36**,** 291-300.

WEIL, Z. M., NORMAN, G. J., DEVRIES, A. C. & NELSON, R. J. 2008. The injured nervous system: A Darwinian perspective. *Progress in Neurobiology,* 86**,** 48-59.

WEISS, P. 1945. Experiments on cell and axon orientation in vitro - the role of colloidal exudates in tissue organization. *Journal of Experimental Zoology,* 100**,** 353-386.

WILBUR, J. L., KUMAR, A., KIM, E. & WHITESIDES, G. M. 1994. Microfabrication by microcontact printing of self-assembled monolayers. *Advanced Materials,* 6**,** 600-604.

YANG, L. J. S. & SCHNAAR, R. L. 2008. Axon regeneration inhibitors. *Neurological Research,* 30**,** 1047-1052.

YAO, L., WANG, S. G., CUI, W. J., SHERLOCK, R., O'CONNELL, C., DAMODARAN, G., GORMAN, A., WINDEBANK, A. & PANDIT, A. 2009. Effect of functionalized micropatterned PLGA on guided neurite growth. *Acta Biomaterialia,* 5**,** 580-588.

YIU, G. & HE, Z. G. 2006. Glial inhibition of CNS axon regeneration. *Nature Reviews Neuroscience,* 7**,** 617-627.

ZECK, G. & FROMHERZ, P. 2001. Noninvasive neuroelectronic interfacing with synaptically connected snail neurons immobilized on a semiconductor chip. *Proceedings of the National Academy of Sciences of the United States of America,* 98**,** 10457-10462.

ZHANG, L.-Z., MEI, J., QIAN, Z.-K., CAI, X.-S., JIANG, Y. & HUANG, W.-D. 2010. The Role of VE-cadherin in Osteosarcoma Cells. *Pathology & Oncology Research,* 16**,** 111-117.

ZHOU, J., ELLIS, A. V. & VOELCKER, N. H. 2010. Recent developments in PDMS surface modification for microfluidic devices. *Electrophoresis,* 31**,** 2-16.

ZHOU, J., KHODAKOV, D. A., ELLIS, A. V. & VOELCKER, N. H. 2012. Surface modification for PDMS-based microfluidic devices. *Electrophoresis,* 33**,** 89-104.